

2010-12-12

# MRI Contrast Agent Studies of Compartmental Differentiation, Dose-dependence, and Tumor Characterization in the Brain

Mohammed Salman Shazeeb  
*Worcester Polytechnic Institute*

Follow this and additional works at: <https://digitalcommons.wpi.edu/etd-dissertations>

---

## Repository Citation

Shazeeb, M. S. (2010). *MRI Contrast Agent Studies of Compartmental Differentiation, Dose-dependence, and Tumor Characterization in the Brain*. Retrieved from <https://digitalcommons.wpi.edu/etd-dissertations/417>

This dissertation is brought to you for free and open access by Digital WPI. It has been accepted for inclusion in Doctoral Dissertations (All Dissertations, All Years) by an authorized administrator of Digital WPI. For more information, please contact [wpi-etd@wpi.edu](mailto:wpi-etd@wpi.edu).

**MRI CONTRAST AGENT STUDIES OF COMPARTMENTAL  
DIFFERENTIATION, DOSE-DEPENDENCE, AND TUMOR  
CHARACTERIZATION IN THE BRAIN**

A Dissertation Presented

By

**MOHAMMED SALMAN SHAZEEB**

Submitted to the Faculty of the

**UNIVERSITY OF MASSACHUSETTS MEDICAL SCHOOL**

and

**WORCESTER POLYTECHNIC INSTITUTE**

in partial fulfillment of the requirements for the degree of

**DOCTOR OF PHILOSOPHY**

November 23, 2010

**BIOMEDICAL ENGINEERING AND MEDICAL PHYSICS**

**MRI CONTRAST AGENT STUDIES OF COMPARTMENTAL  
DIFFERENTIATION, DOSE-DEPENDENCE, AND TUMOR  
CHARACTERIZATION IN THE BRAIN**

A Dissertation Presented

By

Mohammed Salman Shazeeb

The signatures of the Dissertation Defense Committee signifies  
completion and approval as to style and content of the Dissertation



Christopher Sotak, Ph.D., Thesis Advisor



Michael King, Ph.D., Member of Committee



Ann Rittenhouse, Ph.D., Member of Committee

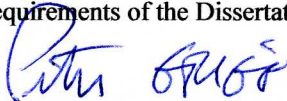


Alexei Bogdanov Jr., Ph.D., Member of Committee



Karl Helmer, Ph.D., Member of Committee

The signature of the Chair of the Committee signifies that the written dissertation meets  
the requirements of the Dissertation Committee



Peter Grigg, Ph.D., Chair of Committee

The signature of the Dean of the Graduate School of Biomedical Sciences signifies  
that the student has met all graduation requirements of the school.



Anthony Carruthers, Ph.D.,

Dean of the Graduate School of Biomedical Sciences  
Program

Biomedical Engineering and Medical Physics

November 23, 2010

إهداء  
إلى والِدَي محمد رفيق العالم و ديلارا بيغم شيرين،  
و إلى أمتي

*Dedicated to my parents,  
Mohammed Rafique Al-Alam and Dilara Begum Shirin,  
and to my Ummah (Nation)*

## Acknowledgements

In the name of Allah, the All Merciful, the Especially Merciful, the Creator and Lord of the Worlds, the Master of the Day of Judgment. I begin by thanking and praising Almighty Allah Who gave me the ability to complete this work. Then, I thank my parents for all their love and support without whom I would not be in this position today. Mom and Dad, this one's for you. I also thank my sister Rizwana Seeham for her annoyance 😊.

I would like to thank my major advisor, Dr. Christopher H. Sotak, for all his support, guidance, and dedicated mentorship during my stay here at Worcester Polytechnic Institute (WPI) and University of Massachusetts Medical School (UMMS). I learned a lot from him not only in the field of academia but also in the general pursuits of life. Thank you Dr. Sotak for everything. I hope and pray for your complete recovery so that you may continue to affect the lives of many other students in years to come. I also thank your wife, Mrs. Sandy Sotak, who acted as an intermediary in conveying my messages to you during your leave of absence. I am especially thankful for her help in the submission of this dissertation. Also, I want to thank Dr. George Pins (WPI) for all his help in the BME department in the absence of Dr. Sotak.

I would also like to thank Dr. Peter Grigg, my committee chair, and Dr. Alexei Bogdanov Jr., my co-advisor, for their support especially in the last few months when Dr. Sotak was taken ill. I would also like to extend my thanks to all my committee members (qualifying, TRAC, and dissertation): Dr. Ann Rittenhouse (UMMS), Dr. Michael King (UMMS), Dr. Karl Helmer (Massachusetts General Hospital), Dr. Mitchell Albert (UMMS), Dr. Stephen Glick (UMMS), and Dr. Glenn Gaudette (WPI). I especially thank

Dr. Grigg, Dr. Rittenhouse, and Dr. Helmer for their extensive help in editing my dissertation. Thank you so much for your time and efforts. I really appreciate it. I also thank Dr. Mitchell Albert for allowing me to share his lab space and resources after the closing of the WPI NMR lab.

I also thank Mr. Van Gould from the Department of Animal Medicine at UMMS for his help in training me to perform surgeries and injections in rodents. I also thank Dr. Homer Walker, Dr. Joseph Petrucci, and Dr. Balgobin Nandram from the Department of Mathematical Sciences at WPI for their helpful conversations. I especially thank Mr. Stephen Baker at UMMS for all the help he provided me in understanding the statistical analysis of my data. I would also like to thank Jean Siequist and Jeannette Dailida from WPI and Gaile Arcouette, Annette Stratton, and Rose Daniels from UMMS for all their help throughout the years in completing all types of logistical tasks dealing with the BME department at WPI and the Graduate School of Biomedical Sciences at UMMS.

I extend special thanks to my beloved friends Dr. Ghaith Hammouri, Ali Bourisly, Mohammed Kazim, Paul Dasari, and Ronn Walvick for their company and all their help in ways that cannot be measured. You guys made it all worth it. Thank you so much. I also thank my fellow colleagues over the past few years, Govind Bhagavatheeshwaran, Dave Bennett, Erica Henning, James Bouley, Jaime O'Callaghan, and Austin Reno, who were always around to share some useful advice or to just have a conversation.

Last but not least, I would like to thank my family in Worcester, the community at Worcester Islamic Center (WIC). You guys have become an integral part of my life.

## Preface

This dissertation describes the use of contrast agents in magnetic resonance imaging (MRI) studies to differentiate compartments, to study dose dependence of relaxation times, and to characterize tumors using signal amplifying enzymes in the brain. The work described in this dissertation was carried out at the University of Massachusetts Medical School. I completed all aspects of the works presented in Chapters III-V under the supervision of Dr. Christopher Sotak, which included performing animal MRI experiments, data analysis, and writing of the manuscripts. These works are in the process of being submitted for publications. The work presented in Chapter VI has been submitted to *Cancer Research* (2010) and is currently in review. This work was done under the supervision of Dr. Alexei Bogdanov, Jr. My responsibilities in this study included collecting all the MRI data, performing the data analysis, and principal authorship in writing the manuscript. The synthesis of contrast agents, histological and immunofluorescence work, and *in vitro* cell experiments were completed by Dr. Bogdanov. The methods section of the manuscript describing these techniques and the corresponding figures were prepared by Dr. Bogdanov.

## Abstract

Magnetic resonance imaging (MRI) has increasingly become the preferred imaging modality in modern day research to study disease. MRI presents an imaging technique that is practically non-invasive and without any ionizing radiation. This dissertation presents the use of contrast agents in MRI studies to differentiate compartments, to study dose dependence of relaxation times, and to characterize tumors using signal amplifying enzymes in the brain.

Differentiating compartments in the brain can be useful in diffusion studies to detect stroke at an early stage. Diffusion-weighted NMR techniques have established that the apparent diffusion coefficient (ADC) of cerebral tissue water decreases during ischemia. However, it is unclear whether the ADC change occurs due to changes in the intracellular (IC) space, extracellular (EC) space, or both. To better understand the mechanism of water ADC changes in response to ischemic injury, making IC and EC compartment specific measurements of water diffusion is essential. The first study was done where manganese ( $Mn^{2+}$ ) was used as an IC contrast agent.  $Mn^{2+}$  uptake by cells causes shortening of the  $T_1$  relaxation time of IC water. The relative difference in  $T_1$  relaxation times between the IC and EC compartments can be used to discriminate between the MR signals arising from water in the respective compartments.

$Mn^{2+}$  is also widely used in manganese-enhanced MRI (MEMRI) studies to visualize functional neural tracts and anatomy in the brain *in vivo*. In animal studies, the goal is to use a dose of  $Mn^{2+}$  that will maximize the contrast while minimizing its toxic effects. The goal of dose study was to investigate the MRI dose response of  $Mn^{2+}$  in rat



brain following SC administration of  $Mn^{2+}$ . The dose dependence and temporal dynamics of  $Mn^{2+}$  after SC injection can prove useful for longitudinal *in vivo* studies that require brain enhancement to persist for a long period of time to visualize neuroarchitecture like in neurodegenerative disease studies.

Contrast agents, in addition to their use in compartmental differentiation and dose studies, can be used for imaging tumors. The last study in this dissertation focuses on imaging EGF receptors in brain tumors. We tested a novel pretargeting imaging approach that includes the administration of humanized monoclonal antibody (anti-EGFR mAb, EMD72000) linked to enzymes with complementing activities that use a low-molecular weight paramagnetic molecule (diTyr-GdDTPA) as a reducing substrate administered following the mAb conjugates. We analyzed the differential MR tumor signal decay *in vivo* using orthotopic models of human glioma. The patterns of MR signal change following substrate administration revealed differences in elimination patterns that allowed distinguishing between non-specific and specific modes of MR signal decay.

## Table of Contents

Acknowledgments.....	iv
Preface.....	vi
Abstract.....	vii
Table of Contents.....	ix
List of Figures.....	xv
List of Tables.....	xix
List of Abbreviations, Symbols, and Nomenclature.....	xx

### **Chapter I – Introduction to Nuclear Magnetic Resonance**

1.1. Introduction.....	2
1.1.1. Magnetic Resonance Imaging: Its Advent and Beyond.....	2
1.2. Basic Physical Principles of Nuclear Magnetic Resonance.....	3
1.2.1. Electromagnetic Wave Theory.....	3
1.2.1.1. Wave Concept.....	3
1.2.1.2. Particle Concept.....	4
1.2.1.3. Electromagnetic Spectrum.....	5
1.2.2. Nuclear Spin.....	6
1.2.2.1. Nuclear Angular Momentum.....	6
1.2.2.2. Nuclear Magnetic Dipole Moment.....	7
1.2.2.3. Quantum Mechanical Constraints.....	8
1.2.2.4. Nuclear Energy State Quantization.....	9
1.2.2.5. The Boltzmann Equilibrium.....	12
1.2.3. Classical Description of NMR.....	13
1.2.4. The Bloch Equations.....	15
1.2.5. Free Induction Decay.....	18
1.2.6. Relaxation Mechanisms.....	20
1.2.6.1. Spin-Lattice ( $T_1$ ) Relaxation.....	20
1.2.6.2. Measuring $T_1$ Relaxation time.....	21

1.2.6.3.	Spin-Spin ( $T_2$ ) Relaxation.....	23
1.2.6.4.	Measuring $T_2$ Relaxation Time.....	25
1.2.6.5.	Generation of Tissue Contrast.....	26
1.2.7.	The Fourier Transform.....	28
1.3.	Principles of Magnetic Resonance Imaging.....	28
1.3.1.	Slice Selection.....	29
1.3.2.	Frequency Encoding.....	31
1.3.3.	Phase Encoding.....	32
1.3.4.	Fourier Reconstruction in k-space.....	34
1.3.5.	Imaging Sequences.....	35
1.3.5.1.	Spin Echo Sequence.....	35
1.3.5.2.	Gradient Echo Sequence.....	38
	References.....	40

## Chapter II – Cerebral Ischemia and Apparent Diffusion Coefficient

2.1.	Statistics.....	42
2.2.	Cerebral Physiology.....	43
2.2.1.	Normal Cell Function.....	43
2.2.2.	Pathophysiology of Ischemic Stroke.....	44
2.3.	Apparent Diffusion Coefficient.....	46
2.4.	ADC Decline Hypotheses.....	46
2.5.	Exogenous and Metabolite Surrogates.....	50
2.6.	Diffusigraphy.....	52
2.7.	Relaxo-diffusigraphy.....	53
2.8.	Manganese-Enhanced MRI.....	54
	References.....	56

### Chapter III – Deconvolving the Intra- and Extracellular Water Components in the Rat Brain Using Manganese Enhanced MRI (MEMRI)

3.1. Preface.....	61
3.2. Abstract.....	62
3.3. Introduction.....	63
3.4. Theory.....	65
3.5. Materials and Methods.....	69
3.5.1. Animal Preparation.....	69
3.5.2. MR Measurements.....	70
3.5.3. Data Analysis.....	72
3.6. Results.....	74
3.6.1. Dose Dependence and Time Course of Manganese Distribution.....	74
3.6.2. Time Course and Dose Dependence of Monoexponential $T_1$ Values.....	75
3.6.3. Time Course & Dose Dependence of the Effective Long $T_1$ Relaxation Time ( $T'_{1b}$ ).....	79
3.6.4. Time Course of the Effective Volume Fraction of the Long $T_1$ Component ( $M'_{ob}$ ).....	89
3.6.5. The Effective Short $T_1$ Relaxation Time ( $T'_{1a}$ ).....	91
3.7. Discussion.....	93
3.8. Conclusion.....	96
References.....	97

### Chapter IV – Simulation Study

4.1. Simulation Study.....	102
----------------------------	-----

## **Chapter V – Dose Dependence and Temporal Evolution of the $T_1$ Relaxation Time and MRI Contrast in the Rat Brain after Subcutaneous Injection of Manganese Chloride**

5.1. Preface.....	114
5.2. Abstract.....	115
5.3. Introduction.....	116
5.4. Materials and Methods.....	119
5.4.1. Animal Preparation.....	119
5.4.2. MR Measurements.....	120
5.4.2.1. $MnCl_2$ Phantom Experiments.....	120
5.4.2.2. MEMRI Experiments.....	120
5.4.3. Data Analysis.....	123
5.5. Results.....	124
5.5.1. $MnCl_2$ Phantoms.....	124
5.5.2. Time Course of Manganese Distribution.....	126
5.5.3. Dose Dependence and Time Course of Manganese Distribution.....	128
5.5.4. Time Course and Dose Dependence of Regional $T_1$ Values.....	130
5.5.5. Temporal Evolution of Change in Manganese Relaxivity.....	139
5.6. Discussion.....	142
5.7. Conclusion.....	146
5.8. Acknowledgements.....	147
References.....	148

## **Chapter VI – Magnetic Resonance Imaging of Epidermal Growth Factor Receptor Expression in an Orthotopic Human Glioma Model Using Targeted MR Signal-Amplifying Enzymes**

6.1. Preface.....	153
6.2. Abstract.....	154
6.3. Introduction.....	155

6.4. Materials and Methods.....	158
6.4.1. Syntheses of Reagents and Cell Culture Experiments.....	158
6.4.1.1. Synthesis of DTPA Bis-tyramide.....	158
6.4.1.2. Synthesis of Monoclonal Antibody Conjugates.....	159
6.4.2. In Vitro Cell Culture Experiments.....	161
6.4.2.1. Flow Cytometry and Fluorescence Microscopy.....	162
6.4.2.2. Internalization Experiments.....	164
6.4.2.3. Membrane Proteins Extraction From the Cells.....	164
6.4.3. Histology.....	166
6.4.4. Animal Model and Imaging.....	167
6.4.4.1. MRI Protocol, Pulse Sequences, and Measurements.....	167
6.4.5. Image Analysis.....	168
6.5. Results.....	173
6.5.1. Synthesis and Testing of Targeted MR Signal Amplification System In Vitro .....	173
6.5.2. In Vivo Imaging Experiments and Corroboration.....	178
6.6. Discussion.....	187
6.6.1. Derivation of Relationship Between Decay Time Constant and EES Volume Using the Tofts and Kermode Model.....	192
6.7. Conclusion.....	194
6.8. Acknowledgements.....	194
References.....	195

## Chapter VII – Conclusion

7.1. Concluding Remarks.....	202
7.1.1. Compartmental Differentiation.....	202
7.1.2. Dose Response.....	203
7.1.3. Tumor Characterization.....	204

References..... 208

**Appendix**

Curriculum Vitae..... 212  
Publications and Selected Conference Proceedings..... 217

## List of Figures

1.1	Vector representation of the components of electromagnetic radiation.....	4
1.2	The electromagnetic (EM) spectrum.....	5
1.3	Quantum mechanical view of the nuclear spin angular momentum, $\rho$ , and the nuclear magnetic dipole moment, $\mu$ , for a spin- $1/2$ nucleus.....	9
1.4	Quantization of the nuclear energy states for spin- $1/2$ nuclei in the presence and absence of an external magnetic field ( $B_0$ ) and/or RF pulse radiation ( $B_1$ ).....	11
1.5	Precession of spin- $1/2$ nuclei in the presence of an external magnetic field ( $B_0$ ) using the laboratory frame of reference.....	16
1.6	Precession of spin- $1/2$ nuclei in the presence of a $B_0$ and a $B_1$ field using the rotating frame of reference.....	19
1.7	Methods for measuring $T_1$ relaxation time.....	23
1.8	Method for measuring $T_2$ relaxation time.....	26
1.9	Image contrast resulting from different values of repetition time (TR) and echo time (TE).....	27
1.10	Fourier transform (FT) of a free induction decay (FID) signal.....	29
1.11	Fourier transform (FT) of a sinc ( $\frac{\sin(x)}{x}$ ) pulse.....	30
1.12	Imaging of the k-space.....	34
1.13	A complete spin echo pulse sequence diagram.....	37
1.14	A complete gradient echo pulse sequence diagram.....	39
2.1	Cartoon illustrating ionic movement in normal and ischemic cells.....	45
2.2	Cartoon illustrating Hypotheses #1–#4 of overall water ADC decline in ischemic cells.....	49-50
3.1	ROI definitions for different brain regions.....	71
3.2	Dose dependence and time-course of MEMRI contrast.....	76
3.3	Bar-plots of <i>in vivo</i> monoexponential $T_1$ relaxation times as a function of time after subcutaneous injection of $MnCl_2$ at three different doses in <b>A</b> ) cortex ROI, <b>B</b> ) sub-cortical region ROI, and <b>C</b> ) caudate nucleus ROI.....	78-79
3.4	Plots of <i>in vivo</i> effective long $T_1$ relaxation times ( $T'_{1b}$ ) as a function of time after subcutaneous injection of $MnCl_2$ at three different doses (75 mg/kg, 150 mg/kg, and 300 mg/kg) in <b>A</b> ) cortex ROI, <b>B</b> ) sub-cortical region ROI, and <b>C</b> ) caudate nucleus ROI.....	83-84
3.5	Plots of the <i>in vivo</i> effective long $T_1$ relaxation times as a function of $Mn^{2+}$ dose administered at four different time points in <b>A</b> ) cortex ROI, <b>B</b> ) sub-cortical ROI, and <b>C</b> ) caudate nucleus ROI.....	86-87



3.6	Plots of <i>in vivo</i> effective volume fraction of long $T_1$ component as a function of time after subcutaneous injection of $\text{MnCl}_2$ at three different doses in <b>A)</b> cortex ROI, <b>B)</b> sub-cortical region ROI, and <b>C)</b> caudate nucleus ROI.....	89-90
4.1	Flowchart showing the generation of noisy inversion recovery (IR) data using free induction decay (FID) curves to perform simulated biexponential fitting analysis.....	103
4.2	<b>Top:</b> Sequence of spectra for noisy inversion recovery data generated at SNR~25 using the following parameters: $M_{0a} = 0.8$ , $M_{0a} = 0.2$ , $T_{1a} = 75$ ms, $T_{1b} = 750$ ms, and $b = 2$ . <b>Bottom:</b> Simulated inversion recovery data generated from the spectra shown on top. Each spectral window peak is represented by a single time point in the inversion recovery curve.....	104
4.3	<b>Top:</b> Simulated biexponential inversion recovery data set from Fig. 4.2 at SNR~25 with the following parameters: $M_{0a} = 0.8$ , $M_{0a} = 0.2$ , $T_{1a} = 75$ ms, $T_{1b} = 750$ ms, and $b = 2$ . <b>Bottom:</b> Semi-log plot corresponding to the data points in the encircled region on the top graph. The semi-log plot can clearly distinguish between the two different slopes (dotted lines) which correspond to the two different $T_1$ relaxation times.....	106
4.4	Biexponential fitting of simulated inversion recovery data with the 3-parameter model (Eq. [3.2a]) at SNR~25 with different ratios of the $T_1$ relaxation times and the volume fractions.....	109-110
4.5	Biexponential fitting of simulated inversion recovery data with the 4-parameter model (Eq. [3.2b]) at SNR~25 with different ratios of the $T_1$ relaxation times and the volume fractions.....	111-112
5.1	ROI definitions for different brain regions.....	122
5.2	<b>A)</b> Plot of $R_1$ ( $1/T_1$ ) relaxation rate ( $\text{s}^{-1}$ ) as a function of $\text{MnCl}_2$ concentration (mM) at 2 Tesla. <b>B)</b> Plot of $R_2$ ( $1/T_2$ ) relaxation rate ( $\text{s}^{-1}$ ) as a function of $\text{MnCl}_2$ concentration (mM).....	125-126
5.3	Time-course of $\text{Mn}^{2+}$ distribution in rat brain.....	127-128
5.4	Dose dependence and time-course of MEMRI contrast. $T_1$ -weighted ( $T_1$ -WT) axial MR image sets (TR/TE = 700/15 ms) of Slice #3 from Fig. 5.1 are shown as a function of varying doses of $\text{MnCl}_2$ and as a function of time after subcutaneous injection of $\text{MnCl}_2$ .....	129
5.5	Plots of <i>in vivo</i> $T_1$ relaxation times as a function of time after subcutaneous injection of $\text{MnCl}_2$ at three different doses in <b>A)</b> cortex ROI, <b>B)</b> sub-cortical region ROI, and <b>C)</b> caudate nucleus ROI.....	131-132

5.6	Plots of the <i>in vivo</i> $T_1$ relaxation times as a function of $Mn^{2+}$ dose administered at four different time points in <b>A</b> ) cortex ROI, <b>B</b> ) sub-cortical ROI, and <b>C</b> ) caudate nucleus ROI.....	135-136
5.7	Plots of change in relaxivity $\Delta R_1$ as a function of time after subcutaneous injection of $MnCl_2$ at three different doses in <b>A</b> ) cortex ROI, <b>B</b> ) sub-cortical region ROI, and <b>C</b> ) caudate nucleus ROI.....	140-141
6.1	<b>A</b> ) Synthesis of peroxidase-reducing paramagnetic substrate di(tyramido)-DTPA(Gd); <b>B</b> ) Reaction of diTyr-GdDTPA with the peroxidase/glucose oxidase enzyme pair conjugated to anti-EGFR mAb.....	159
6.2	<b>A, B</b> – flow cytometry of Gli36 $\Delta$ EGFR and Gli36wt cells incubated with cetuximab (C225 antibody, A) and EMD72000 (B). <b>C, D</b> – Cross-titration of two mAb EMD72000 conjugates: mAb-HRP and mAb-GOX in live Gli36 $\Delta$ EGFR ( <b>C</b> ) and Gli36wt ( <b>D</b> ) cell cultures using ABTS/glucose for visualization of HRP activity.....	163
6.3	Placement of ROI for image analysis.....	172
6.4	<b>A</b> ) SDS-PAGE (4-15% gradient) of anti-EGFR mAb (EMD72000) conjugation products or with deglycosylated enzymes: HRP (37 kD, lanes 1 and 2) and with GOX (69 kD subunit, lanes 3, 4) Lanes 1 and 3- before and 2,4- after the purification of conjugates; <b>B</b> ) immunoblotting of membrane protein fraction isolated from Gli36 $\Delta$ EGFR ( $\Delta$ ) and Gli36wt (WT) cells using mouse monoclonal anti-EGFR antibody C225 or by using HRP-EMD72000 conjugate. EGFR variants are identified on the right; <b>C</b> ) titration of the mixture of anti-EGFR mAb-HRP and mAb-GOX on Gli36 $\Delta$ EGFR cells at the optimized complementing ratio (1:2, w/w); <b>D</b> ) binding and internalization of conjugate mixture at the optimized ratio (1:2, w/w) in Gli36 $\Delta$ EGFR ( $\Delta$ ) and Gli36wt (WT) cells 1,3, 5,7 – cell-surface bound fraction of conjugates; 2,4,6,8 – internalized fraction of conjugates.....	175
6.5	<b>A</b> ) 3T MR imaging of Gli36 $\Delta$ EGFR human glioma xenografts without and with pre-injection of targeted conjugates. $T_1$ -WT sequential rat brain images depicting enhancement as a function of time post injection of diTyr-GdDTPA. The top row - temporal washout of diTyr-GdDTPA with no conjugate pre-injection (Day 1). The bottom row - washout of diTyr-GdDTPA following pre-treatment with anti-EGFR conjugates (Day 2) in the same slice for the same animal. Time intervals (in minutes) after the injection of diTyr-GdDTPA are shown below; <b>B</b> ) MRI and comparative histology. Note distal expansion of the tumor along the ventricle. The images were obtained pre-, immediately post- and 1 h post-CA	

---

	administration; <b>C</b> ) Detection of EGFR overexpression using anti-EGFR antibody-digoxigenin/anti-digoxigenin-AP system in the tumor shown in Fig. 6.5B; <b>D</b> ) Detection of EGFR expression (anti-EGFR-DIG/anti-DIG-AP staining, left; and HRP activity (right) in the same tumor on the parallel sections. HRP activity was detected by using diaminobenzidine staining. Arrowheads point to tumor location; arrows show presence of tumor expansion as microdeposits in normal brain tissue stained for EGFR expression. Bars in B, C = 1 mm.....	180-181
6.6	Immunofluorescent detection of EGF receptor, endothelial cells and mAb conjugate delivery in Gli36 $\Delta$ EGFR tumors.....	183-184
6.7	Normalized $T_1$ -WT signal intensities measured in the interface or core regions of the representative Gli36 $\Delta$ EGFR tumors prior to injection of conjugates ( <b>A</b> ), or after the pre-injection of either specific anti-EGFR (“EGFR”) or non-specific EpCAM (“EpCAM”) conjugates ( <b>B</b> ) as a function of time post-diTyr-GdDTPA injection.....	185

## List of Tables

3.1	Statistical Significance of Differences of Least Squares Means of Effective Long $T_1$ Relaxation Times in the Rat Brain Between the Different $Mn^{2+}$ Doses Administered. <i>NS</i> = not significant ( $P > 0.05$ ), $*0.01 < P < 0.05$ (ANOVA with Tukey-Kramer HSD multiple comparisons procedure), $**0.001 < P < 0.01$ , and $***P < 0.001$ .....	85
3.2	Statistical Significance of Differences of Least Squares Means of Effective Long $T_1$ Relaxation Times in the Rat Brain Between the Different Time Points after $Mn^{2+}$ Administration. <i>NS</i> = not significant ( $P > 0.05$ ), $*0.01 < P < 0.05$ (ANOVA with Tukey-Kramer HSD multiple comparisons procedure), $**0.001 < P < 0.01$ , and $***P < 0.001$ .....	88
3.3	Effective Short $T_1$ Relaxation Times in the Rat Brain at Different $Mn^{2+}$ Doses and Time After $Mn^{2+}$ Injection. The Mean Effective Short $T_1$ Relaxation Times are shown in milliseconds ( $\pm 1$ SD) and the number in parentheses indicates number of animals. The values displayed in the table were obtained from animals that showed statistical significance of biexponential over monoexponential model of inversion MRI data using F-statistics. The monoexponential model was a better model for the animals in the empty cell groups.....	92
5.1	Statistical Significance of Differences of Least Squares Means of $T_1$ Relaxation Times Between the Different Time Points in Three Different Regions of the Rat Brain After SC Administration of $Mn^{2+}$ . <i>NS</i> = not significant ( $P > 0.05$ ), $*0.01 < P < 0.05$ (ANOVA with Tukey-Kramer HSD multiple comparisons procedure), $**0.001 < P < 0.01$ , and $***P < 0.001$ .....	133
5.2	Statistical Significance of Differences of Least Squares Means of $T_1$ Relaxation Times Between the Different $Mn^{2+}$ Doses in Three Different Regions of the Rat Brain After SC Administration of $Mn^{2+}$ Administered in the Rat Brain. <i>NS</i> = not significant ( $P > 0.05$ ), $*0.01 < P < 0.05$ (ANOVA with Tukey-Kramer HSD multiple comparisons procedure), $**0.001 < P < 0.01$ , and $***P < 0.001$ .....	137
6.1	Changes of longitudinal relaxivity of Gd as a result of conjugate catalytic activity.....	177
6.2	Decay time constants (DTC) for diTyr-GdDTPA or its products in the tumor interface and core regions with (Day 2) and without conjugate pre-treatment (Day 1) .....	186

## List of Abbreviations, Symbols, and Nomenclature

ADC:	apparent diffusion coefficient
ANOVA:	analysis of variance (statistical test)
ATP:	adenosine triphosphate
<i>b</i> :	efficiency of inversion recovery
$B_0$ :	external magnetic field
$B_1$ :	magnetic field component of the radio frequency pulse
BBB:	blood-brain barrier
CA:	contrast agent
CPMG:	Carr-Purcell-Meiboom-Gill pulse sequence
CR:	contrast reagent
CSF:	cerebrospinal fluid
diTyr-GdDTPA:	di(tyramido) gadolinium diethylene triamine pentaacetic acid
DTC:	decay time constant
DTPA:	diethylene triamine pentaacetic acid
DW-EPI:	diffusion-weighted echo-planar imaging
DW-IRSE:	diffusion-weighted inversion-recovery spin-echo spectroscopy
<i>E</i>	energy
EC:	extracellular
ECS:	extracellular space
EES:	extravascular extracellular space
EGFR:	epidermal growth factor receptor
EM:	electromagnetic
<i>F</i> :	statistical value generated using an F-test
FID:	free induction decay
FOV:	field of view
FT:	Fourier transform
FWHM:	full-width-half-maximum
Gd:	gadolinium

---

GOX:	glucose oxidase
h:	hour(s)
$h$ :	Planck's constant
HRP:	horse radish peroxidase
HSD:	honestly significant differences
$I$ :	spin quantum number
IC:	intracellular
ICS:	intracellular space
IP:	intraperitoneal
IR:	inversion recovery
IV:	intravenous
kD :	kilo-Dalton
$k$ :	Boltzmann constant
$K^{trans}$ :	volume transfer constant
LD <sub>50</sub> :	lethal dose, 50%
$M_0$ :	net magnetization at Boltzmann equilibrium/ overall compartmental signal
$M_{0a}$ :	signal emanating from compartment 'a'
$M_{0b}$ :	signal emanating from compartment 'b'
mAb:	monoclonal antibody
MEMRI:	manganese-enhanced magnetic resonance imaging
$m_j$ :	magnetic quantum number
min:	minute(s)
MHz:	mega-Hertz
mM:	millimolar
MRI:	magnetic resonance imaging
ms:	millisecond
$M_{xy}$ :	transverse component of net magnetization
$M_z$ :	signal intensity/ longitudinal component of net magnetization
$\mu$ :	magnetic dipole moment

---

nm:	nanometer
NMR:	nuclear magnetic resonance
$P$ :	statistical p-value
PBS:	phosphate buffered saline
RF:	radio frequency
ROI:	region of interest
SC:	subcutaneous
SID:	signal intensity decay
SNR:	signal-to-noise ratio
T:	Tesla (unit of magnetic flux density)
$t$ :	time
$T'_{1a}$ :	effective short $T_1$ relaxation time (compartment 'a')
$T'_{1b}$ :	effective long $T_1$ relaxation time (compartment 'b')
$T_1$ :	longitudinal or spin-lattice relaxation time constant
$T_{1a}$ :	actual short $T_1$ relaxation time (compartment 'a')
$T_{1b}$ :	actual long $T_1$ relaxation time (compartment 'b')
$T_1$ -WT:	$T_1$ -weighted
$T_2^*$ :	total transverse relaxation time constant including contributions from local magnetic-field inhomogeneities
$T_2$ :	transverse or spin-spin relaxation time constant
TE:	echo time in MRI pulse sequence
TI:	inversion time in MRI pulse sequence
TR:	repetition time in MRI pulse sequence
$\gamma$ :	gyromagnetic ratio
$\rho$ :	spin angular momentum
$\tau_a, \tau_b$ :	water residence times (in compartments 'a' and 'b')
$\omega_0$ :	Larmor frequency

# **CHAPTER I**

## **INTRODUCTION TO NUCLEAR MAGNETIC RESONANCE**



## **1.1. Introduction**

Principles of nuclear magnetic resonance (NMR) will be discussed in this chapter. In brief, MR utilizes a strong external magnetic field, magnetic field gradients, and radio frequency (RF) waves tuned to a specific frequency to selectively excite nuclei in a region of interest in a biological sample. Once the RF waves are turned off, the nuclei relax back to the equilibrium state dissipating energy and inducing an electrical signal, which can be detected, amplified and processed to obtain MR images. Several sources of information were used as references for the preparation of this chapter (1-7).

### **1.1.1. Magnetic Resonance Imaging: Its Advent and Beyond**

NMR is a powerful noninvasive technique that allows investigation of physical and chemical properties of biological entities at the molecular level. Even though the existence of nuclear spins, the entity essential to NMR, was first proposed by Wolfgang Pauli in 1924, the first NMR experiments were not done until 1946 by Felix Bloch and co-workers at Stanford University (8) and independently by Edward Purcell's group at Harvard University (9). Jasper Jackson extended the idea of MR to studies on humans. In 1967, he produced what are believed to be the first MR signals from a live animal (10). In 1971, Damadian (11) demonstrated that NMR can be useful to diagnose cancer based on differences in NMR measurements between malignant tumors and normal tissue. It was not until 1973, with Lauterber's (12) generation of the first two-

dimensional proton MR image of a water sample at Stony Brook, New York, that NMR began to evolve as a valuable biomedical imaging modality due to the abundance of protons in the human body. Since then, magnetic resonance imaging (MRI) has evolved and transformed into a non-invasive diagnostic tool with applications expanding to all fields of research in physics, chemistry, biology, and engineering.

## **1.2. Basic Physical Principles of NMR**

Understanding the NMR phenomenon requires a review of the basic principles of nuclear behavior in an electromagnetic (EM) environment. NMR principles are presented herein in both classical physics and quantum mechanics approach to describe the nuclear response to a static, external magnetic field, and RF radiation.

### **1.2.1. Electromagnetic Wave Theory**

#### **1.2.1.1. Wave Concept**

EM radiation propagates through space in the form of waves. By Maxwell's wave theory, the waves are composed of a magnetic field component, **B**, and an electric field component, **E**, which are perpendicular to each other and have the same frequency. Both travel at the speed of light in a direction, **C**, which is perpendicular to both the electrical and magnetic field components (Fig. 1.1).

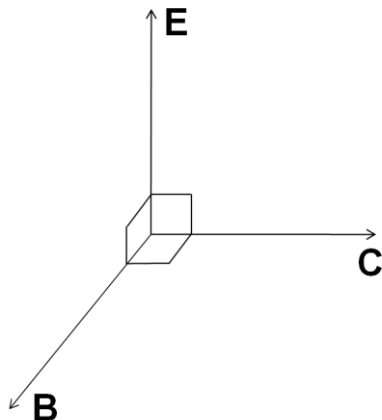


**Figure 1.1** – Vector representation of the components of electromagnetic radiation: electric field component (**E**), magnetic field component (**B**), and direction of propagation (**C**).

Using the classical wave equation, the waves can be characterized as follows:

$$c = \lambda \cdot \nu \quad [1.1]$$

where  $c$  is the speed of light ( $3 \times 10^8 \text{ m}\cdot\text{s}^{-1}$ ),  $\lambda$  is the wavelength (m), and  $\nu$  is the frequency ( $\text{s}^{-1}$ ). Only the magnetic field component, **B**, is relevant for the NMR discussion.

#### 1.2.1.2. Particle Concept

EM radiation with short wavelengths, like x-rays, reacts with matter as if they were particles rather than waves. These particles are discrete bundles of energy called a quantum or photon and are characterized by a specific frequency

of radiation. Using this frequency, the actual amount of energy of the photon can be calculated as follows:

$$E = h \cdot \nu \quad [1.2]$$

where  $E$  is the energy (keV),  $h$  is the Planck's constant ( $4.13 \times 10^{-18}$  keV·s), and  $\nu$  is the frequency ( $\text{s}^{-1}$ ).

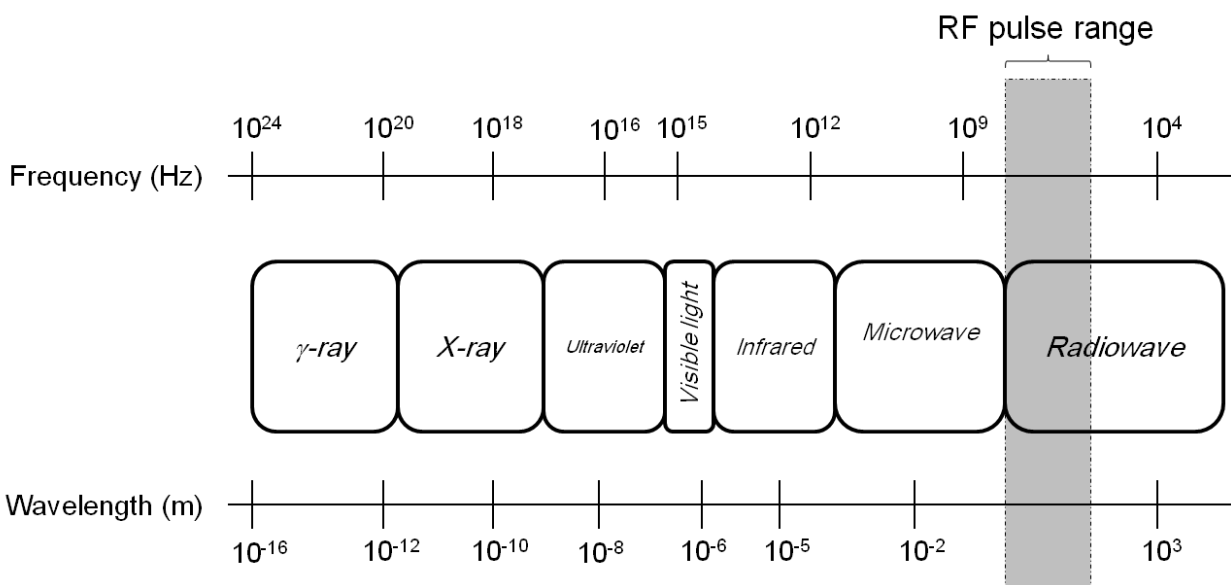


**Figure 1.2** – The electromagnetic (EM) spectrum. Various types of EM radiation are noted ranging from high-frequency  $\gamma$  rays to the low-frequency radiowaves. The approximate frequency and wavelength window for type of EM radiation is depicted. The range shaded in grey represents the typical range of radiofrequency (RF) pulses that are used in MR imaging.

### 1.2.1.3. Electromagnetic Spectrum

EM radiation covers a wide range of wavelengths and frequencies (Fig. 1.2). Biologic tissue is relatively transparent to x-rays and opaque to radiation

with intermediate wavelengths. This holds true for ultraviolet, visible light, and to some extent infrared and microwaves. MR study is associated with absorption of frequency components in the radiowave band (radio frequency (RF)) of the EM spectrum which typically ranges from 5–200 MHz.

## 1.2.2. Nuclear Spin

### 1.2.2.1. Nuclear Angular Momentum

NMR signal is generated as a result of the nuclear angular momentum. The nuclear angular momentum (composed of orbital and spin angular momentum) arises as a result of orbital and spin rotational motions of the nucleons (protons and neutrons). For a nucleus the orbital motion of the nucleons is caused by the spinning motion of the entire nucleus rather than the orbital motion of individual nucleons while the spin rotational is an intrinsic property of the nucleons. The magnitude of the spin angular momentum is quantized as follows:

$$\rho = \hbar[I(I+1)]^{1/2} \quad [1.3]$$

where  $\rho$  is the spin angular momentum (J·s),  $\hbar$  is Planck's constant ( $4.13 \times 10^{-18}$  keV·s) divided by  $2\pi$ , and  $I$  is the spin quantum number (unitless). Depending on the combination of protons and neutrons in the nucleus, the value of  $I$  is either an integer or a half-integer. Each individual proton and neutron in the nucleus has a spin quantum number  $I = 1/2$  which results in the protons and neutrons having a

spin-up (+1/2) and spin-down (-1/2) state. The protons pair with protons and the neutrons pair with neutrons. This pairing with their anti-aligned counterpart yields a net spin of zero for the pair. The protons and neutrons that remain unpaired determine the total spin angular momentum of the nucleus. Thus, nuclei with an odd number of protons and/or neutrons are NMR observable because  $I$  is a non-zero integer (e.g.  $^1\text{H}$ ,  $^{13}\text{C}$ ,  $^{19}\text{F}$ , and  $^{31}\text{P}$  have spin-1/2 nuclei). With an even number of both protons and neutrons,  $I$  is zero and therefore not NMR observable (e.g.  $^{12}\text{C}$  and  $^{16}\text{O}$ ).

#### 1.2.2.2. Nuclear Magnetic Dipole Moment

The nucleus that has a net non-zero spin angular momentum will generate a local magnetic field around the nucleus due to the spin and orbital rotational motions. The direction and magnitude of this magnetic field is called the nuclear magnetic dipole moment and has the following relationship with the nuclear angular momentum:

$$\mu = \gamma \cdot \rho \quad [1.4]$$

where  $\mu$  is the nuclear magnetic dipole moment ( $\text{J}\cdot\text{T}^{-1}$ ),  $\gamma$  is the gyromagnetic ratio ( $\text{Hz}\cdot\text{T}^{-1}$ , a nucleus-specific parameter), and  $\rho$  is the spin angular momentum ( $\text{J}\cdot\text{s}$ ). Notice that when the nuclear angular momentum is zero (i.e.,  $I = 0$ ), then the nucleus has no magnetic moment and hence will not produce an NMR signal.

### 1.2.2.3. Quantum Mechanical Constraints

The nuclear angular momentum and magnetic moment vectors are restricted to a finite number of possible orientations that are described by the set of magnetic quantum numbers,  $m$ , determined from  $I$  and given by the following series:

$$m_I = I, (I - 1), (I - 2), \dots, -I \quad [1.5]$$

For example, nuclei with spin quantum number  $I = 1/2$ , two possible spin quantum numbers exist:  $+1/2$  and  $-1/2$ . For  $I = 1$ , there are three possible states:  $+1$ ,  $0$ , and  $-1$ . In general, there are  $(2 \cdot I + 1)$  possible states for a given  $I$  value.

In addition to the magnitude, the nuclear spin angular momentum has a directional component. If the external magnetic field ( $B_0$ ) is taken to be oriented along the z-axis,  $\rho_z$  will be the component of the nuclear angular momentum along the z-axis specifying the orientation of  $\rho$  as follows:

$$\rho_z = \hbar \cdot m_I \quad [1.6]$$

Similarly, the magnetic dipole moment,  $\mu$ , is also quantized where combining Eqs. [1.3] and [1.4] for the magnitude, we get:

$$\mu = \gamma \cdot \hbar [I(I + 1)]^{1/2} \quad [1.7]$$

The orientation of  $\mu$  is also constrained to discrete values as determined by  $\mu_z$  where

$$\mu_z = \gamma \cdot \rho_z = \gamma \cdot \hbar \cdot m_I \quad [1.8]$$

To illustrate with an example for a spin- $\frac{1}{2}$  nucleus like  $^1\text{H}$ ,  $I = \frac{1}{2}$ . Therefore,  $m_I$  can only be  $+\frac{1}{2}$  or  $-\frac{1}{2}$  giving only two possible orientations of  $\rho_z$  and  $\mu_z$ . Fig. 1.3 illustrates the two orientations for a spin- $\frac{1}{2}$  nucleus: spin-up and spin-down.

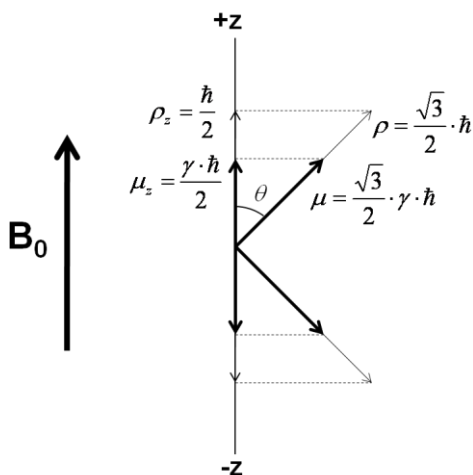


**Figure 1.3** – Quantum mechanical view of the nuclear spin angular momentum,  $\rho$ , and the nuclear magnetic dipole moment,  $\mu$ , for a spin- $\frac{1}{2}$  nucleus. The  $B_0$  field is oriented in the positive z-axis direction. The magnitudes of the vectors,  $\rho$  and  $\mu$ , are their projections on the z-axis,  $\rho_z$  and  $\mu_z$ , are shown.

#### 1.2.2.4. Nuclear Energy State Quantization

Interaction between  $\mu$  and  $B_0$  field gives rise to potential energy  $E$ , according to the relation

$$E = \mu_z \cdot B_0 \quad [1.9]$$



where  $\mu_z$  is the component of nuclear magnetic dipole moment along the direction of the external magnetic field,  $B_0$ . Thus, for a spin- $1/2$  nucleus there are two possible energy states corresponding to two possible orientations of the nuclear magnetic dipole moment. The parallel orientation has a lower energy state,  $E_1$ , and the anti-parallel orientation has a higher energy state,  $E_2$ :

$$E_1 = -\frac{\gamma \cdot \hbar \cdot B_0}{2} \quad [1.10]$$

$$E_2 = +\frac{\gamma \cdot \hbar \cdot B_0}{2} \quad [1.11]$$

The lower energy state is termed spin-up and the higher energy state is termed spin-down (Fig. 1.4(b)). In the absence of the  $B_0$  field the energies of all spins are degenerate (Fig. 1.4(a)), meaning all spins have the same energy value.

Transitions between the two energy levels can occur when EM radiation is absorbed or emitted (Fig. 1.4(c)), depending on whether the spins are transitioning from the lower-to-upper or upper-to-lower energy states. In either case, a characteristic frequency defines the quantum of radiation required for a single transition between the two energy states. From conservation of energy, this frequency can be redefined as:

$$\nu_0 = \frac{\gamma \cdot B_0}{2\pi} \quad [1.12]$$

where  $\nu_0$  is the frequency of absorbed or emitted radiation ( $\text{rad}\cdot\text{s}^{-1}$ ),  $\gamma$  is the gyromagnetic ratio ( $\text{Hz}\cdot\text{T}^{-1}$ ), and  $B_0$  is the external magnetic field strength (T).

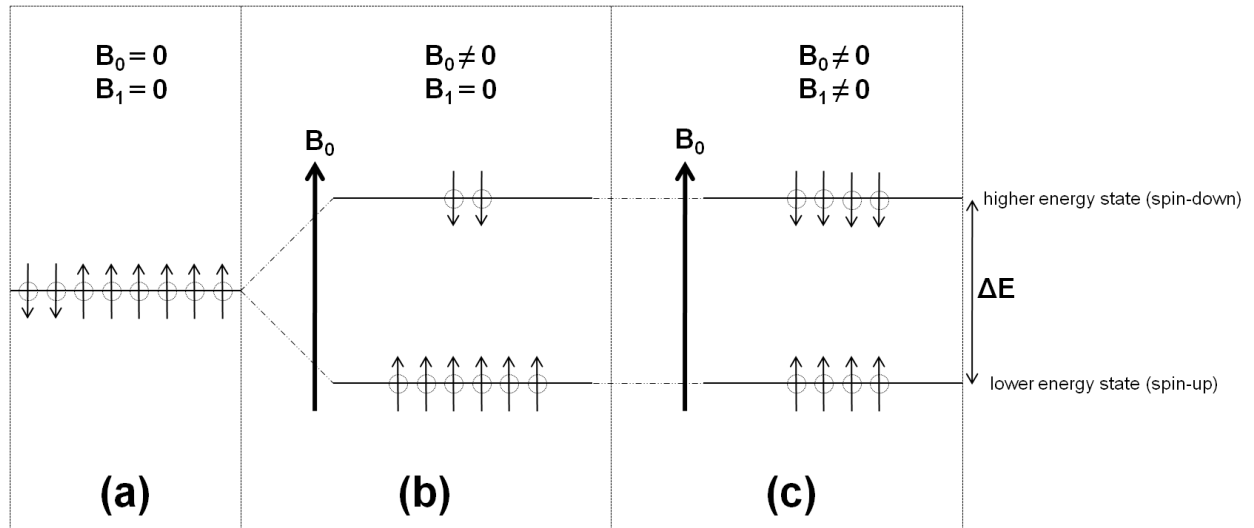


**Figure 1.4** – Quantization of the nuclear energy states for spin- $1/2$  nuclei in the presence and absence of an external magnetic field ( $B_0$ ) and/or RF pulse radiation ( $B_1$ ). The  $B_0$  field is oriented in the positive z-axis direction and the  $B_1$  field is oriented orthogonal to the  $B_0$  field. **(a)** In the absence of both fields, the nucleic spins are in a degenerate state where the energy is equal in all the spins. **(b)** In the presence of only a  $B_0$  field, without any RF radiation, the degeneracy between the energy levels is removed and the spins orient themselves to a spin-up (lower energy) or a spin-down (higher energy) orientation. The lower energy state contains more nuclei than the higher energy state, being distributed according to Boltzmann equilibrium and  $\Delta E$  is the difference between the energy levels. **(c)** With the application of an appropriate  $B_1$  field, some of the spin-up nuclei change their orientation to a spin-down state so that both energy levels are occupied by an equal number of spins. Once the  $B_1$  field is turned off, the spins will return to the orientation in **(b)**. When both fields ( $B_0$  and  $B_1$ ) are turned off, the spins will return to a degenerate state as shown in **(a)**.

### 1.2.2.5. The Boltzmann Equilibrium

As described earlier, the presence of  $B_0$  field causes the spins to orient into a lower and higher energy state (Eqs. [1.10] and [1.11]). The equilibrium distribution of nuclei in a particular energy state is described by the Boltzmann Law:

$$N_I = e^{(-E_I/kT)} \quad [1.13]$$

where  $N_I$  is the number of nuclei in spin state  $I$ ,  $T$  is the temperature ( $^{\circ}\text{K}$ ), and  $k$  is the Boltzmann constant ( $1.38 \times 10^{-23} \text{ J}\cdot\text{K}^{-1}$ ) (see Fig. 1.4b). The NMR signal is proportional to the population between the lower and higher states, which is given by:

$$\Delta n = \frac{N_T \cdot \gamma \cdot \hbar \cdot B_0}{2kT} \quad [1.14]$$

where  $\Delta n$  is the population difference between the energy states,  $N_T$  is the total number of nuclei being considered,  $\gamma$  is the gyromagnetic ratio ( $\text{Hz}\cdot\text{T}^{-1}$ ), and  $\hbar$  is Planck's constant ( $4.13 \times 10^{-18} \text{ keV}\cdot\text{s}$ ) divided by  $2\pi$ . This population difference can also relate to the total magnetic dipole moment of the system, or net magnetization  $M_z$ , which is the sum of all the z-components of the individual magnetic moments:

$$M_z = \sum_{m=-I}^I N_m \cdot \mu_{z,m} \quad [1.15]$$

where  $N_m$  is the total population of nuclei in state  $m$  and  $\mu_{z,m}$  is the z-component of each individual nuclear magnetic moment in state  $m$  ( $\text{J}\cdot\text{T}^{-1}$ ). In a spin- $1/2$  system, the total magnetization at the Boltzmann equilibrium,  $M_0$ , is given by:

$$M_0 = \frac{\gamma \cdot \hbar \cdot \Delta n}{2} \quad [1.16]$$

(shown in Fig. 1.5) which when combined with Eq. [1.14] gives:

$$M_0 = \frac{N_T \cdot \gamma^2 \cdot \hbar^2 \cdot B_0}{4KT} \quad [1.17]$$

### 1.2.3. Classical Description of NMR

In NMR experiments, placing nuclei in an external magnetic field  $B_0$ , exerts a torque  $L$  on the magnetic dipole moment  $\mu$ . Since the magnetic dipole moment is inclined at an angle with respect to  $B_0$ , the interaction of  $\mu$  and  $B_0$  will result in a precessional motion of  $\mu$  around  $B_0$ . In classical physics this precessional motion is described as the cross product of  $\mu$  and  $B_0$  as follows:

$$L = \frac{d\rho}{dt} = \mu \times B_0 \quad [1.18]$$

where the torque  $L$  is the rate of change of the angular momentum. Using the relationship between the nuclear magnetic dipole moment and the nuclear angular momentum, Eq. [1.18] can be rewritten as:

$$\frac{d\mu}{dt} = \gamma \cdot \frac{d\rho}{dt} = \gamma \cdot \mu \times B_0 \quad [1.19]$$

where the rate of change of the nuclear magnetic dipole moment is equal to the product of the rate of change of the nuclear angular momentum and the gyromagnetic ratio. The frequency of precession of the nuclei about  $B_0$  is expressed by the Larmor equation:

$$\omega_0 = \gamma \cdot B_0 \quad [1.20]$$

where  $\omega_0$  is the Larmor frequency (Hz),  $\gamma$  is the gyromagnetic ratio ( $\text{Hz} \cdot \text{T}^{-1}$ ) and  $B_0$  is the external magnetic field strength (T). Resonant absorption of energy will take place when the frequency of the applied radiation matches the natural precessional frequency (Larmor frequency) of the system. Once this resonance condition is satisfied, the system will be perturbed away from the Boltzmann equilibrium distribution where energy will be absorbed and spins in the ground state will be promoted to the first excited state.

Without applied RF energy, the magnetic moment only responds to the  $B_0$  field and precesses at the Larmor frequency. In the presence of an RF field,  $B_1$ , the motion of the magnetic moment will be the result of an interaction with both the fields,  $B_0$  and  $B_1$ :

$$\frac{d\mu}{dt} = \gamma \cdot \frac{d\rho}{dt} = \gamma \cdot \mu \times (B_0 + B_1) \quad [1.21]$$

#### 1.2.4. The Bloch Equations

The Bloch equations can be used to explain the interactions between nuclei (8). For a collection of spins, the vector sum of all individual magnetic moments yields a net magnetization,  $M$ . In the absence of  $B_0$  field, the net magnetization is equal to zero. In the presence of  $B_0$  field, each magnetic moment precesses around the  $B_0$  field at the Larmor frequency,  $\omega_0$ . As per the Boltzmann distribution, more nuclei populate the parallel orientation or the lower energy state, which results in a net longitudinal or z-axis magnetization,  $M_z$ . The vector sum of the transverse or xy-components of  $M$  results in phase cancellation of the individual contributions to the net magnetization of the nuclei which results in no coherent transverse magnetization,  $M_{xy}$ , at the Boltzmann equilibrium. Thus, the net magnetization results in a longitudinal component with magnetization  $M_z$  (also termed  $M_0$ ) (Fig. 1.5).

From Eq. [1.19], the motion of the net magnetization can be described as follows:

$$\frac{dM}{dt} = \gamma \cdot (M \times B_0) \quad [1.22]$$

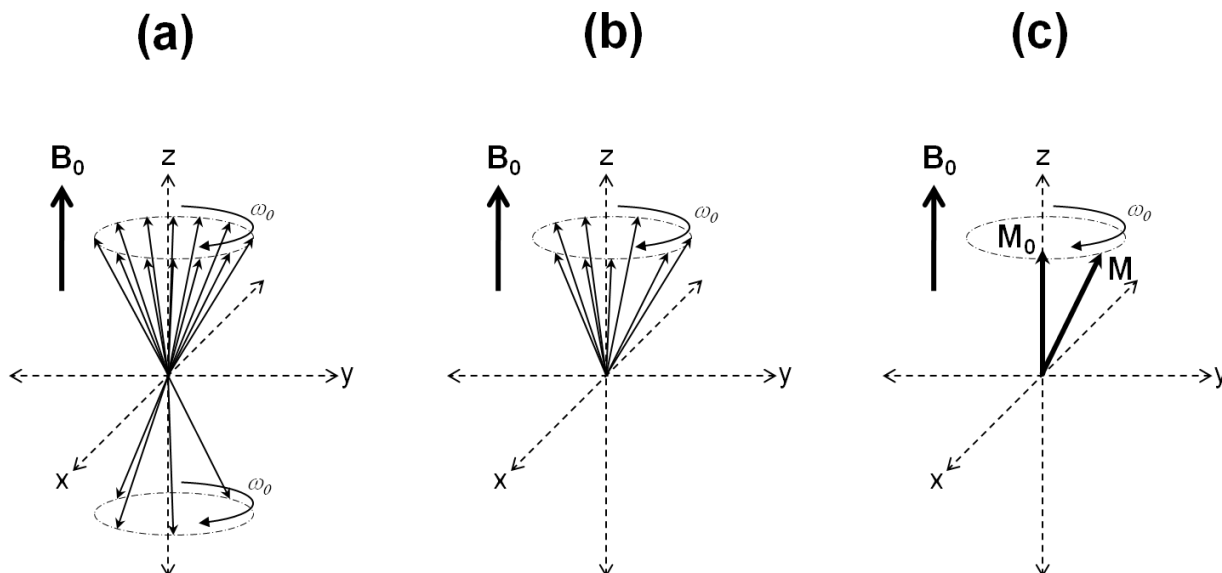


**Figure 1.5** – Precession of spin- $1/2$  nuclei in the presence of an external magnetic field ( $B_0$ ) using the laboratory frame of reference. **(a)** Individual magnetic dipole moments are indicated in the spin-up and spin-down states with the arrows rotating at the Larmor frequency ( $\omega_0$ ). **(b)** Due to the presence of excess nuclei in the spin-up state (lower energy), the spin-down arrows get cancelled out leaving an excess population of spins in the spin-up state. **(c)** A vector sum of all the individual magnetic dipole moments of the nuclei results in a net magnetization vector,  $M$ , which precesses at the same Larmor frequency,  $\omega_0$ , like the individual magnetic moments. The z-component of this net magnetization ( $M_z$ ) is called the longitudinal magnetization and is represented by  $M_0$ .

To include the effect of both  $B_0$  and  $B_1$ , Eq. [1.22] becomes:

$$\frac{dM}{dt} = \gamma \cdot (M \times B) \quad [1.23]$$

where  $B$  consists of static field,  $B_0$ , and the RF field,  $B_1$ . The components of  $B$  are described as follows:

$$B_x = B_1 \cdot \cos(\omega \cdot t) \quad [1.24]$$

$$B_y = B_1 \cdot \sin(\omega \cdot t) \quad [1.25]$$

$$B_z = B_0 \quad [1.26]$$

The net magnetization responds dynamically to the presence of  $B_0$ ,  $B_1$ , and the effects of nuclear relaxation processes. The Bloch differential equations describe the behavior of the constituent components  $\{M_x, M_y, \text{ and } M_z\}$  as follows:

$$\frac{dM_x}{dt} = \gamma \cdot B_0 \cdot M_y + \gamma \cdot B_1 \cdot \sin(\omega \cdot t) \cdot M_z - \frac{M_y}{T_2} \quad [1.27]$$

$$\frac{dM_y}{dt} = -\gamma \cdot B_0 \cdot M_x + \gamma \cdot B_1 \cdot \cos(\omega \cdot t) \cdot M_z - \frac{M_x}{T_2} \quad [1.28]$$

$$\frac{dM_z}{dt} = -\gamma \cdot B_1 \cdot [M_x \cdot \sin(\omega \cdot t) + M_y \cdot \cos(\omega \cdot t)] - \frac{M_z - M_0}{T_1} \quad [1.29]$$

where  $T_1$  and  $T_2$  are longitudinal and transverse time constants, respectively, associated with the equilibrium of the net magnetization. Eqs. [1.27], [1.28], and [1.29] are in the laboratory frame of reference. For convenience the net magnetization  $M$  can be described in the rotating frame reference where the x- and y-axes rotate at the Larmor frequency,  $\omega_0$ . When describing the motion of nuclei in the following sections,  $M_0$  will be discussed in the rotating frame of reference with the rotational axis parallel to  $B_0$ .



### 1.2.5. Free Induction Decay

In NMR experiments, an RF resonant circuit surrounds the sample of interest and is placed such that the generated RF magnetic field ( $B_1$ ) is perpendicular to the static  $B_0$  field. At equilibrium,  $M_0$  is parallel to the  $B_0$  field which is oriented along the positive z-axis (Fig. 1.6). When the  $B_1$  field is applied at the Larmor frequency in the transverse (x-y) plane,  $M_0$  tips to the transverse plane. The angle of rotation is given by:

$$\theta = \gamma \cdot B_1 \cdot \tau \quad [1.30]$$

where  $\theta$  is the tip angle and  $\tau$  is the duration of the  $B_1$  field application.

RF pulses are typically applied to tip the magnetization either completely onto the transverse plane (90° pulse) or onto the negative z-axis (180° pulse). Upon RF pulse application, perturbation of the net magnetization yields a transverse component,  $M_{xy}$ , which is detectable by the RF receive coil. The transverse component arises due to the RF pulse imparting phase coherence to the spins that form the net magnetization in the transverse plane. When the RF pulse is switched off, the net magnetization will precess about the z-axis and the spin system will return to the Boltzmann equilibrium by  $T_1$  relaxation, while the transverse magnetization will decay to zero by  $T_2^*$  relaxation due to loss of phase coherence (see Section 1.2.6 for discussion of relaxation mechanisms). The measured evolution of the transverse signal is an exponentially decaying sinusoid called free induction decay (FID) (Fig. 1.10). The signal decays by  $T_2^*$

relaxation which is a combination of intrinsic  $T_2$  relaxation of the nuclei, and contributions from magnetic susceptibility,  $B_0$ -field inhomogeneities, and molecular diffusion (discussed in Section 1.2.6.3).

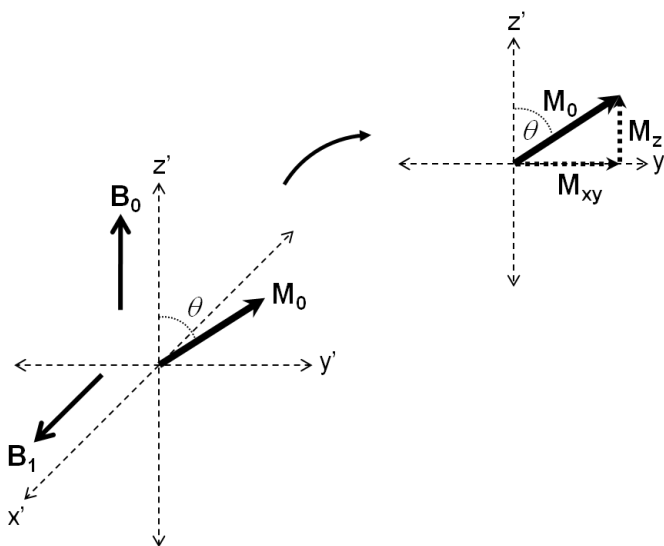


**Figure 1.6** – Precession of spin- $1/2$  nuclei in the presence of a  $B_0$  and a  $B_1$  field using the rotating frame of reference. Notice the axes are labeled  $x'$ ,  $y'$ , and  $z'$  representing the axes rotating at the Larmor frequency. The  $B_1$  field that satisfies the resonance condition of the nuclei is applied orthogonal to the  $B_0$  field. This causes the net magnetization,  $M_0$ , to precess around  $B_1$  which tips  $M_0$  towards the transverse plane at an angle  $\theta$ . The transverse component of  $M_0$ ,  $M_{xy}$ , arises due to the RF pulse imparting phase coherence to the spins which comprise of the net magnetization in the transverse plane. This net transverse component is detected by the RF receive coil giving rise to the NMR signal.

### 1.2.6. Relaxation Mechanisms

Spin-lattice ( $T_1$ ) relaxation and spin-spin ( $T_2$ ) relaxation are the two main relaxation mechanisms in NMR. Once the RF field ( $B_1$ ) is turned off, thus perturbing the net magnetization of the nuclei, the nuclei will return to the Boltzmann equilibrium in an exponential manner. The exponential process by which the longitudinal magnetization,  $M_z$ , returns to its equilibrium state is measured by the time constant  $T_1$ .  $T_2$  is the time constant that measures the exponential decay of the transverse magnetization,  $M_{xy}$ . Nuclei in various tissues and tissue states (normal, diseased, etc.) have intrinsically different values for  $T_1$  and  $T_2$ , thus allowing their manipulation to generate tissue contrast in MR images.

#### 1.2.6.1. Spin-Lattice ( $T_1$ ) Relaxation

$T_1$  is called the longitudinal or the spin-lattice relaxation time. When RF pulse is switched off after exciting the spins onto the transverse plane, the spins in the transverse plane continue to precess around the z-axis, seeking to return to the lower energy state according to the Boltzmann equilibrium. The spins recover by transferring energy to the surrounding "lattice" (the atomic environment) and the  $M_z$  component of the net magnetization slowly recovers along the longitudinal z-axis. This recovery component can be derived from the Bloch equations which give:

$$\frac{dM_z}{dt} = -\frac{M_z - M_0}{T_1} \quad [1.31]$$

Solving this differential equation gives the following equation which describes the growth of the longitudinal magnetization:

$$M_z(t) = M_0 \cdot \left( 1 - b \cdot e^{-\frac{t}{T_1}} \right) \quad [1.32]$$

where  $M_z$  is the change in longitudinal magnetization,  $M_0$  is the value of net magnetization prior to the application of the RF pulse,  $b$  is equal to 1 or 2 depending on whether a  $90^\circ$  or  $180^\circ$  RF pulse is used,  $T_1$  is the time required for the longitudinal component to return to 63% of its original value, and  $t$  is the time following the RF pulse.

#### 1.2.6.2. Measuring $T_1$ Relaxation time

$T_1$  relaxation time can be measured using a progressive saturation method or an inversion recovery method. For a progressive saturation method two  $90^\circ$  RF pulses can be used separated by an interval called the repetition time (TR). Once the first  $90^\circ$  RF pulse is applied, the spins have phase coherence in the transverse plane with no longitudinal magnetization component, i.e.  $M_z = 0$  and  $M_{xy}$  is a maximum. When the  $90^\circ$  RF pulse is switched off, the longitudinal magnetization begins to recover over time  $t = TR$ . The amount of recovery will

depend on the ratio of TR to the  $T_1$  of the sample being measured. At  $t = \text{TR}$ , another  $90^\circ$  RF pulse is applied which tips the recovered longitudinal magnetization onto the transverse plane and an FID of this magnetization is collected by the RF receive coil. By acquiring several different FIDs at different values of TR, the signal amplitude of the FID can be plotted to calculate the  $T_1$  of the sample using Eq. [1.32] with  $b = 1$  (Fig. 1.7, blue curve).

When using the inversion recovery method, a  $180^\circ$  and a  $90^\circ$  RF pulse are used to calculate the  $T_1$  relaxation time. Once the  $180^\circ$  RF pulse is applied, the net magnetization is flipped onto the negative z-axis, i.e.  $M_z = -M_0$  and  $M_{xy} = 0$ . Then, after waiting for one inversion time (TI), a  $90^\circ$  RF pulse is applied. Depending on the ratio of TI and  $T_1$  of the sample, the longitudinal magnetization will begin to recover. When the  $90^\circ$  RF pulse is applied after one TI, the remaining longitudinal magnetization will be flipped onto the transverse plane to create the FID signal. Thus, several FIDs collected at different TI values can be used to plot the inversion recovery of the longitudinal signal and Eq. [1.32] can be used to calculate the  $T_1$  of the sample using  $b = 2$  (Fig. 1.7, red curve).

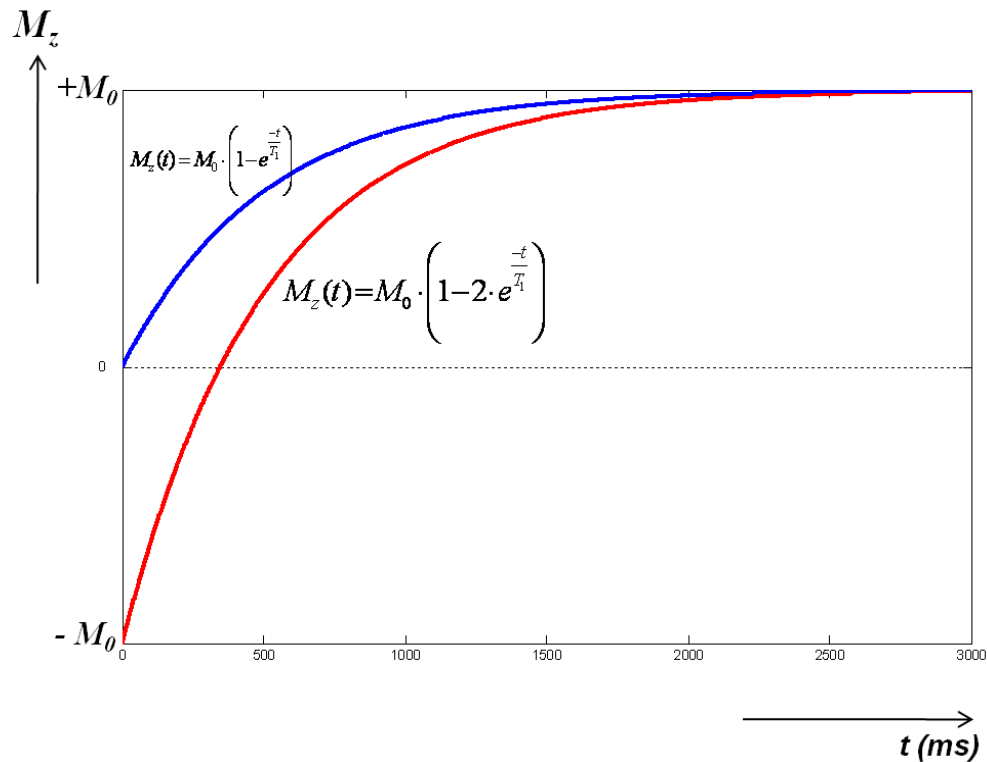


**Figure 1.7** – Methods for measuring  $T_1$  relaxation time. Both curves are shown with a  $T_1$  relaxation time of 500 ms. **Blue (upper) curve:** Progressive saturation method uses two  $90^\circ$  RF pulses separated by one repetition time ( $t = TR$ ) to collect FIDs at different TR values to plot the saturation recovery curve.  $T_1$  relaxation time can be calculated by solving Eq. [1.32] with  $b=1$ . **Red (lower) curve:** Inversion recovery method uses one  $180^\circ$  RF pulse and one  $90^\circ$  RF pulse separated by one inversion time ( $t = TI$ ) to collect FIDs at different TI values to plot the inversion recovery curve.  $T_1$  relaxation time can be calculated by solving Eq. [1.32] with  $b=2$ .

### 1.2.6.3. Spin-Spin ( $T_2$ ) Relaxation

$T_2$  is called the transverse or the spin-spin relaxation time. After the RF pulse is switched off, the vector sum of the spins in the transverse plane are

spinning in phase at the same frequency. With time, due to spin-spin interactions, the transverse component begins to decay as the spins lose their phase coherence. In addition to spin-spin interactions, other factors contribute to the total transverse relaxation time,  $T_2^*$  as follows:

$$\frac{1}{T_2^*} = \frac{1}{T_2} + \frac{1}{T_2^I} + \frac{1}{T_2^S} + \frac{1}{T_2^D} \quad [1.33]$$

where  $T_2^I$  is the dephasing time due to external magnetic field inhomogeneities,  $T_2^S$  is the dephasing time due to differences in magnetic susceptibility, and  $T_2^D$  is the dephasing time due to molecular diffusion effects. The change in transverse component can be derived from the Bloch equations which give:

$$\frac{dM_{xy}}{dt} = -\frac{M_{xy}}{T_2} \quad [1.34]$$

The decay following a 90° RF pulse follows a time constant  $T_2^*$  and the exponential decay is given by:

$$M_{xy}(t) = M_0 \cdot e^{-\frac{t}{T_2^*}} \quad [1.35]$$

where  $M_{xy}$  is the change in the transverse magnetization,  $M_0$  is the value of net magnetization prior to the application of the 90°-RF pulse,  $t$  is the time following the RF pulse, and  $T_2^*$  is the time required for the transverse component to decay by 37% of the original net transverse magnetization prior to switching off the RF pulse.

#### 1.2.6.4. Measuring $T_2$ Relaxation time

$T_2$  relaxation time can be measured using a Hahn spin echo method which utilizes a  $90^\circ$  RF pulse followed by a  $180^\circ$  RF pulse separated by a time period of  $t = TE/2$ , where TE is called the echo time. After the  $90^\circ$  RF pulse is applied, the spins have phase coherence in the transverse plane with no net longitudinal magnetization component, i.e.  $M_z = 0$  and  $M_{xy}$  is a maximum. When the  $90^\circ$  RF pulse is switched off spin dephasing will begin to occur by  $T_2^*$  relaxation processes as shown in Eq. [1.33]. The application of  $180^\circ$  RF pulse at  $t = TE/2$  reverses the phases of the individual spins relative to the Larmor frequency resulting in the transverse magnetization being again in phase by  $t = TE$ . This magnetization is called the spin echo and is measured by the RF receive coil. Several spin echoes, collected at different TE values, generate a decay curve from which the  $T_2$  relaxation time can be calculated using Eq. [1.35] (Fig. 1.8). Notice that the effects of  $T_2^*$  relaxation processes caused by external magnetic field inhomogeneities and differences in magnetic susceptibility are eliminated using this method due to the formation of the spin echo by the  $180^\circ$  RF pulse (see Section 1.3.5.1).



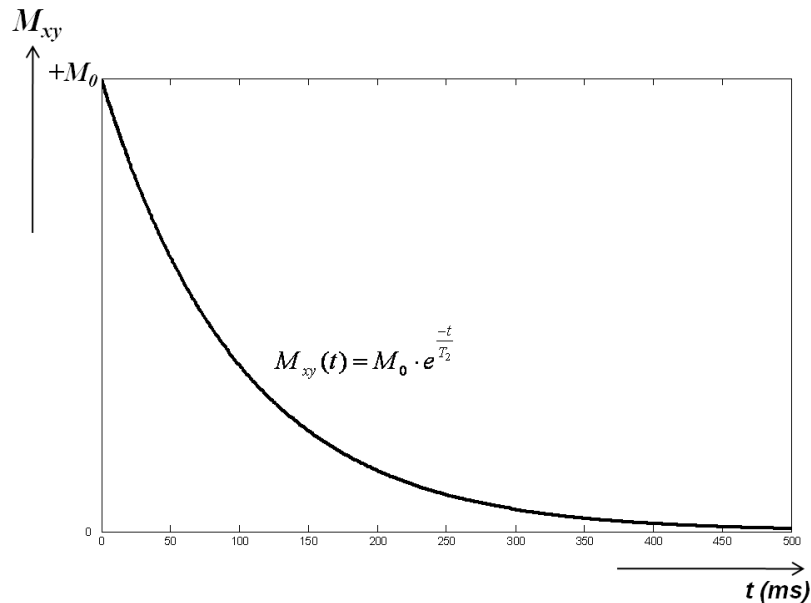


**Figure 1.8** – Method for measuring  $T_2$  relaxation time. The curve is shown with a  $T_2$  relaxation time of 100 ms. Hahn spin echo method uses a  $90^\circ$  RF pulse followed by a  $180^\circ$  RF pulse separated by one half the echo time ( $t = TE/2$ ) to collect spin echoes at different TE values to plot the transverse decay curve.  $T_2$  relaxation time can be calculated by solving Eq. [1.35]. Effects of  $T_2^*$  relaxation processes caused by magnetic field inhomogeneities and magnetic susceptibilities are eliminated using this method due to the formation of the spin echo by the  $180^\circ$  RF pulse.

#### 1.2.6.5. Generation of Tissue Contrast

In the body, different tissues have different  $T_1$  and  $T_2$  relaxation times at a particular magnetic field strength. In general, the  $T_2$  relaxation time is much shorter than the  $T_1$  relaxation time. Thus, the signal in the transverse plane will decay more quickly than the recovery of the longitudinal signal to its equilibrium state. If the second  $90^\circ$  RF pulse is applied when the signal in the transverse

plane is completely decayed and the longitudinal signal has not reached an equilibrium state, then the signal collected will be proportional to the  $T_1$  relaxation time. The image formed from this signal will have high  $T_1$  contrast and low  $T_2$  contrast, thereby generating a  $T_1$ -weighted image. On the other hand, if the longitudinal signal reaches the equilibrium state and the echo time is fairly long, then the signal collected will be weighted by  $T_2$  or  $T_2^*$  depending on whether a  $90^\circ$  or  $180^\circ$  RF pulse is used as the second RF pulse. A proton-density image is formed if the echo is collected at a long TR and short TE, where the image is neither  $T_1$ - nor  $T_2$ -weighted (Fig. 1.9).

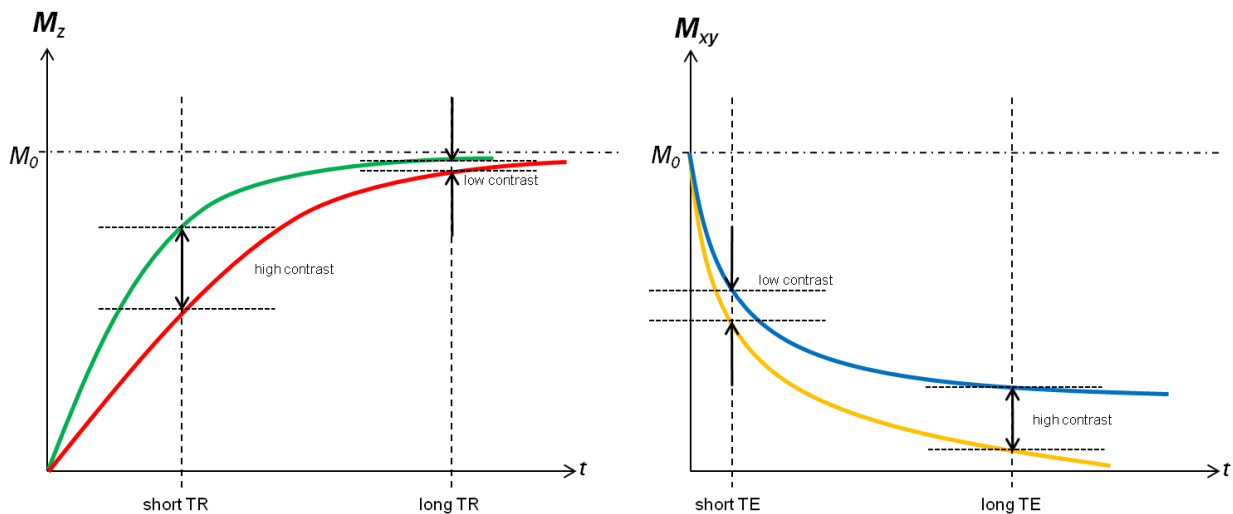


**Figure 1.9** – Image contrast resulting from different values of repetition time (TR) and echo time (TE). A short TR and short TE acquisition results in a  $T_1$ -weighted image due to the high  $T_1$  contrast. A long TR and long TE acquisition results in a  $T_2$ -weighted image due to the high  $T_2$  contrast. A long TR and short TE acquisition results in low  $T_1$  and low  $T_2$  contrast; this type of image is called a proton-density image.

### 1.2.7. The Fourier Transform

The Fourier transform (FT) is a mathematical process which mediates the interconversion of time (in seconds) and frequency (in Hertz). The FID signal received from NMR is in the form of amplitude versus time in the time domain. This FID has phase, frequency, and amplitude. FT of this signal transforms the FID from the time domain to the frequency domain where the FID will yield a plot of signal strength versus frequency. If the FID contains a single frequency of oscillation, then there will be a single Lorentzian peak located symmetrically about that frequency whose full-width-at-half-maximum (FWHM) height is related to the time constant  $T_2^*$  of exponential decay (Fig. 1.10). If the FID contains multiple frequencies of oscillations, then the frequency domain will show as many Lorentzian peaks symmetrically disposed about each individual frequency. When studying chemical structures, obtaining FIDs would be sufficient; however, when performing MRI of biological tissue, NMR signals are composed of varying frequencies and amplitudes due to heterogeneity in tissues, e.g. fat, muscle, etc. In order to distinguish between the different tissues, spatial encoding is essential which is achieved by the application of a linear field gradient.

## 1.3. Principles of Magnetic Resonance Imaging

Magnetic resonance imaging (MRI) entails the encoding of spatial information into the frequency and phase of the NMR signal using linear magnetic field gradients.

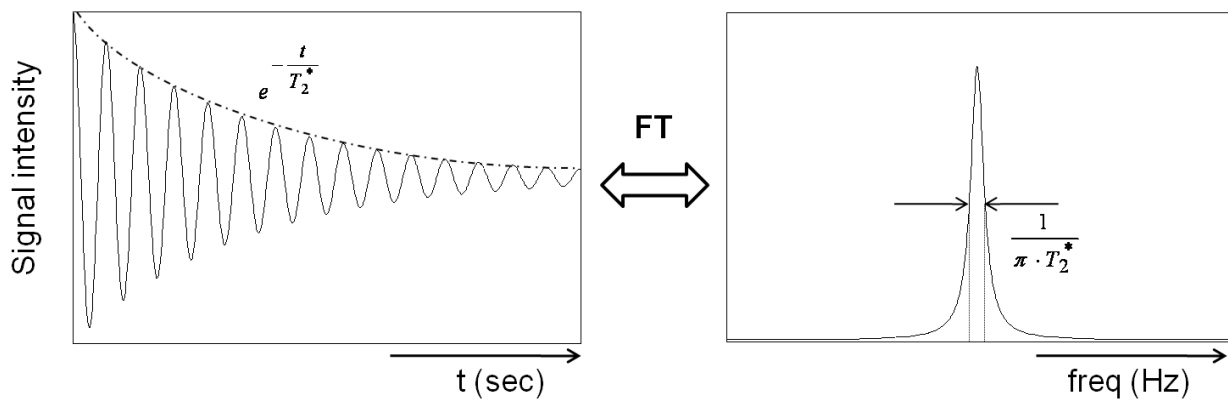


**Figure 1.10** – Fourier transform (FT) of a free induction decay (FID) signal. The FID signal is an exponentially decaying sinusoidal signal (Left) is in the time domain and a Lorentzian waveform in the frequency domain (Right).  $T_2^*$  characterizes both signals where the exponential decay in the time domain decays by  $T_2^*$  while the full-width-half-maximum (FWHM) is characterized by  $T_2^*$  in the frequency domain.

### 1.3.1. Slice Selection

Selective excitation of a slice of the sample of interest is accomplished by imposing a linear magnetic field gradient orthogonal to the chosen plane size. This linear gradient causes a linear variation of the local magnetic field, thus altering the resonance frequencies of the nuclei along the gradient axis. Thus, the Larmor frequency depends on the spatial location of the nuclei in addition to  $B_0$  as follows:

$$\omega(z) = \gamma \cdot (B_0 + G_z \cdot z) \quad [1.36]$$

where  $\omega(z)$  is the angular frequency,  $\gamma$  is the gyromagnetic ratio,  $B_0$  is the external magnetic field,  $G_z$  is the linear gradient applied along the z-axis direction, and  $z$  is the position along the gradient direction. For slice selection, a narrow bandwidth of frequencies must be excited which corresponds to a narrow spatial distribution of nuclei within the sample. A sinc-pulse ( $\frac{\sin(x)}{x}$ ) is used to restrict the bandwidth of the RF pulse which yields a rectangular RF power spectrum (Fig. 1.11).

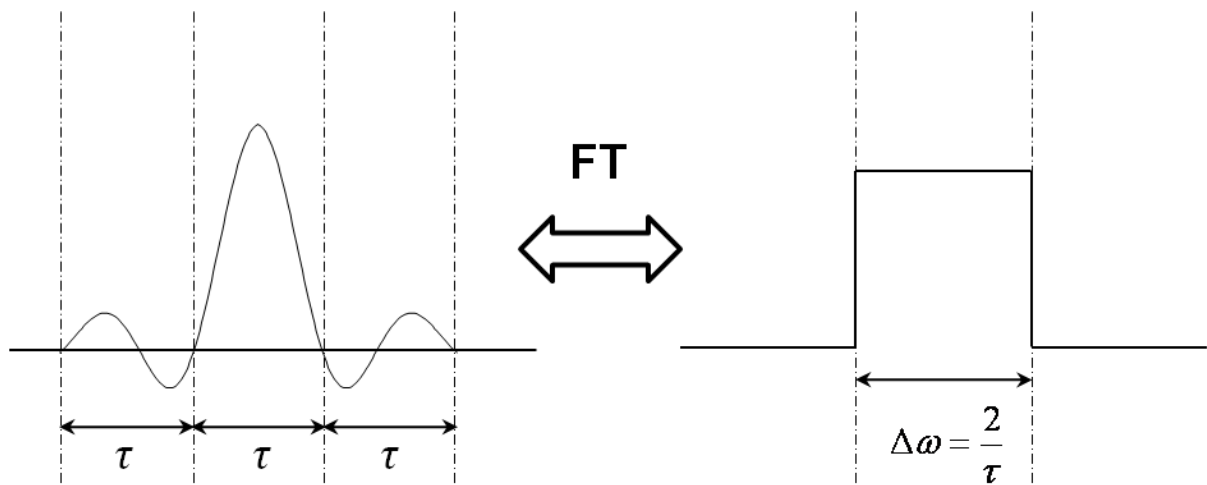


**Figure 1.11** – Fourier transform (FT) of a sinc ( $\frac{\sin(x)}{x}$ ) pulse. The sinc pulse in the time domain corresponds to a rectangular pulse in the frequency domain.

The bandwidth is proportional to the slice thickness as follows:

$$\Delta z = \frac{\Delta \omega}{\gamma \cdot G_z} \quad [1.37]$$

where  $\Delta z$  is the slice thickness,  $\Delta \omega$  is the frequency bandwidth,  $\gamma$  is the gyromagnetic ratio, and  $G_z$  is the linear gradient applied along the z-axis direction. The thickness of the slice can be altered by either changing the frequency bandwidth of the RF pulse or the amplitude of the gradient. For imaging slices away from the isocenter of the magnet, the imaging slice can be offset in the slice plane by changing the center frequency of the RF pulse:

$$\omega(z) = \gamma \cdot G_z \cdot z \quad [1.38]$$

Thus, for a desired offset of a 0.5 cm ( $z$ ) in the presence of a 1 G/cm gradient, the frequency of the RF pulse must be increased by 2129 Hz ( $\gamma = 4258$  Hz/G).

### 1.3.2. Frequency Encoding

Analogous to the spatial encoding of the slice-selection process, the in-plane frequency encoding process applies a linear field gradient along the x-axis (called the read-out gradient) during the data acquisition process period to encode spatial information along the x-direction (x-axis is chosen arbitrarily here for the read-out gradient). As in the case of slice selection, the read-out gradient results in a linear variation of the precessional frequencies of the nuclei which

correspond to the spatial location of the nuclei and is dependent on the gradient amplitude. This relationship is equivalent to:

$$FOV_x = \frac{BW}{\gamma \cdot G_x} \quad [1.39]$$

where  $FOV_x$  is the field of view (FOV) along the readout or x-direction in this case (cm),  $\gamma$  is the gyromagnetic ratio (Hz/G),  $G_x$  is the gradient amplitude (G/cm) and  $BW$  is the signal bandwidth (Hz) specified as:

$$BW = \frac{N_f}{AT} \quad [1.40]$$

where  $N_f$  is the number of data points used to digitize the NMR signal during acquisition time,  $AT$ .

### 1.3.3. Phase Encoding

The second dimension of the image is spatially encoded in the phase of NMR signal by applying a gradient,  $G_y$ , along the y-direction of the slice plane.  $G_y$  must be applied before the echo readout either between or after slice-selective RF pulses (in the case of spin-echo experiment). Upon the application of phase-encoding gradient, a phase shift is induced based on the spatial location of the nuclei along the direction of the gradient at each voxel. The precessional frequencies of the nuclei correspond to the spatial position of the nuclei and are dependent on the gradient amplitude:

$$\omega(y) = \gamma \cdot G_y \cdot y \quad [1.41]$$

where  $\omega(y)$  is the frequency of precession experienced along the y-axis,  $\gamma$  is the gyromagnetic ratio,  $y$  is the direction along the phase-encoding or y-direction in this case, and  $G_y$  is the gradient applied along the y-axis direction.

A phase shift is induced in the nuclei when  $G_y$  is applied for time  $t$ :

$$\Delta\phi = \gamma \cdot G_y \cdot y \cdot t \quad [1.42]$$

Since the phase information imparted to the nuclei is retained through the experiment, the pulse sequence must be repeated a number of times ( $N_p$ ) using an equivalent number of phase-encoding gradients ( $G_{y,inc}$ ). This increment is dependent on the desired FOV in the phase-encoding direction ( $FOV_y$ ) which is equal to:

$$FOV_y = \frac{1}{\gamma \cdot G_{y,inc} \cdot t} \quad [1.43]$$

where  $G_{y,inc}$  is the minimum gradient increment required and  $t$  is the duration of the gradient application. From this relationship and the number of phase-encoding steps ( $N_p$ ), the minimum and maximum gradient values can be determined as:

$$G_{y,range} = \pm \left( \frac{N_p - 1}{2} \right) \cdot G_{y,inc} \quad [1.44]$$

$G_{y,range}$  is the range of possible values for the gradient amplitude.



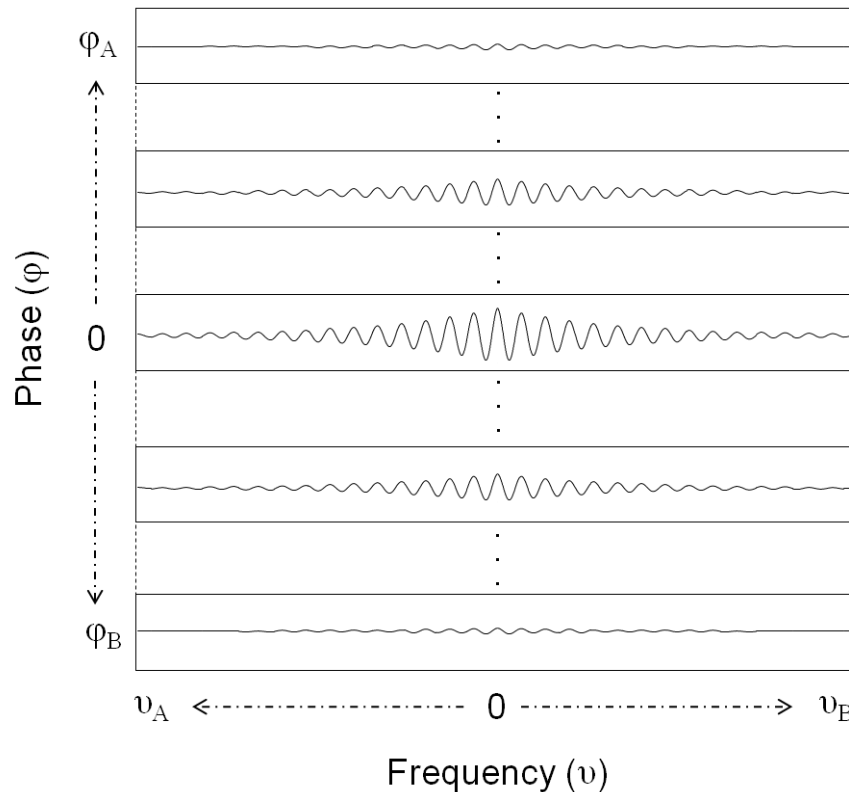


**Figure 1.12** – Imaging of the k-space. The phase encoding direction is shown in the vertical axis while the frequency encoding direction is shown in the horizontal axis. At zero frequency the maximum amplitude appears in all lines of k-space due to the collection of spin echoes with the nuclei in phase. Moving away from center frequency the nuclei become out of phase resulting in weaker signals at  $\nu_A$  and  $\nu_B$ . With phase encoding the maximum amplitude appears at zero phase since no dephasing is experienced by the nuclei. With dephasing the signal amplitude decreases causing the lowest signals to occur at  $\varphi_A$  and  $\varphi_B$ .

#### 1.3.4. Fourier Reconstruction in k-space

The frequency and phase encoding information for each slice is depicted in a two-dimensional (2D) k-space (Fig. 1.12). Each line of the k-space is collected at a particular phase increment. On the frequency encoding axis, each

increment represents a single sampling point. The total length of the frequency axis is equal to the total number of sampling points ( $N_f$ ) in Eq. [1.40]. Notice that the center of k-space (0,0) contains the maximum amplitude because the phase and frequency shifts are near zero. On the other with a phase and frequency shift the signal is attenuated due to dephasing of the spin coherence. The center of the k-space contains the low-frequency spatial information while the peripheral region contains the detail information (high-frequency information). Taking the 2D-FT of the k-space will result in the formation of a 2D MR image.

### 1.3.5. Imaging Sequences

In order to collect a complete 2D image, multiple signal acquisitions are required as discussed in the earlier portion of Section 1.3. In summary, a slice selective RF pulse is required to tip the magnetization onto the transverse plane. As soon as the RF pulse is turned off, a phase encoding gradient needs to be applied. Then a readout gradient must be applied during the echo acquisition.

#### 1.3.5.1. Spin Echo Sequence

The spin echo sequence uses  $90^\circ$  and  $180^\circ$  RF pulses (Fig. 1.13). The  $90^\circ$  RF pulse is first applied while the slice-select gradient ( $G_z$ ) is on, rotating the magnetization of a particular slice onto the transverse plane. The phase-encoding gradient ( $G_y$ ) is applied immediately at the first increment value of  $G_{y,l}$  to begin phase encoding. Then a  $180^\circ$  RF pulse is applied to rephase the nuclei

that began to dephase as a result of  $T_2^*$  relaxation. This way the collected signal will contain information of the intrinsic  $T_2$  relaxation (discussed earlier in Section 1.2.6.4). During the  $180^\circ$  RF pulse the slice-select gradient is turned on to affect the nuclei in the same slice as elected earlier. Then, the readout gradient is turned on during the spin echo acquisition to encode in the frequency direction. Notice the grey lobes in the  $G_z$  and  $G_x$  gradients. These are rephasing gradients that are applied for phase-shift correction due to dephasing of nuclei as a result of the application of the  $G_z$  and  $G_x$  gradients. After the first sequence is complete, the sequence repeats with the next  $G_y$  increment value ( $G_{y,2}$ ) until the end of the phase encoding steps. The main disadvantage of this technique is that the echo time (TE) cannot be very short due to the presence of the finite  $180^\circ$  RF pulse. However, the signal received with this technique will have a higher magnitude, compared to the gradient echo technique (discussed in Section 1.3.5.2).

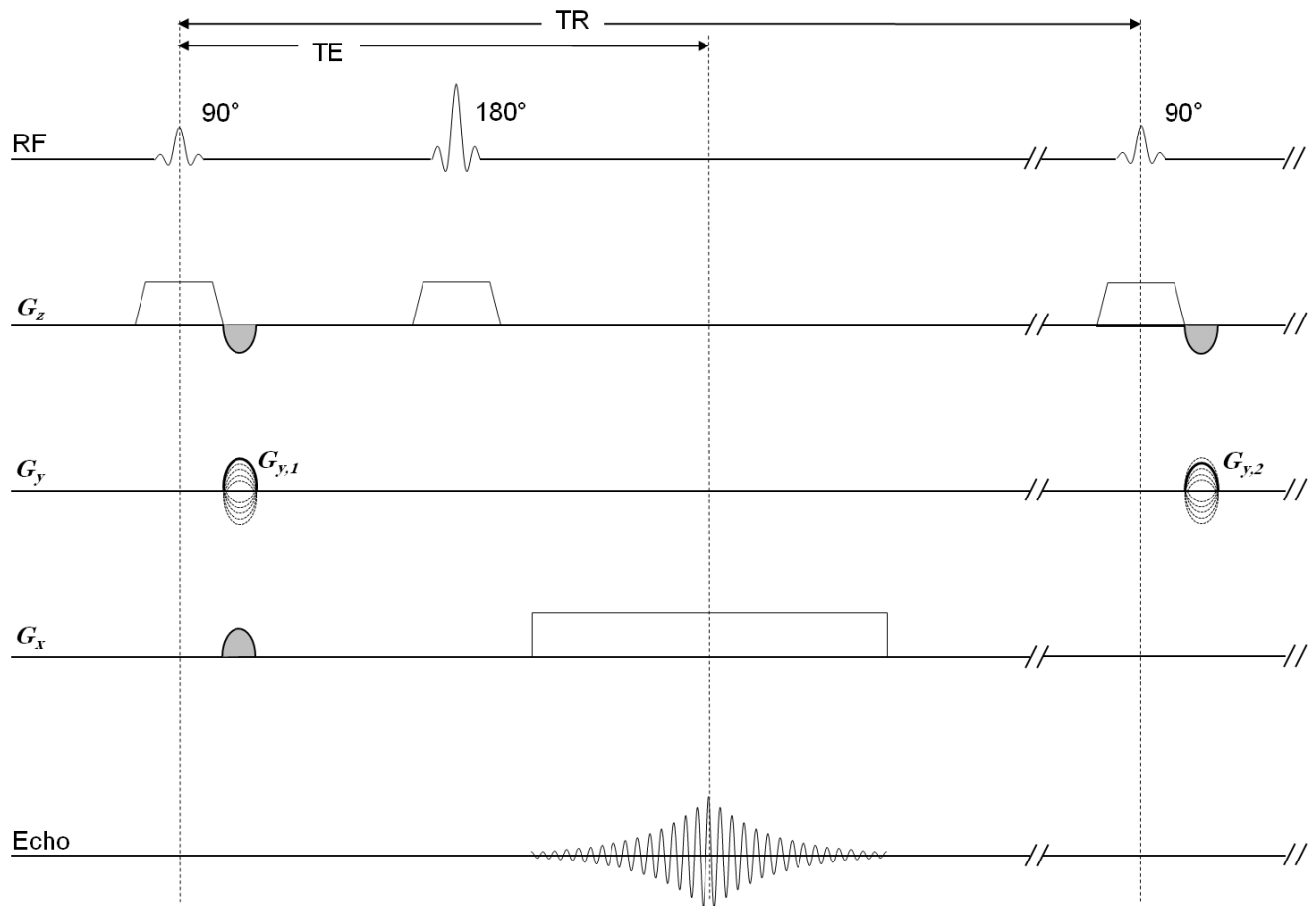


**Figure 1.13** – A complete spin echo pulse sequence diagram showing two different gradient values of  $G_y$ ,  $G_{y,1}$  and  $G_{y,2}$ . The repetition time (TR) is the duration between the applications of two  $90^\circ$  RF pulses. The echo time (TE) is the time between the center of the  $90^\circ$  RF pulse and center of the generated spin echo. A  $90^\circ$  RF pulse is applied at a slice-selective gradient. The phase encoding gradient,  $G_{y,1}$ , is then applied immediately after which a slice-selective  $180^\circ$  RF pulse is applied. During the signal acquisition time the readout gradient is turned on for frequency encoding. The grey lobes represent rephasing gradients that apply a phase-shift correction. The sequence then repeats with the next phase encoding gradient,  $G_{y,2}$ , until the end of the phase encoding steps.

### 1.3.5.2. Gradient Echo Sequence

The gradient echo sequence is similar to the spin echo sequence in terms of gradient application and signal acquisition (discussed in Section 1.3.5.1). The main difference is that only a single RF pulse is used with gradient echo. The RF pulse used in a gradient echo sequence is typically less than  $90^\circ$  (Fig. 1.14). A single RF pulse flips the magnetization onto the transverse plane and over time,  $T_2^*$  relaxation occurs. There is no  $180^\circ$  RF pulse to correct for the dephasing of the nuclei. As a result the image formed by this technique will be  $T_2^*$ -weighted. Only the rephasing gradients are present for phase-shift correction due to the application of the gradients. The low flip angle RF pulses allows for considerable shortening of the TR time since spins experiencing smaller flip angles will return to the equilibrium state at a quicker rate. Also, the absence of a  $180^\circ$  RF pulse allows the gradient echo sequence to achieve very short TE times. The disadvantage of this technique is acquiring images at a lower signal-to-noise compared to the spin echo technique.

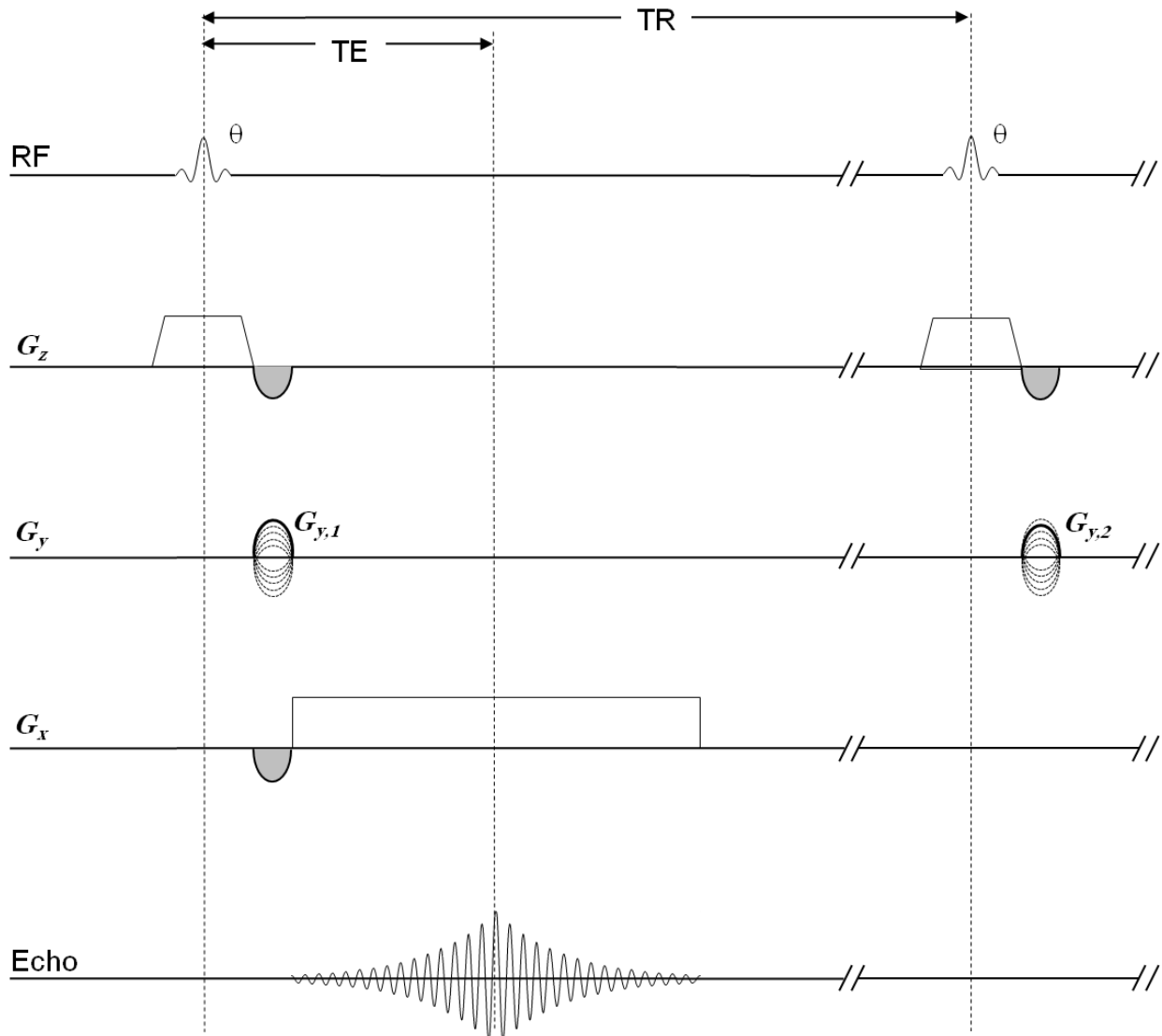


**Figure 1.14** – A complete gradient echo pulse sequence diagram showing two different gradient values of  $G_y$ ,  $G_{y,1}$  and  $G_{y,2}$ . The repetition time (TR) is the duration between the applications of two RF pulses at angle  $\theta$ . The echo time (TE) is the time between the center of the RF pulse and center of the generated spin echo. The RF pulse is applied at a slice-selective gradient. The phase encoding gradient,  $G_{y,1}$ , is then applied immediately. During the signal acquisition time the readout gradient is turned on for frequency encoding. The grey lobes represent rephasing gradients that apply a phase-shift correction. The sequence then repeats with the next phase encoding gradient,  $G_{y,2}$ , until the end of the phase encoding steps.

## References

1. Gadian DG. NMR and its Applications to Living Systems (Oxford Science Publications): Oxford University Press, USA; 1996. 300 p.
2. Hashemi R, Bradley Jr. W, Lisanti C. MRI The basics. Philadelphia: Lippincott Williams & Wilkins; 2004. 353 p.
3. Bernstein M, King K, Zhou X. Handbook of MRI Pulse Sequences: Academic Press; 2004. 1040 p.
4. Curry T, Dowdey J, Murry R. Christensen's Physics of Diagnostic Radiology: Lippincott Williams & Wilkins; 1990. 522 p.
5. Dixon RL, Ekstrand KE. The physics of proton NMR. Med Phys 1982;9(6):807-818.
6. Axel L. Relaxation times and NMR signals. Magnetic Resonance Imaging 1984;2:121-130.
7. Wright GA. Magnetic Resonance Imaging. IEEE Signal Processing Magazine 1997;14(1):56-66.
8. Bloch F, Hansen W, Packard M. Nuclear Induction. Phy Rev 1946;69:127.
9. Purcell E, Torrey H, Pound R. Resonance absorption by nuclear magnetic moments in a solid. Phys Rev 1946;69:37-38.
10. Wehrli F. Principles of magnetic resonance. In: Stark DD, Bradley WG Jr (eds): Magnetic resonance imaging. The C.V. Mosby Company, St. Louis, MO; 1988. p 3-23.
11. Damadian R. Tumor detection by nuclear magnetic resonance. Science 1971;171(976):1151-1153.
12. Lauterbur P. Image formation by induced local interactions: examples employing nuclear magnetic resonance. Nature 1973;242:190-191.

**CHAPTER II**

**CEREBRAL ISCHEMIA AND**

**APPARENT DIFFUSION**

**COEFFICIENT**



## **2.1. Statistics**

Stroke is caused by a disturbance of cerebral blood flow that leads to reduction of oxygen and nutrient supply to cerebral tissue resulting in loss of normal physiological cell function and eventually cell death. Stroke is the third largest cause of death, ranking behind heart disease and cancer, and a leading cause of long-term disability in the United States. According to the National Institute of Neurological Disorders and Stroke (NINDS), about 795,000 people suffer a new or recurrent stroke each year. In 2006, stroke claimed the lives of 137,119 people according to the figures from the American Heart Association (AHA). The AHA also estimates there are about 6.4 million stroke survivors today in the United States which is almost twice the number recorded in 1998. The increase in survival is owed to the methods of treatment and drugs that have been available during the past decade. Aspirin and tissue plasminogen activator (tPA) are drugs commonly used that attempt to restore blood flow to the brain by their anti-coagulant effect and clot-dissolving ability, respectively. Depending on the severity of the cerebral blood flow blockage, surgical treatments such as mechanical removal of clots, carotid endarterectomy, angioplasty, and stent placement can aid to not only restore cerebral blood flow, but prevent the occurrence of another stroke in that location. In the more severe hemorrhagic stroke cases, surgery can be used to repair blood vessel abnormalities using procedures like aneurysm clipping. In any case, a reliable method of identifying the severity of stroke within its onset could allow appropriate specific therapy to

be instituted as early as possible to the patient to further increase the chances of survival.

## **2.2. Cerebral Physiology**

The function of cells under normal and pathological conditions will be discussed in this section.

### **2.2.1. Normal Cell Function**

Cerebral tissue maintains normal cell function by receiving oxygen and nutrients from the cerebral blood circulation. The main fuel for cells in the cerebral tissue is glucose. Since glucose storage in the brain is negligible, the cells depend on the cerebral circulation for a constant supply of glucose. Thus, maintenance of perfusion is crucial to ensure normal cell function. In normal cells, mitochondria use oxygen to produce adenosine triphosphate (ATP) via aerobic respiration. The energy generated from ATP metabolism supports all cell functions including maintenance of the sodium-potassium pump ( $\text{Na}^+\text{-K}^+\text{-ATPase}$ ). This pump, amongst its other functions, maintains the normal ionic gradient (resting potential) across the cell membrane and stabilizes the cell volume by maintaining osmotic balance (2). Under resting conditions, the intracellular (IC) level of  $\text{K}^+$  far exceeds the extracellular (EC) concentration while  $\text{Na}^+$ , chloride ( $\text{Cl}^-$ ), and calcium ( $\text{Ca}^{2+}$ ) dominate in the EC space.

### 2.2.2. Pathophysiology of Ischemic Stroke

Stroke is a cerebrovascular disease that occurs in two categories: ischemic and hemorrhagic. Ischemic strokes are caused by disruption in normal cerebral blood flow due to occlusion of a blood vessel, while hemorrhagic strokes result from the rupture of a blood vessel. In either case, the disruption of cerebral blood flow initiates a chain of biochemical events that disrupts normal cell function. The reduction in blood flow leads to limited supply of oxygen in the cell for aerobic respiration to produce ATP. To compensate for the loss in oxygen supply, the cells begin anaerobic respiration from glucose metabolism to maintain an adequate level of ATP. Once the limited reserve of glucose is depleted in the brain, anaerobic metabolism results in an accumulation of lactic acid which disrupts the normal acid-base balance in the brain. Lack of ATP prevents the cells from maintaining the sodium-potassium pump, thus compromising the resting potential of the cell. Failure of ion homeostasis leads to anoxic depolarization of the cell membrane, in which  $K^+$  leaves the cell and  $Na^+$ ,  $Ca^{2+}$ , and  $Cl^-$  move into the cell. This movement of ions disrupts the osmotic balance causing an influx of water from the EC space to the IC space which leads to cell swelling (cytotoxic edema) (Fig. 2.1). Elevated  $Ca^{2+}$  levels in the cells trigger the release of excitatory amino acid neurotransmitters such as glutamate, which further activates other receptors resulting in excessive accumulation of  $Ca^{2+}$  in the cell. Excess  $Ca^{2+}$  activates enzyme systems such as proteases, lipases, and endonucleases which break down the cellular structure.

Free radicals, reactive oxygen species, and other harmful chemicals are released as metabolic products of enzyme activity. These agents further increase the rate of cellular breakdown. Once the mitochondria breaks down, apoptotic factors are released in the cell which initiates the caspase-dependent apoptosis cascade that leads to cell death. Cell death can also occur by necrosis, which is a sudden and uncontrolled cell death unlike apoptosis, which is classified by a complex set of events in response to ischemic injury.

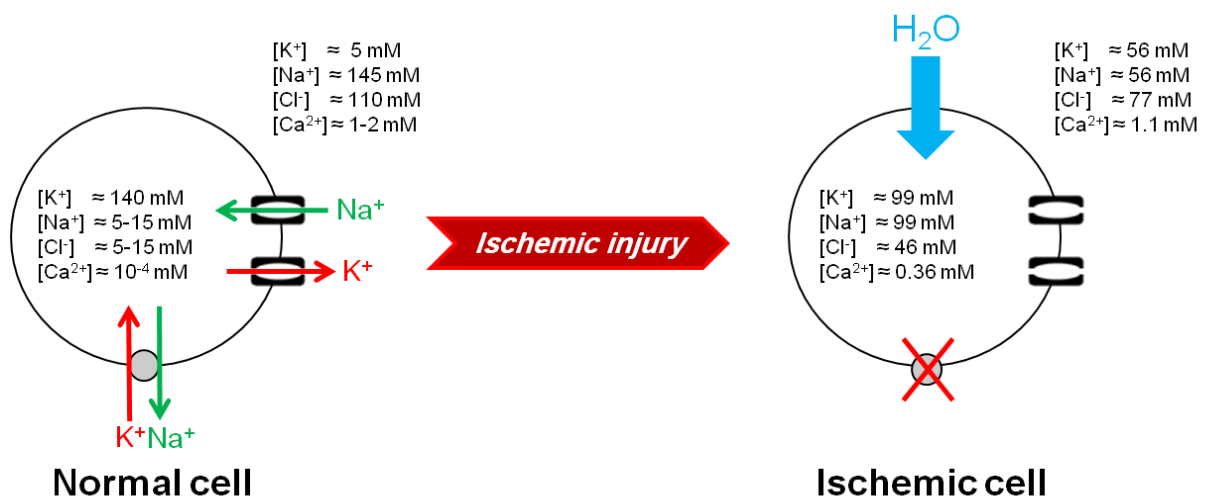


**Figure 2.1** – Cartoon illustrating ionic movement in normal and ischemic cells. Left: In normal cells, the sodium-potassium pump (Na<sup>+</sup>-K<sup>+</sup>-ATPase) maintains a high level of K<sup>+</sup> in the ICS and a high level of Na<sup>+</sup>, Ca<sup>2+</sup>, and Cl<sup>-</sup> in the ECS. Right: In ischemic cells, lack of Na<sup>+</sup>-K<sup>+</sup>-ATPase function leads to movement of K<sup>+</sup> from the ICS to ECS and movement of Na<sup>+</sup>, Ca<sup>2+</sup>, and Cl<sup>-</sup> from the ECS to the ICS, which results in a net movement of water molecules from the ECS to the ICS. This water movement results in intracellular swelling (cytotoxic edema). ECS = Extracellular space, ICS = Intracellular space, K<sup>+</sup> = potassium ions, Na<sup>+</sup> = sodium ions, Ca<sup>2+</sup> = calcium ions, Cl<sup>-</sup> = chloride ions. Ion concentrations shown were obtained from Alberts *et al.* (1).

### 2.3. Apparent Diffusion Coefficient

The apparent diffusion coefficient (ADC), measured using diffusion-weighted MRI, is a diffusion parameter that can measure the magnitude of water molecule movement in cerebral tissue. In normal tissue, the ADC of water in the EC space is presumed to be greater than that of the IC space because the cell membrane and IC organelles can restrict water diffusion, thereby reducing the ADC of IC water. Wesbey *et al.* and Le Bihan *et al.* first demonstrated the application of diffusion-weighted NMR techniques to *in vivo* systems (3,4). Due to the sensitivity of ADC to changes in tissue water diffusion properties that occur during cerebral ischemia, ADC measurement has been established as an effective technique which has been extensively used to study acute stroke. Moseley *et al.* demonstrated in a cat stroke model that during cerebral ischemia, there is a reduction in the ADC value of cerebral tissue water (5). In addition to cerebral ischemia, decline in ADC of cerebral water has been observed in other neurological disorders such as cortical spreading depression, low-grade astrocytoma (4), status epilepticus (6) and hypoglycemia. Even though the cell volume changes in all these pathophysiological states follow a similar pattern, the reason for ADC decline is not very well understood.

### 2.4. ADC Decline Hypotheses

Several hypotheses have been suggested in the last two decades to explain the decrease in overall ADC in response to cerebral injury (Fig. 2.2):

1. During ischemia, movement of water occurs from the EC space to the IC space resulting in cytotoxic edema. This results in a net loss of fast diffusing water molecules (high ADC) in the EC space and a net increase of slow diffusing water molecules (low ADC) in the IC space. Thus, in the final state there is a larger population of water molecules with lower ADC values (in the IC space) which is responsible for the overall ADC decline (5-9).
2. Due to energy depletion on the onset of ischemic injury, there is a loss of intracytoplasmic motion and/or an increase in the viscosity of IC milieu. This leads to further retardation of water molecule motion resulting in a lowering of IC water ADC. This lowering of IC water ADC is responsible for the overall ADC decline (6,10-14).
3. Ischemia causes a net movement of water from the EC space to the IC space causing cytotoxic edema. This causes an increase in the IC volume fraction and a decrease in the EC volume fraction. As a result, due to loss of EC volume, EC water diffuses with more restrictions and increased tortuosity. That causes the EC water ADC to decrease. This decrease in EC water ADC is responsible for the overall ADC decline (10,15-17).
4. Reduction in movement of water molecules across the cell membrane due to membrane permeability changes is responsible for the overall ADC decline (18).

Even though one mechanism may dominate the reduction of overall water ADC decline, the more likely scenario is that the change in overall water ADC is a result from a combination of all these mechanisms due to the complex nature of water diffusion (19).

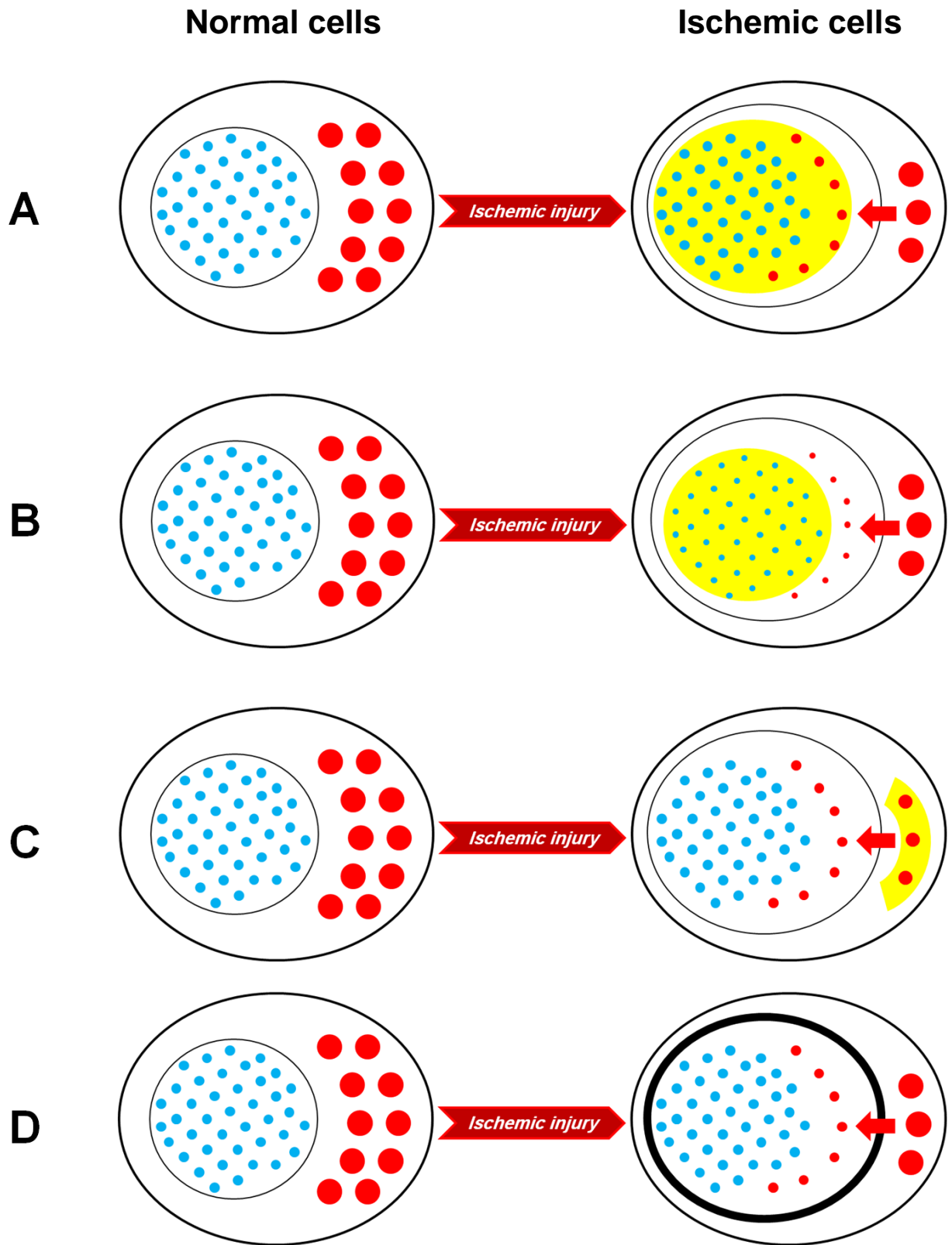




**Figure 2.2** – Cartoon illustrating Hypotheses #1–#4 of overall water ADC decline in ischemic cells. The blue circles and red circles represent ICS and ECS water molecules, respectively. The number of circles corresponds to water volume and the size of the circles corresponds to water ADC magnitude in the respective compartments. Thus, in normal cells, the ICS water volume is approximately four times larger than the ECS water volume (IC/EC fraction  $\approx 80/20$ ). The size of the water molecules in the ICS is smaller than that of the ECS indicating a lower ADC value of ICS water compared to ECS water in normal cells. A – Hypothesis #1: Following ischemic injury, ECS water moves into the ICS resulting in a loss of high ADC water from the ECS and an increase of low ADC water in the ICS. In the final state, a larger population of water is comprised of low ADC values (water molecules shaded in yellow), which causes an overall water ADC decline. B – Hypothesis #2: Following ischemic injury, energy depletion in normal cells results in a loss of intracytoplasmic motion and/or an increase in the viscosity of ICS milieu. This leads to further retardation of ICS water resulting in lowering of ICS water ADC. This lowering of ICS water ADC is responsible for the overall ADC decline (water molecules shaded in yellow). C – Hypothesis #3: Following ischemic injury, ECS water moves into the ICS space causing an increase in the ICS volume and a decrease in the ECS volume. Loss of ECS volume causes the ECS water to diffuse with more restrictions and increased tortuosity resulting in a decrease in the ECS water ADC. This decrease in ECS water ADC is responsible for the overall ADC decline (water molecules shaded in yellow). D – Hypothesis #4: Following ischemic injury, there is a reduction in movement of water molecules across the cell membrane due to membrane permeability changes (represented by thick dark line). This causes an overall ADC water decline. ADC = Apparent diffusion coefficient; ECS = Extracellular space; ICS = Intracellular space.

## 2.5. Exogenous and Metabolite Surrogates

Since conventional NMR data contains combined signals from the IC and EC water, it is difficult to determine which compartment is responsible for the

overall change in water ADC during cerebral ischemia. To isolate the diffusion properties of IC and EC water, many studies have employed the use of exogenous and metabolite surrogates as an indirect method of gaining insight about compartmental water diffusion (10-14). Neil *et al.* studied the *in vivo* diffusion properties of cesium-133 ( $^{133}\text{Cs}$ ), an IC marker and  $\text{K}^+$  analog, and found that the changes in the  $^{133}\text{Cs}$  ADC correlated with the reduction of water ADC within the same order of magnitude following cerebral ischemia (12). Duong *et al.* investigated the use of 2-[ $^{19}\text{F}$ ]luoro-2-deoxyglucose-6-phosphatase (2FDG-6P) as a compartment-specific marker that could be selectively isolated either to the IC space or EC space depending on the method on 2FDG-6P infusion (13). This study concluded that the change in 2FDG-6P ADC in the IC and EC spaces matched the water ADC decline during global ischemia in a rat model. Another study by Duong *et al.* measured the ADC of extracellular markers – mannitol, phenylphosphonate, and polyethylene glycol – to infer the ADC of EC water (14). Other spectroscopic studies of cerebral metabolites suggest that changes in IC water dominate the overall ADC change during ischemia based on reduction in the ADCs of metabolites such as N-acetyl-aspartate, creatine, and choline during focal ischemia in rat brain (10,11). In all these studies, changes in water ADC are being inferred from the behavior of exogenous molecular tracers and/or metabolites, which may have different molecular sizes, binding properties, diffusion coefficient temperature dependence, and exchange properties in normal and ischemic tissue compared to water.

## 2.6. Diffusigraphy

Diffusigraphy is another technique that has been used to isolate IC and EC diffusion water properties (20). This method involves acquiring a series of diffusion-weighted NMR data while systematically changing the diffusion-weighting parameter (b values) over a large range, and then fitting the diffusion signal attenuation curves to a sum of two decaying exponentials (biexponential model). As per the conventional hypothesis, the fast ADC value should correlate with the EC volume fraction while the slow ADC value should correlate with the IC volume fraction. Results from studies in the rat and human brain showed that the ADC values did not agree with the known fractions of IC and EC volume (21-23). This discrepancy could be attributed to  $T_2$  relaxation time differences between the IC and EC water and diffusion anisotropy (24). Moreover, Mulkern *et al.* admit that even though the biexponential model of the diffusion attenuation curves allowed extraction of two ADC values, there was not enough experimental evidence to conclude that the two exponential decay terms arise from two independently diffusing compartments, i.e. the IC and EC compartments (23). A study by Helmer *et al.* showed that due to restriction effects, a single compartment can exhibit biexponential decay of a diffusion signal (25). Thus, a biexponential model of diffusion signal attenuation does not necessarily imply the signal must arise from two compartments. Biexponential signal decay could occur due to restrictions, water exchange, relaxation time effects, compartmental ADC differences or a combination of these effects in a single or multiple-

compartment system. Thus, application of diffusigraphy alone is not enough to for accurate compartmental water ADC measurements.

## 2.7. Relaxo-diffusigraphy

Silva *et al.* demonstrated a unique technique where they combined relaxography with diffusion encoding to measure compartment-specific ADC values using diffusion-weighted inversion-recovery spin-echo spectroscopy (DW-IRSE) and diffusion-weighted echo-planar imaging (DW-EPI) (26,27). Relaxography is a technique that uses a contrast reagent (CR) to distinguish between IC and EC water signal based on differences in their respective  $T_1$  relaxation times (28). Silva *et al.* used gadopentate dimeglumine (Gd-DTPA) as the CR which is selective to the EC compartment (27). As a result, the CR enhanced the relaxation of EC water by decreasing the  $T_1$  relaxation time in the EC space, thereby separating the signal contributions of IC and EC water signal. Diffusion experiments were then performed which enabled direct measurement of apparent  $T_1$ ,  $T_2$ , ADC, and volume fraction of the IC space. The apparent  $T_1$ ,  $T_2$ , ADC, and volume fraction of the EC space was calculated indirectly from the IC data. The volume fraction for the IC space calculated using this method matches the physiologically known values for IC fraction (~80%) which was not obtained when using diffusigraphy alone. Thus, this method of combined diffusigraphy and relaxography allows compartment-specific measurement of ADC.

Silva *et al.* concluded from their study that the ADC value measured in normal brain (comprised of IC and EC water) were statistically similar to the ADC value of the CR-infused brain (comprised only of IC water) suggesting that the major determinant of overall ADC value in the rat cerebral tissue is the water ADC of the IC space (26). In cerebral ischemic rats, the reduction of ADC measured in the CR-free brain was statistically similar to the ADC value measured in the CR-infused brain. From these results, Silva *et al.* conclude that the diffusion-weighted contrast during cerebral ischemia is primarily a result of the ADC reduction in the IC compartment. This finding is in agreement with Hypothesis #2 and with results obtained using ADC of exogenous and metabolite surrogates to infer the ADC of water (10-14). Nonetheless, in spite of these promising findings, the other hypotheses cannot be completely ruled out.

## 2.8. Manganese-Enhanced MRI

Divalent manganese ion ( $Mn^{2+}$ ) is a widely used  $T_1$  CR in manganese-enhanced MRI (MEMRI) studies for animal neuroimaging.  $Mn^{2+}$  acts as  $Ca^{2+}$  analog and enters the neuronal IC space via voltage-gated calcium channels (29) following neuronal activation (30-33) which results in accumulation of IC  $Mn^{2+}$ .  $T_1$ -weighted MRI can then readily detect a reduction of regional water proton  $T_1$  due to the paramagnetic  $Mn^{2+}$ . This approach is different from the previous case that used Gd-DTPA since Gd-DTPA only resides in the EC space, while  $Mn^{2+}$  ends up in both the EC and IC space mainly populating the IC space. Using  $Mn^{2+}$

as an IC CR could provide interesting insight in relation to IC and EC ADC measurements compared to the use of an EC-CR. Residence of  $Mn^{2+}$  in the larger water volume fraction affects the relaxation time of the majority of water in the cell, whereas the EC-CR only affects a small water volume fraction in the EC space. Application of relaxo-diffusigraphy using  $Mn^{2+}$  will be interesting to see if this method yields similar or different results compared to EC-CR. This information could provide further insight into the role of ADC decline during cerebral ischemia.

## References

1. Alberts B, Johnson A, Lewis J, Raff M, Roberts K, Walter P. *Molecular Biology of the Cell*, Fourth Edition: Garland Science; 2002. 1616 p.
2. Sweadner KJ GS. Active transport of sodium and potassium ions: mechanism, function, and regulation. *N Engl J Med* 1980;302(14):777-783.
3. Wesbey GE, Moseley ME, Ehman RL. Translational molecular self-diffusion in magnetic resonance imaging. II. Measurement of the self-diffusion coefficient. *Invest Radiol* 1984;19(6):491-498.
4. Le Bihan D, Breton E, Lallemand D, Grenier P, Cabanis E, Laval-Jeantet M. MR imaging of intravoxel incoherent motions: application to diffusion and perfusion in neurologic disorders. *Radiology* 1986;161(2):401-407.
5. Moseley ME, Cohen Y, Mintorovitch J, Chileuitt L, Shimizu H, Kucharczyk J, Wendland MF, Weinstein PR. Early detection of regional cerebral ischemia in cats: comparison of diffusion- and T2-weighted MRI and spectroscopy. *Magn Reson Med* 1990;14(2):330-346.
6. Zhong J, Petroff OA, Prichard JW, Gore JC. Changes in water diffusion and relaxation properties of rat cerebrum during status epilepticus. *Magn Reson Med* 1993;30(2):241-246.
7. van Gelderen P, de Vleeschouwer MH, DesPres D, Pekar J, van Zijl PC, Moonen CT. Water diffusion and acute stroke. *Magn Reson Med* 1994;31(2):154-163.
8. Benveniste H, Hedlund LW, Johnson GA. Mechanism of detection of acute cerebral ischemia in rats by diffusion-weighted magnetic resonance microscopy. *Stroke* 1992;23(5):746-754.
9. Anderson AW, Zhong J, Petroff OA, Szafer A, Ransom BR, Prichard JW, Gore JC. Effects of osmotically driven cell volume changes on diffusion-weighted imaging of the rat optic nerve. *Magn Reson Med* 1996;35(2):162-167.

10. van der Toorn A, Sykova E, Dijkhuizen RM, Vorisek I, Vargova L, Skobisova E, van Lookeren Campagne M, Reese T, Nicolay K. Dynamic changes in water ADC, energy metabolism, extracellular space volume, and tortuosity in neonatal rat brain during global ischemia. *Magn Reson Med* 1996;36(1):52-60.
11. Wick M, Nagatomo Y, Prielmeier F, Frahm J. Alteration of intracellular metabolite diffusion in rat brain in vivo during ischemia and reperfusion. *Stroke* 1995;26(10):1930-1933; discussion 1934.
12. Neil JJ, Duong TQ, Ackerman JJ. Evaluation of intracellular diffusion in normal and globally-ischemic rat brain via  $^{13}\text{C}$  NMR. *Magn Reson Med* 1996;35(3):329-335.
13. Duong TQ, Ackerman JJ, Ying HS, Neil JJ. Evaluation of extra- and intracellular apparent diffusion in normal and globally ischemic rat brain via  $^{19}\text{F}$  NMR. *Magn Reson Med* 1998;40(1):1-13.
14. Duong TQ, Sehy JV, Yablonskiy DA, Snider BJ, Ackerman JJ, Neil JJ. Extracellular apparent diffusion in rat brain. *Magn Reson Med* 2001;45(5):801-810.
15. Latour LL, Svoboda K, Mitra PP, Sotak CH. Time-dependent diffusion of water in a biological model system. *Proc Natl Acad Sci U S A* 1994;91(4):1229-1233.
16. Sykova E, Svoboda J, Polak J, Chvatal A. Extracellular volume fraction and diffusion characteristics during progressive ischemia and terminal anoxia in the spinal cord of the rat. *J Cereb Blood Flow Metab* 1994;14(2):301-311.
17. Norris DG, Niendorf T, Leibfritz D. Healthy and infarcted brain tissues studied at short diffusion times: the origins of apparent restriction and the reduction in apparent diffusion coefficient. *NMR Biomed* 1994;7(7):304-310.



18. Helpert J, Ordidge R, Knight R. The effect of cell membrane permeability on the apparent diffusion coefficient of water, *in Proc.*, SMRM, 11th Annual Meeting. 1992; Berlin, Germany. p 1201.
19. Szafer A, Zhong J, Gore JC. Theoretical model for water diffusion in tissues. *Magn Reson Med* 1995;33(5):697-712.
20. Vetek G, Palyka I, Sotak C, Springer C. CR-free discrimination of intra- and extracellular  $^1\text{H}_2\text{O}$  signals from yeast cell suspensions by diffusion-space relaxography (diffusigraphy), *Proc. Soc. Magn. Reson.*; 1994. p 1051.
21. Niendorf T, Dijkhuizen RM, Norris DG, van Lookeren Campagne M, Nicolay K. Biexponential diffusion attenuation in various states of brain tissue: implications for diffusion-weighted imaging. *Magn Reson Med* 1996;36(6):847-857.
22. Mulkern RV, Gudbjartsson H, Westin CF, Zengingonul HP, Gartner W, Guttman CR, Robertson RL, Kyriakos W, Schwartz R, Holtzman D, Jolesz FA, Maier SE. Multi-component apparent diffusion coefficients in human brain. *NMR Biomed* 1999;12(1):51-62.
23. Mulkern RV, Zengingonul HP, Robertson RL, Bogner P, Zou KH, Gudbjartsson H, Guttman CR, Holtzman D, Kyriakos W, Jolesz FA, Maier SE. Multi-component apparent diffusion coefficients in human brain: relationship to spin-lattice relaxation. *Magn Reson Med* 2000;44(2):292-300.
24. Clark CA, Le Bihan D. Water diffusion compartmentation and anisotropy at high b values in the human brain. *Magn Reson Med* 2000;44(6):852-859.
25. Helmer KG, Dardzinski BJ, Sotak CH. The application of porous-media theory to the investigation of time-dependent diffusion in in vivo systems. *NMR Biomed* 1995;8(7-8):297-306.
26. Silva MD, Omae T, Helmer KG, Li F, Fisher M, Sotak CH. Separating changes in the intra- and extracellular water apparent diffusion coefficient

- following focal cerebral ischemia in the rat brain. *Magn Reson Med* 2002;48(5):826-837.
27. Silva MD, Helmer KG, Lee JH, Han SS, Springer CS, Jr., Sotak CH. Deconvolution of compartmental water diffusion coefficients in yeast-cell suspensions using combined T(1) and diffusion measurements. *J Magn Reson* 2002;156(1):52-63.
  28. Labadie C, Lee JH, Vetek G, Springer CS, Jr. Relaxographic imaging. *J Magn Reson B* 1994;105(2):99-112.
  29. Catterall W, Perez-Reyes E, Snutch T, Striessnig J. International Union of Pharmacology. XLVIII. Nomenclature and Structure-Function Relationships of Voltage-Gated Calcium Channels. *Pharmacological Reviews* 2005;57(4):411-425.
  30. Naritaa K, Kawasakia F, Kita H. Mn and Mg influxes through Ca channels of motor nerve terminals are prevented by verapamil in frogs. *Brain Research* 1990;510:289-295.
  31. Lin YJ, Koretsky AP. Manganese ion enhances T1-weighted MRI during brain activation: an approach to direct imaging of brain function. *Magn Reson Med* 1997;38(3):378-388.
  32. Sloot W, Gramsbergen J. Axonal transport of manganese and its relevance to selective neurotoxicity in the rat basal ganglia. *Brain Res* 1994;657(1-2):124-132.
  33. Drapeau P, Nachshen DA. Manganese fluxes and manganese-dependent neurotransmitter release in presynaptic nerve endings isolated from rat brain. *J Physiol* 1984;348:493-510.

## **CHAPTER III**

# **DECONVOLVING THE INTRA- AND EXTRACELLULAR WATER COMPONENTS IN THE RAT BRAIN USING MANGANESE ENHANCED MRI (MEMRI)**

# Deconvolving the Intra- and Extracellular Water Components in the Rat Brain Using Manganese Enhanced MRI (MEMRI)

Mohammed Salman Shazeeb<sup>1,4</sup>, Christopher H. Sotak<sup>1-3</sup>

Departments of <sup>1</sup>Biomedical Engineering and <sup>2</sup>Chemistry & Biochemistry

Worcester Polytechnic Institute

Worcester, MA 01609

<sup>3</sup>Department of Radiology and <sup>4</sup>Graduate School of Biomedical Sciences

University of Massachusetts Medical School

Worcester, MA 01655

## 3.1. Preface

This study was done to determine if manganese ( $Mn^{2+}$ ) can be used to separate the intracellular and extracellular water components in the rat brain. I completed all aspects of this study by performing animal injections, collecting NMR data, reconstructing images, MATLAB programming for image analysis, and principal authorship in the writing of the manuscript. The manuscript work is in progress to be submitted for publication.

### 3.2. Abstract

Diffusion-weighted NMR techniques have established that the apparent diffusion coefficient (ADC) of cerebral tissue water decreases during ischemia. However, it is unclear whether the ADC change occurs due to changes in the intracellular (IC) space, extracellular (EC) space, or both. To better understand the mechanism of water ADC changes in response to ischemic injury, making IC and EC compartment specific measurements of water diffusion is essential. Past studies have measured compartment-specific diffusion coefficients using gadolinium (Gd-DTPA) as the MR contrast agent in yeast cells to distinguish between the IC and EC water proton signals based on differences in their respective longitudinal ( $T_1$ ) relaxation times. Gd-DTPA was employed as an EC contrast agent, thereby reducing the  $T_1$  value of the EC space. In this study we apply an alternate approach by using manganese ( $Mn^{2+}$ ) as the IC contrast agent.  $Mn^{2+}$  uptake by cells causes shortening of the  $T_1$  relaxation time of IC water. The relative difference in  $T_1$  relaxation times between the IC and EC compartments can be used to discriminate between the MR signals arising from water in the respective compartments.

### **3.3. Introduction**

Water is an essential fluid necessary to sustain life. All cells of the body live in a highly regulated fluid environment. The fluid within the cells occupies what is known as the intracellular (IC) compartment whereas the fluid outside the cells occupies the extracellular (EC) compartment. The cell membrane is a barrier that separates these two compartments and plays a crucial role in maintaining the volume and composition of the two compartments by regulating transport across the membrane. Movement of water between the two compartments and also within the cells is of particular interest since abnormalities in water movement and changes in compartmental volume fractions can lead to pathophysiological states such as acute ischemic stroke.

Over three decades ago, Andrasko (2) observed that the NMR signal measured from human erythrocytes could be emanating from a mixture of water molecule signals exchanging from both IC and EC compartments. Thus, the measured NMR signal may contain information that is a composite of NMR parameters (e.g., longitudinal and transverse relaxation times) and physical parameters (e.g., diffusion coefficients and membrane permeability) of the two compartments. Since these parameters can change values in response to pathology, it is essential to distinguish between the signals arising from the IC and EC compartments separately so that we can determine if one or both compartments are responsible for the change in overall NMR signal.

The apparent diffusion coefficient (ADC), measured using diffusion-weighted MRI (DW-MRI), is a diffusion parameter that can measure the magnitude of water molecule diffusion in cerebral tissue. DW-MRI techniques have established that the ADC of cerebral tissue water decreases during ischemia (3-5). Several hypotheses have been proposed assigning the ischemic ADC decrease to changes in the IC space, EC space, or both (5-18). However, the exact mechanism responsible for the ADC change remains a subject of debate due to the complex nature of water diffusion process in cells.

To better understand the mechanism of water ADC changes in response to ischemic injury, making IC and EC compartment specific measurements of water diffusion would be useful. Silva *et al.* (19) measured compartment-specific diffusion coefficients using gadolinium (Gd-DTPA) as the MR contrast reagent (CR) in yeast cells to distinguish between the IC and EC water proton signals based on differences in their respective longitudinal  $T_1$  relaxation times. Gd-DTPA was employed as an EC CR, thereby reducing the  $T_1$  value of the EC space. Silva *et al.* (18) extended the study to animals and measured compartment-specific diffusion coefficients in the brain in normal and ischemic rats using an EC CR.

In this study, we applied an alternate approach by using manganese ( $Mn^{2+}$ ), which is a widely used  $T_1$  CR in manganese-enhanced MRI (MEMRI) studies for animal neuroimaging.  $Mn^{2+}$  acts as  $Ca^{2+}$  analog and enters the neuronal intracellular space via voltage-gated calcium channels (20) following

neuronal activation (21-24). This results in accumulation of intracellular  $Mn^{2+}$ .  $T_1$ -weighted MRI can then readily detect a reduction of regional water proton  $T_1$  due to the paramagnetic  $Mn^{2+}$ . The relative difference in  $T_1$  relaxation times between the IC and EC compartments can be used to discriminate between the MR signals arising from water in the respective compartments.

The goal of this project was to separate the IC compartment from the EC compartment based on their respective longitudinal  $T_1$  relaxation times and water content in rat brains using MEMRI.

### 3.4. Theory

Signal intensity data obtained from inversion recovery MRI can be fit using non-linear least squares fitting to inversion recovery models derived from the Bloch equations to extract  $T_1$  relaxation times. A one-compartment model is illustrated by the following equation:

$$M_z(TI; M_0, b, T_1) = M_0 \cdot (1 - b \cdot e^{-\frac{TI}{T_1}}) \quad [3.1]$$

where  $M_z$  is the signal intensity,  $TI$  is the inversion time,  $b$  is the efficiency of inversion,  $M_0$  corresponds to the overall compartmental signal, and  $T_1$  is the longitudinal relaxation time.



For a two-compartment system, Eq. [3.1] can be modified to include the signals arising from each compartment:

$$M_z(TI; M_{0a}, M_{0b}, b, T_{1a}, T_{1b}) = M_{0a} \cdot (1 - b \cdot e^{-\frac{TI}{T_{1a}}}) + M_{0b} \cdot (1 - b \cdot e^{-\frac{TI}{T_{1b}}}) \quad [3.2]$$

where  $M_{0a}$  and  $M_{0b}$  correspond to the signals emanating from compartments  $a$  and  $b$ , and  $T_{1a}$  and  $T_{1b}$  are the longitudinal relaxation times for the respective compartments.

With slight modification to Eq. [3.2], the two-compartment exchange equation has been analytically solved (25) where the normalized signal intensity is given by the following equation:

$$M_{norm}(TI) = \frac{M_z(TI; M'_{0a}, M'_{0b}, b, T'_{1a}, T'_{1b})}{M_0} = M'_{0a} \cdot (1 - b \cdot e^{-\frac{TI}{T'_{1a}}}) + M'_{0b} \cdot (1 - b \cdot e^{-\frac{TI}{T'_{1b}}}) \quad [3.3]$$

where

$$M'_{0a} = 1 - M'_{0b} \quad [3.4]$$

$$M'_{0b} = \frac{1}{2} \cdot \left[ 1 - \frac{\left\{ (M_{0b} - M_{0a}) \cdot \left( \frac{1}{T_{1a}} - \frac{1}{T_{1b}} \right) + \frac{1}{\tau_a} + \frac{1}{\tau_b} \right\}}{\sqrt{\left\{ \left( \frac{1}{T_{1b}} - \frac{1}{T_{1a}} \right) + \left( \frac{1}{\tau_b} - \frac{1}{\tau_a} \right) \right\}^2 + \frac{4}{\tau_a \cdot \tau_b}}} \right] \quad [3.5]$$

$$\frac{1}{T'_{1a}} = \frac{1}{2} \cdot \left[ \frac{1}{T_{1b}} + \frac{1}{T_{1a}} + \frac{1}{\tau_b} + \frac{1}{\tau_a} - \sqrt{\left\{ \left( \frac{1}{T_{1b}} - \frac{1}{T_{1a}} \right) + \left( \frac{1}{\tau_b} - \frac{1}{\tau_a} \right) \right\}^2 + \frac{4}{\tau_a \cdot \tau_b}} \right] \quad [3.6]$$

$$\frac{1}{T'_{1b}} = \frac{1}{2} \cdot \left[ \frac{1}{T_{1b}} + \frac{1}{T_{1a}} + \frac{1}{\tau_b} + \frac{1}{\tau_a} + \sqrt{\left\{ \left( \frac{1}{T_{1b}} - \frac{1}{T_{1a}} \right) + \left( \frac{1}{\tau_b} - \frac{1}{\tau_a} \right) \right\}^2 + \frac{4}{\tau_a \cdot \tau_b}} \right] \quad [3.7]$$

where  $T'_{1a}$  and  $M'_{0a}$  correspond to the fast recovering components of the signal, and  $T'_{1b}$  and  $M'_{0b}$  correspond to the slow recovering components of the signal;  $T_{1a}$ ,  $T_{1b}$ ,  $M_{0a}$ , and  $M_{0b}$  correspond to the actual compartmental longitudinal relaxation times and volume fractions;  $\tau_a$  and  $\tau_b$  are the mean lifetimes (residence times) of the spins in their respective compartments.

We can notice from the equations that when the system is in slow exchange (i.e., the spins in the respective compartments reside therein for a long

period of time causing  $\tau_a \rightarrow \infty$  and  $\tau_b \rightarrow \infty$ ), the fast and slow recovering components of relaxation approach the actual fast and slow relaxation times of the respective compartments (i.e.,  $T'_{1a} \rightarrow T_{1a}$  and  $T'_{1b} \rightarrow T_{1b}$ ), thus causing a biexponential recovery of the signal. On the contrary, when the system exhibits fast exchange (i.e.,  $\tau_a \rightarrow 0$  and  $\tau_b \rightarrow 0$ ), the exchange rate constants,  $\frac{1}{\tau_a}$  and  $\frac{1}{\tau_b}$ , dominate the effect causing a monoexponential signal recovery.

In the absence of any CR, a two-compartment system displaying a monoexponential signal recovery indicates that the system is in fast exchange and the signal distribution represents a weighted average of water signal emanating from both the compartments (IC and EC). When sufficient amounts of  $Mn^{2+}$  (an IC CR) is added to the system, relaxation times of the water in the IC space will decrease, and the IC  $T_1$  will dominate the fast recovering terms in Eqs. [3.6] and [3.7] causing the system to shift from a fast-exchange ( $\tau_a$  and  $\tau_b$  dominated) to a slow-exchange ( $T_{1a}$  and  $T_{1b}$  dominant) regime. Thus, a biexponential recovery will be exhibited by the inversion signal containing an effective fast relaxation component ( $T'_{1a}$ ) with an effective compartmental volume fraction ( $M'_{0a}$ ), and an effective slow relaxation component ( $T'_{1b}$ ) with an effective compartmental volume fraction ( $M'_{0b}$ ).

## 3.5. Materials and Methods

### 3.5.1. Animal Preparation

All procedures were performed as approved by the Institute Animal Care and Use Committee (IACUC) of the University of Massachusetts Medical School (Worcester, MA, USA). Adult male Sprague-Dawley rats (weighing from 200-450 g) were anesthetized using 5% isoflurane.  $\text{MnCl}_2$  (Sigma-Aldrich, St. Louis, MO, USA) was administered via subcutaneous (SC) injection at three different doses: 75 mg/kg using 25 mM  $\text{MnCl}_2$  (N=3), 150 mg/kg using 50 mM  $\text{MnCl}_2$  (N=3), and 300 mg/kg using 100 mM  $\text{MnCl}_2$  (N=6). Different concentrations of  $\text{Mn}^{2+}$  were used for the three administered doses to ensure an approximately equal volume of  $\text{MnCl}_2$  solution injection. The SC injections were administered on the dorsal region, bilaterally, slightly posterior to the midline. Following the injection, rats were returned to their cages and allowed normal access to food and water.

During the imaging sessions, animals were anesthetized with 3% isoflurane. After anesthesia was induced, the anesthetic level was reduced to 2%. The head of the anesthetized animal was positioned in a birdcage RF coil with a nose cone providing a continuous supply of the anesthetic. The animals were placed prone into the magnet bore. A respiratory sensor was placed on the chest area to monitor the respiration rate throughout the imaging session. MEMRI was performed in each animal before SC injection of  $\text{Mn}^{2+}$ , and then at 6, 12, 24, 72, and 168 h after  $\text{Mn}^{2+}$  injection.

### 3.5.2. MR Measurements

All MR imaging was performed on a Bruker BioSpin 2.0-T/45-cm horizontal bore system (Bruker BioSpin, Billerica, MA, USA) equipped with 200 mT/m gradients and an in-house-built, 45-mm-diameter, birdcage RF coil that was 30 mm long for RF transmit and receive. Three 2-mm-thick axial MRI slices were acquired anterior to the pituitary gland with the imaging plane referenced to the tip of the pituitary in the sagittal plane.  $T_1$ -weighted imaging was performed using the following acquisition parameters: TR/TE = 700/15 ms; FOV = 38.4 mm × 38.4 mm; data acquisition matrix = 256 × 128 (zero-filled to 256 × 256); and number of averages (NEX) = 2. The  $T_1$  relaxation times were measured using a spin-echo inversion recovery sequence. A sech pulse was used for adiabatic spin-inversion and 16 inversion time values were logarithmically spaced from 15–3300 ms. Other imaging parameters were: TR = 10 s, TE = 4.8 ms, FOV = 38.4 mm × 38.4 mm; data acquisition matrix = 128 × 64 (zero-filled to 128 × 128); and NEX = 1.  $T_2$  relaxation times were measured using a Carr-Purcell-Meiboom-Gill (CPMG) spin-echo sequence (TR = 2 s, TE = 5 ms, echoes = 16).

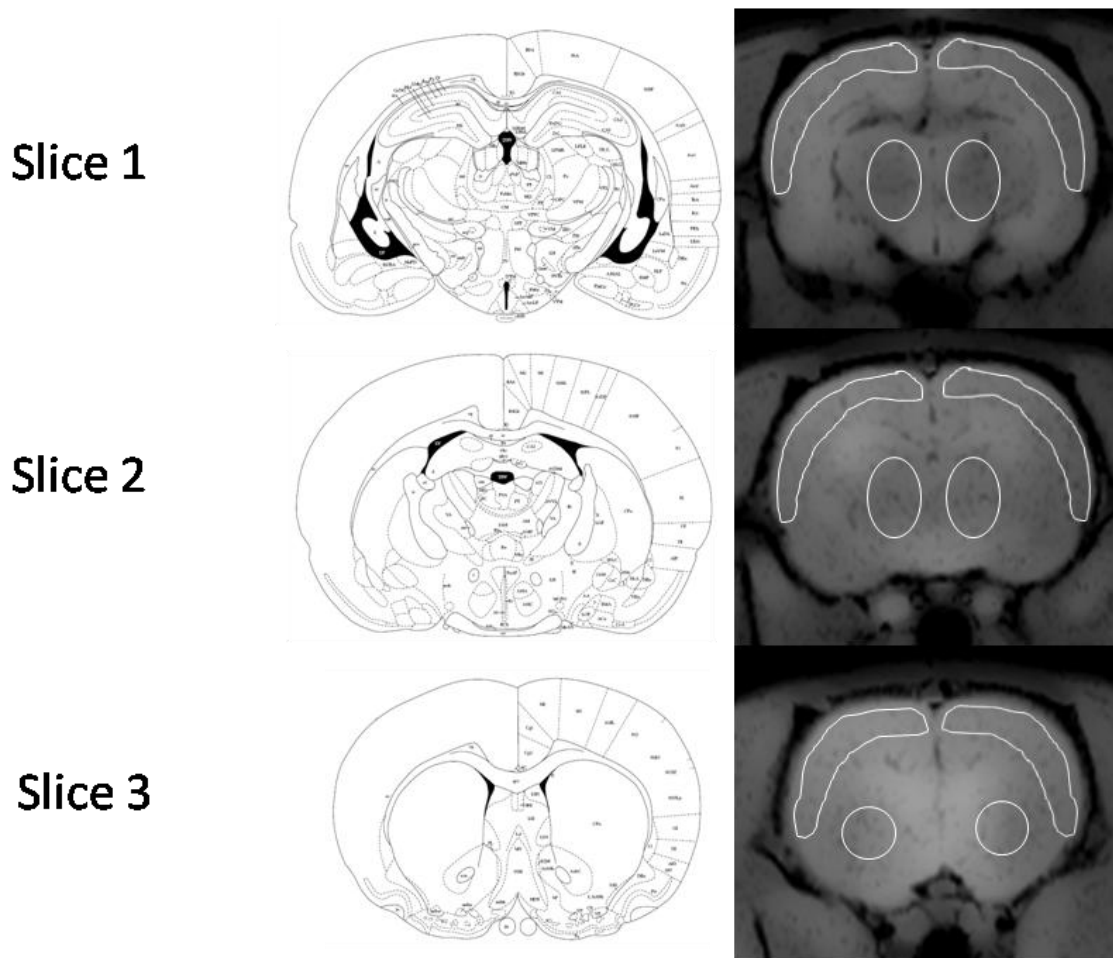


**Figure 3.1** – ROI definitions for different brain regions. Three 2-mm-thick axial MRI slices (slice gap of 0.2 mm) were selected anterior to the pituitary gland with the imaging plane referenced to the tip of the pituitary in the sagittal plane. Representative axial slices from  $T_1$ -weighted image of a rat after 300 mg/kg injection of  $MnCl_2$  at the 24 h time point are shown (right) correlated with corresponding schematic brain slices from the rat brain atlas (1). The schematic brain slices correspond to the initial part of the 2-mm-thick MR image slices. The ROI along the perimeter of the brain corresponds to the right and left cortex ROIs in all the three slices. These ROIs were averaged together to obtain an averaged cortex ROI. The left and right ROIs at the center of the brain in Slice 1 and Slice 2 were averaged together to obtain an averaged sub-cortical ROI. The left and right ROIs in Slice 3 were averaged together to obtain an averaged caudate nucleus ROI.

### 3.5.3. Data Analysis

Using the ImageJ software package (26), three different regions of interest (ROI) were selected: cortex, sub-cortical region, and caudate nucleus, from the collected slices as shown in Fig. 3.1. They were correlated with the corresponding schematic slices from the rat brain atlas (1). The mean signal intensity values within each of the ROIs were calculated using ImageJ and non-linear least squares fitting calculations were performed using MATLAB (The Mathworks Inc., Natick, MA). For each animal, the signal intensity data obtained from inversion recovery MRI was fit using Eqn. [3.1]. Mean  $T_1$  relaxation time values were obtained for each ROI. Student's paired  $t$  test was performed to check for any significant changes in  $T_1$  relaxation time between different doses on  $Mn^{2+}$  administered. Note that ANOVA measurements on monoexponential  $T_1$  measurements were performed and are reported in a separate study in Chapter 5 of this dissertation.

The signal intensity data was also fit using variants of Eqn. [3.3] and semi-log plots (procedures explained in the Simulation Study Section) to extrapolate the short and long effective  $T_1$  relaxation times ( $T'_{1a}$  and  $T'_{1b}$ ) and the corresponding effective volume fractions ( $M'_{0a}$  and  $M'_{0b}$ ). Mean values of  $T'_{1b}$  and  $M'_{0b}$  (from semi-log plots) were obtained for each ROI of each animal. Analysis of variance (ANOVA) for mixed models was used to determine if there

was a significant change in  $T'_{1b}$  and  $M'_{0b}$  values: 1) after the administration of  $Mn^{2+}$ , 2) at the different doses of  $Mn^{2+}$  administered via the SC route, and 3) due to interaction between the time after  $Mn^{2+}$  injection and the  $Mn^{2+}$  dose administered. In the presence of significant effects (main or interaction), the Tukey-Kramer HSD multiple comparisons procedure was used to compare the mean  $T_1$  times of the same anatomical region between different time points and to determine if any difference existed among various  $Mn^{2+}$  doses administered. Statistical analyses were carried out using the SAS statistical software package.

To determine which model (monoexponential or biexponential) better represented the normalized data, the  $\chi^2$  statistics for the monoexponential ( $\chi^2_{monoexp}$ ) and biexponential ( $\chi^2_{biexp}$ ) models were compared using an  $F$  test based on a variant of the reduced  $\chi^2$ -squares ratio:

$$F_{(v_{monoexp}-v_{biexp}, v_{biexp})} = \frac{(\chi^2_{monoexp} - \chi^2_{biexp})(v_{monoexp} - v_{biexp})}{\chi^2_{biexp} / v_{biexp}} \quad [3.8]$$

where  $v_{monoexp}$  and  $v_{biexp}$  are the number of degrees of freedom corresponding to  $\chi^2_{monoexp}$  and  $\chi^2_{biexp}$  for the monoexponential and biexponential model, respectively (27). For this study, the  $F$  statistic ratio simplifies to:

$$F_{(1, N-4)} = \frac{(\chi^2_{monoexp} - \chi^2_{biexp})}{\chi^2_{biexp} / (N-4)} \quad [3.9]$$



where  $N$  is the number of data points. This ratio measures how much the additional exponential term in the biexponential model improves the reduced  $\chi^2$  by taking into account the number of parameters in the fitting equation (28). This calculated  $F$  statistic was compared to tabulated values of the  $F$  statistic with 1 and  $N - 4$  degrees of freedom. If the  $F$  statistic was greater than the tabulated  $F$  value for the desired statistical confidence, then the biexponential model was accepted as the better fitting model for the data. If the  $F$  statistic was less than the tabulated  $F$  value, then the monoexponential model was chosen for fitting the data.

## 3.6. Results

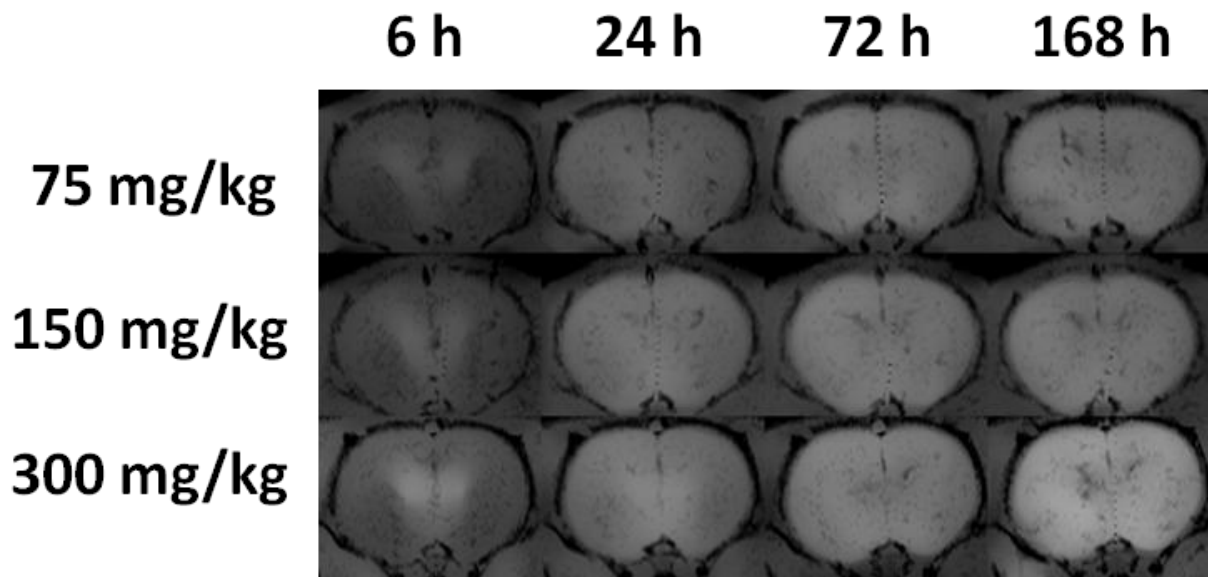
### 3.6.1. Dose Dependence and Time Course of Manganese Distribution

Fig. 3.2 shows a series of  $T_1$ -WT MEMRI data sets of Slice 3 (defined in Fig. 3.1) in the rat brain both as a function of varying doses of  $Mn^{2+}$  and as a function of time after SC administration of  $Mn^{2+}$ . At 6 h following  $Mn^{2+}$  injection,  $T_1$ -WT signal enhancement was apparent around the ventricle regions (which contain the CSF) at all doses. With time, the  $T_1$ -WT signal enhancement uniformly expanded to the cortical and sub-cortical regions. Uniform enhancement was achieved throughout the brain by the 72 h time point at all

administered  $\text{Mn}^{2+}$  doses. The  $T_1$ -WT signal enhancement persisted in all the images up to the 168 h time point for all  $\text{Mn}^{2+}$  doses. The  $T_1$ -WT signal enhancement was proportional to the dose of  $\text{Mn}^{2+}$  administered: image slices at 300 mg/kg showed the most  $T_1$ -WT signal enhancement while the image slices at 75 mg/kg showed the least  $T_1$ -WT signal enhancement at all time points observed (data not shown).

### 3.6.2. Time Course and Dose Dependence of Monoexponential $T_1$ Values

The temporal evolution of monoexponential  $T_1$  relaxation times at three different doses of  $\text{Mn}^{2+}$  in the cortex region of the rat brain is shown in Fig. 3.3A. The  $T_1$  relaxation times reduced steadily from  $1156 \pm 79$  ms and leveled off near the 72 h time point. The largest reduction in the  $T_1$  relaxation time ( $\sim 407$  ms) was observed at the highest  $\text{Mn}^{2+}$  dose administered (300 mg/kg) and the smallest reduction in the  $T_1$  relaxation time ( $\sim 258$  ms) was observed at the lowest  $\text{Mn}^{2+}$  dose administered (75 mg/kg). Student's paired  $t$  test showed a significant differences in monoexponential  $T_1$  relaxation times between different doses of  $\text{Mn}^{2+}$  administered as indicated in Fig. 3.3A.

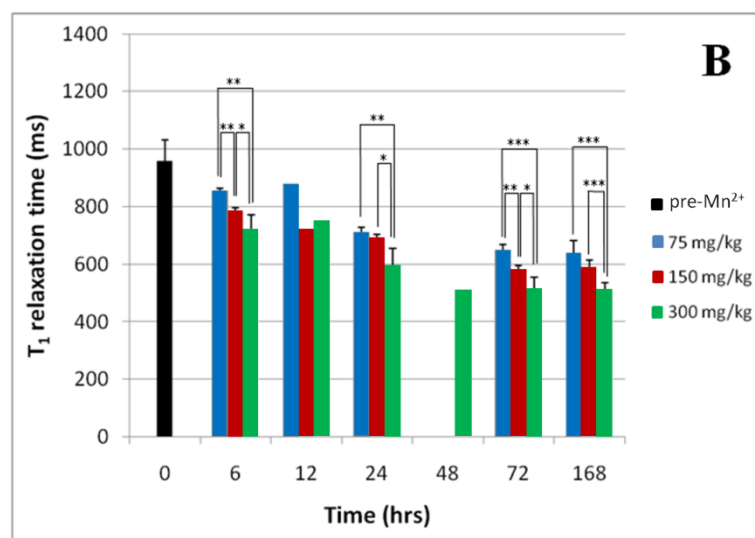
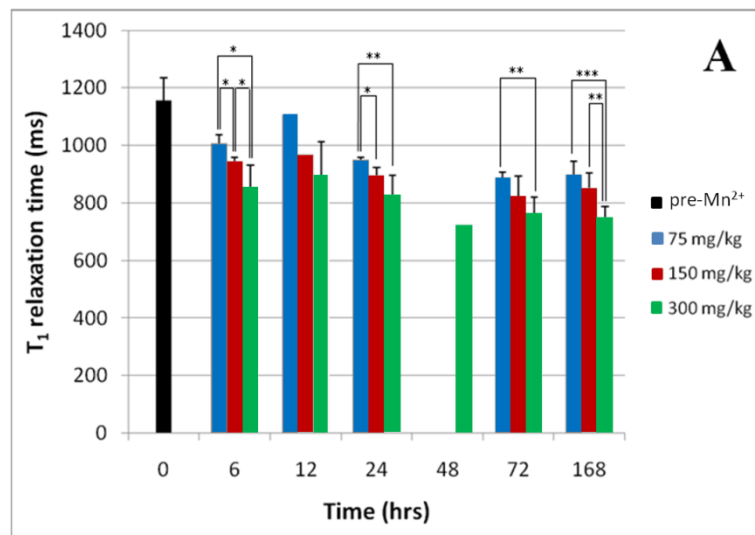


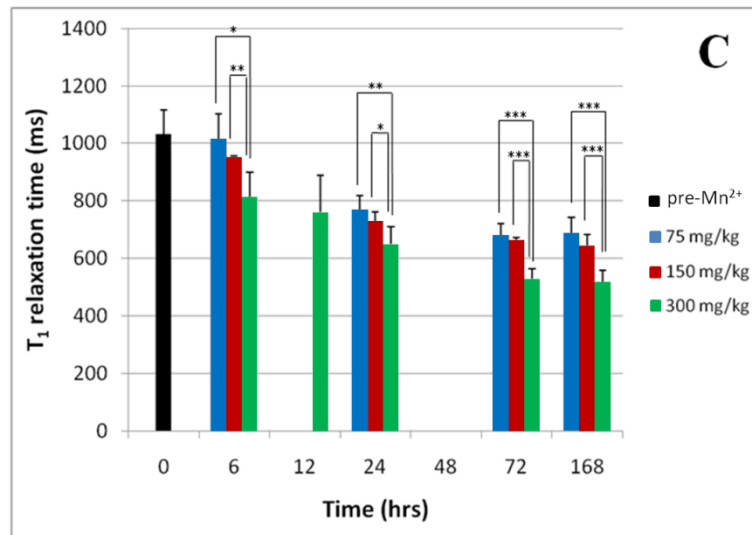
**Figure 3.2** – Dose dependence and time-course of MEMRI contrast.  $T_1$ -weighted ( $T_1$ -WT) axial MR image sets (TR/TE = 700/15 ms) of Slice #3 from Fig. 3.1 are shown as a function of varying doses of  $MnCl_2$  and as a function of time after subcutaneous injection of  $MnCl_2$ .  $T_1$ -WT signal enhancement was apparent in all the 2-mm-thick slices around the ventricle regions which contain the cerebrospinal fluid. Over time, the region of  $T_1$ -WT signal enhancement expanded to the cortical and sub-cortical regions. The images at 75 mg/kg and 150 mg/kg achieved uniform enhancement throughout the brain by the 24 h time point, whereas the image at 300 mg/kg achieved uniform enhancement by the 72 h time point (see Fig. 3.1). The  $T_1$ -WT signal enhancement was proportional to the dose of  $MnCl_2$  administered: image slices at 300 mg/kg showed the most  $T_1$ -WT signal enhancement while the image slices at 75 mg/kg showed the least  $T_1$ -WT signal enhancement at all time points observed (data not shown). All images have the same relative intensity scaling; therefore, changes in  $T_1$ -WT signal contrast are directly proportional to changes in tissue  $Mn^{2+}$  concentration over time. These images were filtered to remove high-intensity pixel artifacts caused by motion.

Fig. 3.3B shows the temporal evolution of monoexponential  $T_1$  relaxation times at three different doses of  $Mn^{2+}$  in the sub-cortical region of the rat brain. The  $T_1$  relaxation times reduced steadily from  $959 \pm 74$  ms and leveled off near the 72 h time point similar to the cortex region in Fig. 3.3A. However, the reduction in  $T_1$  relaxation times was greater in the sub-cortical region than that observed in the cortex region at the same administered dose. The largest reduction in the  $T_1$  relaxation time ( $\sim 448$  ms) was observed at the highest  $Mn^{2+}$  dose administered (300 mg/kg) and the smallest reduction in the  $T_1$  relaxation time ( $\sim 320$  ms) was observed at the lowest  $Mn^{2+}$  dose administered (75 mg/kg). Student's paired  $t$  test showed significant differences in monoexponential  $T_1$  relaxation times between different doses of  $Mn^{2+}$  administered as indicated in Fig. 3.3B. These differences were more significant than that observed in the cortex region.

The temporal evolution of monoexponential  $T_1$  relaxation times at three different doses of  $Mn^{2+}$  in the caudate nucleus region of the rat brain is shown in Fig. 3.3C. The  $T_1$  relaxation times reduced steadily from  $1033 \pm 84$  ms and leveled off near the 72 h time point similar to the cortex and sub-cortical regions; however, the reduction in  $T_1$  relaxation times was greater in the caudate nucleus region than that observed in the cortex region and similar to that observed in the sub-cortical region at the same administered dose. The largest reduction in the  $T_1$  relaxation time ( $\sim 515$  ms) was observed at the highest  $Mn^{2+}$  dose administered (300 mg/kg) and the smallest reduction in the  $T_1$  relaxation time

(~343 ms) was observed at the lowest  $Mn^{2+}$  dose administered (75 mg/kg). Student's paired  $t$  test showed significant differences in monoexponential  $T_1$  relaxation times between different doses of  $Mn^{2+}$  administered as indicated in Fig. 3.3C. These differences were more significant than that observed in the cortex region.





**Figure 3.3** – Bar-plots of *in vivo* monoexponential  $T_1$  relaxation times as a function of time after subcutaneous injection of  $MnCl_2$  at three different doses in **A**) cortex ROI, **B**) sub-cortical region ROI, and **C**) caudate nucleus ROI. A total of 13 animals were used in this study with the following  $Mn^{2+}$  doses: 75 mg/kg (N=3), 150 mg/kg (N=3), and 300 mg/kg (N=7). Three of the thirteen animals were imaged before administration of  $MnCl_2$ . All the animals were imaged at the following time points after  $MnCl_2$  injection: 6, 24, 72, and 168 h. Some animals were also imaged at 12 h and 48 h. For each ROI, the mean (+1 SD) ROI monoexponential  $T_1$  relaxation times were plotted against the time point after  $Mn^{2+}$  injection for all animals at the same administered dose. Statistical comparisons between the different time points at each ROI were performed using Student's paired  $t$  test. \* $0.01 < P < 0.05$  (Student's  $t$  test using multiple comparisons), \*\* $0.001 < P < 0.01$ , and \*\*\* $P < 0.001$ .

### 3.6.3. Time Course & Dose Dependence of the Effective Long $T_1$

#### Relaxation Time ( $T'_{1b}$ )

The temporal evolution of the effective long  $T_1$  relaxation time ( $T'_{1b}$ ) at three different doses of  $Mn^{2+}$  in the cortex region of the rat brain is shown in Fig.

3.4A. The  $T_1$  relaxation times reduced steadily from  $1160 \pm 88$  ms and leveled off near the 72 h time point. The largest reduction in the  $T_1$  relaxation time ( $\sim 415$  ms) was observed at the highest  $\text{Mn}^{2+}$  dose administered (300 mg/kg) and the smallest reduction in the  $T_1$  relaxation time ( $\sim 275$  ms) was observed at the lowest  $\text{Mn}^{2+}$  dose administered (75 mg/kg). Fig. 3.5A shows the same information as Fig. 3.4A with the effective long  $T_1$  relaxation times plotted as a function of  $\text{Mn}^{2+}$  dose at different time points after  $\text{Mn}^{2+}$  injection. In Fig. 3.5A, the effective long  $T_1$  relaxation times reduced with increasing  $\text{Mn}^{2+}$  dose. The largest reduction in the  $T_1$  relaxation times occurred at the 72 h and 168 h time points. ANOVA test for mixed models showed a significant effect of  $\text{Mn}^{2+}$  dose ( $P < 0.01$ ) and time point after  $\text{Mn}^{2+}$  injection ( $P < 0.0001$ ) on the reduction of the effective long  $T_1$  relaxation times. There was no significant effect of the interaction between the  $\text{Mn}^{2+}$  dose and time after  $\text{Mn}^{2+}$  injection. Table 3.1 and Table 3.2 show the statistical significance of differences of least square means of the effective long  $T_1$  relaxation times between the different time points after  $\text{Mn}^{2+}$  injection and between the different  $\text{Mn}^{2+}$  doses administered, respectively, in the cortex region.

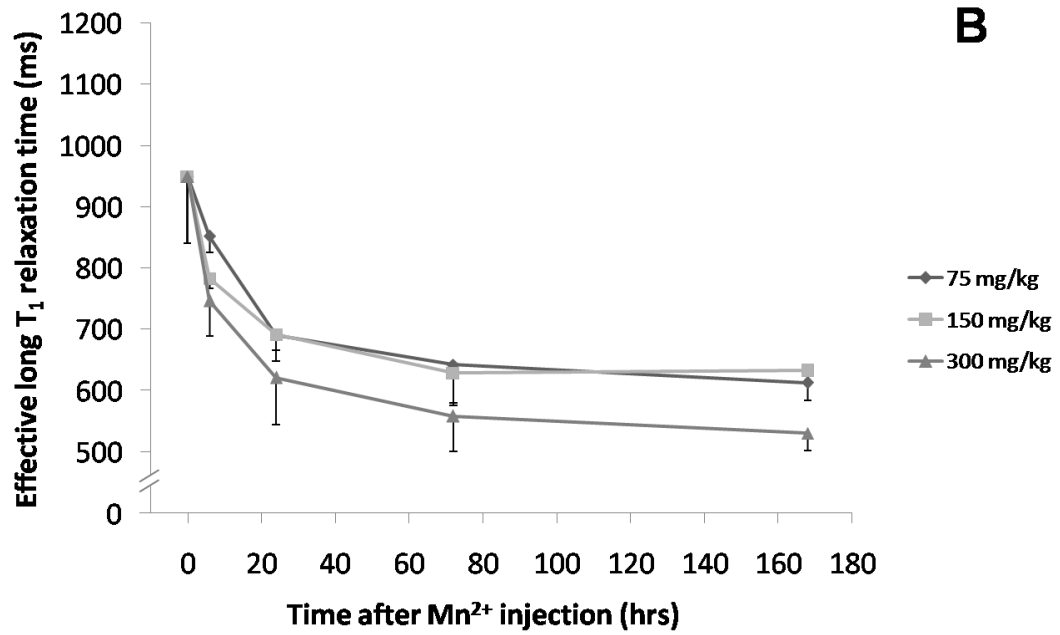
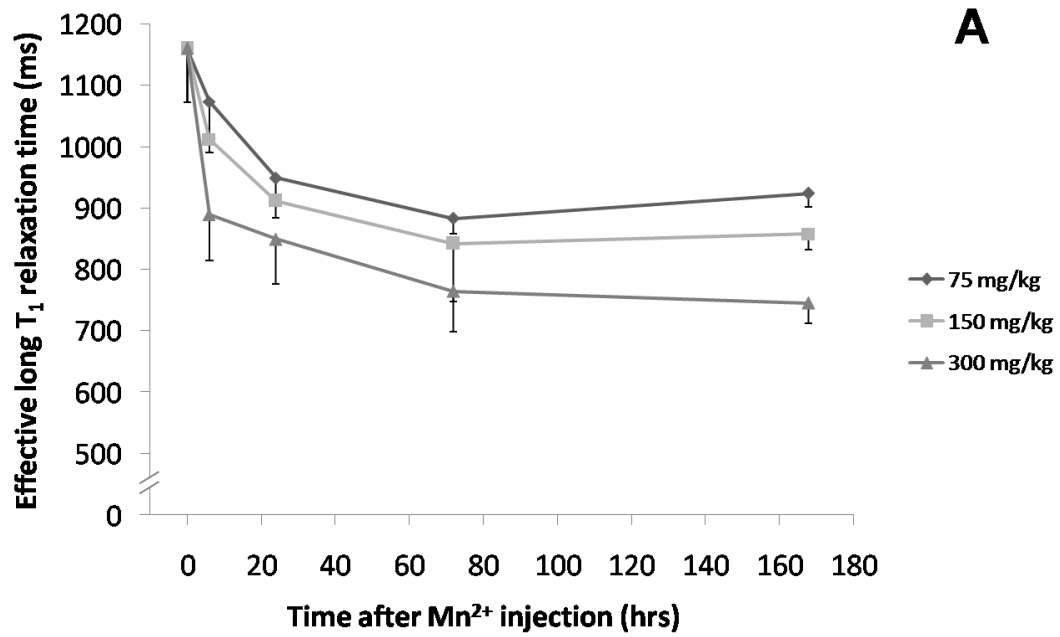
Fig. 3.4B shows the temporal evolution of the effective long  $T_1$  relaxation times at three different doses of  $\text{Mn}^{2+}$  in the sub-cortical region of the rat brain. The effective long  $T_1$  relaxation times reduced steadily from  $950 \pm 108$  ms and leveled off near the 72 h time point similar to the cortex region in Fig. 3.4A; however, the reduction in effective long  $T_1$  relaxation times was greater in the sub-cortical region than that observed in the cortex region at the same

administered dose. The largest reduction in the effective long  $T_1$  relaxation time (~420 ms) was observed at the highest  $Mn^{2+}$  dose administered (300 mg/kg) and the smallest reduction in the effective long  $T_1$  relaxation time (~340 ms) was observed at the lowest  $Mn^{2+}$  dose administered (75 mg/kg). Fig. 3.5B shows the same information as Fig. 3.4B with the effective long  $T_1$  relaxation times plotted as a function of  $Mn^{2+}$  dose at different time points after  $Mn^{2+}$  injection. In Fig. 3.5B, the effective long  $T_1$  relaxation times reduced with increasing  $Mn^{2+}$  dose similar to the cortex region in Fig. 3.5A; however, the reduction in effective long  $T_1$  relaxation times of the sub-cortical region was greater than that of the cortex region. The largest reduction in the effective long  $T_1$  relaxation times occurred at the 72 h and 168 h time points. ANOVA test for mixed models showed a significant effect of  $Mn^{2+}$  dose ( $P < 0.01$ ) and time point after  $Mn^{2+}$  injection ( $P < 0.0001$ ) on the reduction of the effective long  $T_1$  relaxation times. The interaction between the  $Mn^{2+}$  dose and time after  $Mn^{2+}$  injection was not significant. Table 3.1 and Table 3.2 show the statistical significance of differences of least square means of effective long  $T_1$  relaxation times between the different time points after  $Mn^{2+}$  injection and between the different  $Mn^{2+}$  doses administered, respectively, in the sub-cortical region.

The temporal evolution of the effective long  $T_1$  relaxation times at three different doses of  $Mn^{2+}$  in the caudate nucleus region of the rat brain is shown in Fig. 3.4C. The effective long  $T_1$  relaxation times reduced steadily from  $1083 \pm 144$  ms and leveled off near the 72 h time point similar to the cortex and sub-



cortical regions; however, the reduction in effective long  $T_1$  relaxation times was greater in the caudate nucleus region than that observed in the cortex region and similar to that observed in the sub-cortical region at the same administered dose. The largest reduction in the effective long  $T_1$  relaxation time (~580 ms) was observed at the highest  $Mn^{2+}$  dose administered (300 mg/kg) and the smallest reduction in the effective long  $T_1$  relaxation time (~415 ms) was observed at the lowest  $Mn^{2+}$  dose administered (75 mg/kg). Fig. 3.5C shows the same information as Fig. 3.4C with the effective long  $T_1$  relaxation times plotted as a function of  $Mn^{2+}$  dose at different time points after  $Mn^{2+}$  injection. In Fig. 3.5C, the effective long  $T_1$  relaxation times reduced with increasing  $Mn^{2+}$  dose similar to the cortex and sub-cortical regions; however, the reduction in effective long  $T_1$  relaxation times of the caudate nucleus region was greater than that of the cortex region and similar to that of the sub-cortical region. The largest reduction in the effective long  $T_1$  relaxation times occurred at the 72 h and 168 h time points. ANOVA test for mixed models showed a significant effect of  $Mn^{2+}$  dose ( $P < 0.001$ ) and time point after  $Mn^{2+}$  injection ( $P < 0.0001$ ) on the reduction of effective long  $T_1$  relaxation times. There was no significant effect of the interaction between the  $Mn^{2+}$  dose and time point after  $Mn^{2+}$  injection. Table 3.1 and Table 3.2 show the statistical significance of differences of least square means of effective long  $T_1$  relaxation times between the different time points after  $Mn^{2+}$  injection and between the different  $Mn^{2+}$  doses administered, respectively, in the caudate nucleus region.



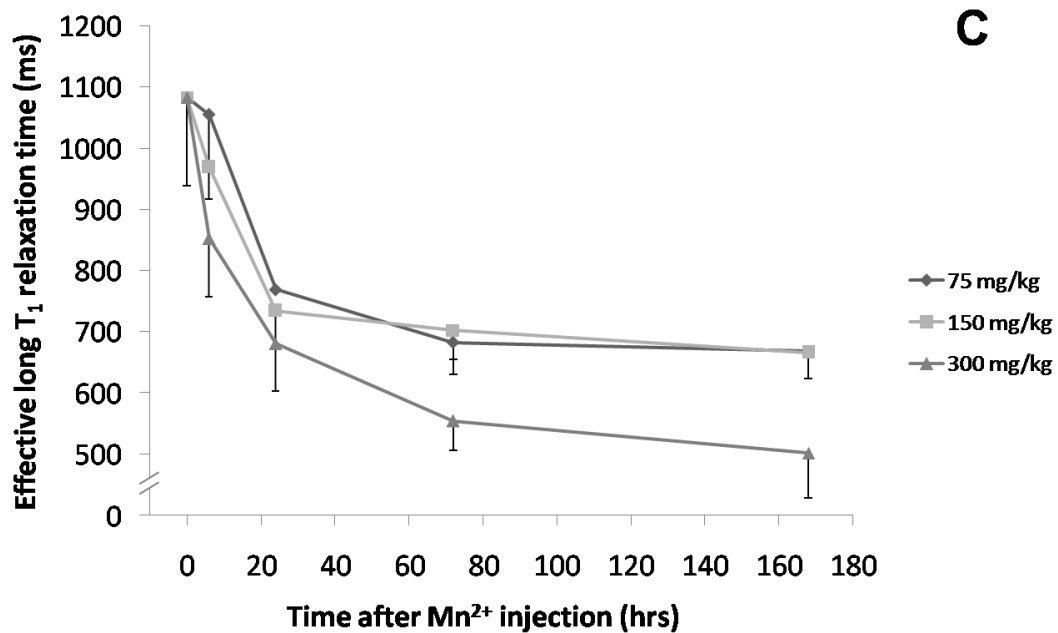
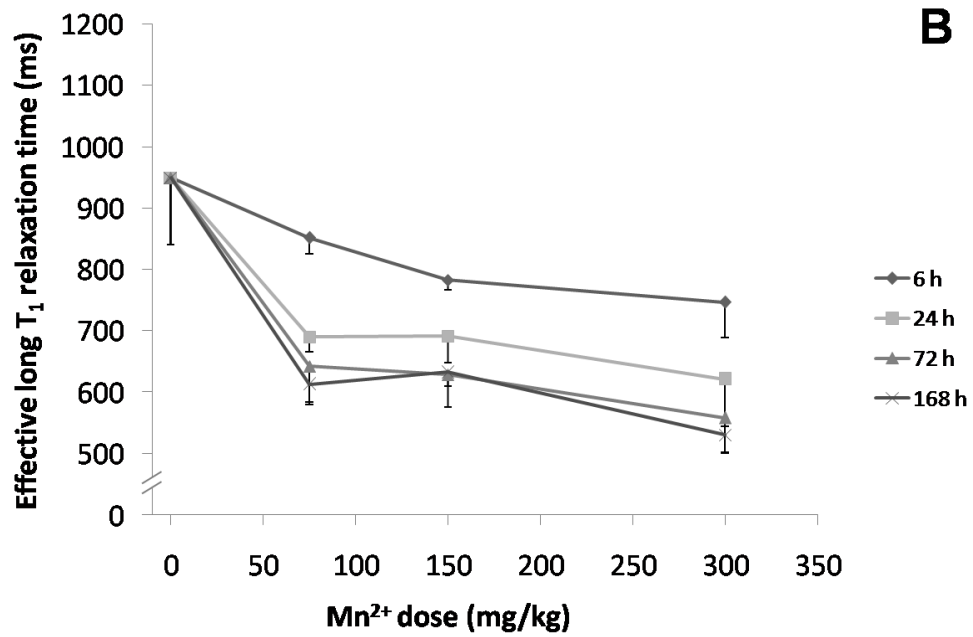
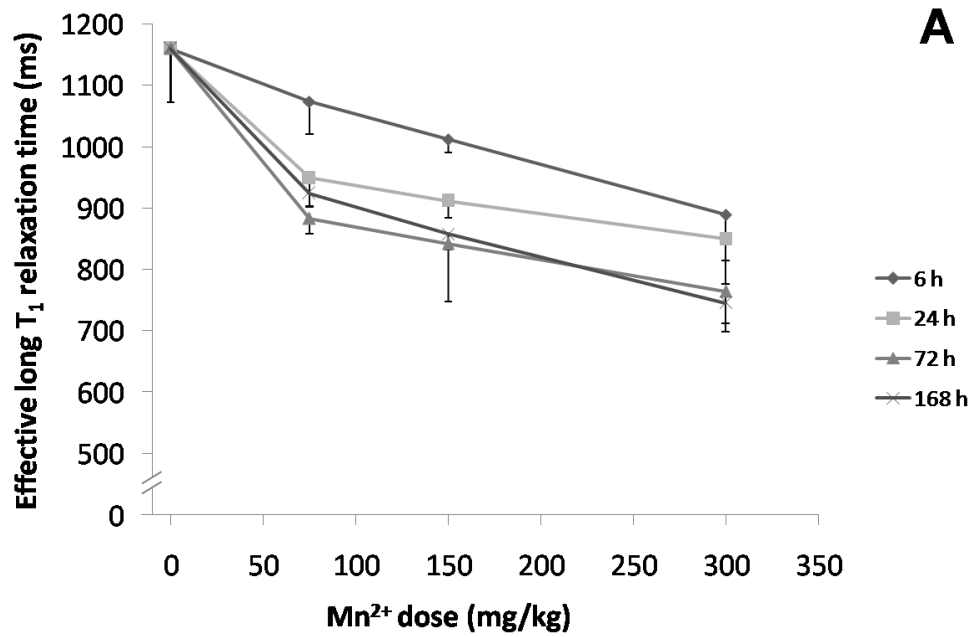


**Figure 3.4** – Plots of *in vivo* effective long  $T_1$  relaxation times ( $T'_{1b}$ ) as a function of time after subcutaneous injection of  $MnCl_2$  at three different doses (75 mg/kg, 150 mg/kg, and 300 mg/kg) in **A**) cortex ROI, **B**) sub-cortical region ROI, and **C**) caudate nucleus ROI. All the animals were imaged at the following time points after  $MnCl_2$  injection: 6, 24, 72, and 168 h. For each ROI, the mean ( $-1$  SD) ROI effective long  $T_1$  relaxation times were plotted against the time point after  $Mn^{2+}$  injection for all animals at the same administered dose. Statistical comparisons between the different time points at each ROI were performed using analysis of variance (ANOVA) shown in Table 3.1.

**Table 3.1**

Statistical Significance of Differences of Least Squares Means of Effective Long  $T_1$  Relaxation Times in the Rat Brain Between the Different  $Mn^{2+}$  Doses Administered. *NS* = not significant ( $P > 0.05$ ),  $*0.01 < P < 0.05$  (ANOVA with Tukey-Kramer HSD multiple comparisons procedure),  $**0.001 < P < 0.01$ , and  $***P < 0.001$ .

	$Mn^{2+}$ dose (mg/kg)		
<b>Cortex</b>		<b>150</b>	<b>300</b>
	<b>75</b>	<i>NS</i>	<b>**</b>
	<b>150</b>	-	<b>*</b>
<b>Sub-cortical Region</b>		<b>150</b>	<b>300</b>
	<b>75</b>	<i>NS</i>	<b>*</b>
	<b>150</b>	-	<b>*</b>
<b>Caudate Nucleus</b>		<b>150</b>	<b>300</b>
	<b>75</b>	<i>NS</i>	<b>***</b>
	<b>150</b>	-	<b>**</b>



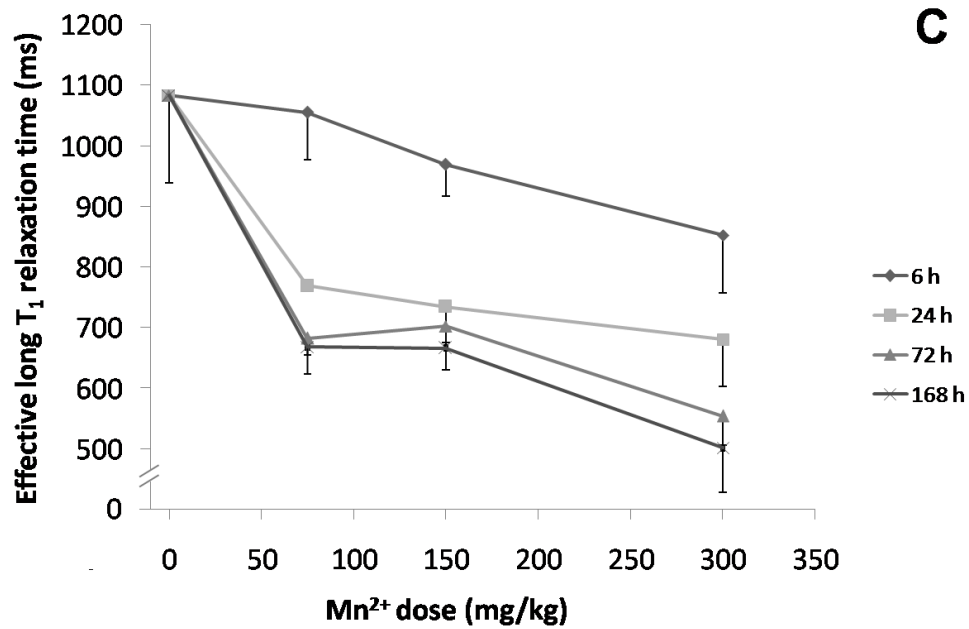


**Figure 3.5** – Plots of the *in vivo* effective long  $T_1$  relaxation times as a function of  $Mn^{2+}$  dose administered at four different time points in **A**) cortex ROI, **B**) sub-cortical ROI, and **C**) caudate nucleus ROI. These plots contain the same information as the respective plots in Fig. 3.4 representing the data as a function of dose instead of time. For each ROI, the mean ( $-1$  SD) ROI effective long  $T_1$  relaxation times were plotted against  $Mn^{2+}$  dose for all animals at the same time point after  $Mn^{2+}$  injection. Statistical comparisons between the different  $Mn^{2+}$  doses at each ROI were performed using analysis of variance (ANOVA) shown in Table 3.2.

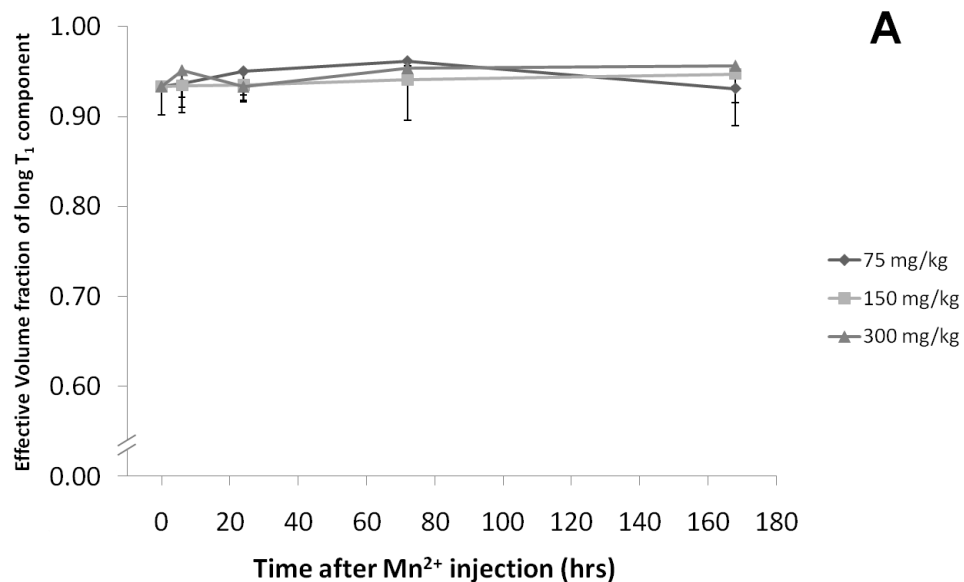
**Table 3.2**

Statistical Significance of Differences of Least Squares Means of Effective Long  $T_1$  Relaxation Times in the Rat Brain Between the Different Time Points after  $Mn^{2+}$  Administration. *NS* = not significant ( $P > 0.05$ ),  $*0.01 < P < 0.05$  (ANOVA with Tukey-Kramer HSD multiple comparisons procedure),  $**0.001 < P < 0.01$ , and  $***P < 0.001$ .

	Time after $Mn^{2+}$ injection (hrs)			
		24	72	168
<b>Cortex</b>				
	<b>6</b>	<b>***</b>	<b>***</b>	<b>***</b>
	<b>24</b>	-	<b>**</b>	<b>*</b>
	<b>72</b>	-	-	<i>NS</i>
<b>Sub-cortical Region</b>		<b>24</b>	<b>72</b>	<b>168</b>
	<b>6</b>	<b>***</b>	<b>***</b>	<b>***</b>
	<b>24</b>	-	<b>*</b>	<b>**</b>
	<b>72</b>	-	-	<i>NS</i>
<b>Caudate Nucleus</b>		<b>24</b>	<b>72</b>	<b>168</b>
	<b>6</b>	<b>***</b>	<b>***</b>	<b>***</b>
	<b>24</b>	-	<b>*</b>	<b>**</b>
	<b>72</b>	-	-	<i>NS</i>

### 3.6.4. Time Course of the Effective Volume Fraction of the Long $T_1$ Component ( $M'_{ob}$ )

The temporal evolution of the effective volume fraction of the long  $T_1$  component ( $M'_{ob}$ ) at three different doses of  $Mn^{2+}$  in the cortex, sub-cortical, and caudate nucleus regions of the rat brain are shown in Figs. 3.6A, 3.6B, and 3.6C, respectively. The effective volume fraction values varied between approximately 0.9 and 1 for all  $Mn^{2+}$  doses administered at all the time points. Thus, the effective long  $T_1$  component was associated with the effective large volume fraction. There were no significant effects of  $Mn^{2+}$  dose and time point after  $Mn^{2+}$  injection on the effective volume fraction of the long  $T_1$  component in all three ROIs.





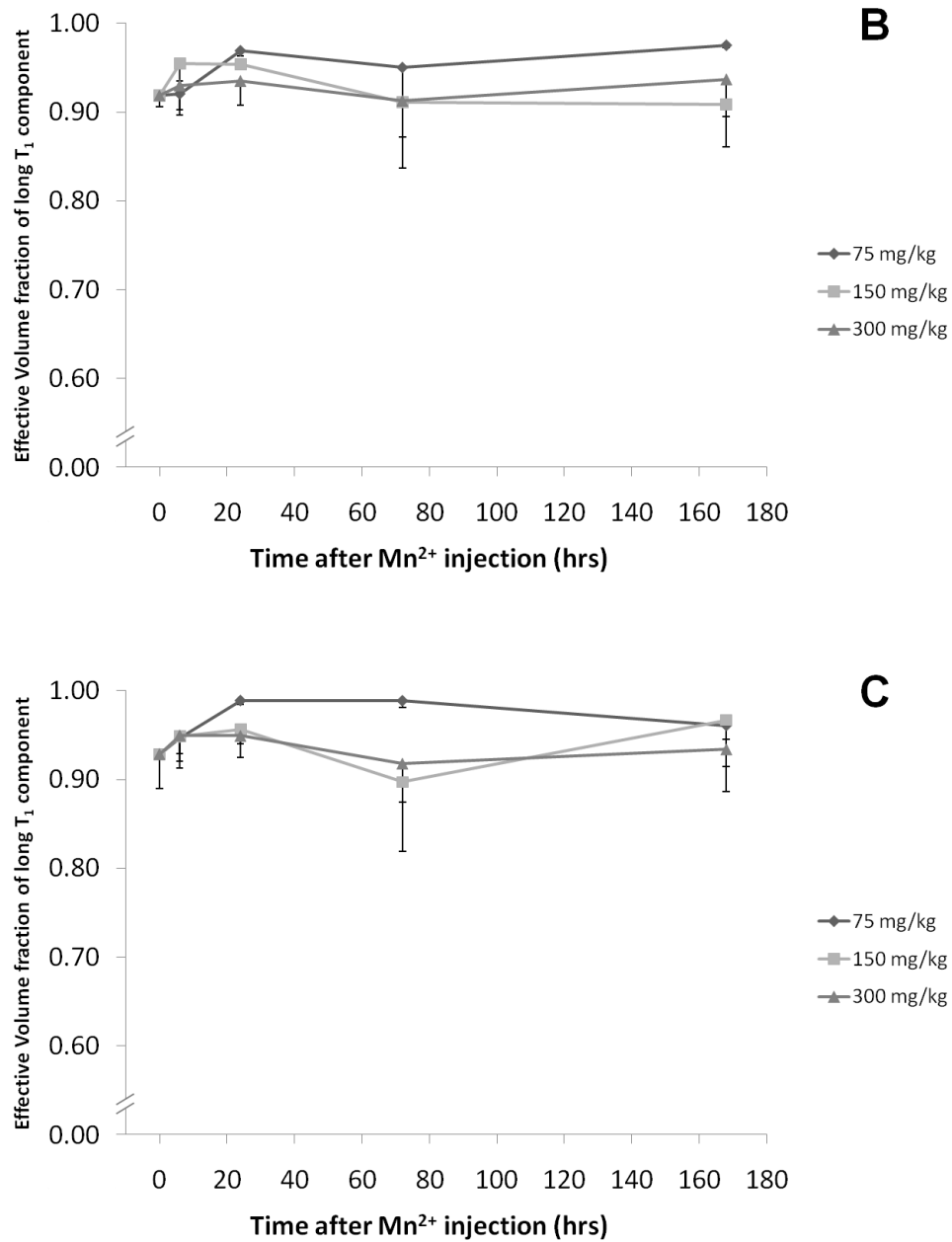


**Figure 3.6** – Plots of *in vivo* effective volume fraction of long  $T_1$  component as a function of time after subcutaneous injection of  $MnCl_2$  at three different doses in **A**) cortex ROI, **B**) sub-cortical region ROI, and **C**) caudate nucleus ROI. For each ROI, the mean ( $-1$  SD) ROI effective volume fraction of long  $T_1$  component were plotted against the time point after  $Mn^{2+}$  injection for all animals at the same administered dose. There were no statistically significant differences between either different time points or different  $Mn^{2+}$  doses at each ROI using analysis of variance (ANOVA).

### 3.6.5. The Effective Short $T_1$ Relaxation Time ( $T'_{1a}$ )

Table 3.3 lists the effective short  $T_1$  relaxation times ( $T'_{1a}$ ) in the cortex, sub-cortical, and caudate nucleus regions of the rat brain at the respective  $Mn^{2+}$  dose and time after  $Mn^{2+}$  injection. Values are displayed only for the MRI data that showed a better fit for the biexponential model [Eq. 3.2] than the monoexponential model [Eq. 3.1] using an  $F$  test on  $\chi^2$  statistics. The empty cells in the table showed a better fit with the monoexponential model. We can notice from the displayed data that the overwhelming biexponential behavior was observed at the highest  $Mn^{2+}$  dose administered (300 mg/kg). Due to the sparse number of animals displaying biexponential behavior, no statistical conclusions could be made in regards to the dependence of time after  $Mn^{2+}$  injection on the effective short  $T_1$  relaxation times.

**Table 3.3**

Effective Short  $T_1$  Relaxation Times in the Rat Brain at Different  $Mn^{2+}$  Doses and Time After  $Mn^{2+}$  Injection. The Mean Effective Short  $T_1$  Relaxation Times are shown in milliseconds ( $\pm 1$  SD) and the number in parentheses indicates number of animals. The values displayed in the table were obtained from animals that showed statistical significance of biexponential over monoexponential model of inversion MRI data using F-statistics. The monoexponential model was a better model for the animals in the empty cell groups.

			Time after $Mn^{2+}$ injection (hrs)				
			6	12	24	72	168
Cortex	$Mn^{2+}$ dose (mg/kg)	75	-	-	-	-	-
		150	-	-	-	-	-
		300	27 $\pm$ 0.1 (2)	28 $\pm$ 19 (2)	33 $\pm$ 11 (3)	35 $\pm$ 5 (2)	33 $\pm$ 18 (2)
Sub-cortical Region	$Mn^{2+}$ dose (mg/kg)	75	-	-	-	-	-
		150	-	-	-	45 (1)	-
		300	21 (1)	31 (1)	29 $\pm$ 20 (4)	47 $\pm$ 25 (2)	37 $\pm$ 18 (2)
Caudate Nucleus	$Mn^{2+}$ dose (mg/kg)	75	-	-	-	-	-
		150	-	-	-	-	-
		300	24 (1)	-	41 $\pm$ 16 (3)	-	23 (1)

### 3.7. Discussion

In order to shift the water exchange system from a fast exchange regime ( $\frac{1}{\tau_b} + \frac{1}{\tau_a} \gg \left| \frac{1}{T_{1b}} - \frac{1}{T_{1a}} \right|$ ) to a slow exchange regime ( $\frac{1}{\tau_b} + \frac{1}{\tau_a} \ll \left| \frac{1}{T_{1b}} - \frac{1}{T_{1a}} \right|$ ), a high dose of  $\text{Mn}^{2+}$  is required to affect the relaxation time of the IC compartment. We chose the SC route to administer  $\text{Mn}^{2+}$  based on a study which concluded that SC injection of  $\text{Mn}^{2+}$  affects  $T_1$  relaxation time the most compared to administration of  $\text{Mn}^{2+}$  via intravenous or intraperitoneal injection (29). We used three different doses on SC  $\text{Mn}^{2+}$  injection in an attempt to identify the dose at which the slow exchange regime of water becomes apparent, thereby allowing distinct measurements of compartmental  $T_1$  relaxation times and volume fractions. An attempt was made to resolve a longitudinal relaxogram for  $\text{Mn}^{2+}$ , similar to the one established with EC  $\text{GdDTPA}^{2-}$  for yeast cell suspensions by Labadie *et al.* (30).

With a SC injection,  $\text{Mn}^{2+}$  primarily enters the cerebrospinal fluid via the choroid plexus and diffuses in the proximity of the ventricles into the sub-cortical region (sub-cortical region and caudate nucleus ROIs). With time,  $\text{Mn}^{2+}$  diffuses throughout the brain and eventually reaches the cortex. This is clearly evident in the enhanced regions (bright areas) across the brain slices in Fig. 3.2. A dose-dependent behavior was also observed in MEMRI contrast (Fig. 3.2) which correlated with the monoexponential  $T_1$  relaxation times (Fig. 3.3). The general trend from the bar plots indicates that the monoexponential  $T_1$  relaxation time

significantly decreased when a higher dose of  $\text{Mn}^{2+}$  was administered. An extended dose study was done as described in Chapter 5 of this dissertation.

Separation of IC and EC  $T_1$  relaxation times was observed only in a limited number of ROIs at a SC  $\text{Mn}^{2+}$  dose of 300 mg/kg (Table 3.3). The majority of ROI slices in this study depicted a monoexponential recovery of IR data. The dose-dependent reduction of effective long  $T_1$  relaxation times in all ROIs (Fig. 3.5) was very similar to that of monoexponential  $T_1$  relaxation times (compare Figs. 3.3 and 3.4) suggesting that the second  $T_1$  relaxation component is either too small to be detected or is completely absent. This might occur due to a decrease in the IC  $T_2$  value because of the presence of  $\text{Mn}^{2+}$ . Lowering the echo time in data acquisition could perhaps resolve this issue; however, we used the lowest possible echo time in all our experiments and thus were bound by hardware limits. In spite of this, several ROI slices showed a significant presence of an effective short  $T_1$  relaxation time (Table 3.3) with values in the range of ~30-40 ms. From our simulation study we know that this value is approximately a 30% underestimate of the actual parameter. Thus, the actual effective short  $T_1$  relaxation time falls in the range of ~43-57ms.

The ROI slices that showed biexponential  $T_1$  relaxation times had the effective long  $T_1$  relaxation times (~700 ms) associated with the effective large volume fractions (~0.95) (Fig. 3.6) and the effective short  $T_1$  relaxation times (~50 ms) associated with the effective small volume fractions (~0.05). These

associations are contrary to the hypothesis that  $\text{Mn}^{2+}$  enters the IC compartment.

There are several reasons why this reverse association might occur:

- 1.)  $\text{Mn}^{2+}$  could be getting sequestered in the IC organelles, thereby not affecting the IC water  $T_1$  relaxation times significantly. The  $\text{Mn}^{2+}$  that remains in the EC space affects the  $T_1$  relaxation time of the EC water since there is no  $\text{Mn}^{2+}$  sequestration in the EC compartment. This could explain the association of the long  $T_1$  relaxation time with the large volume fraction and the short  $T_1$  relaxation time with the small volume fraction.
- 2.) Attenuation of the IC  $T_2$  signal from  $\text{Mn}^{2+}$  entry could be killing off the NMR signal making it difficult to decipher the short  $T_1$  relaxation time. As a result, the effective long  $T_1$  relaxation time is essentially portraying the EC compartment  $T_1$  relaxation time.
- 3.) The concentration of  $\text{Mn}^{2+}$  used was not enough to shift the water exchange system from the fast exchange regime to the slow exchange regime. Since most of the ROI data exhibited the monoexponential model as a better fit than the biexponential model, the water exchange system might still be in the fast exchange regime where the water residence times ( $\tau_a$  and  $\tau_b$ ) dominate the effective  $T_1$  relaxation times instead of the compartmental  $T_1$  relaxation times.

### 3.8. Conclusion

$Mn^{2+}$ , when injected at a high dose using the SC route, appears to give a local concentration of  $Mn^{2+}$  in the brain that might be sufficient to achieve the slow exchange regime for water exchange in the rat brain. Biexponential  $T_1$  behavior was observed in some ROIs only at the highest dose of  $Mn^{2+}$  (300 mg/kg) administered possibly indicating a distinction between the IC and EC spaces; however, the corresponding signal fractions did not agree with the known water volume fractions of cerebral tissue. In spite of that, this approach, when combined with diffusion measurements, might allow separate measurements of the corresponding component ADCs under both normal and pathological conditions.

## References

1. Paxinos G, Watson, C. *The Rat Brain in Stereotaxic Coordinates*: Academic Press, San Diego; 1998.
2. Andrasko J. Water diffusion permeability of human erythrocytes studied by a pulsed gradient NMR technique. *Biochim Biophys Acta* 1976;428(2):304-311.
3. Wesbey GE, Moseley ME, Ehman RL. Translational molecular self-diffusion in magnetic resonance imaging. II. Measurement of the self-diffusion coefficient. *Invest Radiol* 1984;19(6):491-498.
4. Le Bihan D, Breton E, Lallemand D, Grenier P, Cabanis E, Laval-Jeantet M. MR imaging of intravoxel incoherent motions: application to diffusion and perfusion in neurologic disorders. *Radiology* 1986;161(2):401-407.
5. Moseley ME, Cohen Y, Mintorovitch J, Chileuitt L, Shimizu H, Kucharczyk J, Wendland MF, Weinstein PR. Early detection of regional cerebral ischemia in cats: comparison of diffusion- and T2-weighted MRI and spectroscopy. *Magn Reson Med* 1990;14(2):330-346.
6. van Gelderen P, de Vleeschouwer MH, DesPres D, Pekar J, van Zijl PC, Moonen CT. Water diffusion and acute stroke. *Magn Reson Med* 1994;31(2):154-163.
7. Zhong J, Petroff OA, Prichard JW, Gore JC. Changes in water diffusion and relaxation properties of rat cerebrum during status epilepticus. *Magn Reson Med* 1993;30(2):241-246.
8. Benveniste H, Hedlund LW, Johnson GA. Mechanism of detection of acute cerebral ischemia in rats by diffusion-weighted magnetic resonance microscopy. *Stroke* 1992;23(5):746-754.
9. Anderson AW, Zhong J, Petroff OA, Szafer A, Ransom BR, Prichard JW, Gore JC. Effects of osmotically driven cell volume changes on diffusion-



- weighted imaging of the rat optic nerve. *Magn Reson Med* 1996;35(2):162-167.
10. van der Toorn A, Sykova E, Dijkhuizen RM, Vorisek I, Vargova L, Skobisova E, van Lookeren Campagne M, Reese T, Nicolay K. Dynamic changes in water ADC, energy metabolism, extracellular space volume, and tortuosity in neonatal rat brain during global ischemia. *Magn Reson Med* 1996;36(1):52-60.
  11. Wick M, Nagatomo Y, Prielmeier F, Frahm J. Alteration of intracellular metabolite diffusion in rat brain in vivo during ischemia and reperfusion. *Stroke* 1995;26(10):1930-1933; discussion 1934.
  12. Neil JJ, Duong TQ, Ackerman JJ. Evaluation of intracellular diffusion in normal and globally-ischemic rat brain via  $^{13}\text{C}$ s NMR. *Magn Reson Med* 1996;35(3):329-335.
  13. Duong TQ, Ackerman JJ, Ying HS, Neil JJ. Evaluation of extra- and intracellular apparent diffusion in normal and globally ischemic rat brain via  $^{19}\text{F}$  NMR. *Magn Reson Med* 1998;40(1):1-13.
  14. Duong TQ, Sehy JV, Yablonskiy DA, Snider BJ, Ackerman JJ, Neil JJ. Extracellular apparent diffusion in rat brain. *Magn Reson Med* 2001;45(5):801-810.
  15. Sykova E, Svoboda J, Polak J, Chvatal A. Extracellular volume fraction and diffusion characteristics during progressive ischemia and terminal anoxia in the spinal cord of the rat. *J Cereb Blood Flow Metab* 1994;14(2):301-311.
  16. Latour LL, Svoboda K, Mitra PP, Sotak CH. Time-dependent diffusion of water in a biological model system. *Proc Natl Acad Sci U S A* 1994;91(4):1229-1233.
  17. Norris DG, Niendorf T, Leibfritz D. Health and infarcted brain tissues studied at short diffusion times: the origins of apparent restriction and the

- reduction in apparent diffusion coefficient. *NMR Biomed* 1994;7(7):304-310.
18. Silva MD, Omae T, Helmer KG, Li F, Fisher M, Sotak CH. Separating changes in the intra- and extracellular water apparent diffusion coefficient following focal cerebral ischemia in the rat brain. *Magn Reson Med* 2002;48(5):826-837.
  19. Silva MD, Helmer KG, Lee JH, Han SS, Springer CS, Jr., Sotak CH. Deconvolution of compartmental water diffusion coefficients in yeast-cell suspensions using combined T(1) and diffusion measurements. *J Magn Reson* 2002;156(1):52-63.
  20. Catterall W, Perez-Reyes E, Snutch T, Striessnig J. International Union of Pharmacology. XLVIII. Nomenclature and Structure-Function Relationships of Voltage-Gated Calcium Channels. *Pharmacological Reviews* 2005;57(4):411-425.
  21. Slood W, Gramsbergen J. Axonal transport of manganese and its relevance to selective neurotoxicity in the rat basal ganglia. *Brain Res* 1994;657(1-2):124-132.
  22. Drapeau P, Nachshen DA. Manganese fluxes and manganese-dependent neurotransmitter release in presynaptic nerve endings isolated from rat brain. *J Physiol* 1984;348:493-510.
  23. Lin YJ, Koretsky AP. Manganese ion enhances T1-weighted MRI during brain activation: an approach to direct imaging of brain function. *Magn Reson Med* 1997;38(3):378-388.
  24. Naritaa K, Kawasakia F, Kita H. Mn and Mg influxes through Ca channels of motor nerve terminals are prevented by verapamil in frogs. *Brain Research* 1990;510:289-295.
  25. Kärger J, Pfeiffer H, Heink W. Principle and Application of Self-Diffusion Measurements by Nuclear Magnetic Resonance. *Adv Magn Reson* 1988;12:1-89.

26. Rasband W. ImageJ. Bethesda, Maryland, USA: <http://rsb.info.nih.gov/ij/>; 1997-2006.
27. Clark PR, Chua-anusorn W, St Pierre TG. Bi-exponential proton transverse relaxation rate (R2) image analysis using RF field intensity-weighted spin density projection: potential for R2 measurement of iron-loaded liver. *Magn Reson Imaging* 2003;21(5):519-530.
28. Bevington P, Robinson K. *Data Reduction and Error Analysis for the Physical Sciences*. New York: McGraw-Hill; 2003.
29. Kuo YT, Herlihy AH, So PW, Bhakoo KK, Bell JD. In vivo measurements of T1 relaxation times in mouse brain associated with different modes of systemic administration of manganese chloride. *J Magn Reson Imaging* 2005;21(4):334-339.
30. Labadie C, Lee JH, Vetek G, Springer CS, Jr. Relaxographic imaging. *J Magn Reson B* 1994;105(2):99-112.

# **CHAPTER IV**

## **SIMULATION STUDY**

## 4.1. Simulation Study

A simulation study was conducted on simulated inversion recovery (IR) data sets in MATLAB to assess the robustness of the biexponential fitting model and accuracy of the fit parameters. IR data sets were generated with two exponential signal recovery components, each having a known  $T_1$  value and a known volume fraction. These data sets were mathematically generated and summed together to form a biexponential IR data set. The resulting data set was then subjected to decomposition by adding noise to it. Simulated IR data were generated and processed as illustrated in the flowchart in Fig. 4.1. Simulated IR data sets were generated at different signal-to-noise ratios (SNRs) for different combinations of the fitting parameters in Eq. [3.2]:  $M_{0a}$ ,  $M_{0b}$ ,  $T_{1a}$ ,  $T_{1b}$ , and  $b$ . Fig. 4.2 shows an example of simulated IR data with an SNR of  $\sim 25$  (approximate SNR of the slice ROI data in our animal experiments). Each spectral window (Fig. 4.2, Top) corresponds to a single point in the inversion recovery curve (Fig. 4.2, Bottom). The IR curve was generated with the following parameters which we would expect to see if  $Mn^{2+}$  is isolated in the IC compartment:  $M_{0a} = 0.8$ ,  $M_{0b} = 0.2$ ,  $T_{1a} = 75$  ms,  $T_{1b} = 750$  ms, and  $b = 2$ ; i.e.,  $Mn^{2+}$  will reduce the IC water (80% water fraction)  $T_1$  relaxation time.

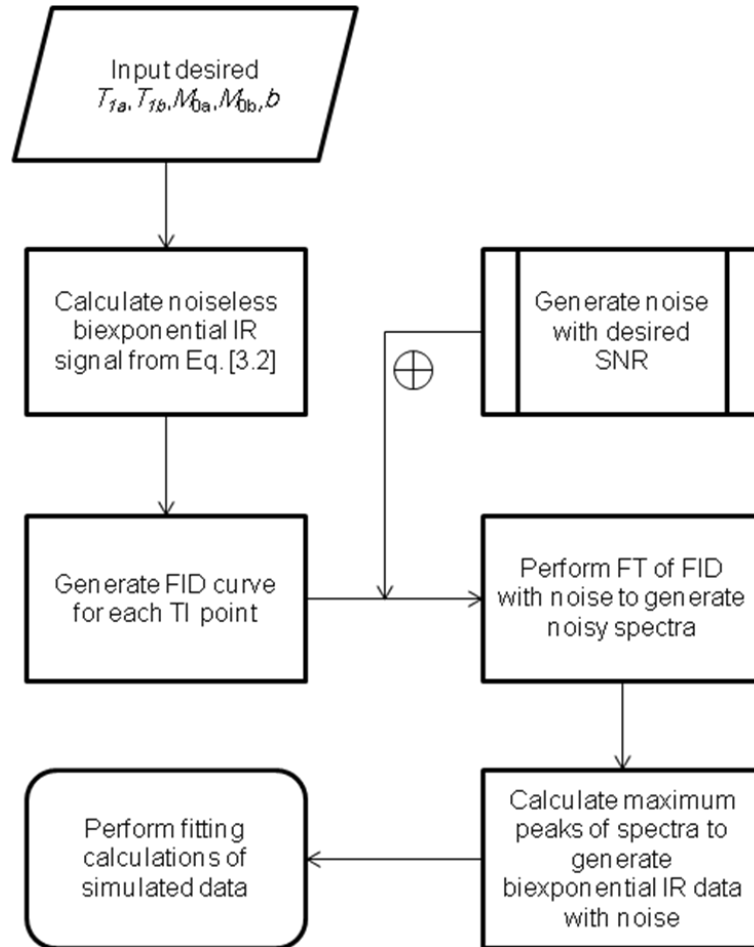


**Figure 4.1** – Flowchart showing the generation of noisy inversion recovery (IR) data using free induction decay (FID) curves to perform simulated biexponential fitting analysis.

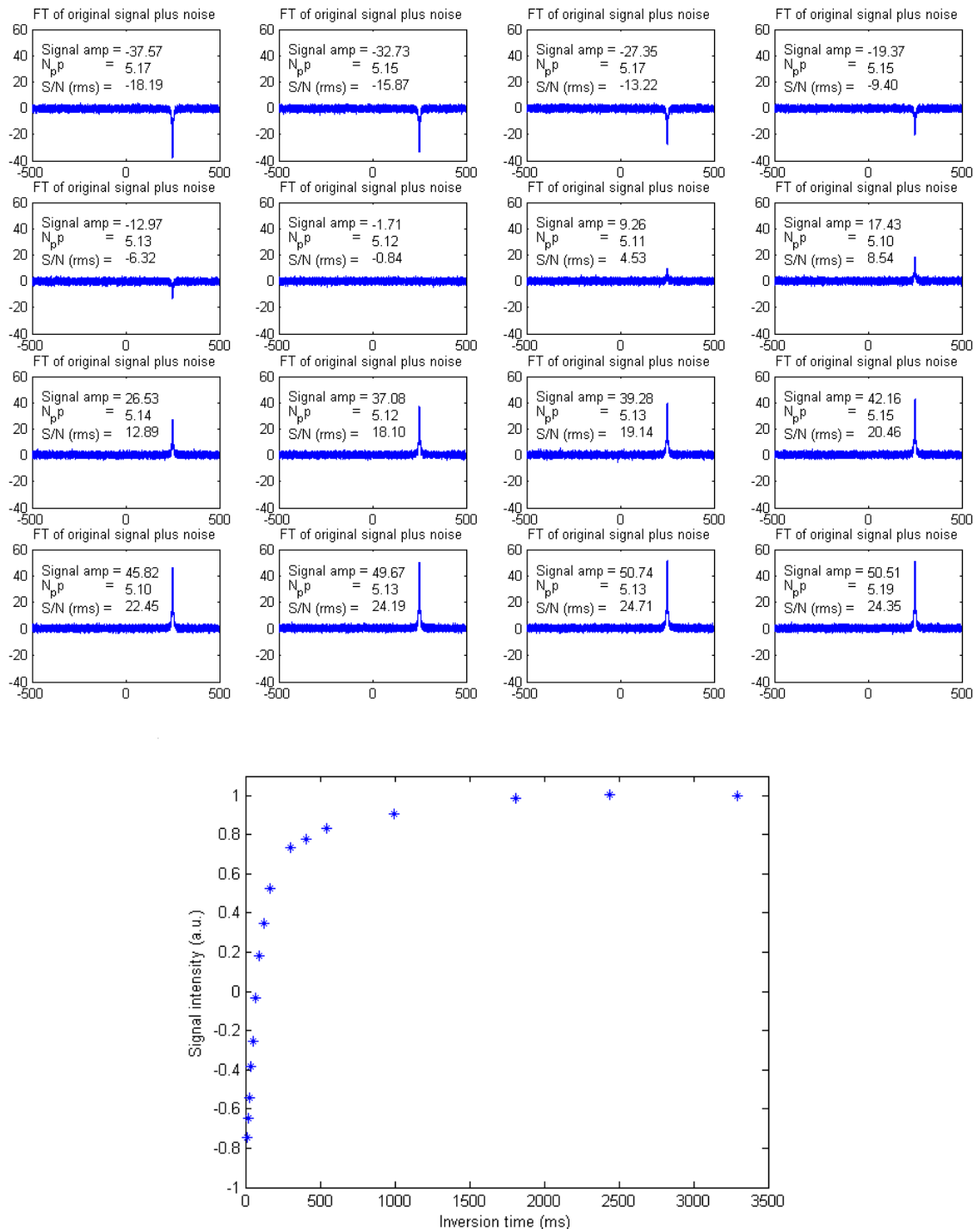


**Figure 4.2 – Top:** Sequence of spectra for noisy inversion recovery data generated at SNR~25 using the following parameters:  $M_{0a} = 0.8$ ,  $M_{0b} = 0.2$ ,  $T_{1a} = 75$  ms,  $T_{1b} = 750$  ms, and  $b = 2$ . **Bottom:** Simulated inversion recovery data generated from the spectra shown on top. Each spectral window peak is represented by a single time point in the inversion recovery curve.

Five-parameter biexponential fitting (Eq. [3.2]) showed a large degree of error on the fit parameters compared to the actual  $T_1$  relaxation times and their compartmental volume fractions. So, to increase the robustness of biexponential non-linear least squares fitting, the inversion recovery data were normalized and Eq. [3.2] was modified to Eq. [3.2a] reducing a 5-parameter fit to a 4-parameter fit model:

$$M_z(TI; M_{0b}, b, T_{1a}, T_{1b}) = (1 - M_{0b}) \cdot \left(1 - b \cdot e^{-\frac{TI}{T_{1a}}}\right) + M_{0b} \cdot \left(1 - b \cdot e^{-\frac{TI}{T_{1b}}}\right) \quad [3.2a]$$

where  $M_{0a}$  is replaced by  $(1 - M_{0b})$ .

A 3-parameter fit model was derived from Eq. [3.2] as follows:

$$M_z(TI; M_{0a}, b, T_{1a}) = M_{0a} \cdot \left(1 - b \cdot e^{-\frac{TI}{T_{1a}}}\right) + M_{0b} \cdot \left(1 - b \cdot e^{-\frac{TI}{T_{1b}}}\right) \quad [3.2b]$$

where  $T_{1b}$  and  $M_{0b}$  are constants (derived from semi-log plots), and  $T_{1a}$  and  $M_{0a}$  are the short  $T_1$  relaxation time and the corresponding compartmental volume fraction.  $T_{1b}$  and  $M_{0b}$  are the long  $T_1$  relaxation time and the corresponding compartmental volume fraction which can be derived from semi-log plots as shown in Fig. 4.3.



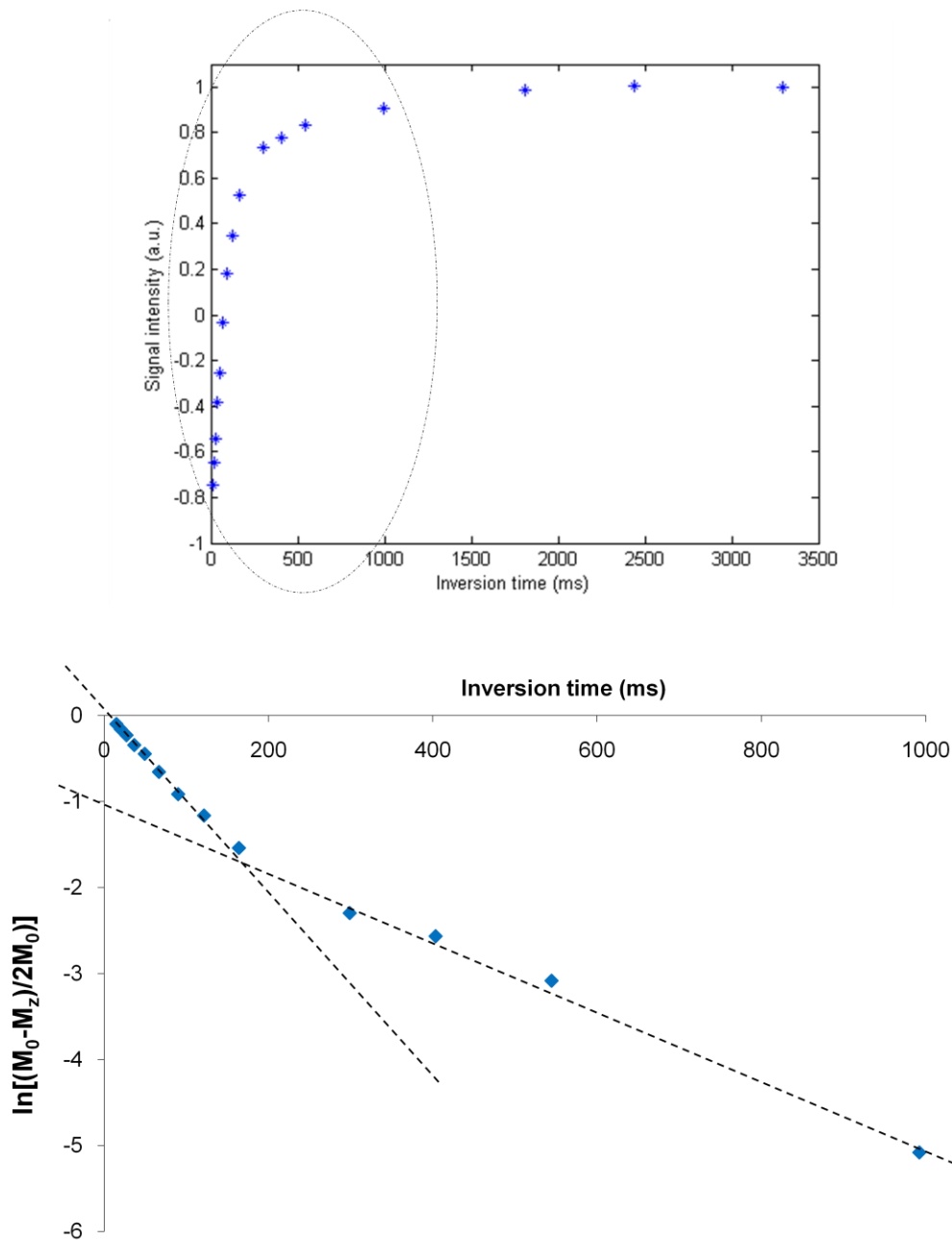


**Figure 4.3 – Top:** Simulated biexponential inversion recovery data set from Fig. 4.2 at SNR~25 with the following parameters:  $M_{0a} = 0.8$ ,  $M_{0b} = 0.2$ ,  $T_{1a} = 75$  ms,  $T_{1b} = 750$  ms, and  $b = 2$ . **Bottom:** Semi-log plot corresponding to the data points in the encircled region on the top graph. The semi-log plot can clearly distinguish between the two different slopes (dotted lines) which correspond to the two different  $T_1$  relaxation times.

In the ROI IR data sets obtained from our animal experiments, the long  $T_1$  relaxation time from biexponential IR did not necessarily correspond to the smaller volume fraction. To validate errors in fits due to mixed volume fractions, we ran several simulation scenarios with the 3- and 4-parameter fit models assigning the long  $T_1$  relaxation time to the large volume fraction and the short  $T_1$  relaxation time to the small volume fraction and vice versa. As seen in Figs. 4.4 and 4.5, simulations were run with different ratios of the  $T_1$  relaxation times and the volume fractions. Our experimental data happened to fall in the category of the circled graph shown in Figs. 4.4 and 4.5: the ratio of the short to long  $T_1$  relaxation times was  $\sim 1:10$  and the ratio of the small to large volume fractions was also  $\sim 1:10$ .

However, contrary to our hypothesis that the long  $T_1$  relaxation time will be associated with the small volume fraction, we found in all our animal experiments that the long  $T_1$  relaxation time was always associated with the larger volume fraction. This would increase the error in the fitting for the smaller  $T_1$  relaxation time using the 3-parameter fit (Eq. [3.2b]) as illustrated in the circled graph in Fig. 4.4: after 100 fits, the error in the short  $T_1$  relaxation time was  $\sim 130\%$  (a specified value of 75 ms returned a fit value of  $172 \pm 73$  ms in 100 runs). On the contrary, when the long  $T_1$  relaxation time is associated with the smaller volume fraction (data not shown), the error associated with short  $T_1$  relaxation time was only  $\sim 5\%$  (a specified value of 75 ms returned a fit value of  $71 \pm 2$  ms in 100 runs).

Thus, for all our experimental data, we used the semi-log plots to calculate the long  $T_1$  relaxation time and the large volume fraction. This inherently provided us with the small volume fraction since we fit normalized data. The short  $T_1$  relaxation time was difficult to decipher in the semi-log plots due to the association of the small volume fraction with the short  $T_1$  relaxation time; thus, we used the 4-parameter fit model (Eq. [3.2a]) to calculate the short  $T_1$  relaxation time even though the fit values underestimated the actual short  $T_1$  relaxation time as shown in Fig. 4.5 (error with the 4-parameter fit was ~30% compared to ~130% for the 3-parameter fit). The error associated with fitting the short  $T_1$  relaxation time using the 4-parameter model may still cause a misrepresentation of the actual short  $T_1$  relaxation time. From 100 fits of simulated IR data, a specified value of 75 ms returned a fit value of  $53 \pm 79$  ms (Fig. 4.5). Even though the error is ~30%, the standard deviation associated with the fit is quite large. This might further introduce errors in the calculated value of the short  $T_1$  relaxation times in our experimental data.

$M_{0a} : M_{0b}$

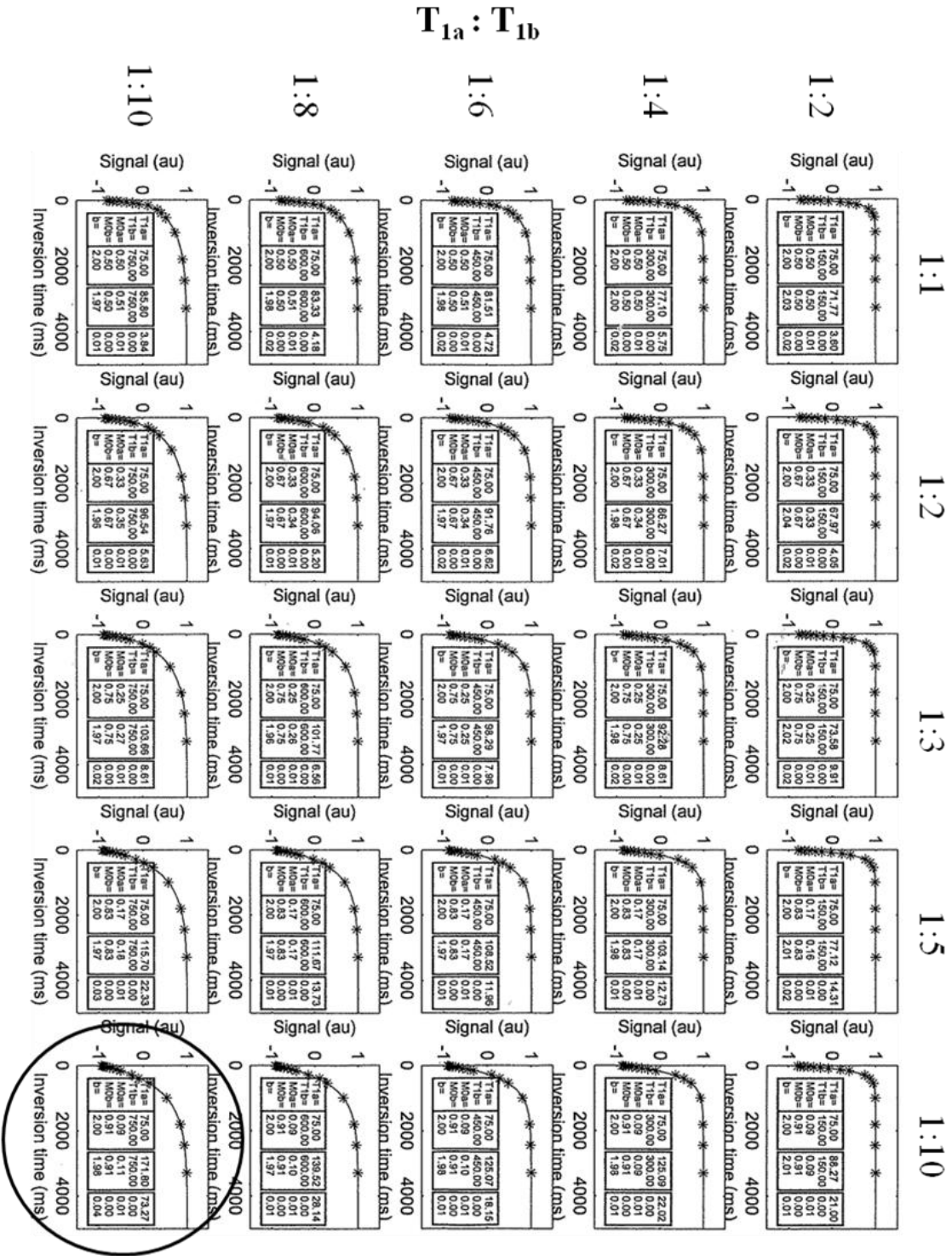


**Figure 4.4** – Biexponential fitting of simulated inversion recovery data with the 3-parameter model (Eq. [3.2a]) at SNR~25 with different ratios of the  $T_1$  relaxation times and the volume fractions. The long  $T_1$  relaxation times are associated with the large volume fractions and the short  $T_1$  relaxation times are associated with the small volume fractions. In each graph, the first, second, third, and fourth columns show the parameter labels, the specified input parameters, the fit parameter average of 100 fits, and the standard deviation of the fit parameter in 100 runs, respectively. The encircled graph shows the ratios of  $T_1$  relaxation times and volume fractions that we observed in our animal experiments. Notice, the error in the short  $T_1$  relaxation time was ~130% (a specified value of 75 ms returned a fit value of  $172 \pm 73$  ms).

$T_{1a} : T_{1b}$

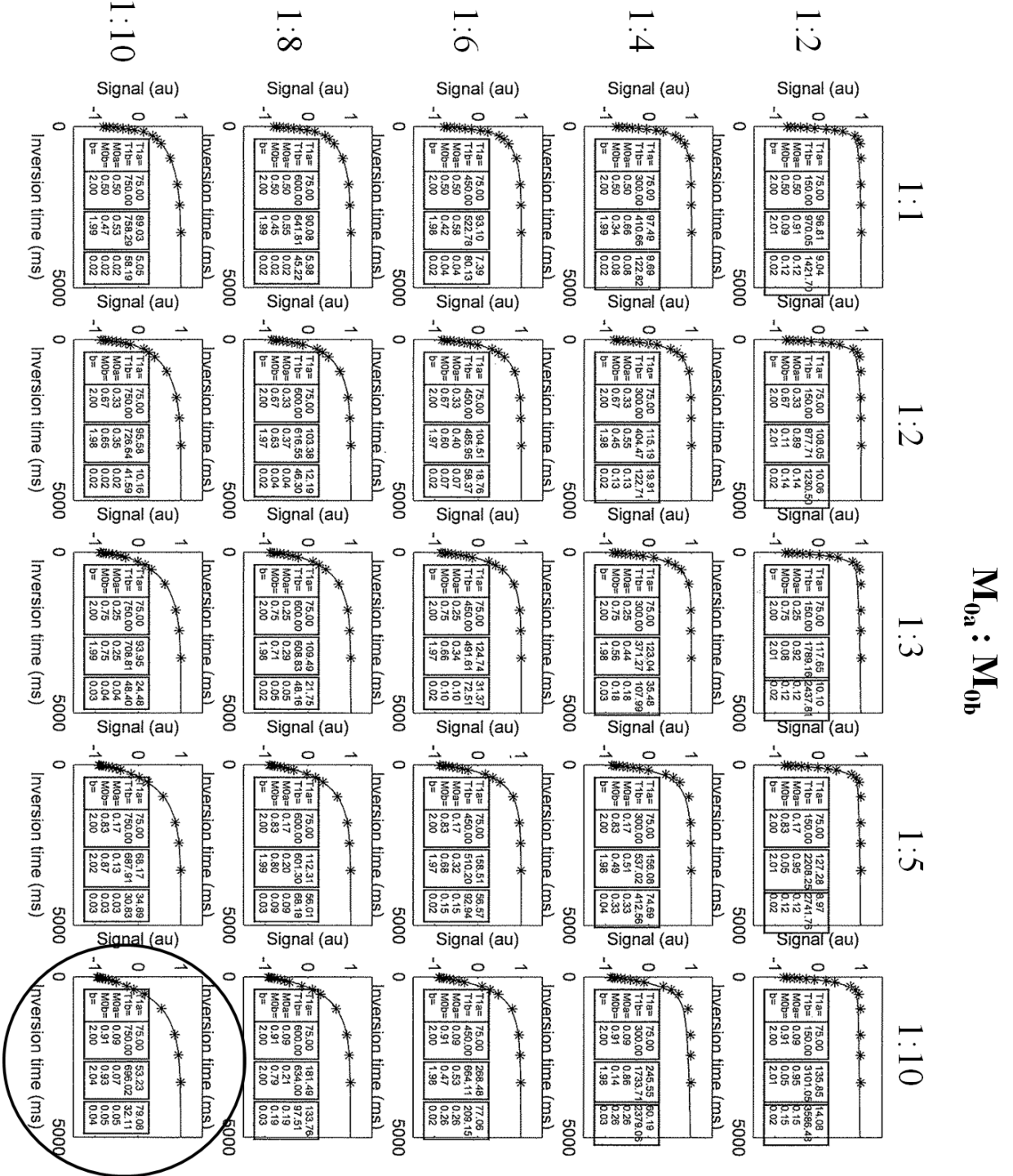


**Figure 4.5** – Biexponential fitting of simulated inversion recovery data with the 4-parameter model (Eq. [3.2b]) at SNR~25 with different ratios of the  $T_1$  relaxation times and the volume fractions. The long  $T_1$  relaxation times are associated with the large volume fractions and the short  $T_1$  relaxation times are associated with the small volume fractions. In each graph, the first, second, third, and fourth columns show the parameter labels, the specified input parameters, the fit parameter average of 100 fits, and the standard deviation of the fit parameter in 100 runs, respectively. The encircled graph shows the ratios of  $T_1$  relaxation times and volume fractions that we observed in our animal experiments. Notice, the error in the short  $T_1$  relaxation time was ~30% (a specified value of 75 ms returned a fit value of  $53 \pm 79$  ms).

**CHAPTER V**

**DOSE DEPENDENCE AND**

**TEMPORAL EVOLUTION OF THE**

**T<sub>1</sub> RELAXATION TIME AND MRI**

**CONTRAST IN THE RAT BRAIN**

**AFTER SUBCUTANEOUS**

**INJECTION OF MANGANESE**

**CHLORIDE**



# Dose Dependence and Temporal Evolution of the $T_1$ Relaxation Time and MRI Contrast in the Rat Brain after Subcutaneous Injection of Manganese Chloride

Mohammed Salman Shazeeb<sup>1,4</sup>, Christopher H. Sotak<sup>1-3</sup>

Departments of <sup>1</sup>Biomedical Engineering and <sup>2</sup>Chemistry & Biochemistry

Worcester Polytechnic Institute

Worcester, MA 01609

<sup>3</sup>Department of Radiology and <sup>4</sup>Graduate School of Biomedical Sciences

University of Massachusetts Medical School

Worcester, MA 01655

## 5.1. Preface

This study was done to investigate the MRI dose response of manganese ( $Mn^{2+}$ ) in the rat brain following subcutaneous administration of  $MnCl_2$ . I completed all aspects of this study by performing animal injections, collecting NMR data, reconstructing images, MATLAB programming for image analysis, and principal authorship in the writing of the manuscript. The manuscript work is in progress to be submitted for publication.

## 5.2. Abstract

Divalent manganese ion ( $\text{Mn}^{2+}$ ) is a widely used  $T_1$  contrast agent in manganese-enhanced MRI (MEMRI) studies to visualize functional neural tracts and anatomy in the brain *in vivo*. In animal studies, the goal is to use a dose of  $\text{Mn}^{2+}$  that will maximize the contrast while minimizing its toxic effects. In rodents, systemic administration of  $\text{Mn}^{2+}$  via intravenous (IV) injection creates a unique MRI contrast in the brain at a maximum dose of 175 mg/kg. The subcutaneous (SC) route can deliver  $\text{Mn}^{2+}$  at a maximum dose of 320 mg/kg ( $\text{LD}_{50}$  value). However, IV administration of  $\text{Mn}^{2+}$  results in faster bioelimination of excess  $\text{Mn}^{2+}$  from the plasma due to a steep concentration gradient between plasma and bile. By contrast, following SC injection,  $\text{Mn}^{2+}$  is released more slowly into the bloodstream, thus avoiding immediate hepatic elimination. Therefore, SC administration of  $\text{Mn}^{2+}$  will result in prolonged accumulation of  $\text{Mn}^{2+}$  in the brain via the choroid plexus than that obtained via IV administration of  $\text{Mn}^{2+}$ . The goal of this study was to investigate the MRI dose response of  $\text{Mn}^{2+}$  in rat brain following SC administration of  $\text{Mn}^{2+}$ . The dose dependence and temporal dynamics of  $\text{Mn}^{2+}$  after SC injection can prove useful for longitudinal *in vivo* studies that require brain enhancement to persist for a long period of time to visualize neuroarchitecture like in neurodegenerative disease studies.

### 5.3. Introduction

Divalent manganese ion ( $Mn^{2+}$ ) is a widely used  $T_1$  contrast agent in manganese-enhanced MRI (MEMRI) studies for animal neuroimaging.  $Mn^{2+}$  is highly paramagnetic making it an excellent contrast agent for visualizing brain neuroarchitecture. Applications of MEMRI have been described in three main areas as outlined by Silva *et al.* (1): neuronal tract tracing, activation-induced MEMRI (AIM-MEMRI), and whole-brain contrast enhancement. In neuronal tract tracing,  $Mn^{2+}$  is directly injected into a specific brain region; for the other two MEMRI applications,  $Mn^{2+}$  is administered either systemically into the bloodstream via intraperitoneal (IP) (2-4), intravenous (IV) (2,5,6) or subcutaneous (SC) (2,7-9) injections, or directly into the cerebrospinal fluid (CSF) via intrathecal (10) or intracerebroventricular injection (8,11).

Under normal conditions,  $Mn^{2+}$  in the bloodstream gains entry into the brain through facilitated transport in the capillary endothelial cells of the blood-brain barrier, and by filtration through the choroid plexus of the blood-CSF barrier which delivers  $Mn^{2+}$  directly into the ventricles (12). However, at high systemic doses, transport across the blood-brain barrier is saturated; so,  $Mn^{2+}$  primarily enters the CSF via the choroid plexus (13,14).  $Mn^{2+}$  acts as calcium ion ( $Ca^{2+}$ ) analog and enters the neuronal intracellular space via voltage-gated calcium channels (15) following neuronal activation (16-19) and accumulates in the

intracellular compartment.  $T_1$ -weighted ( $T_1$ -WT) MRI can then readily detect a reduction of regional water proton  $T_1$  due to the paramagnetic  $Mn^{2+}$ .

In MEMRI applications involving systemic administration of  $Mn^{2+}$ , the concentration of  $Mn^{2+}$  needs to be sufficiently high in order to attain better MR contrast and signal-to-noise ratio. However,  $Mn^{2+}$  is toxic at high concentrations producing both systemic and neurological effects (20,21). When administered in low doses, only a small fraction of  $Mn^{2+}$  reaches the brain. Disruption of the blood-brain barrier is an option where even at a low dose  $Mn^{2+}$  can gain access to the brain achieving efficient detection by MRI (1,22). Since the concentration of  $Mn^{2+}$  accumulation in the brain is proportional to the  $Mn^{2+}$  dose administered systemically, the easiest alternative without compromising the blood-brain barrier is to deliver a relatively high dose of  $Mn^{2+}$  while staying within the limits of toxic effects.

The maximum dose of  $Mn^{2+}$  administered in MEMRI studies in rodent brains vary depending upon the route of administration taken. The maximum nontoxic dose of  $Mn^{2+}$  administered via IV injection ranges between 175–180 mg/kg (1,23). The maximum nontoxic  $Mn^{2+}$  dose administered via the IP route in previous MEMRI studies has been 100 mg/kg (2,24). Via the SC route, we found a maximum nontoxic dose of 200 mg/kg (2) administered. In comparison to IV and IP injections, SC injection leads to a slower release of  $Mn^{2+}$  into the bloodstream, thus avoiding the ‘first wave’ hepatic loss (25). Therefore, a much

larger dose of  $Mn^{2+}$  can be injected via the SC route while minimizing any acute effects on the cardiovascular system; any higher dose of  $Mn^{2+}$  via IV or IP route will exceed the  $LD_{50}$  values, thereby increasing the likelihood of mortality due to toxic effects of  $Mn^{2+}$ .

In this study, dose dependence and temporal evolution of  $T_1$  relaxation time was investigated in the rat brain using SC injection of  $Mn^{2+}$  at doses up to 300 mg/kg, which is slightly less than the  $LD_{50}$  value of 320 mg/kg (*Source: Material Safety Data Sheet for  $MnCl_2$ ; product number M3634, Sigma-Aldrich, Castle Hill, Australia*). Most MEMRI studies report the time course of contrast enhancement in different regions of the brain at a single dose of  $MnCl_2$ . Fewer studies have quantified the  $T_1$  values of different brain regions at their respective administered dose (2,5,6,9,10,23,26). Only a single study to date has investigated dose dependence and temporal evolution with calculated  $T_1$  values using IV injection of  $Mn^{2+}$  in the mouse brain (5). In this study, we looked at dose effects from 6–168 hrs and at doses up to 300 mg/kg in the rat brain. Dose effects were quantified by calculating  $T_1$  values of different brain regions.

## 5.4. Materials and Methods

### 5.4.1. Animal preparation

All procedures were performed as approved by the Institute Animal Care and Use Committee (IACUC) of the University of Massachusetts Medical School (Worcester, MA, USA). Adult male Sprague-Dawley rats (weighing from 200-450 g) were anesthetized using 5% isoflurane.  $\text{MnCl}_2$  (Sigma-Aldrich, St. Louis, MO, USA) was administered via SC injection at three different doses: 75 mg/kg using 25 mM  $\text{MnCl}_2$  (N=3), 150 mg/kg using 50 mM  $\text{MnCl}_2$  (N=3), and 300 mg/kg using 100 mM  $\text{MnCl}_2$  (N=6). Different concentrations of  $\text{Mn}^{2+}$  were used for the three administered doses to ensure an approximately equal volume of  $\text{MnCl}_2$  solution injection. The SC injections were administered on the dorsal region, bilaterally, slightly posterior to the midline. Following the injection, rats were returned to their cages and allowed normal access to food and water.

During the imaging sessions, animals were anesthetized with 3% isoflurane. After anesthesia was induced, the anesthetic level was reduced to 2%. The head of the anesthetized animal was positioned in a birdcage RF coil with a nose cone providing a continuous supply of the anesthetic. The animals were placed prone into the magnet bore. A respiratory sensor was placed on the chest area to monitor the respiration rate throughout the imaging session. MEMRI was performed on each animal before SC injection of  $\text{Mn}^{2+}$ , and then at 6, 12, 24, 72, and 168 h after  $\text{Mn}^{2+}$  injection.

## 5.4.2. MR Measurements

### 5.4.2.1. $\text{MnCl}_2$ Phantom Experiments

Nine 1-cm spherical phantoms containing  $\text{MnCl}_2$  standards (25, 50, 100, 250, 500, 1000, 2000, 3000, and 5000  $\mu\text{M}$ ) were prepared in PBS.  $T_1$  relaxation time measurements were performed using inversion recovery spectroscopy with 20 inversion time values logarithmically spaced from 15–4400 ms. Other parameters were: TR = 10 s, TE = 7.4 ms, field-of-view (FOV) = 103.4 mm  $\times$  103.4 mm; data acquisition matrix = 128  $\times$  128. With the same dimensions,  $T_2$  relaxation time measurements were performed using a Carr-Purcell-Meiboom-Gill (CPMG) sequence. At least sixteen echoes were acquired with intervening TE values of 7 ms and TR = 2 s.

### 5.4.2.2. MEMRI Experiments

All MR imaging was performed on a Bruker BioSpin 2.0-T/45-cm horizontal bore system (Bruker BioSpin, Billerica, MA, USA) equipped with 200 mT/m gradients and an in-house-built, 45-mm-diameter, birdcage RF coil that was 30 mm long for RF transmit and receive. Three 2-mm-thick axial MRI slices (slice gap of 0.2 mm) were acquired anterior to the pituitary gland with the imaging plane referenced to the tip of the pituitary in the sagittal plane.  $T_1$ -weighted imaging was performed using the following acquisition parameters:

TR/TE = 700/15 ms; FOV = 38.4 mm × 38.4 mm; data acquisition matrix = 256 × 128 (zero-filled to 256 × 256); and number of averages (NEX) = 2. The  $T_1$  relaxation times were measured using a spin-echo inversion recovery sequence. A sech pulse was used for adiabatic spin-inversion and 16 inversion time values were logarithmically spaced from 15–3300 ms. Other imaging parameters were: TR = 10 s, TE = 4.8 ms, FOV = 38.4 mm × 38.4 mm; data acquisition matrix = 128 × 64 (zero-filled to 128 × 128); and NEX = 1.  $T_2$  relaxation times were measured using a Carr-Purcell-Meiboom-Gill (CPMG) spin-echo sequence (TR = 2 s, TE = 5 ms, echoes = 16).



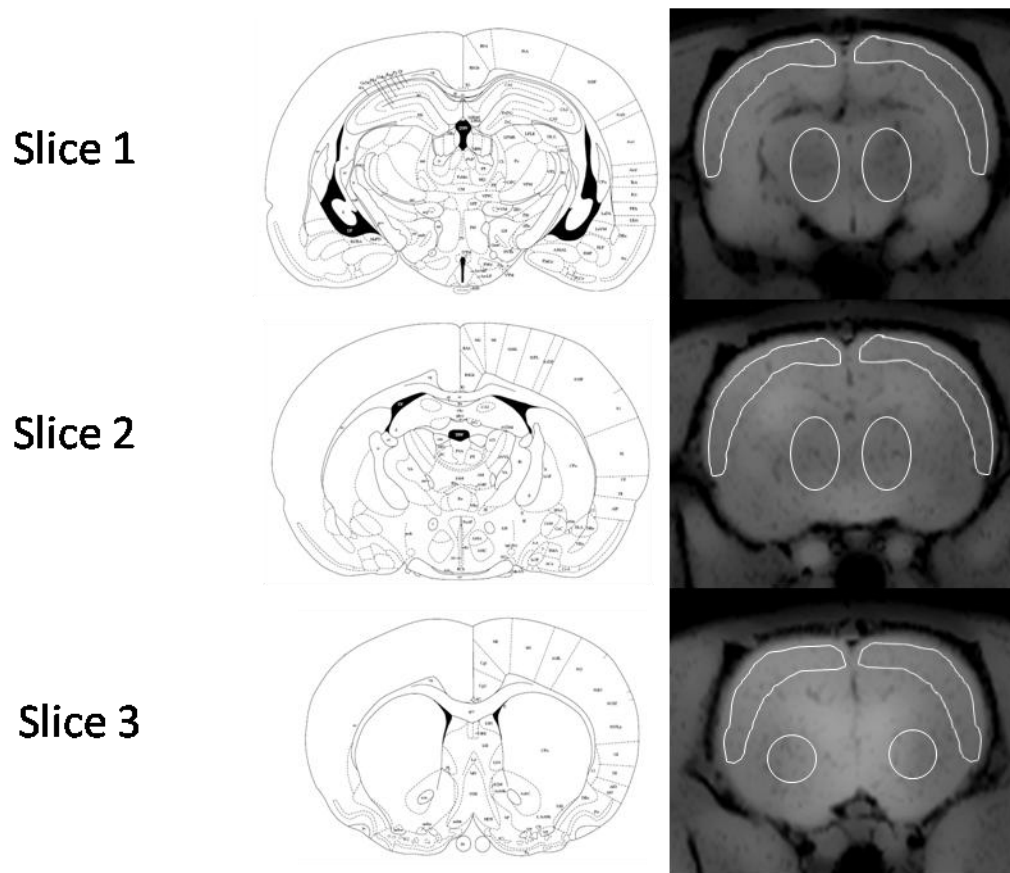


**Figure 5.1** – ROI definitions for different brain regions. Three 2-mm-thick axial MRI slices (slice gap of 0.2 mm) were selected anterior to the pituitary gland with the imaging plane referenced to the tip of the pituitary in the sagittal plane. Representative axial slices from  $T_1$ -weighted image of a rat after 300 mg/kg injection of  $MnCl_2$  at the 24 h time point are shown (right) correlated with corresponding schematic brain slices from the rat brain atlas (27). The schematic brain slices correspond to the initial part of the 2-mm-thick MR image slices. The ROI along the perimeter of the brain corresponds to the right and left cortex ROIs in all the three slices. These ROIs were averaged together to obtain an averaged cortex ROI. The left and right ROIs at the center of the brain in Slice 1 and Slice 2 were averaged together to obtain an averaged sub-cortical ROI. The left and right ROIs in Slice 3 were averaged together to obtain an averaged caudate nucleus ROI. This figure is identical to Fig. 3.1.

### 5.4.3 Data Analysis

Using the ImageJ software package (28), three different regions of interest (ROI) were selected (cortex, sub-cortical region, and caudate nucleus) from the collected slices as shown in Fig. 5.1 and correlated with the corresponding schematic slices from the rat brain atlas (27). Due to the position of the brain slices and relatively low resolution to capture detailed neuroarchitecture, the ROIs were selected accordingly where all relaxation time measurements from these regions represent an average over the heterogeneity within the tissues in the ROIs. The mean signal intensity values within each of the ROIs were calculated using ImageJ and non-linear least squares fitting calculations were performed using MATLAB (The Mathworks Inc., Natick, MA) to calculate the relaxation times. Analysis of variance (ANOVA) for mixed models was used to determine if there was a significant change in  $T_1$  relaxation times: 1) after the administration of  $Mn^{2+}$ , 2) at the different doses of  $Mn^{2+}$  administered via the SC route, and 3) due to interaction between the time after  $Mn^{2+}$  injection and the  $Mn^{2+}$  dose administered. In the presence of significant effects (main or interaction), the Tukey-Kramer HSD multiple comparisons procedure was used to compare the mean  $T_1$  times of the same anatomical region among different time points and to determine if any difference existed between the different  $Mn^{2+}$  doses administered. Statistical analyses were carried out using the SAS statistical software package.

## 5.5 Results

### 5.5.1. MnCl<sub>2</sub> Phantoms

Fig. 5.2A shows a plot of  $R_1$  ( $1/T_1$ ) relaxation rate ( $s^{-1}$ ) as a function of  $Mn^{2+}$  concentration (mM). The best-fit straight line through all of the data gives:  $R_1 = 7.19 \pm 0.16 \cdot [Mn^{2+}]$  (mM) +  $0.15 \pm 0.34$  ( $r^2 = 0.9993$ ). The errors on the least-square fitting parameters are  $\pm 1$  SE. From the slope of the line, the  $r_1$  relaxivity of  $Mn^{2+}$  is equal to  $7.19 \pm 0.16 s^{-1}mM^{-1}$ . Fig. 5.2B shows a plot of  $R_2$  ( $1/T_2$ ) relaxation rate ( $s^{-1}$ ) as a function of  $Mn^{2+}$  concentration (mM). The best-fit straight line through all of the data gives:  $R_2 = 97.4 \pm 7.78 \cdot [Mn^{2+}]$  (mM) +  $4.58 \pm 16.27$  ( $r^2 = 0.9909$ ). The errors on the least-square fitting parameters are  $\pm 1$  SE. The  $r_2$  relaxivity of  $Mn^{2+}$  is equal to  $97.4 \pm 7.78 s^{-1}mM^{-1}$ .

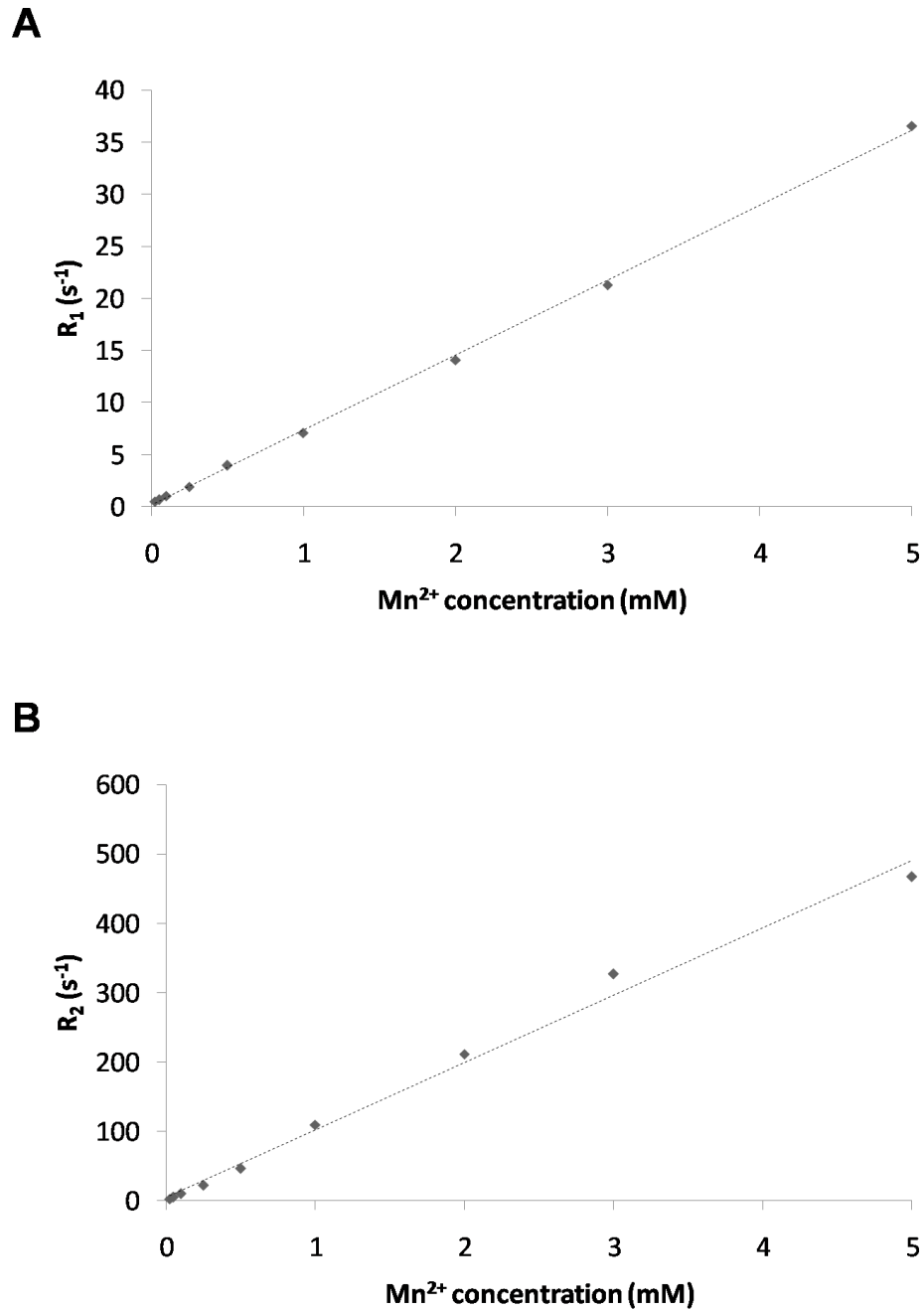


**Figure 5.2 – A)** Plot of  $R_1$  ( $1/T_1$ ) relaxation rate ( $s^{-1}$ ) as a function of  $MnCl_2$  concentration (mM) at 2 Tesla. The best-fit straight line through all of the data gives:  $R_1 = 7.19 \cdot [MnCl_2]$  (mM) + 0.15. The  $r_1$  relaxivity given by the slope of the line was equal to  $7.19 s^{-1}mM^{-1}$ . **B)**

Plot of  $R_2$  ( $1/T_2$ ) relaxation rate ( $s^{-1}$ ) as a function of  $MnCl_2$  concentration (mM). The best-fit straight line through all of the data gives:  $R_2 = 97.4 \cdot [MnCl_2] \text{ (mM)} + 4.58$ . The  $r_2$  relaxivity given by the slope of the line was equal to  $97.4 \text{ s}^{-1}\text{mM}^{-1}$ .

### 5.5.2. Time Course of Manganese Distribution

Fig. 5.3 shows a series of  $T_1$ -weighted ( $T_1$ -WT) MEMRI data sets as a function of time after SC administration of 300 mg/kg  $Mn^{2+}$  in the rat brain. At 6 h following  $Mn^{2+}$  injection,  $T_1$ -WT signal enhancement was apparent in all three slices around the ventricle regions which contain the CSF. With time, the  $T_1$ -WT signal enhancement uniformly expanded to the cortical and sub-cortical regions. By the 72 h time point there was a uniform enhancement throughout the brain which persisted up to the 168 h time point.

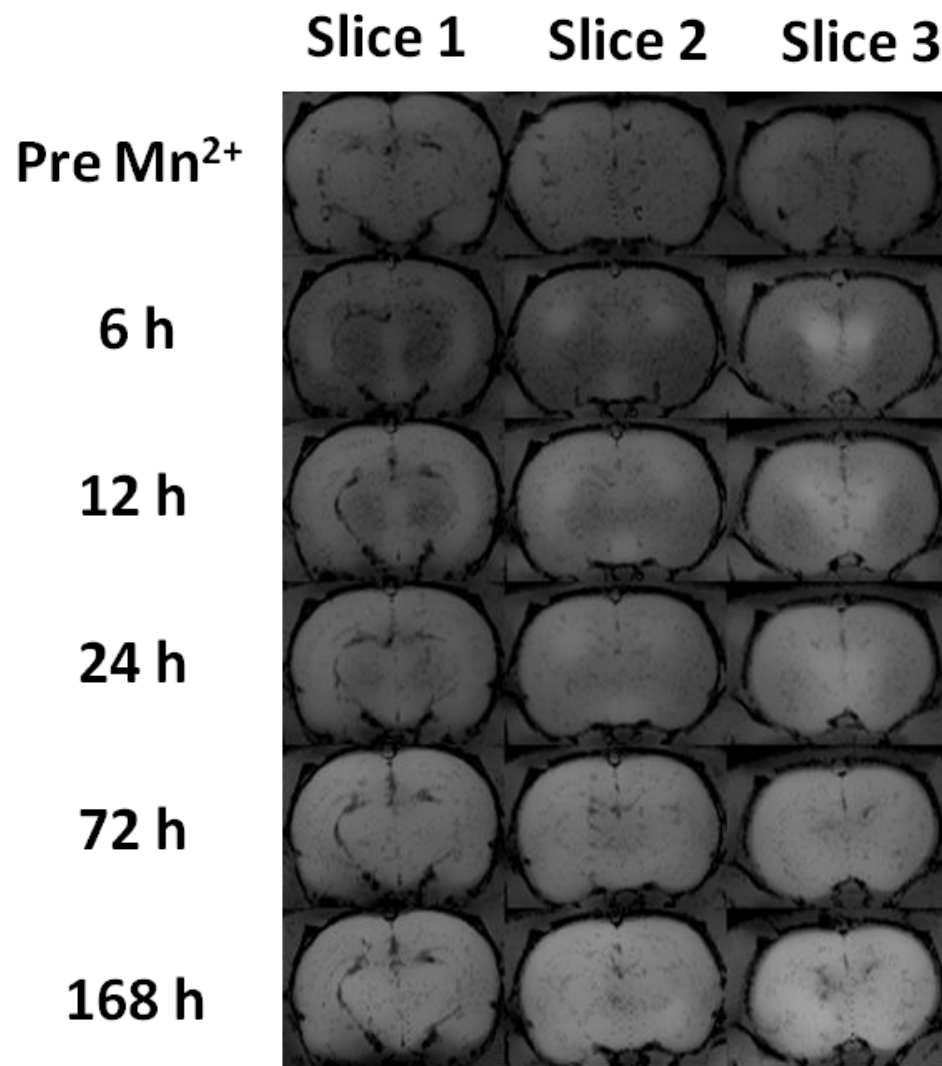


**Figure 5.3** – Time-course of Mn<sup>2+</sup> distribution in rat brain. Three-slice  $T_1$ -weighted ( $T_1$ -WT) axial MR image sets (TR/TE = 700/15 ms) are shown as a function of time after subcutaneous injection of MnCl<sub>2</sub> (100 mM, dose = 300 mg/kg). At 6 h following MnCl<sub>2</sub> injection,  $T_1$ -WT signal enhancement was apparent in the three 2-mm-thick slices around the ventricle regions which contain the cerebrospinal fluid. Over time, the region of  $T_1$ -WT signal enhancement expanded to the cortical and sub-cortical regions. By the 72 h time point there was uniform  $T_1$ -WT signal enhancement throughout the brain which is apparent even at the 168 h time point. All images have the same relative intensity

scaling; therefore, changes in  $T_1$ -WT signal contrast are directly proportional to changes in tissue  $Mn^{2+}$  concentration over time. These images were filtered to remove high-intensity pixel artifacts caused by motion.

### 5.5.3. Dose Dependence and Time Course of Manganese Distribution

Fig. 5.4 shows a series of  $T_1$ -WT MEMRI data sets of Slice 3 in the rat brain (defined in Fig. 5.1) both as a function of varying doses of  $Mn^{2+}$  and as a function of time after SC administration of  $Mn^{2+}$ . At 6 h following  $Mn^{2+}$  injection,  $T_1$ -WT signal enhancement was apparent in the slices at all doses around the ventricle regions which contain the CSF. With time, the  $T_1$ -WT signal enhancement uniformly expanded to the cortical and sub-cortical regions. Uniform enhancement was achieved throughout the brain by the 72 h time point at all administered  $Mn^{2+}$  doses. The  $T_1$ -WT signal enhancement persisted in all the images up to the 168 h time point for all  $Mn^{2+}$  doses. The  $T_1$ -WT signal enhancement was proportional to the dose of  $Mn^{2+}$  administered: image slices at 300 mg/kg showed the most  $T_1$ -WT signal enhancement while the image slices at 75 mg/kg showed the least  $T_1$ -WT signal enhancement at all time points observed (data not shown).

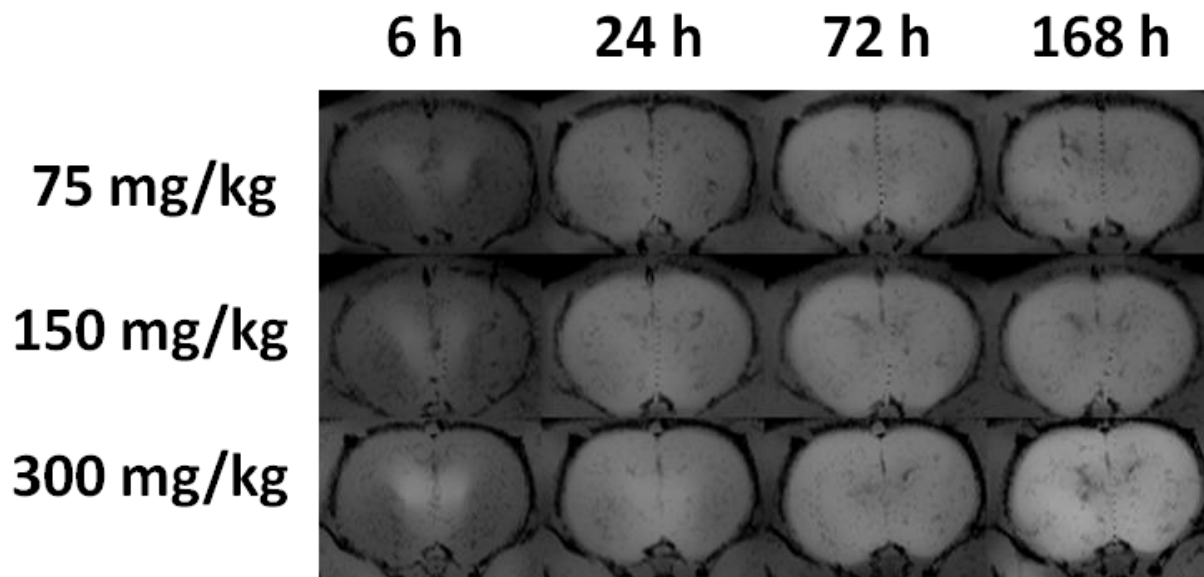
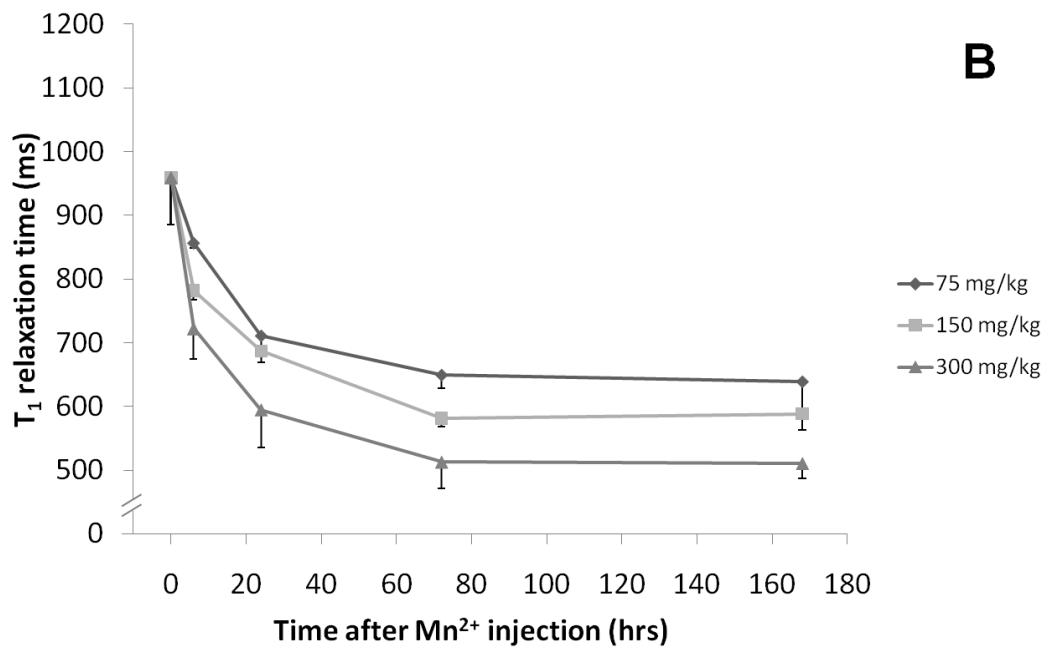
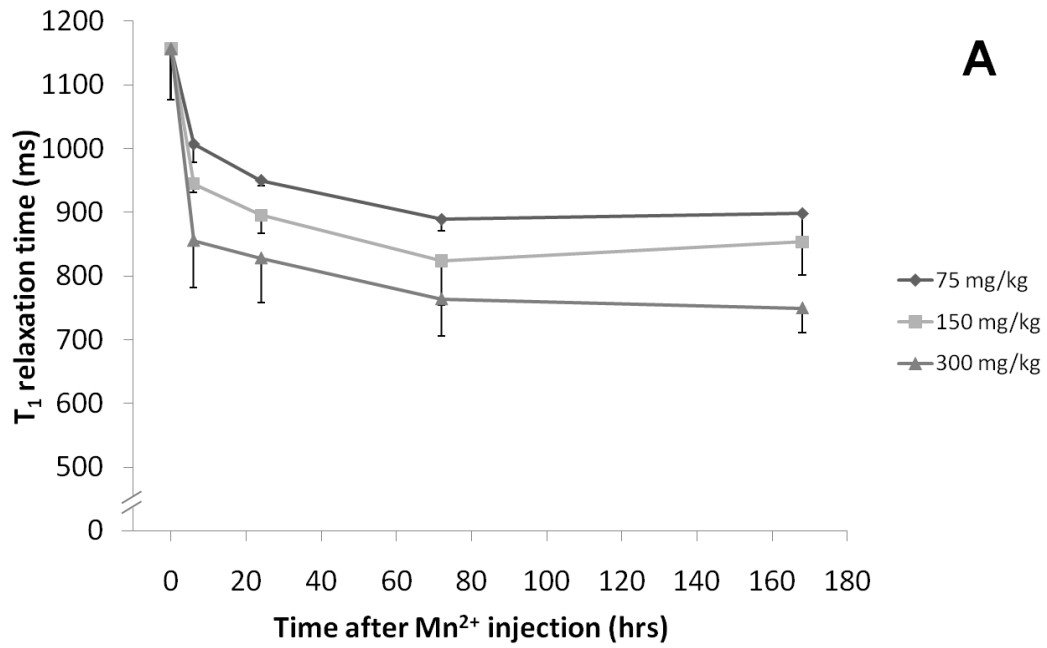


**Figure 5.4** – Dose dependence and time-course of MEMRI contrast.  $T_1$ -weighted ( $T_1$ -WT) axial MR image sets (TR/TE = 700/15 ms) of Slice #3 from Fig. 5.1 are shown as a function of varying doses of  $MnCl_2$  and as a function of time after subcutaneous injection of  $MnCl_2$ .  $T_1$ -WT signal enhancement was apparent in all the 2-mm-thick slices around the ventricle regions which contain the cerebrospinal fluid. Over time, the region of  $T_1$ -WT signal enhancement expanded to the cortical and sub-cortical regions. The images at 75 mg/kg and 150 mg/kg achieved uniform enhancement throughout the brain by the 24 h time point, whereas the image at 300 mg/kg achieved uniform enhancement by the 72 h time point (see Fig. 5.1). The  $T_1$ -WT signal enhancement was proportional to the dose of  $MnCl_2$  administered: image slices at 300 mg/kg showed the most  $T_1$ -WT signal enhancement while the image slices at 75 mg/kg showed the least  $T_1$ -WT signal enhancement at all time points observed (data not shown). All images have the same relative intensity scaling; therefore, changes in  $T_1$ -WT signal contrast are directly proportional to changes in tissue  $Mn^{2+}$  concentration over time. These images were filtered to remove high-intensity pixel artifacts caused by motion. This figure is identical to Fig. 3.2.



#### 5.5.4. Time Course and Dose Dependence of Regional $T_1$ Values

The temporal evolution of  $T_1$  relaxation times at three different doses of  $Mn^{2+}$  in the cortex region of the rat brain is shown in Fig. 5.5A. The  $T_1$  relaxation times reduced steadily from  $1156 \pm 79$  ms and leveled off near the 72 h time point. The largest reduction in the  $T_1$  relaxation time ( $\sim 407$  ms) was observed at the highest  $Mn^{2+}$  dose administered (300 mg/kg) and the smallest reduction in the  $T_1$  relaxation time ( $\sim 258$  ms) was observed at the lowest  $Mn^{2+}$  dose administered (75 mg/kg). Fig. 5.6A shows the same information as Fig. 5.5A with the  $T_1$  relaxation times plotted as a function of  $Mn^{2+}$  dose at different time points after  $Mn^{2+}$  injection. In Fig. 5.6A, the  $T_1$  relaxation times reduced with increasing  $Mn^{2+}$  dose. The largest reduction in the  $T_1$  relaxation times occurred at the 72 h and 168 h time points. ANOVA test for mixed models showed a significant effect of  $Mn^{2+}$  dose ( $P < 0.01$ ) and time point after  $Mn^{2+}$  injection ( $P < 0.0001$ ) on the reduction of  $T_1$  relaxation times. There was no significant effect of the interaction between the  $Mn^{2+}$  dose and time point after  $Mn^{2+}$  injection. Table 1 and Table 2 show the statistical significance of differences of least square means of  $T_1$  relaxation times between the different time points after  $Mn^{2+}$  injection and between the different  $Mn^{2+}$  doses administered, respectively, in the cortex region of the rat brain.



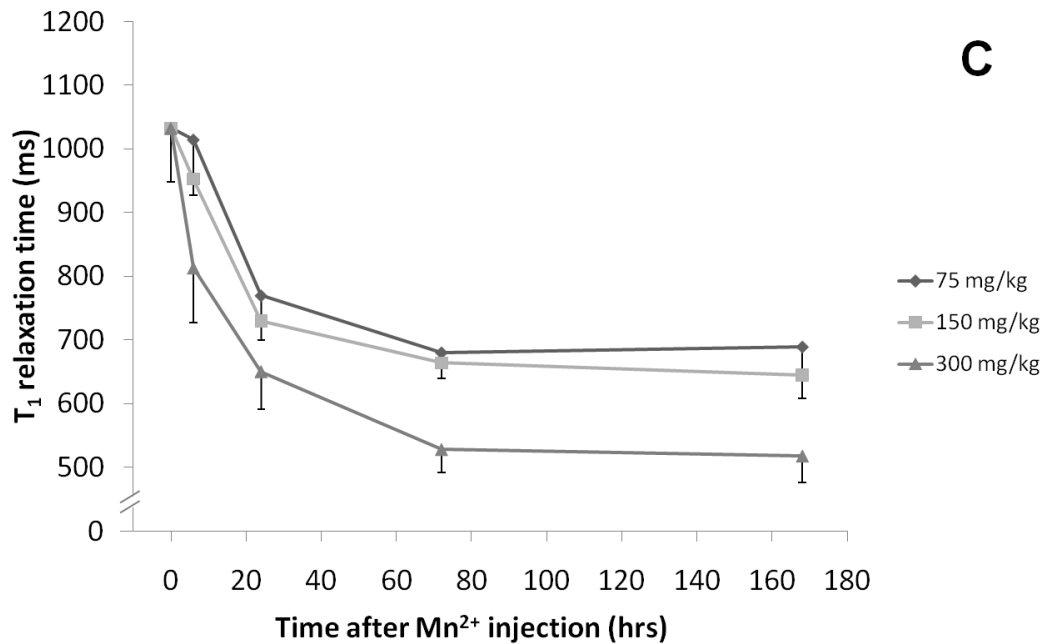


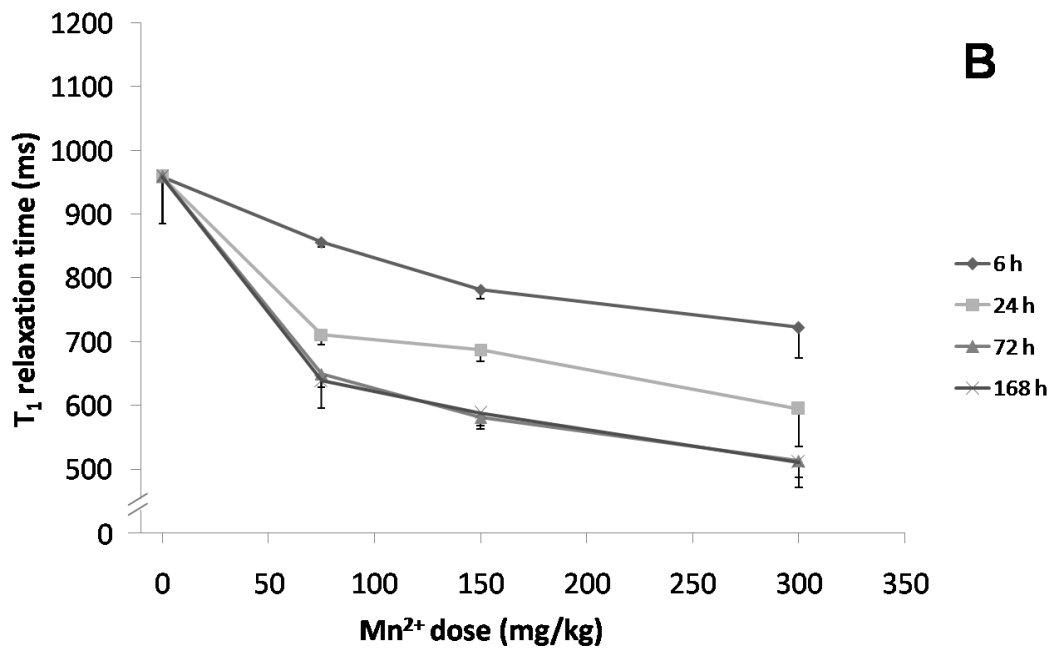
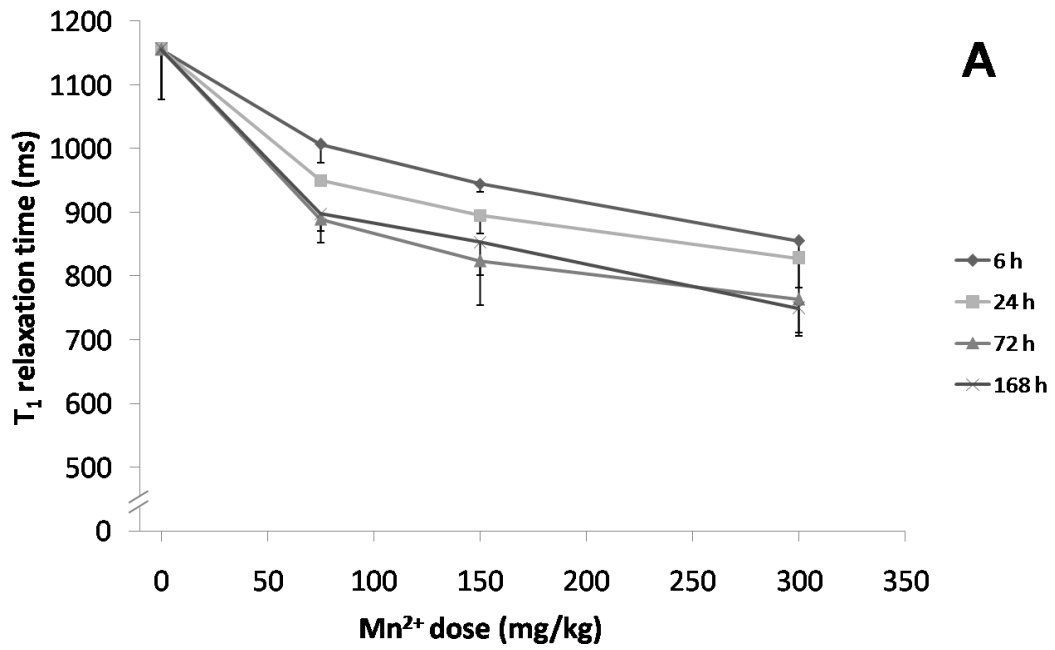
**Figure 5.5** – Plots of *in vivo*  $T_1$  relaxation times as a function of time after subcutaneous injection of  $MnCl_2$  at three different doses in **A**) cortex ROI, **B**) sub-cortical region ROI, and **C**) caudate nucleus ROI. A total of 13 animals were used in this study with the following  $Mn^{2+}$  doses: 75 mg/kg (N=3), 150 mg/kg (N=3), and 300 mg/kg (N=7). Three of the thirteen animals were imaged before administration of  $MnCl_2$ . All the animals were imaged at the following time points after  $MnCl_2$  injection: 6, 24, 72, and 168 h. For each ROI, the mean ( $-1$  SD) ROI  $T_1$  relaxation times were plotted against the time point after  $Mn^{2+}$  injection for all animals at the same administered dose. Statistical comparisons between the different time points at each ROI were performed using analysis of variance (ANOVA) shown in Table 5.1.

**Table 5.1**

Statistical Significance of Differences of Least Squares Means of  $T_1$  Relaxation Times Between the Different Time Points in Three Different Regions of the Rat Brain After SC Administration of  $Mn^{2+}$ . *NS* = not significant ( $P > 0.05$ ),  $*0.01 < P < 0.05$  (ANOVA with Tukey-Kramer HSD multiple comparisons procedure),  $**0.001 < P < 0.01$ , and  $***P < 0.001$ .

	Time after $Mn^{2+}$ injection (hrs)			
		24	72	168
<b>Cortex</b>				
	<b>6</b>	*	***	***
	<b>24</b>	-	***	***
	<b>72</b>	-	-	<i>NS</i>
<b>Sub-cortical Region</b>		<b>24</b>	<b>72</b>	<b>168</b>
	<b>6</b>	***	***	***
	<b>24</b>	-	***	**
	<b>72</b>	-	-	<i>NS</i>
<b>Caudate Nucleus</b>		<b>24</b>	<b>72</b>	<b>168</b>
	<b>6</b>	***	***	***
	<b>24</b>	-	***	***
	<b>72</b>	-	-	<i>NS</i>

Fig. 5.5B shows the temporal evolution of the  $T_1$  relaxation times at three different doses of  $Mn^{2+}$  in the sub-cortical region of the rat brain. The  $T_1$  relaxation times reduced steadily from  $959 \pm 74$  ms and leveled off near the 72 h time point similar to the cortex region in Fig. 5.5A; however, the reduction in  $T_1$  relaxation times was greater in the sub-cortical region than that observed in the cortex region at the same administered dose. The largest reduction in the  $T_1$  relaxation time ( $\sim 448$  ms) was observed at the highest  $Mn^{2+}$  dose administered (300 mg/kg) and the smallest reduction in the  $T_1$  relaxation time ( $\sim 320$  ms) was observed at the lowest  $Mn^{2+}$  dose administered (75 mg/kg). Fig. 5.6B shows the same information as Fig. 5.5B with the  $T_1$  relaxation times plotted as a function of  $Mn^{2+}$  dose at different time points after  $Mn^{2+}$  injection. In Fig. 5.6B, the  $T_1$  relaxation times reduced with increasing  $Mn^{2+}$  dose similar to the cortex region in Fig. 5.6A; however, the reduction in  $T_1$  relaxation times of the sub-cortical region was greater than that of the cortex region. The largest reduction in the  $T_1$  relaxation times occurred at the 72 h and 168 h time points. ANOVA test for mixed models showed a significant effect of  $Mn^{2+}$  dose ( $P < 0.001$ ) and time point after  $Mn^{2+}$  injection ( $P < 0.0001$ ) on the reduction of  $T_1$  relaxation times. There was no significant effect of the interaction between the  $Mn^{2+}$  dose and time point after  $Mn^{2+}$  injection. Table 1 and Table 2 show the statistical significance of differences of least square means of  $T_1$  relaxation times between the different time points after  $Mn^{2+}$  injection and between the different  $Mn^{2+}$  doses administered, respectively, in the sub-cortical region of the rat brain.



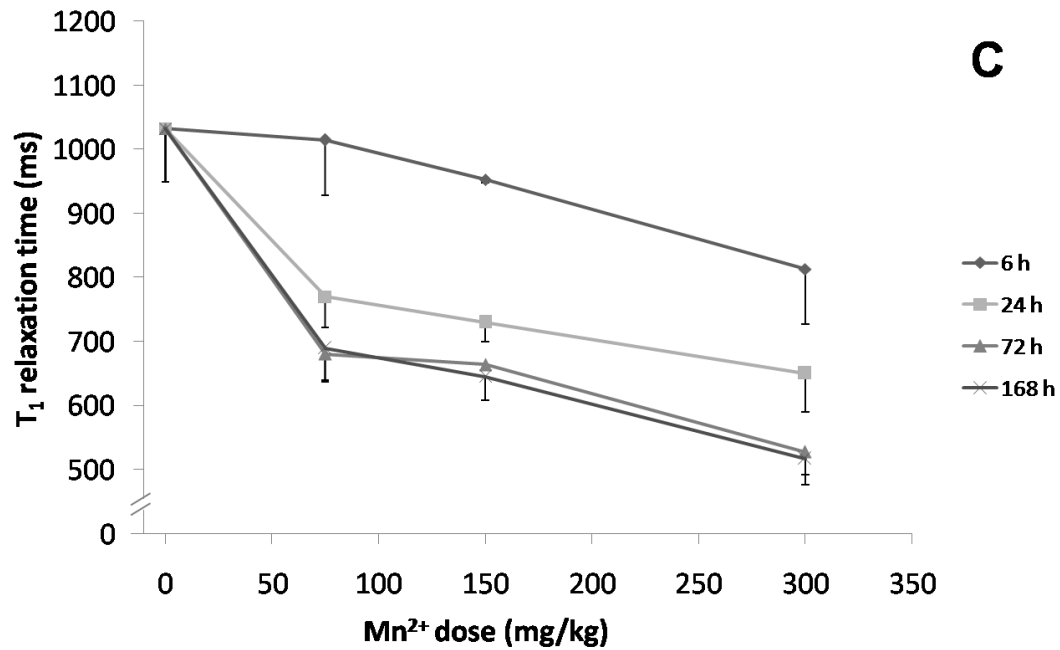


**Figure 5.6** – Plots of the *in vivo*  $T_1$  relaxation times as a function of  $Mn^{2+}$  dose administered at four different time points in **A)** cortex ROI, **B)** sub-cortical ROI, and **C)** caudate nucleus ROI. These plots contain the same information as the respective plots in Fig. 5.5 representing the data as a function of dose instead of time. For each ROI, the mean ( $-1$  SD) ROI  $T_1$  relaxation times were plotted against  $Mn^{2+}$  dose for all animals at the same time point after  $Mn^{2+}$  injection. Statistical comparisons between the different  $Mn^{2+}$  doses at each ROI were performed using analysis of variance (ANOVA) shown in Table 5.2.

**Table 5.2**

Statistical Significance of Differences of Least Squares Means of  $T_1$  Relaxation Times Between the Different  $Mn^{2+}$  Doses in Three Different Regions of the Rat Brain After SC Administration of  $Mn^{2+}$  Administered in the Rat Brain. *NS* = not significant ( $P > 0.05$ ),  $*0.01 < P < 0.05$  (ANOVA with Tukey-Kramer HSD multiple comparisons procedure),  $**0.001 < P < 0.01$ , and  $***P < 0.001$ .

	$Mn^{2+}$ dose (mg/kg)		
		150	300
<b>Cortex</b>			
	<b>75</b>	<i>NS</i>	<b>**</b>
	<b>150</b>	-	<i>NS</i>
<b>Sub-cortical Region</b>		<b>150</b>	<b>300</b>
	<b>75</b>	<i>NS</i>	<b>***</b>
	<b>150</b>	-	<b>**</b>
<b>Caudate Nucleus</b>		<b>150</b>	<b>300</b>
	<b>75</b>	<i>NS</i>	<b>***</b>
	<b>150</b>	-	<b>***</b>

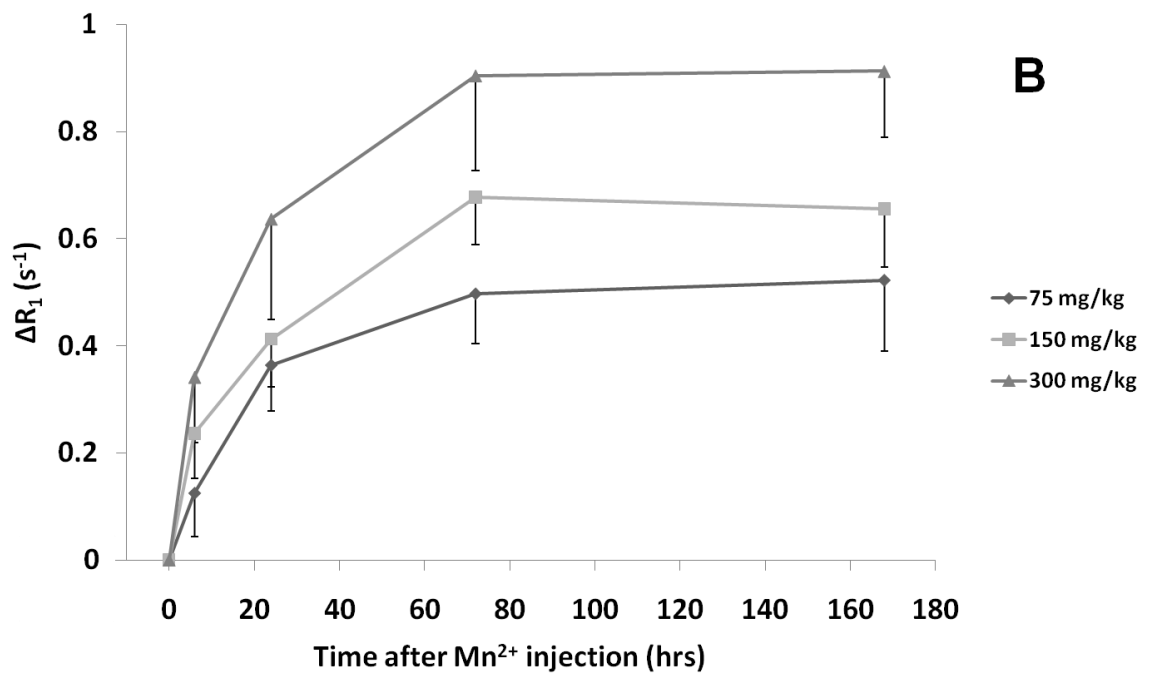
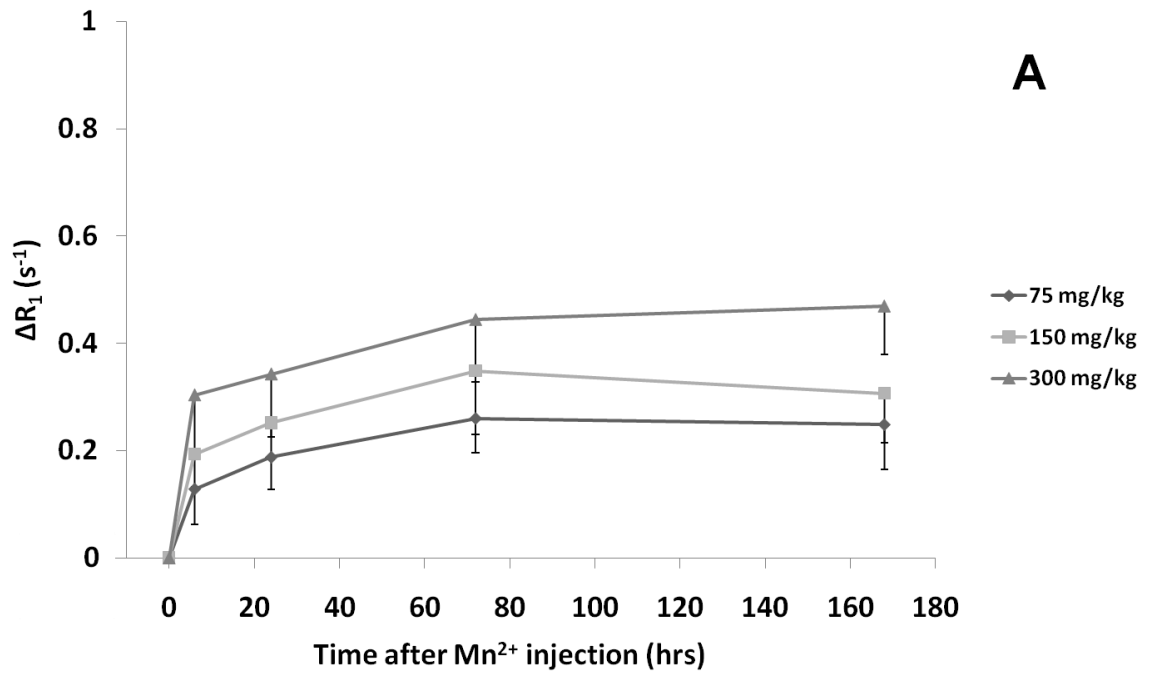


The temporal evolution of the  $T_1$  relaxation times at three different doses of  $Mn^{2+}$  in the caudate nucleus region of the rat brain is shown in Fig. 5.5C. The  $T_1$  relaxation times reduced steadily from  $1033 \pm 84$  ms and leveled off near the 72 h time point similar to the cortex and sub-cortical regions; however, the reduction in  $T_1$  relaxation times was greater in the caudate nucleus region than that observed in the cortex region and similar to that observed in the sub-cortical region at the same administered dose. The largest reduction in the  $T_1$  relaxation time ( $\sim 515$  ms) was observed at the highest  $Mn^{2+}$  dose administered (300 mg/kg) and the smallest reduction in the  $T_1$  relaxation time ( $\sim 343$  ms) was observed at the lowest  $Mn^{2+}$  dose administered (75 mg/kg). Fig. 5.6C shows the same information as Fig. 5.5C with the  $T_1$  relaxation times plotted as a function of  $Mn^{2+}$  dose at different time points after  $Mn^{2+}$  injection. In Fig. 5.6C, the  $T_1$  relaxation times reduced with increasing  $Mn^{2+}$  dose similar to the cortex and sub-cortical regions; however, the reduction in  $T_1$  relaxation times of the caudate nucleus region was greater than that of the cortex region and similar to that of the sub-cortical region. The largest reduction in the  $T_1$  relaxation times occurred at the 72 h and 168 h time points. ANOVA test for mixed models showed a significant effect of  $Mn^{2+}$  dose ( $P < 0.0001$ ) and time point after  $Mn^{2+}$  injection ( $P < 0.0001$ ) on the reduction of  $T_1$  relaxation times. There was no significant effect of the interaction between the  $Mn^{2+}$  dose and time point after  $Mn^{2+}$  injection. Table 1 and Table 2 show the statistical significance of differences of least square means of  $T_1$  relaxation times between the different time points after  $Mn^{2+}$  injection and

between the different  $\text{Mn}^{2+}$  doses administered, respectively, in the caudate nucleus region of the rat brain.

### 5.5.5. Temporal Evolution of Change in Manganese Relaxivity

Figs. 5.7A, 5.7B, and 5.7C show the time course of change in relaxivity ( $\Delta R_1$ ) after SC injection of  $\text{Mn}^{2+}$  at three different doses in the cortex region, sub-cortical region, and caudate nucleus region of the rat brain, respectively. The graphs in Fig. 5.7 essentially contain the same information as Fig. 5.5.  $\Delta R_1$  was calculated as  $\Delta R_1 = R_1 - R_0$ , where  $R_1$  is the inverse of  $T_1$  relaxation time ( $1/T_1$ ) at a given  $\text{Mn}^{2+}$  concentration and  $R_0$  is the inverse of  $T_1$  relaxation time without any injected manganese.  $\Delta R_1$  corresponds to the uptake of  $\text{Mn}^{2+}$  in the rat brain. The largest change in  $\Delta R_1$  was observed at the highest  $\text{Mn}^{2+}$  dose administered (300 mg/kg) and the smallest change in  $\Delta R_1$  was observed at the lowest  $\text{Mn}^{2+}$  dose (75 mg/kg). The maximum  $\Delta R_1$  value measured in the cortex ROI was smaller than that in the sub-cortical region and caudate nucleus ROI for all doses administered. The maximum  $\Delta R_1$  was observed using 300 mg/kg  $\text{Mn}^{2+}$  dose at the 168 h time point for each ROI region:  $0.47 \pm 0.09 \text{ s}^{-1}$  in the cortex ROI,  $0.91 \pm 0.12 \text{ s}^{-1}$  in the sub-cortical region ROI, and  $0.96 \pm 0.17 \text{ s}^{-1}$  in the caudate nucleus ROI.



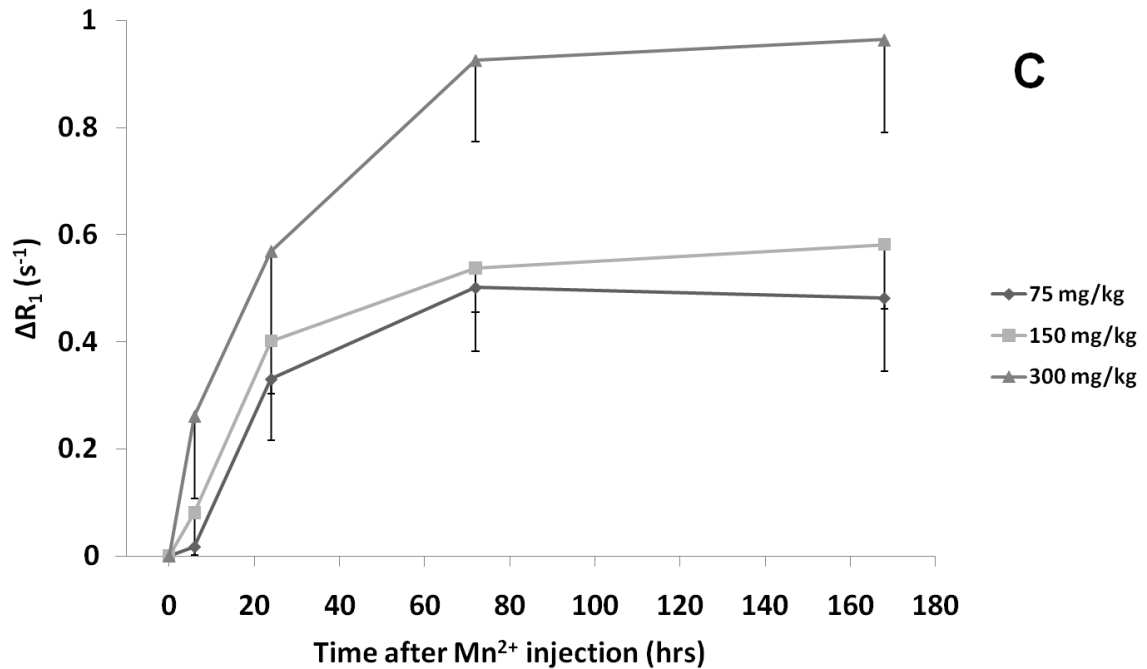


**Figure 5.7** – Plots of change in relaxivity  $\Delta R_1$  as a function of time after subcutaneous injection of  $\text{MnCl}_2$  at three different doses in **A**) cortex ROI, **B**) sub-cortical region ROI, and **C**) caudate nucleus ROI. These plots contain the same information as the respective plots in Fig. 5.5 representing the change in relaxivity as a function of time for quantitative comparison with other studies. For each ROI, the mean ( $-1$  SD) ROI  $\Delta R_1$  values were plotted against the time point after  $\text{Mn}^{2+}$  injection for all animals at the same administered dose. Statistical comparisons between the different time points at each ROI were identical to Fig. 5.5.

## 5.6. Discussion

This study investigated the dose dependence of  $\text{Mn}^{2+}$  on the  $T_1$  relaxation time in the rat brain following SC administration of  $\text{Mn}^{2+}$ . The uptake of  $\text{Mn}^{2+}$  into the cells was evaluated by monitoring the temporal evolution of: 1.) MEMRI signal enhancement, 2.)  $T_1$  relaxation times, and 3.) change in  $\Delta R_1$  in three different regions of the rat brain: cortex, sub-cortical region, and the caudate nucleus (Fig. 5.1). In this study, the  $r_1$  and  $r_2$  relaxivities of  $\text{MnCl}_2$  were measured (Fig. 5.2). To our knowledge, these values have not been reported at 2 T. The values are consistent with the extrapolated values mentioned in previous studies (1,29).

Due to the high doses of  $\text{Mn}^{2+}$  administered in this study, there is limited transport of  $\text{Mn}^{2+}$  across the BBB; thus,  $\text{Mn}^{2+}$  primarily enters the CSF via the choroid plexus and diffuses in the proximity of the ventricles into the sub-cortical region (sub-cortical region and caudate nucleus ROIs). With time,  $\text{Mn}^{2+}$  diffuses throughout the brain and eventually reaches the cortex. This is clearly evident in the enhanced regions across the three brain slices in Fig. 5.3. However, the amount of  $\text{Mn}^{2+}$  that reaches the cortex is less compared to the amount of  $\text{Mn}^{2+}$  that is available near the sub-cortical region. Thus, greater  $\text{Mn}^{2+}$  uptake occurs in the sub-cortical region than the cortex for all the SC  $\text{Mn}^{2+}$  doses administered causing greater shortening of the  $T_1$  relaxation time in the sub-cortical region and caudate nucleus ROIs than the cortex ROI (Fig. 5.5). The enhancement

observed with a very high SC dose of  $\text{Mn}^{2+}$  (300 mg/kg) at the 6 h time point in Fig. 5.3 is in agreement with previous studies that administered  $\text{Mn}^{2+}$  using SC injection at much lower doses (7,8,30).

SC injection of  $\text{Mn}^{2+}$  resulted in a dose-dependent behavior of MEMRI contrast (Fig. 5.4) and  $T_1$  relaxation time (Fig. 5.6) in the rat brain. Due to a greater presence of  $\text{Mn}^{2+}$  near the sub-cortical region than the cortex, the sub-cortical region and caudate nucleus ROIs showed greater significant differences in  $T_1$  relaxation times between the  $\text{Mn}^{2+}$  doses than the cortex ROI (Table 2). Proximity of the sub-cortical region and caudate nucleus ROIs to the ventricles exposed them to the bulk of  $\text{Mn}^{2+}$  that diffused from the choroid plexus into the CSF in the ventricles resulting in a significant dose effect.

The dose dependent behavior of MEMRI contrast in this study is consistent with results from other studies. A study in the mouse brain at 11.7 T observed a similar dose-dependent behavior of  $T_1$  relaxation times in different brain regions after IV injection of  $\text{Mn}^{2+}$  (5). Both studies showed significant decreases in  $T_1$  relaxation times with increasing  $\text{Mn}^{2+}$  dose indicating a route-independent dependence of  $\text{Mn}^{2+}$  dose on  $T_1$  relaxation times (Table 2 and Fig. 5.2b in (5)). Another study in the mouse brain at 9.4 T reported a 25% decrease in  $T_1$  relaxation times in the cortex region by the 72 h time point using SC injection of 200 mg/kg of  $\text{Mn}^{2+}$  (2), while we observed a 30% decrease in the cortex ROI with SC injection of 300 mg/kg of  $\text{Mn}^{2+}$  at the same time point. Our

findings are consistent with the fact that a larger dose of  $\text{Mn}^{2+}$  causes a greater decrease in  $T_1$  relaxation time.

At 2 T, a study was done in the rat brain which reported  $T_1$  relaxation times during postnatal development; at 24 h post-IV  $\text{Mn}^{2+}$  injection of 175 mg/kg, they reported  $T_1$  relaxation time of  $860 \pm 40$  ms in the cortex of 31-day old rats (6). Our study recorded  $T_1$  relaxation times of  $895 \pm 28$  ms at 24 h post-SC  $\text{Mn}^{2+}$  injection of 150mg/kg and  $828 \pm 69$  ms at 24 h post-SC  $\text{Mn}^{2+}$  injection of 300 mg/kg. Even though the route of administration and the age of rats were different in our study, the  $T_1$  relaxation time at 175 mg/kg of IV- $\text{Mn}^{2+}$  injection falls within the boundary of the  $T_1$  relaxation times at 150 mg/kg and 300 mg/kg of SC-  $\text{Mn}^{2+}$  injection, conforming to consistent dose-dependent behavior. This comparison attests to the validity of our relaxation times, not just in terms of percent change but the actual value of the  $T_1$  relaxation times as well, since this study and our study were both done at 2 T.

Following SC injection,  $\text{Mn}^{2+}$  gets released into the systemic circulation at a slow rate of absorption thus avoiding the 'first wave' of elimination via the hepatic system (25). Thus, uptake of  $\text{Mn}^{2+}$  by cells also occurs at a slow rate. This is demonstrated in Fig. 5.3 where enhancement of the brain slices continues to increase until the 72 h time point, which is consistent with the reduction in  $T_1$  relaxation times in Fig. 5.5 at the same time point. SC delivery of  $\text{Mn}^{2+}$  also causes the  $\text{Mn}^{2+}$  to remain within the cells for a longer period of time before

being eliminated. After reaching a maximum level of enhancement in the brain slices by the 72 h time point (Fig. 5.3), the enhancement persisted up to the 168 h time point. This is also supported by the statistical insignificance between the  $T_1$  relaxation times at the 72 h and the 168 h time point (Table 1). This observation is consistent with a toxicology study which reported maximum  $Mn^{2+}$  concentration levels in the rodent brain even at the 168 h time point following SC injection of  $MnCl_2$  (31).

The results of prolonged enhancement obtained with SC injection of  $Mn^{2+}$  are contrary to the results of Aoki *et al.* (32) who injected  $Mn^{2+}$  via the IV route. When  $Mn^{2+}$  was administered IV at the highest non-toxic IV dose of 175 mg/kg, maximum enhancement was observed at the 24 h time point after which there was a decrease in enhancement by the 96 h time point (32). A high-dose  $Mn^{2+}$  injection directly into the plasma creates a steep concentration gradient between plasma and bile resulting in an immediate elimination of  $Mn^{2+}$  in the bile. As a result, lower amounts of  $Mn^{2+}$  reach the brain and thereby reside there for a shorter period of time before being eliminated by the cells. A similar result was observed when 50 $\mu$ L of 25 mM  $MnCl_2$  was administered via intrathecal injection in the mouse brain (10). Maximum enhancement occurred at the 48 h time point, and by the 96 h time point a decline in enhancement was observed. SC administration of  $Mn^{2+}$ , on the other hand, results in maximum enhancement that persists up to at least 168 h after  $Mn^{2+}$  injection.



To compare uptake of  $\text{Mn}^{2+}$  across studies at different magnet strengths and with different administered doses of  $\text{Mn}^{2+}$ ,  $\Delta R_1$  graphs can be used for quantitative comparison (Fig. 5.7). An MEMRI study showed that a greater enhancement in the brain could be achieved using the intrathecal injection as opposed to the IV or IP injection route with an intact BBB (10). They reported maximum  $\Delta R_1$  values of  $0.29 \pm 0.13 \text{ s}^{-1}$  and  $0.49 \pm 0.30 \text{ s}^{-1}$  in the frontal cortex and basal ganglia, respectively, which were achieved 3-4 days after intrathecal injection of  $50\mu\text{L}$  of  $25 \text{ mM MnCl}_2$  and declined gradually thereafter. The volume and concentration combination of the injection used was optimum to avoid animal mortality. With the SC injection of  $\text{Mn}^{2+}$  at a dose of  $300 \text{ mg/kg}$ , our calculated  $\Delta R_1$  values were approximately 1.5 times greater in the cortex ROI (compared to the frontal cortex) and approximately two times greater in the sub-cortical region ROI (compared to basal ganglia). Moreover, even after 7 days, there was no indication of a decline in the  $\Delta R_1$  values across all ROIs using SC injection. Thus, a high dose SC injection of  $\text{Mn}^{2+}$  can achieve greater enhancement in the brain for a longer duration of time than that obtained with intrathecal injection.

## 5.7. Conclusion

This study showed a dose-dependent response of  $\text{Mn}^{2+}$  on  $T_1$  relaxation times in the cortex, sub-cortical region, and caudate nucleus ROIs in the rat brain following SC injection of  $\text{Mn}^{2+}$  which was comparable to a previous dose

response study using IV injection of  $Mn^{2+}$ . This study also suggests that SC administration of  $Mn^{2+}$  at a high dose (near  $LD_{50}$  value) can deliver a greater amount of  $Mn^{2+}$  than the highest non-toxic dose possible with intrathecal injection in the rodent brain. SC administration of  $Mn^{2+}$  can also lead to prolonged enhancement in the brain than IV administration since SC route avoids the immediate elimination of  $Mn^{2+}$  from plasma via bile upon injection which occurs during IV injection. A high dose SC  $Mn^{2+}$  injection releases  $Mn^{2+}$  in the plasma at a slow rate, thus avoiding systemic toxic effects; the same high dose  $Mn^{2+}$  injection via IV route releases the entire dose directly into the plasma which can lead to cardiac dysfunction. The dose dependence and temporal dynamics of  $Mn^{2+}$  after SC injection can prove useful for longitudinal *in vivo* studies that require brain enhancement to persist for a long period of time to visualize neuroarchitecture like in Alzheimer's disease, Parkinson's disease, amyotrophic lateral sclerosis, and other neurodegenerative diseases.

## 5.8. Acknowledgements

We are thankful to Dr. Peter Grigg, Dr. Alan Koretsky, and Dr. Alexei Bogdanov for reviewing this paper.

## References

1. Silva AC, Lee JH, Aoki I, Koretsky AP. Manganese-enhanced magnetic resonance imaging (MEMRI): methodological and practical considerations. *NMR Biomed* 2004;17(8):532-543.
2. Kuo YT, Herlihy AH, So PW, Bhakoo KK, Bell JD. In vivo measurements of T1 relaxation times in mouse brain associated with different modes of systemic administration of manganese chloride. *J Magn Reson Imaging* 2005;21(4):334-339.
3. Wadghiri YZ, Blind JA, Duan X, Moreno C, Yu X, Joyner AL, Turnbull DH. Manganese-enhanced magnetic resonance imaging (MEMRI) of mouse brain development. *NMR Biomed* 2004;17(8):613-619.
4. Bissiga D, Berkowitz BA, b. Manganese-enhanced MRI of layer-specific activity in the visual cortex from awake and free-moving rats. *NeuroImage* 2009;44(3):627-635.
5. Lee JH, Silva AC, Merkle H, Koretsky AP. Manganese-enhanced magnetic resonance imaging of mouse brain after systemic administration of MnCl<sub>2</sub>: dose-dependent and temporal evolution of T1 contrast. *Magn Reson Med* 2005;53(3):640-648.
6. de Sousa PL, de Souza SL, Silva AC, de Souza RE, de Castro RM. Manganese-enhanced magnetic resonance imaging (MEMRI) of rat brain after systemic administration of MnCl<sub>2</sub>: changes in T1 relaxation times during postnatal development. *J Magn Reson Imaging* 2007;25(1):32-38.
7. Watanabe T, Natt O, Boretius S, Frahm J, Michaelis T. In vivo 3D MRI staining of mouse brain after subcutaneous application of MnCl<sub>2</sub>. *Magn Reson Med* 2002;48(5):852-859.
8. Watanabe T, Radulovic J, Boretius S, Frahm J, Michaelis T. Mapping of the habenulo-interpeduncular pathway in living mice using manganese-enhanced 3D MRI. *Magn Reson Imaging* 2006;24(3):209-215.

9. Watanabe T, Frahm J, Michaelis T. Myelin mapping in the living mouse brain using manganese-enhanced magnetization transfer MRI. *Neuroimage* 2010;49(2):1200-1204.
10. Liu CH, D'Arceuil HE, de Crespigny AJ. Direct CSF injection of MnCl<sub>2</sub> for dynamic manganese-enhanced MRI - Liu - 2004 - *Magnetic Resonance in Medicine - Wiley Online Library*. *Magn Reson Med* 2004;51(5):978-987.
11. Gallez B, Demeure R, Baudalet C, Abdelouahab N, Beghein N, Jordan B, Geurts M, Roels HA. Non Invasive Quantification of Manganese Deposits in the Rat Brain by Local Measurement of NMR Proton T1 Relaxation Times. *NeuroToxicology* 2001;22(3):387-392.
12. Crossgrove J, Zheng W. Manganese toxicity upon overexposure. *NMR Biomed* 2004;17(8):544-553.
13. Murphy VA, Wadhvani KC, Smith QR, Rapoport SI. Saturable transport of manganese(II) across the rat blood-brain barrier. *J Neurochem* 1991;57(3):948-954.
14. Rabin O, Hegedus L, Bourre JM, Smith QR. Rapid brain uptake of manganese(II) across the blood-brain barrier. *J Neurochem* 1993;61(2):509-517.
15. Catterall W, Perez-Reyes E, Snutch T, Striessnig J. International Union of Pharmacology. XLVIII. Nomenclature and Structure-Function Relationships of Voltage-Gated Calcium Channels. *Pharmacological Reviews* 2005;57(4):411-425.
16. Sloot W, Gramsbergen J. Axonal transport of manganese and its relevance to selective neurotoxicity in the rat basal ganglia. *Brain Res* 1994;657(1-2):124-132.
17. Drapeau P, Nachshen DA. Manganese fluxes and manganese-dependent neurotransmitter release in presynaptic nerve endings isolated from rat brain. *J Physiol* 1984;348:493-510.

18. Lin YJ, Koretsky AP. Manganese ion enhances T1-weighted MRI during brain activation: an approach to direct imaging of brain function. *Magn Reson Med* 1997;38(3):378-388.
19. Naritaa K, Kawasakia F, Kita H. Mn and Mg influxes through Ca channels of motor nerve terminals are prevented by verapamil in frogs. *Brain Research* 1990;510:289-295.
20. Dodd CA WD, Klein BG. Basal Ganglia accumulation and motor assessment following manganese chloride exposure in the C57BL/6 mouse. *Int J Toxicol* 2005;24(6):389-397.
21. Gerber GB LA, Hantson P. Carcinogenicity, mutagenicity and teratogenicity of manganese compounds. *Crit Rev Oncol Hematol* 2002;42(1):25-34.
22. Aoki I, Naruse S, Tanaka C. Manganese-enhanced magnetic resonance imaging (MEMRI) of brain activity and applications to early detection of brain ischemia. *NMR Biomed* 2004;17(8):569-580.
23. Bock NA, Paiva FF, Silva AC. Fractionated manganese-enhanced MRI. *NMR Biomed* 2008;21(5):473-478.
24. London RE TG, Gabel SA, Funk A. Magnetic resonance imaging studies of the brains of anesthetized rats treated with manganese chloride. *Brain Res Bull* 1989;23(3):229-235.
25. Bertinchamps AJ, Miller ST, Cotzias GC. Interdependence of routes excreting manganese. *Am J Physiol* 1966;211(1):217-224.
26. Chuang KH, Koretsky A. Improved neuronal tract tracing using manganese enhanced magnetic resonance imaging with fast T(1) mapping. *Magn Reson Med* 2006;55(3):604-611.
27. Paxinos G, Watson, C. *The Rat Brain in Stereotaxic Coordinates*: Academic Press, San Diego; 1998.
28. Rasband W. ImageJ. Bethesda, Maryland, USA: <http://rsb.info.nih.gov/ij/>; 1997-2006.

29. Caravan P, Farrar CT, Frullano L, Uppal R. Influence of molecular parameters and increasing magnetic field strength on relaxivity of gadolinium- and manganese-based T1 contrast agents. *Contrast Media Mol Imaging* 2009;4(2):89-100.
30. Watanabe T, Frahm J, Michaelis T. Functional mapping of neural pathways in rodent brain in vivo using manganese-enhanced three-dimensional magnetic resonance imaging. *NMR Biomed* 2004;17(8):554-568.
31. Gianutsos G, Seltzer MD, Saymeh R, Wu ML, Michel RG. Brain manganese accumulation following systemic administration of different forms. *Arch Toxicol* 1985;57(4):272-275.
32. Aoki I, Wu Y-JL, Silva AC, Lynch RM, Koretsky AP. In vivo detection of neuroarchitecture in the rodent brain using manganese-enhanced MRI. *NeuroImage* 2004;22:1046-1059.

**CHAPTER VI**

**MAGNETIC RESONANCE**

**IMAGING OF EPIDERMAL**

**GROWTH FACTOR RECEPTOR**

**EXPRESSION IN AN ORTHOTOPIC**

**HUMAN GLIOMA MODEL USING**

**TARGETED MR SIGNAL-**

**AMPLIFYING ENZYMES**

# Magnetic Resonance Imaging of Epidermal Growth Factor Receptor Expression in an Orthotopic Human Glioma Model Using Targeted MR Signal-Amplifying Enzymes

Mohammed Salman Shazeeb<sup>1,5</sup>, Christopher H. Sotak<sup>1-3</sup>, Michael DeLeo III<sup>3</sup>,

Alexei Bogdanov, Jr<sup>3,4</sup>

Departments of <sup>1</sup>Biomedical Engineering and <sup>2</sup>Chemistry & Biochemistry

Worcester Polytechnic Institute

Worcester, MA 01609

Departments of <sup>3</sup>Radiology and <sup>4</sup>Cell Biology and <sup>5</sup>Graduate School of Biomedical  
Sciences

University of Massachusetts Medical School

Worcester MA 01655

## **6.1. Preface**

This study was done to target EGF receptors in human glioma model using MR signal-amplifying enzymes. My contributions to this work were collection of the NMR data, reconstructing images, MATLAB programming for image analysis, development of mathematical models and statistical analysis of contrast washout kinetics, and principal authorship in the writing of the manuscript. This work has been submitted to Cancer Research (2010, in review).



## 6.2. Abstract

The imaging of EGF receptors in brain tumors is essential for visualizing overexpression of EGFRvIII variant as a signature of highly aggressive gliomas and for identifying patients that would benefit from anti-EGFR therapy. We tested a novel pretargeting imaging approach that includes the administration of humanized monoclonal antibody (anti-EGFR mAb, EMD72000) linked to enzymes with complementing activities that use a low-molecular weight paramagnetic molecule (diTyr-GdDTPA) as a reducing substrate administered following the mAb conjugates. The conjugates reacted with both membrane-isolated wild-type EGFR and EGFRvIII. However, the conjugates bound primarily to EGFRvIII-expressing cells (Gli36 $\Delta$ EGFR) and not to EGFRwt-expressing Gli36 cells. We analyzed the differential magnetic resonance (MR) tumor signal decay *in vivo* using orthotopic models of human glioma. We hypothesized that diTyr-GdDTPA becomes enzyme-activated and retained due to the binding to tissue proteins. The patterns of MR signal change following substrate administration revealed differences in elimination patterns that allowed distinguishing between non-specific and specific modes of MR signal decay. We observed biexponential signal decay in tumors only if Gli36 $\Delta$ EGFR tumor-bearing animals were preinjected with EGFR-targeted mAb conjugates. The endpoint MR *in vivo* imaging after preinjection of conjugates showed detailed images of tumors, which correlated with immunohistochemical detection of EGFR expression.

### 6.3. Introduction

Epidermal growth factor receptor (EGFR) is a member of ErbB receptor kinase family, which is overexpressed predominantly in non-small cell lung cancer, colorectal and squamous carcinomas as well as in glioma cells (1-3). EGFR plays an important role in cancer pathogenesis by readily undergoing ligand-dependent dimerization followed by autophosphorylation of the EGFR dimer resulting in downstream proliferative and anti-apoptotic signaling in cancer cells (4). Wild-type EGFR<sub>wt</sub> overexpression closely correlates with receptor gene amplification and has been previously established as a significant and independent unfavorable predictor of overall survival of glioblastoma patients (5). The truncated EGFR<sub>vIII</sub> variant of the receptor is constitutively activated and is a hallmark of aggressive gliomas (6,7). Since EGFR level is low or even undetectable in normal brain cells, this receptor is an appealing molecular target not only for molecular therapies but also as a potential marker molecule for visualization and characterization of gliomas during their response to therapy. Several recombinant monoclonal antibodies (mAbs) have been developed during the past decade for achieving specific targeting of the N-terminal extracellular domain III of EGFR with the resultant inhibition of EGF binding and/or receptor dimerization (8-10). Anti-EGFR monoclonal antibodies (11,12) and EGF ligand (13,14) have recently been suggested for imaging of EGFR expression using near-infrared fluorescence. Unlike *in vivo* imaging of fluorescence, MRI does not suffer from the drawback of limited depth penetration and scattering of light.

However, the sensitivity of MRI to the local molar concentration of contrast agent (CA) is orders of magnitude lower than fluorescence or radionuclide imaging, which limits applicability of MRI for receptor imaging (15-17). Proton MR receptor imaging relies on the ability of CAs associated with the receptor site to shorten relaxation times of nearby water molecules. The number of CA molecules, e.g. chelated paramagnetic cations that can be used for direct labeling of mAbs – while maintaining the appropriate binding affinity of mAbs to the target site – is usually not sufficient for generating adequate MR contrast. Other studies circumvented the problem of insufficient sensitivity by coating iron oxides with mAbs (18-22), or by using gadolinium (Gd)-based targeted micelles (23) and dendrimers (24). MRI sensitivity is thus increased due to either clustering of many Gd cations or, alternatively, due to high superparamagnetism of iron oxide. However, linking of nano-sized CAs to antibodies can result in a decrease in tissue penetration after extravasation in tumors and in an increase of non-specific MR signal (25,26).

Several studies have looked into alternate use of mAbs for imaging tumor-associated receptors using contrast-enhanced MRI (27-29). For example, a pre-targeting technique has been suggested for enhancing mammary adenocarcinomas by injecting Gd-labeled avidin (25) or dendrimers (29) for achieving specific association with HER-2/*neu*-bound biotinylated mAb (trastuzumab) (28). We have previously developed a novel pre-targeting approach based on an enzyme-mediated amplification of MR signal as a result of

accumulation of small molecular weight, Gd-labeled substrates at the target site (30). The advantage of this imaging strategy is that small CA molecules accumulate in brain tumors at a faster rate and with lesser heterogeneity than macromolecular agents (26). The resultant target-to-background contrast ratio can potentially be achieved earlier than in the case of nanoparticle or dendrimer pretargeting due to much faster elimination of the non-reacted CA substrate from the circulation as compared to non-bound Gd-labeled macromolecules or nanoparticles. The other potential advantage is in achieving higher MR signal due to the Gd relaxivity increase that results from the enzyme-activated substrate binding to proteins (31,32). The increase in relaxivity depends on magnetic field strength and is strongly contributing to MR signal increase at 1.0-2.0 Tesla.

The main goals of the current work were to: 1) test *in vitro* and *in vivo* tumor-pretargeted enzyme-mediated amplification system using cells expressing either EGFRwt, or both EGFRwt and EGFRvIII; 2) to compare *in vivo* kinetics of MR signal decay after the administration of Gd-labeled peroxidase substrate (diTyr-GdDTPA) with or without pre-targeting of the EGF receptor with mAb conjugated to a signal-amplification pair of enzymes.

## 6.4. Materials and Methods

### 6.4.1 Syntheses of Reagents and Cell Culture Experiments

#### 6.4.1.1. Synthesis of DTPA Bis-tyramide

One mmol DTPA-bis (anhydride) was reacted with 2.2 mmol tyramine in the presence of triethylamine in dry dimethylformamide for 48h at room temperature followed by purification by repeated acetone precipitation from 50% methanol. The resultant compound was analyzed using  $^1\text{H}$  NMR and mass-spectrometry (FAB-MS: found: 632  $[\text{M}+\text{H}]^+$ , theoretical m/e, 631.29). The gadolinium salt of DTPA bis-tyramide (diTyr-DTPA(Gd)) was prepared (Fig. 6.1) by dissolving 0.1 mmol of DTPA bis-tyramide in 0.5M trimethylammonium citrate (pH 6) and adding 1.05 eq.  $\text{GdCl}_3$  hexahydrate under argon in the dark for 72 h at room temperature. The solution was dried in vacuum, solubilized in water, and purified using reversed-phase HPLC.

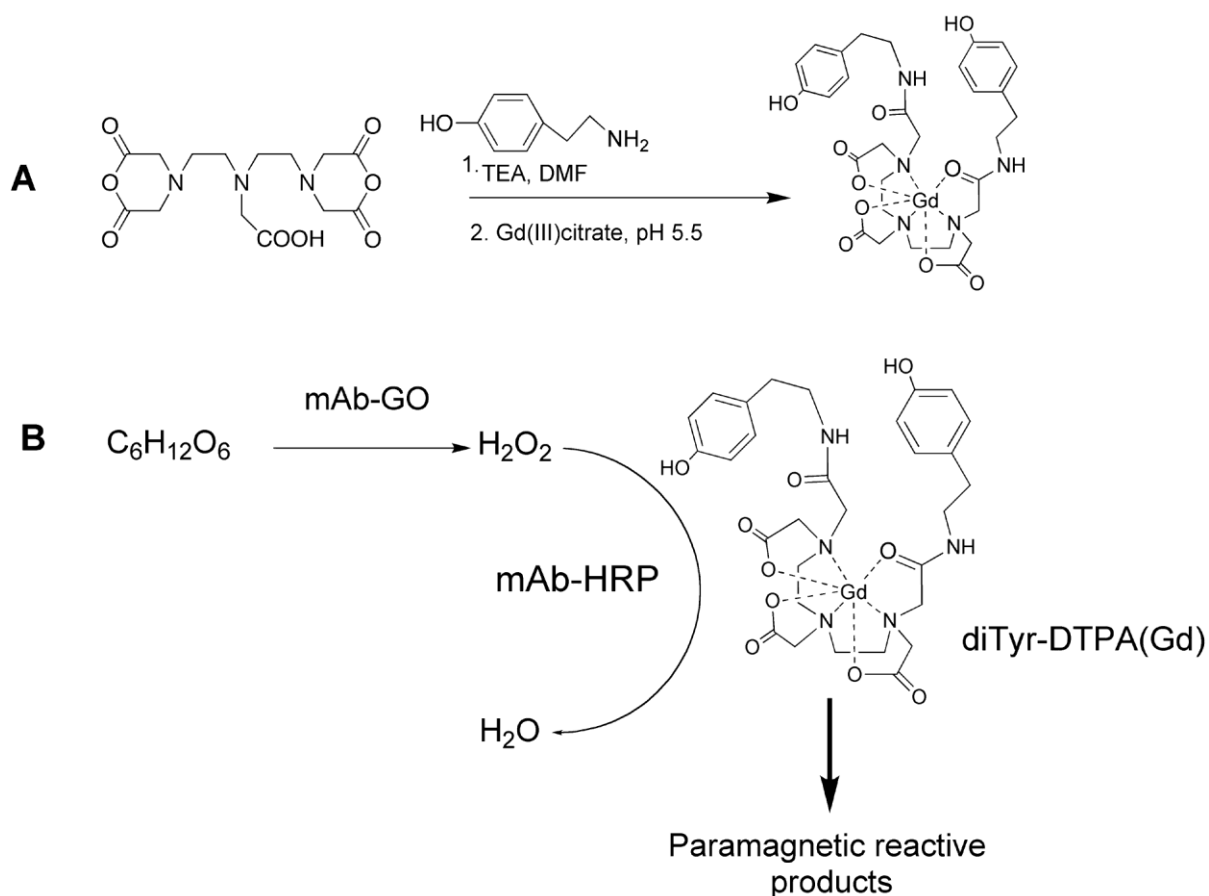


**Figure 6.1 – A)** Synthesis of peroxidase-reducing paramagnetic substrate di(tyramido)-DTPA(Gd); **B)** Reaction of diTyr-GdDTPA with the peroxidase/glucose oxidase enzyme pair conjugated to anti-EGFR mAb.

#### 6.4.1.2. Synthesis of Monoclonal Antibody Conjugates

Conjugates were synthesized and purified as described in (30). Humanized anti-EGFR EMD72000 (humanized mAb 425 (33)) and anti-EpCAM were from Merck KGaA, Darmstadt, Germany. Antibodies were dialyzed against 10 mM PBS, pH 7.5 before use. EMD72000 (60  $\mu$ M in 0.1M sodium bicarbonate

pH 8) was covalently modified using SANH (Thermo-Fisher Corp.) in DMF (final concentration - 300 $\mu$ M) for 30 min at room temperature. The modified antibody was purified on Sephadex G25m spin-columns (PD10, GE Healthcare BioSciences Corp., Piscataway NJ) equilibrated with 0.1 M sodium acetate, pH 4.9. Recombinant glucose oxidase (GOX) from *Aspergillus niger* (EMD Merck-Calbiochem), 120  $\mu$ M in 0.1 M sodium bicarbonate pH 8, (25 nmol), was modified by adding 100 nmol C6-SFB (Thermo-Fisher Corp.). After 30 min incubation, GOX-formyl benzoate was purified as described above. Horseradish peroxidase (100 nmol, Type IX, Sigma) in 0.25 ml of 0.1 M sodium acetate, pH 5 was oxidized using 10-molar excess of sodium periodate for 30 min. The reaction was stopped by adding 0.1 M glycerol (final concentration) followed by purification in Sephadex G25m spin-columns. The oxidized peroxidase was incubated in the presence of 0.1 M hydroxylamine for 3 h and purified using Sephadex G25m chromatography. Conjugation of formylbenzoyl groups to peroxidase was performed by using a 10-fold molar excess of C6-SFB. The number of covalently conjugated 4-formylbenzoyl groups was determined by spectrophotometry at 350 nm ( $\epsilon = 18000 \text{ M}^{-1} \text{ cm}$ ). Conjugated 4-hydraziniumnicotinate was determined by using 4-nitrobenzaldehyde and measuring absorbance at 380 nm ( $\epsilon = 22000 \text{ M}^{-1} \text{ cm}^{-1}$ ). Protein concentrations were determined by using Micro BCA assay (Pierce). 4-hydraziniumnicotinate-modified antibody (final concentration – 2 mg/ml) were combined with the modified enzymes at molar ratios of 1:2 (antibody: enzyme) in 0.1 M sodium

acetate, 0.1% Tween-20, pH 4.9. The incubation was completed in 4 h. To block the remaining aldehyde groups, 2-hydrazinopyridine was added at a final concentration of 0.1 mM. The reaction mixture was separated using Superdex 200 columns (GE-Healthcare) in 0.1 M ammonium acetate, pH 7.0. The peaks that eluted before 200 kD protein and contained peroxidase or glucose oxidase activity were pooled separately, concentrated and washed with PBS using Ultracel-50 membrane concentrators (Millipore, Billerica MA). Concentrated conjugates were analyzed using 4-15% gradient SDS-PAGE.

#### **6.4.2. In Vitro Cell Culture Experiments**

Gli36 $\Delta$ EGFR (34) and wild-type Gli36wt cells (35) were propagated on 10%FCS 90% RPMI1640 in the presence of penicillin/streptomycin and 0.5  $\mu$ g/ml puromycin (Gli36 $\Delta$ EGFR). Both cell lines were binding chimeric anti-EGFR antibody (cetuximab, C225) and EMD72000 (Fig. 6.2 A,B). For cross-titration experiments cells were plated in 96 wells and used when confluent. Conjugates were cross-tittered using sequential 2x dilutions (8x8 wells) in 2% FCS in DPBS, pH 7.4 and used in the range of 7.5 – 1000 ng total conjugate (i.e., a mixture of mAb-HRP and mAb-GOX) per well. Cells were incubated with conjugates for 30 min, washed and peroxidase activity associated with the cells was determined at 405 nm using 2 mM ABTS in 5 mM glucose in 50 mM sodium citrate-phosphate buffer, pH 5.7. In some experiments, 2  $\mu$ g of free EMD72000 per well was used



as a competitive inhibitor. Titration of conjugate mixtures in Gli36 $\Delta$ EGFR culture was performed by using dilutions of mAb-HRP/mAb-GOX mixture at 2:1 (w/w ratio). Measurements of longitudinal relaxation time ( $T_1$ ) changes were performed on Bruker Minispec mq20 by using reaction mixtures containing 0.05-0.75 mM diTyr-GdDTPA, 5mM glucose, PBS, pH 7.4 in the presence or in the absence of 1  $\mu$ g conjugate mixture. Cell viability was determined using the XTT technique. Titration data fitting and analysis were performed using GraphPad's Prism4 software (La Jolla, CA).

#### **6.4.2.1. Flow Cytometry and Fluorescence Microscopy**

Flow cytometry and fluorescence of Gli36 $\Delta$ EGFR and Gli36wt cells were performed using 1  $\mu$ g/ml AlexaFluor488-labeled EMD72000 or cetuximab (humanized mAb C225 (36)).

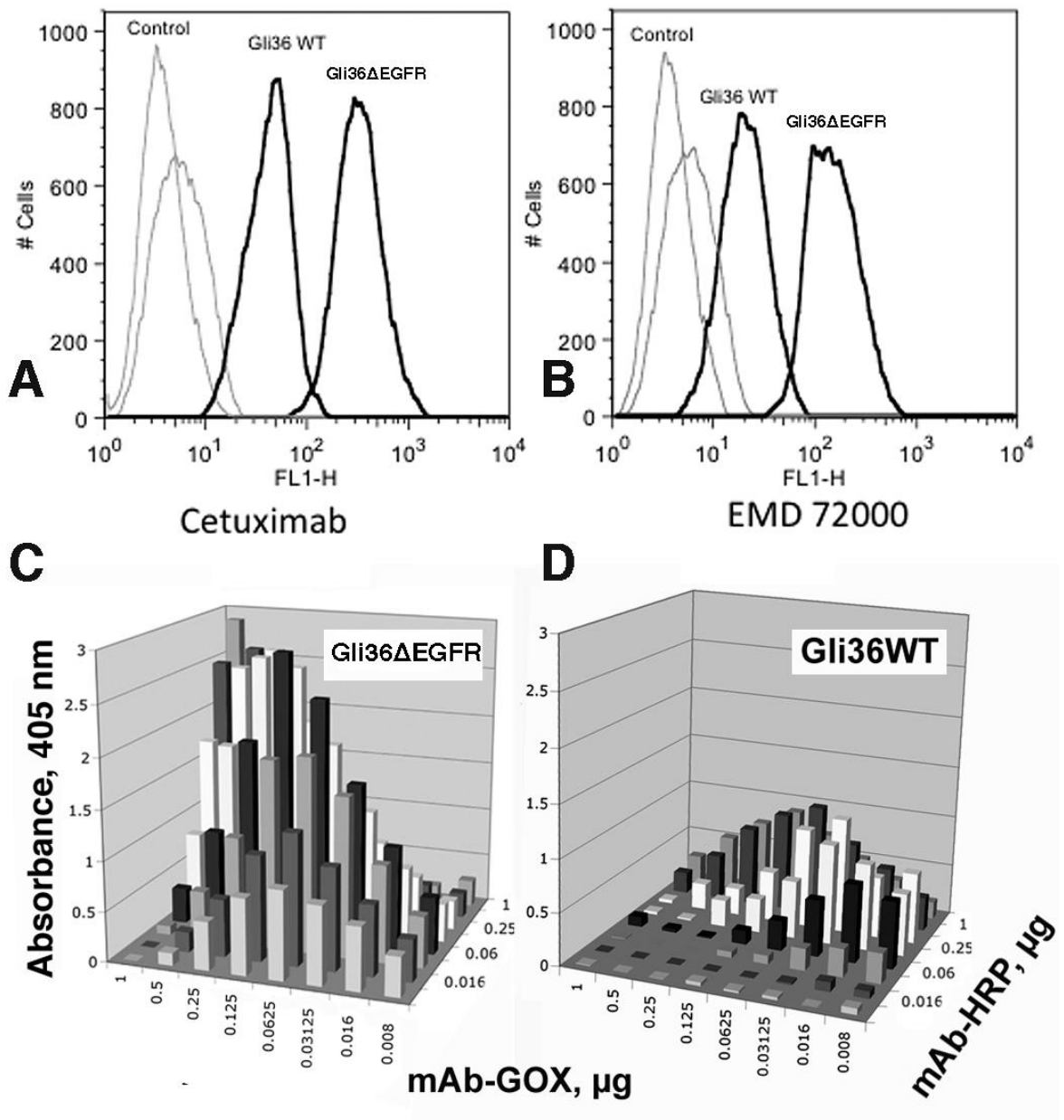


**Figure 6.2** – **A, B** – flow cytometry of Gli36 $\Delta$ EGFR and Gli36wt cells incubated with cetuximab (C225 antibody, **A**) and EMD72000 (**B**). **C, D** – Cross-titration of two mAb EMD72000 conjugates: mAb-HRP and mAb-GOX in live Gli36 $\Delta$ EGFR (**C**) and Gli36wt (**D**) cell cultures using ABTS/glucose for visualization of HRP activity.

#### **6.4.2.2. Internalization Experiments**

Internalization experiments were performed by using mAb-HRP/mAb-GOX conjugate mixture at 2:1 (w/w ratio). Adherent cells in 6-well plates (4 million cells/well) were incubated with conjugate mixtures either at 4<sup>0</sup>C or at 37<sup>0</sup>C. The surface bound conjugates were eluted with 0.5 ml cold glycine solution pH 2.5 for 15 min. The eluate was immediately neutralized with 1M Tris pH 8.0. To extract internalized conjugates 0.5 ml of 1.0% Igepal CA-630 in the presence of protease inhibitors was added to each well and plates were incubated for 15 min. The amount of bound and internalized conjugates were determined by measuring the initial rates of HRP/GOX-coupled ABTS oxidation by adding 5 mM ABTS and 5mM glucose (final concentrations) in sodium citrate, pH 5.5, to the sample aliquots and measuring absorbance at 405 nm over time. The serially diluted conjugate mixture at a constant mAb-HRP:mAb-GOX ratio and known concentrations was used for calibration.

#### **6.4.2.3. Membrane Proteins Extraction From the Cells**

Membrane proteins from Gli36 $\Delta$ EGFR and Gli36WT cells were extracted using CNM compartmental protein extraction kit (BioChain Institute Inc., Hayward, CA) following manufacturer's recommendations. Cells were harvested using TrypLE Express cell detachment solution (Invitrogen Corp. Carlsbad, CA) and washed with PBS buffer. The cells were counted, centrifuged at 1000 RPM

for 5 min and supernatant was removed. A cocktail of protease inhibitors was added to extraction buffers at the recommended concentration before protein extraction. All extraction steps were performed at 4°C.

To the cell pellet ice cold buffer C (2 ml/  $2 \cdot 10^7$  cells) was added. The cells were suspended and rotated using Labquake rotating Micro-Tube mixer for 20 min. Cell mixture was passed ~75 times through a 3 ml syringe fitted with a 28 gauge needle base after removing the needle tip to disrupt the cells. The cell suspension was centrifuged at 15,000 g for 20 min.

The supernatant containing cytoplasmic proteins was transferred to a new tube and saved. The remaining pellet was washed by suspending it in ice cold buffer W (4.0 ml per 20 million cells), rotated for 5 min and centrifuged at 15,000 g for 20 min. The supernatant was discarded and the cell pellet was resuspended in ice cold buffer N at 1.0 ml per 20 million cells and rotated for 20 minutes. Nuclear proteins were recovered by centrifugation at 15,000 g for 20 min. To the remaining pellet, ice cold buffer M at 1.0 ml per 20 million cells was added and tube rotated for 20 min. Cells were spun at 15,000 g for 20 min to recover the membrane proteins in the supernatant. The protein concentration was measured in all the fractions by Micro BCA Protein Assay kit (Thermo Scientific). Fractions were aliquoted and stored at -70°C.

### 6.4.3. Histology

Following the MRI studies, animals were euthanized and their brains were removed. Under a dissecting microscope, histological slices were obtained  $\pm 2$  mm anterior/posterior of the needle track and then embedded in O.C.T. medium. Frozen sections (6  $\mu\text{m}$ ) were treated with acetone: ethanol (1:1,  $-20^{\circ}\text{C}$ ), treated in TBS/EDTA, pH 8 at  $65^{\circ}\text{C}$  for blocking endogenous phosphatase activity and blocked using 2% serum. The sections were incubated with anti-EGFR mouse mAb (Abcam), or anti-HRP mAb (Abcam) followed by anti-mouse alkaline-phosphatase linked antibodies and BCIP/NBT (Roche). Staining for residual peroxidase activity was achieved by using a DAB kit (Vector Labs). Immunofluorescent staining was performed on frozen sections blocked with 2% serum, 0.05% Tween-20, PBS, pH 7.4. AlexaFluor488-labeled EMD72000, Cy3-labeled mouse anti-rat CD31 mAb (clone TLD-3A12, Abcam, Cambridge MA) were used for visualizing EGFR and endothelial CD31 expression, respectively. For detecting HRP in the tissue sections, digoxigenin-labeled mouse anti-HRP mAb (clone 2H11, Abcam, Cambridge MA) was used. Digoxigenin-labeled antibody binding was visualized using custom Cy5.5-labeled anti-digoxigenin  $\text{F(ab')}_2$  (Roche, Indianapolis IN).

#### **6.4.4. Animal Model and Imaging**

All procedures were performed as approved by the Institute Animal Care and Use Committee (IACUC) of the University of Massachusetts Medical School (Worcester, MA).

An orthotopic human glioma xenograft model was obtained by stereotaxically implanting  $1 \cdot 10^5$  Gli36 $\Delta$ EGFR or Gli36WT cells suspended in 3  $\mu$ l of 10% Matrigel<sup>TM</sup> in serum-free RPMI under aseptic conditions at 37°C (2.5 mm posterior to bregma, 2 mm lateral to midline, and depth of 3.5 mm) in the brain of athymic rats (Harlan, 150-200g, n=16) 14 d prior to first imaging session. Throughout imaging the animals were maintained at 37°C and anesthetized using 1.5% isoflurane in a 30% oxygen/70% nitrogen mixture. A 45-mm-diameter, 30-mm-long birdcage RF coil was used. A 26-gauge catheter capped with a needle port was placed in the tail vein for CA administration.

##### **6.4.4.1. MRI Protocol, Pulse Sequences, and Measurements**

MRI measurements were performed using Philips Achieva 3.0T/60 cm bore equipped with 80mT/m actively shielded gradients. To monitor temporal evolution of signal enhancement following CA delivery, multi-slice,  $T_1$ -WT MR images (TR/TE=700/8.2 ms) were acquired at various time points following CA infusion. Other imaging parameters were: slice thickness = 1.5 mm; slice

separation = 0.15 mm; field-of-view = 25.6 mm x 25.6 mm; data acquisition matrix = 256x128, 4 NEX. Two weeks after tumor cell implantation, each animal was imaged on two occasions: on Day 1 (two weeks after tumor cell implantation), a pre-contrast image was acquired followed by IV injection of 0.1 mmol/kg diTyr-GdDTPA. Twenty  $T_1$ -WT images were then acquired continuously over a 2-h period. On Day 2 (the day after Day 1), the animals were first pre-injected with 150  $\mu$ g of mAb-HRP/mAb-GOX mixture at 2:1 (w/w ratio, 0.3 ml) in the tail vein. In a separate group of Gli36 $\Delta$ EGFR tumor animals were preinjected with non-specific antibody conjugates. Five hours later, a pre-contrast image was acquired followed by IV injection of 0.1 mmol/kg diTyr-GdDTPA. Thirty  $T_1$ -WT images were then acquired continuously over a 3-h period. Pre-contrast  $T_2$ -WT images were acquired on both Day 1 and Day 2 to corroborate the presence of tumor observed in the  $T_1$ -WT slices.

#### **6.4.5. Image Analysis**

The temporal evolution of the signal decay in the tumor following infusion of diTyr-GdDTPA was evaluated separately for each of the two groups (Day 1 and Day 2). Depending on the size of the tumor, one to four slices were selected covering the central core region of the tumor at each time point. Using the ImageJ software package (37), a region-of-interest (ROI) was carefully drawn to delineate the boundary of the contrast-enhanced region for each slice. ROIs

were also drawn to distinguish the tumor interface and tumor core regions (Fig. 6.3). The whole ROI was drawn to circumscribe the entire contrast-enhanced region of the tumor visible at the first time point collected after the contrast injection. The core ROI was drawn using a later time point that better depicted the outline of the core region due to the faster signal decay in the core as compared to the interface. The interface ROI was drawn by tracing over the region defined by the difference between the whole ROI and the core ROI. The mean signal intensity values within each of the ROIs were then calculated using ImageJ.

For each animal, the signal intensity data for the core and interface ROIs from each relevant tumor slice was plotted to generate a separate time-series plot for Day 1 (no conjugates) and Day 2 (with conjugates). Due to the heterogeneity of tumor growth and variability in the exact dose of contrast delivered from one animal to another, each signal-intensity time point was normalized relative to the pre-contrast time point for each slice:

$$S_N(t) = \frac{S_{post}(t) - S_{pre}(0)}{S_{pre}(0)} \times 100 \quad [6.1]$$

where  $S_N(t)$  is the normalized signal intensity at time  $t$ ,  $S_{post}(t)$  is the signal intensity at time  $t$ , and  $S_{pre}(0)$  is the signal intensity in the pre-contrast slice.



For each animal, the normalized signal-decay plots for each brain slice from Day 1 and Day 2 were used to calculate signal-decay time constants using a monoexponential and a biexponential model:

$$y_{monoexp}(t) = A_0 \cdot e^{-t/\tau_0} + offset \quad [6.2]$$

$$y_{biexp}(t) = A_1 \cdot e^{-t/\tau_1} + A_2 \cdot e^{-t/\tau_2} \quad [6.3]$$

where  $y_{monoexp}(t)$  and  $y_{biexp}(t)$  are the signal intensities at time  $t$ ,  $A_0$ ,  $A_1$ , and  $A_2$  are the amplitudes of each signal-decay component;  $\tau_0$ ,  $\tau_1$ , and  $\tau_2$  are the signal-decay time constants for the respective models.

For each animal, the normalized signal-decay plots of the core and interface ROIs for each brain slice from Day 1 and Day 2 were fitted with both models. Mean values for  $\tau_0$ ,  $\tau_1$ , and  $\tau_2$  were obtained for the core ROI and the interface ROI for each animal by averaging the respective signal-decay time constants of each ROI from all relevant tumor slices of the same animal. The mean values for  $\tau_0$ ,  $\tau_1$ , and  $\tau_2$  were calculated for each animal on Day 1 and on Day 2. Student's paired  $t$  test was performed on the overall average of the signal-decay time constants from all the animals to check for any significant differences either between the ROIs or between Day 1 and Day 2.

To determine which model (monoexponential or biexponential) better represented the normalized signal-decay data, the  $\chi^2$  statistics for the monoexponential ( $\chi^2_{monoexp}$ ) and biexponential ( $\chi^2_{biexp}$ ) models were compared using an  $F$  test based on a variant of the reduced  $\chi^2$ -squares ratio:

$$F_{(v_{monoexp}-v_{biexp}, v_{biexp})} = \frac{(\chi^2_{monoexp} - \chi^2_{biexp})(v_{monoexp} - v_{biexp})}{\chi^2_{biexp}/v_{biexp}} \quad [6.4]$$

where  $v_{monoexp}$  and  $v_{biexp}$  are the number of degrees of freedom corresponding to  $\chi^2_{monoexp}$  and  $\chi^2_{biexp}$  for the monoexponential and biexponential model, respectively (38). For this study, the  $F$  statistic ratio simplifies to:

$$F_{(1, N-4)} = \frac{(\chi^2_{monoexp} - \chi^2_{biexp})}{\chi^2_{biexp}/(N-4)} \quad [6.5]$$

where  $N$  is the number of data points. This ratio measures how much the additional exponential term in the biexponential model improves the reduced  $\chi^2$  by taking into account the number of parameters in the fitting equation (39). This calculated  $F$  statistic was compared to tabulated values of the  $F$  statistic with 1 and  $N - 4$  degrees of freedom. If the  $F$  statistic was greater than the tabulated  $F$  value for the desired statistical confidence, then the biexponential model was accepted as the better fitting model for the data. If the  $F$  statistic was less than

the tabulated  $F$  value, then the monoexponential model was chosen for fitting the data.  $P$  values less than 0.05 were considered statistically significant.

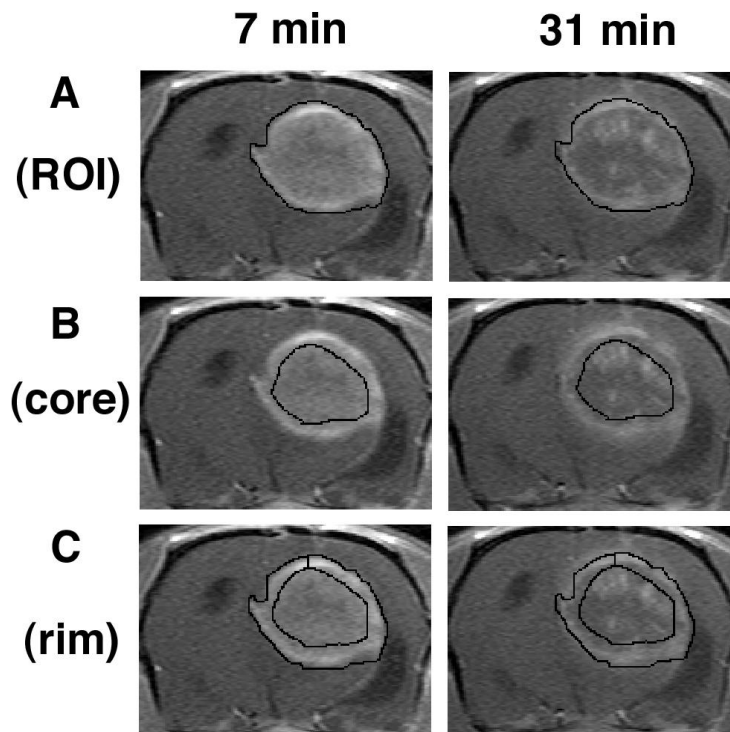


**Fig. 6.3** – Placement of ROI for image analysis. A single tumor slice showing three different ROIs (whole, core, and interface) at 7 min and 31 min post contrast injection drawn using ImageJ is shown as an example. **A** – The whole ROI was drawn around the outline of the enhanced tumor at the first time point collected after the contrast injection; **B** – The core ROI was drawn using a later time point that better depicted the outline of the core due to the faster signal decay in the core as compared to the interface; **C** – The interface ROI was drawn by tracing over the region defined by the difference between the whole ROI and the core ROI.

## 6.5. Results

### 6.5.1. Synthesis and Testing of Targeted MR Signal Amplification System In Vitro

The synthesis of peroxidase (HRP) and glucose oxidase (GOX) conjugates of humanized chimeric antibody (EMD72000, Merck) that catalyze oligomerization of substrate di(tyramido)-DTPA(Gd) (Fig. 6.1) was performed using conditions optimized to facilitate enzyme conjugation via the formation of bisaromatic hydrazones with minimal antibody binding affinity loss (30). Gel electrophoresis of purified conjugates showed the formation of mAb-GOX (290 and 460 kD bands) and mAb-HRP (220 and 400 kD bands) Fig. 6.4A. Since GOX is a two-subunit enzyme, the band corresponding to the 69 kD deglycosylated GOX subunit was present in the SDS-treated mAb-GOX conjugates (Fig. 6.4A, lane 4). The conjugation reaction conditions prevented the formation of cross-linked products that showed no binding specificity to EGFR-positive cells. Immunoblotting experiments showed that optimized conjugates reacted with the same set of receptor variants (i.e. EGFRwt in Gli36wt and EGFRwt/EGFRvIII in Gli36 $\Delta$ EGFR cell lysates) as did the control anti-EGFR antibody (Fig. 6.4B, a2). Overall, Gli36 $\Delta$ EGFR cells contained 2.8-times more mAb-reactive EGF receptors than Gli36wt cells and this result correlated with the results of flow cytometry performed using fluorescent-labeled cetuximab (Fig. 6.2A). However, EMD72000 showed stronger preference for Gli36 $\Delta$ EGFR cells,

i.e. 7.2-times higher binding levels than Gli36wt cells (Fig. 6.2B). Using  $^{111}\text{InDTPA}$ -labeled EMD72000 mAb we determined that Gli36 $\Delta$ EGFR had  $4.6 \pm 0.3 \cdot 10^5$  binding sites/cell as opposed to a control non-binding anti-EpCAM antibody, which showed no detectable binding to the surface of Gli36 $\Delta$ EGFR cells. Optimization of the mAb-HRP:mAb-GOX conjugate ratios was performed to determine the conditions that provide sustainable release of hydrogen peroxide as a result of D-glucose oxidation, without inhibiting the binding of mAb-HRP to cells (Fig. 6.2 B,C). These experiments showed no detectable loss of cell viability observed below 0.25  $\mu\text{g}$  mAb-GOX/well. Cross-titration demonstrated that the highest HRP activity was detectable at the weight ratios of mAb-HRP:mAb-GOX of 1:2 in the range of 0.03(0.06)  $\mu\text{g}$  - 0.25(0.5)  $\mu\text{g}$  of mAb-GOX (mAb-HRP) conjugate/well. In contrast to Gli36 $\Delta$ EGFR, the same dilutions of conjugates added to Gli36wt cells resulted in lower levels of cell-associated enzymatic activity. The titration of mAb-HRP:mAb-GOX conjugate mixture (1:2 w/w) allowed us to determine the effective  $\text{EC}_{50} = 0.21 \mu\text{g}$  (Fig. 6.4C). Finally we studied binding and internalization of optimized conjugate mixtures (Fig. 6.4D) in both cell lines by measuring the complementing enzymatic activities which are essential for MR signal amplification. The differences observed during flow cytometry were further confirmed in these experiments showing that Gli36 $\Delta$ EGFR cells bound 10-times more of mAb conjugate-mediated enzymatic activity than Gli36wt, of which about 25% remained externalized on the surface of the cells.

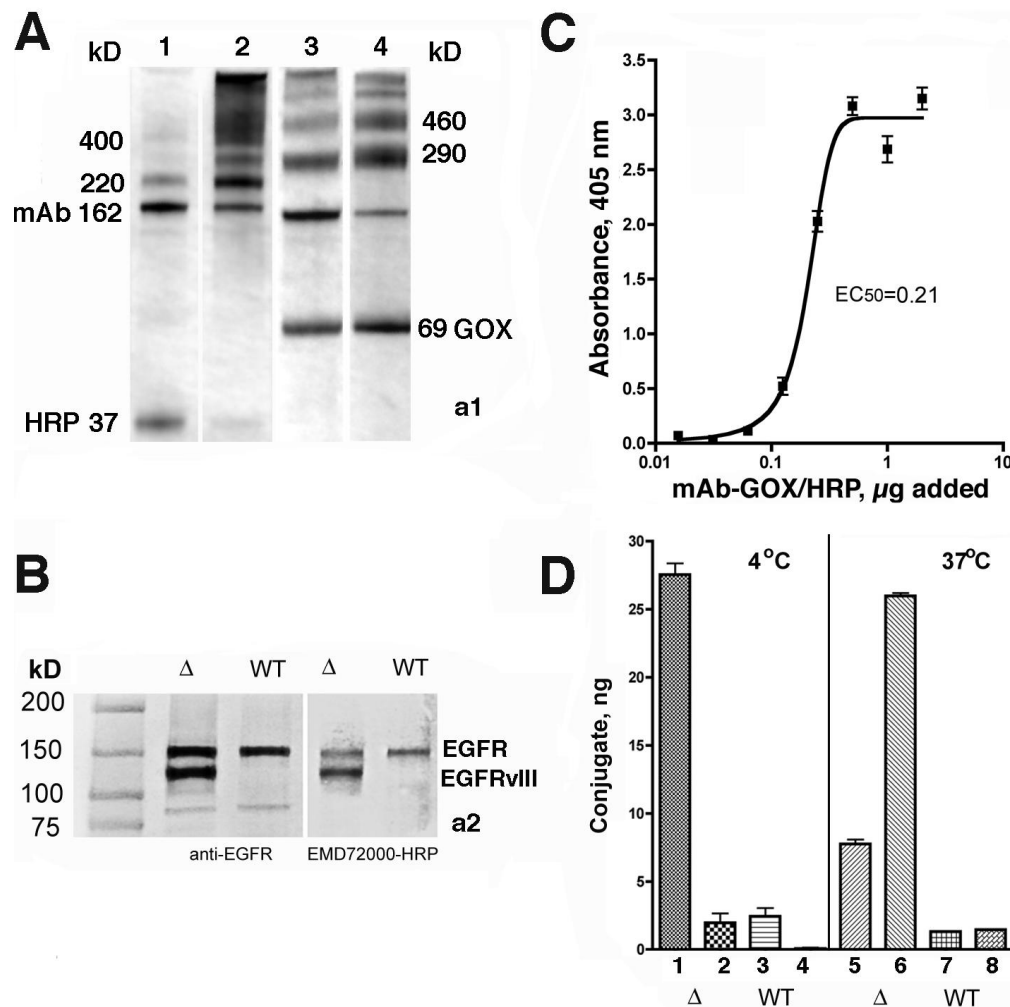


**Figure 6.4 – A)** SDS-PAGE (4-15% gradient) of anti-EGFR mAb (EMD72000) conjugation products or with deglycosylated enzymes: HRP (37 kD, lanes 1 and 2) and with GOX (69 kD subunit, lanes 3, 4) Lanes 1 and 3- before and 2,4- after the purification of conjugates; **B)** immunoblotting of membrane protein fraction isolated from Gli36 $\Delta$ EGFR ( $\Delta$ ) and Gli36wt (WT) cells using mouse monoclonal anti-EGFR antibody C225 or by using HRP-EMD72000 conjugate. EGFR variants are identified on the right; **C)** titration of the mixture of anti-EGFR mAb-HRP and mAb-GOX on Gli36 $\Delta$ EGFR cells at the optimized complementing ratio (1:2, w/w); **D)** binding and internalization of conjugate mixture at the optimized ratio (1:2, w/w) in Gli36 $\Delta$ EGFR ( $\Delta$ ) and Gli36wt (WT) cells 1,3, 5,7 – cell-surface bound fraction of conjugates; 2,4,6,8 – internalized fraction of conjugates.

The HRP/GOX mediated increase of relaxivity in the reaction mixture containing the paramagnetic substrate diTyr-GdDTPA was compared between low external magnetic field and the field of the MR imaging unit that was used for animal experiments. Mixture of conjugates and paramagnetic substrate diTyr-GdDTPA in the presence of D-glucose always resulted in shorter  $T_1$  relaxation times (i.e. higher average longitudinal relaxivity  $r_1$ , Table 6.1). The measured difference in molar relaxivity between the substrate alone and reaction mixtures containing HRP and GOX conjugates was clearly greater at lower magnetic field (0.47T vs. 3T). The reaction resulted in 2.7 times higher  $r_1$  if measured at 0.47T as opposed to 5% increase of  $r_1$  at 3T. The simple addition of proteins in the solution did not result in large relaxivity increases. However, in the presence of both plasma proteins and mAb conjugates, the relaxivity increase was measurable and higher at 3T and showed a 20%  $r_1$  increase.

**Table 6.1**

Changes of longitudinal relaxivity of Gd as a result of conjugate catalytic activity.

Sample components	r1 (average longitudinal relaxivity at 0.47T), 40°C [mM <sup>-1</sup> ·s <sup>-1</sup> ]	Relaxivity increase at 0.47T relative to substrate, %	r1 (average longitudinal relaxivity at 3T), 20°C [mM <sup>-1</sup> ·s <sup>-1</sup> ]	Relaxivity increase at 3T relative to substrate, %
diTyr-GdDTPA <sup>a)</sup>	4.3	-	3.6	-
diTyr-GdDTPA + plasma <sup>b)</sup>	5.0	20	4.0	10
diTyr-GdDTPA + mAb conjugates <sup>c)</sup>	11.8	270	3.8	5
diTyr-GdDTPA + mAb conjugates+plasma <sup>c)</sup>	12.5	290	4.4	20

a) Concentrations used for relaxivity measurements were in the range of 40-250 μM; Goodness of r1 fits – R<sup>2</sup>>0.99. Reaction time – 40 min at 37°C.

b) 50% human or rat plasma solution in heparinized saline was used.

c) 2U/ml HRP and 0.7 U/ml GOX in 5 mM glucose-containing DPBS were used.



### 6.5.2. In Vivo Imaging Experiments and Corroboration

The paramagnetic-substrate-mediated enhancement of human glioma xenografts (Gli36 $\Delta$ EGFR and Gli36wt) was studied using MRI *in vivo*. To account for tumor heterogeneity, the experiments were performed on consecutive days in each animal. On the first day, only the CA substrate was administered (Day 1). On the next day – after CA had been completely eliminated– a second experiment was conducted with pre-injection of mAb conjugates 5 h before injecting the CA (Day 2). Fig. 6.5A shows sequential  $T_1$ -WT rat brain MR images depicting Gli36 $\Delta$ EGFR xenograft enhancement as a function of time post-IV injection of diTyr-GdDTPA. The top row of images shows the temporal washout of diTyr-GdDTPA with no anti-EGFR mAb conjugate pre-treatment (Day 1). The bottom row of images shows the temporal washout of diTyr-GdDTPA at 5 h following pre-treatment with anti-EGFR mAb conjugates (Day 2) in the same slice for the same animal. For both days, the  $T_1$ -WT images showed strong initial enhancement of the tumor within minutes after IV diTyr-GdDTPA injection. However, the initial enhancement, following IV injection of diTyr-GdDTPA, with EGFR-targeted conjugate pre-treatment (Fig. 6.5A: Day 2 – 8 min) was significantly higher than without EGFR-targeted conjugate pre-treatment (Fig. 6.5A: Day 1 – 9 min), especially in the tumor interface region. Moreover, images obtained after the EGFR-targeted conjugate pre-injection (Fig. 6.5A: bottom row) showed more detailed tumor structure with areas of focal enhancement in both the tumor/normal brain interface and core at all time points post-injection of the

paramagnetic MR CA. With or without conjugate pre-treatment, the tumor interface consistently showed higher  $T_1$ -WT signal enhancement compared to the core.

Animals pre-injected with anti-EGFR mAb conjugates displayed a delayed retention of MR CA compared to animals not receiving EGFR-targeted conjugate pre-treatment. Without a pre-injection of anti-EGFR conjugates (Day 1), most of the diTyr-GdDTPA had washed out of both the tumor/normal brain interface and core regions by 117 minutes after IV injection (Fig. 6.5A: top row). However, after allowing the EGFR-targeted conjugates to accumulate in the tumors (Day 2), significant  $T_1$ -WT hyperintensity persisted in the tumor interface at approximately the same time point (Fig. 6.5A: Day 2 – 116 min) post-diTyr-GdDTPA-injection. Furthermore,  $T_1$ -WT enhancement in the tumor interface remained visible for 170 min after CA administration (Fig. 6.5A: Day 2 – 170 min). In contrast to EGFR-targeted conjugates pre-injection, no retention of MR signal was observed when Gli36 $\Delta$ EGFR-bearing animals were pre-injected with anti-EpCAM targeted conjugates which do not bind to Gli36 cells (Fig. 6.5B: compare top and bottom rows).

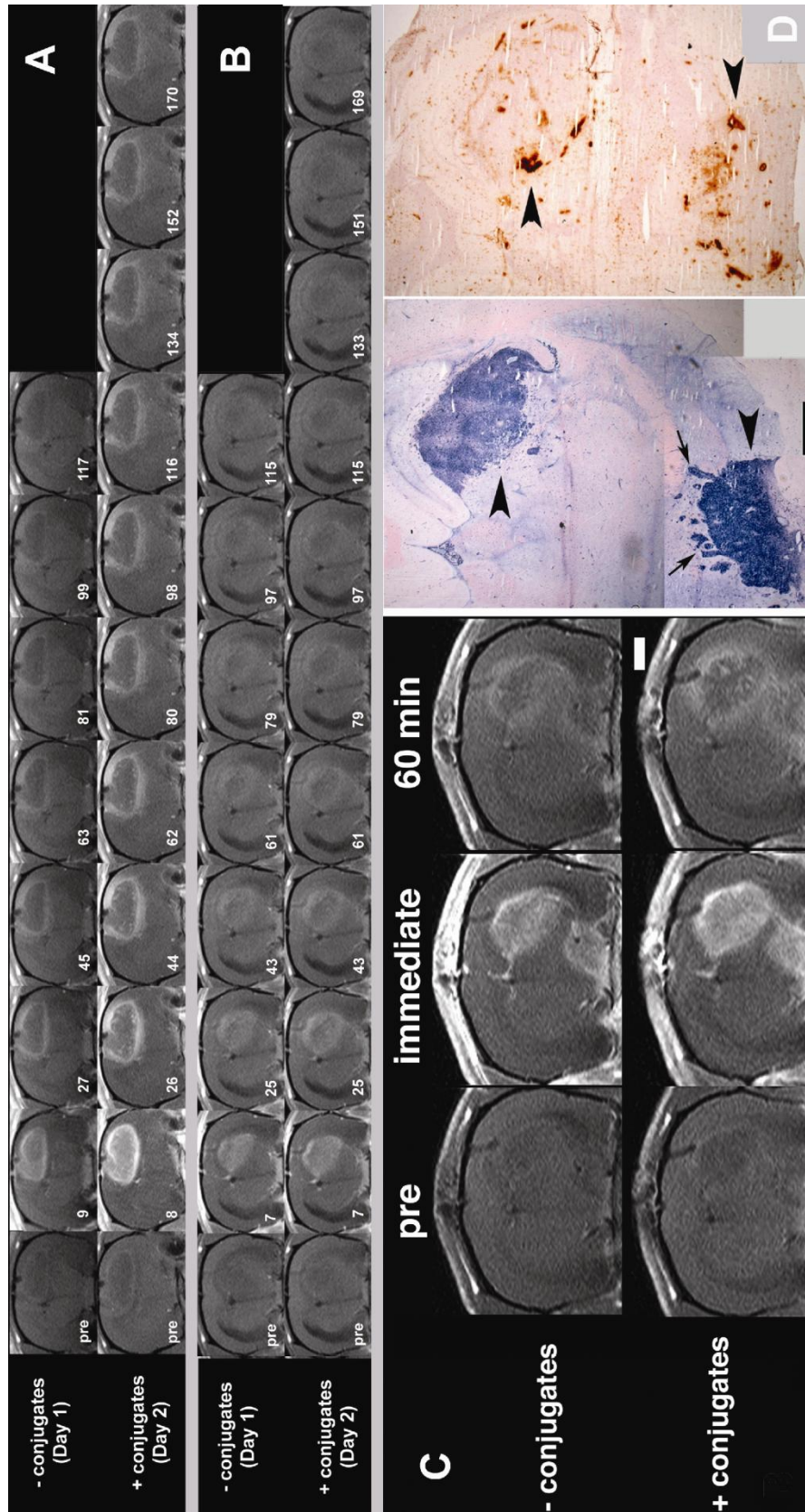


**Figure 6.5 – A)** 3T MR imaging of Gli36 $\Delta$ EGFR human glioma xenografts without and with pre-injection of targeted conjugates.  $T_1$ -WT sequential rat brain images depicting enhancement as a function of time post injection of diTyr-GdDTPA. The top row - temporal washout of diTyr-GdDTPA with no conjugate pre-injection (Day 1). The bottom row - washout of diTyr-GdDTPA following pre-treatment with anti-EGFR conjugates (Day 2) in the same slice for the same animal. Time intervals (in minutes) after the injection of diTyr-GdDTPA are shown below; **B)** MRI and comparative histology. Note distal expansion of the tumor along the ventricle. The images were obtained pre-, immediately post- and 1 h post-CA administration; **C)** Detection of EGFR overexpression using anti-EGFR antibody-digoxigenin/anti-digoxigenin-AP system in the tumor shown in Fig. 6.5B; **D)** Detection of EGFR expression (anti-EGFR-DIG/anti-DIG-AP staining, left; and HRP activity (right) in the same tumor on the parallel sections. HRP activity was detected by using diaminobenzidine staining. Arrowheads point to tumor location; arrows show presence of tumor expansion as microdeposits in normal brain tissue stained for EGFR expression. Bars in B, C = 1 mm.

The corroborative histology performed after the final MRI session showed areas of EGFR-positive staining and revealed two tumor masses (2.7-3 mm in diameter) with multiple microdeposits around the tumor/normal brain interface (arrows, Fig. 6.5D). These same features were also easily identifiable on MR images after the injection of anti-EGFR conjugate followed by the CA (Fig. 6.5C). These areas of tumor/brain were also positively stained for HRP activity using diaminobenzidine (Fig. 6.5D). By performing immunofluorescent visualization of EGFR and CD31 expression, we observed the presence of multiple blood vessels feeding the expanding tumor (Fig. 6.6A). Visualization of HRP

accumulation by using anti-HRP antibodies (Fig. 6.6B) verified the results obtained using peroxidase enzymatic activity detection in brain sections (Fig. 6.5D).

Detailed kinetic analysis of *in vivo* MR signal enhancement as a function of time was performed to assess the efficacy of EGFR targeted imaging. Fig. 6.7 shows the normalized  $T_1$ -WT signal intensities in the Gli36 $\Delta$ EGFR tumor interface and core regions as a function of time post-CA injection. Fig. 6.7A shows diTyr-GdDTPA signal-intensity-decay curves before conjugate injection (Day 1) for tumor interface and core regions. Fig. 6.7B shows CA signal-intensity-decay curves after EGFR-targeted and EpCAM-targeted conjugate injection (Day 2) for tumor interface and core regions. These plots were derived from the tumor images of the same representative animals shown in Figs. 6.5A and 6.5B. The relative percent change in  $T_1$ -WT signal intensity of the interface and core regions was significantly higher with EGFR-targeted conjugate administration (Day 2) – as compared to without pre-treatment (Day 1) – at the initial time points. With EpCAM-targeted conjugate administration (Day 2), there was no significant change in initial  $T_1$ -WT signal intensities of the interface and core regions between Day 1 and Day 2; both days showed similar washout behavior of the interface and core signal-intensity-decay curves (Fig. 6.7).

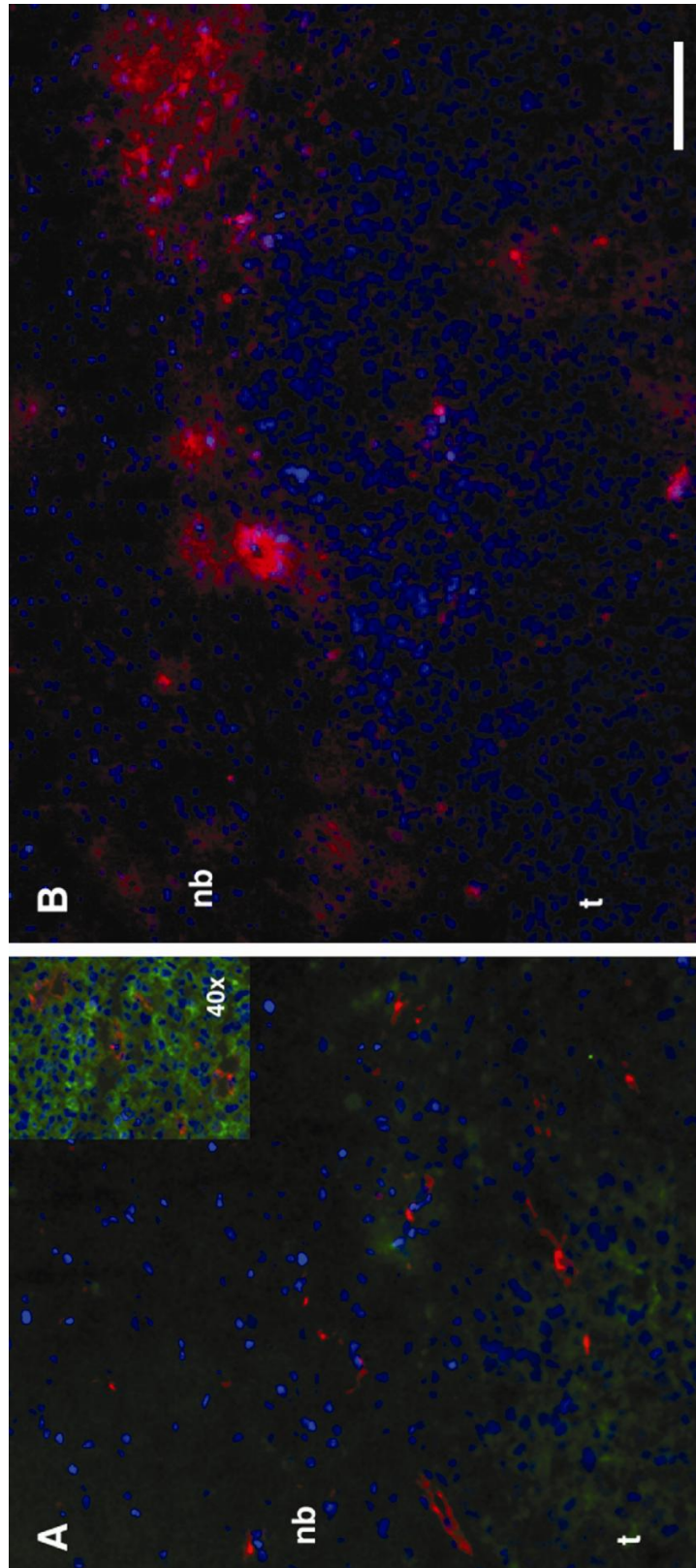


**Figure 6.6** – Immunofluorescent detection of EGF receptor, endothelial cells and mAb conjugate delivery in Gli36 $\Delta$ EGFR tumors. **A)** Detection of EGFR expression (green) and blood vessels (anti-CD31, red). The inset shows area of vascularized tumor/brain interface at higher magnification; **B)** Binding of anti-EGFR-HRP conjugate to cells in the tumor interface after injection of conjugate IV. Binding of digoxigenin-labeled anti-HRP antibody (detected by using anti-digoxigenin F(ab')<sub>2</sub>-Cy5.5 conjugate) is shown in red. Nuclei are stained with DAPI. Bar – 50  $\mu$ m. t- tumor, nb- normal brain.

Interestingly, the signal-intensity-decay curves for tumor interface and core regions in animals pre-treated with EGFR-targeted conjugates (Day 2; Fig. 6.7B) depict two separate decay components (long  $\tau_1$  and short  $\tau_2$ ) whereas the washout curves for the corresponding regions without EGFR-targeted conjugate injection (Day 1; Fig. 6.7A) show only a single decay component ( $\tau_0$ ). Based on the  $\chi^2$  analysis using an  $F$  test discussed earlier, a biexponential function was found to best model the signal-intensity-decay curves for the tumor interface and core regions after injection of EGFR-targeted conjugates (Day 2). Without EGFR-targeted conjugate preinjection (Day 1), a monoexponential function was appropriate fitting model for both the regions. For treatment with and without EpCAM-targeted conjugates, and Gli36 $\Delta$ EGFR tumors (treated with and without EGFR-targeted conjugates), a monoexponential elimination function was the best model for all signal-intensity-decay curves (see Table 6.2 for all decay time constant (DTC) values).

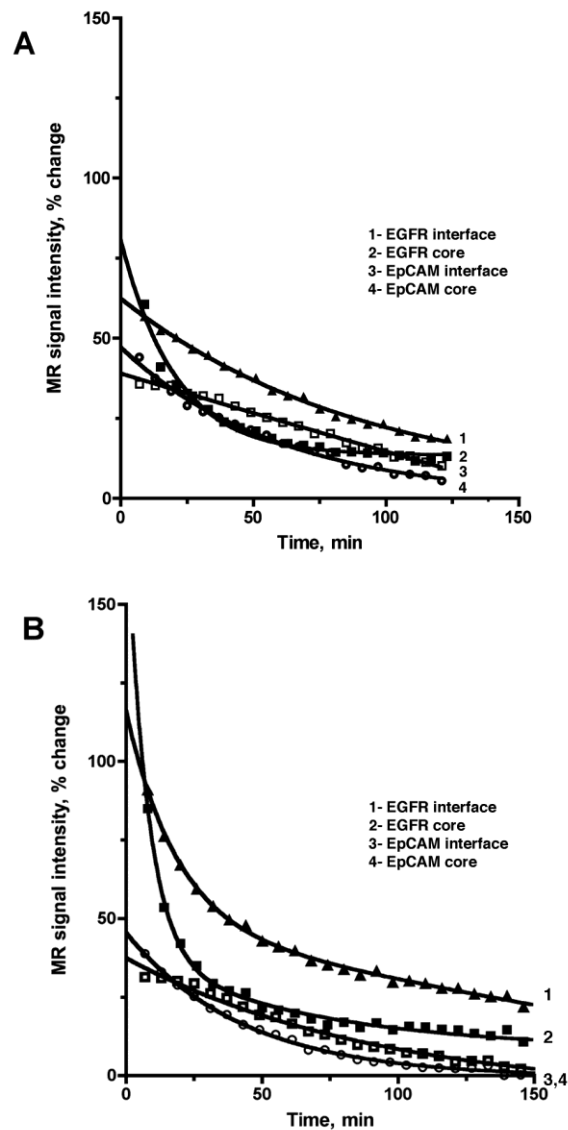


**Figure 6.7** – Normalized  $T_1$ -WT signal intensities measured in the interface or core regions of the representative Gli36 $\Delta$ EGFR tumors prior to injection of conjugates (**A**), or after the pre-injection of either specific anti-EGFR (“EGFR”) or non-specific EpCAM (“EpCAM”) conjugates (**B**) as a function of time post-diTyr-GdDTPA injection. These plots were derived from the same representative tumors shown in Fig. 6.5A and B. The signal intensities are normalized as percent change relative to pre-contrast image. Tumor core and interface regions of animals pre-injected with anti-EGFR conjugates (B, curves 1,2) exhibited biexponential signal decay whereas the MR signal decay curves with no conjugate pre-injection or after the pre-injection of non-specific conjugate (A, curves 1-4, B curves 3,4) showed a single (monoexponential) decay component.



**Table 6.2** – Decay time constants (DTC) for diTyr-GdDTPA or its products in the tumor interface and core regions with (Day 2) and without conjugate pre-treatment (Day 1).

	Gli36ΔE GFR tumors, EMD72000 (anti-E.GFR) conjugates (experiment)		Gli36ΔE GFR tumors, anti-EpCAM conjugates (control)		Gli36-WT tumors, EMD72000 conjugates (control)	
	Tumor core DTC (min) <sup>a)</sup>	Tumor interface DTC (min) <sup>a)</sup>	Tumor core DTC (min) <sup>a)</sup>	Tumor interface DTC (min) <sup>a)</sup>	Tumor core DTC (min) <sup>a)</sup>	Tumor interface DTC (min) <sup>a)</sup>
No preinjection of conjugates (Day 1)	$\tau_0$ (min) <sup>b)</sup>	$\tau_0$ (min) <sup>b)</sup>	$\tau_0$ (min) <sup>b)</sup>	$\tau_0$ (min) <sup>b)</sup>	$\tau_0$ (min) <sup>b)</sup>	$\tau_0$ (min) <sup>b)</sup>
	$\tau_2$ (min) <sup>c)</sup>	$\tau_2$ (min) <sup>c)</sup>	$\tau_2$ (min) <sup>c)</sup>	$\tau_2$ (min) <sup>c)</sup>	$\tau_2$ (min) <sup>c)</sup>	$\tau_2$ (min) <sup>c)</sup>
With pre-injection of conjugates (Day 2)	$\tau_1$ (min) <sup>e)</sup>	$\tau_1$ (min) <sup>e)</sup>	$\tau_1$ (min) <sup>d)</sup>	$\tau_1$ (min) <sup>d)</sup>	$\tau_1$ (min) <sup>e)</sup>	$\tau_1$ (min) <sup>e)</sup>
	$\tau_2$ (min) <sup>k)</sup>	$\tau_2$ (min) <sup>k)</sup>	$\tau_2$ (min) <sup>k)</sup>	$\tau_2$ (min) <sup>k)</sup>	$\tau_2$ (min) <sup>k)</sup>	$\tau_2$ (min) <sup>k)</sup>
P values	$P < 0.005$ <sup>f)</sup>	$P < 0.0002$ <sup>g)</sup>	$P < 0.009$ <sup>h)</sup>	$P < 0.004$ <sup>i)</sup>	NS <sup>m)</sup>	$P < 0.05$ <sup>l)</sup>

a) Region of interest placement is explained in Fig. 6.3;

b) For tumor core and interface regions without conjugates injection (Day 1), a monoexponential function was the most appropriate fitting model;

Based on  $\chi^2$  analysis using an *F* test (Eq. [6.5]): **c)** values in shaded area – a biexponential function was found to best model the signal-intensity-decay (SID) curves for the tumor regions in animals with Gli36ΔEGFR tumors pre-injected with anti-EGFR (EMD72000) conjugates (Day 2); a monoexponential function best modeled the SID curves for the tumor regions in animals with: **d)** Gli36ΔEGFR tumors pre-injected with EpCAM conjugates (Day 2); **e)** Gli36-WT tumors pre-injected with anti-EGFR (EMD72000) conjugates (Day 2).

*P* values correspond to comparisons in animals with Gli36ΔEGFR tumors (preinjected with EMD72000 conjugates) between: **f)**  $\tau_0$  and  $\tau_1$  in the tumor core region; **g)**  $\tau_0$  and  $\tau_2$  in the tumor core region; **h)**  $\tau_0$  and  $\tau_1$  in the tumor interface region; **i)**  $\tau_0$  and  $\tau_2$  in the tumor interface region; **j)**  $P < 0.01$  for  $\tau_0$  values in the tumor core and interface regions; **k)**  $P < 0.03$  for  $\tau_2$  values in the tumor core and interface regions.

**l)** *P* value corresponds to comparisons between  $\tau_0$  values in the tumor core region of animals with Gli36-WT tumors (preinjected with EMD72000 conjugates);

**m)** No significant differences in DTCs were observed in the tumor regions between Day 1 and Day 2 in animals with Gli36ΔEGFR tumors preinjected with EpCAM conjugates.

## 6.6. Discussion

Imaging of receptor expression in cancer with high spatial resolution usually requires MR imaging assisted with imaging probes (40,41). Due to the inherent non-specific uptake of nano-sized probes in non-target cells and slow elimination of non-bound CA from blood the specific imaging signal is frequently obscured. With a goal of imaging EGF receptor expression in gliomas we investigated a novel strategy based on specific local retention of paramagnetic products of di(tyramido)-DTPA(Gd) (diTyr-GdDTPA, Fig. 6.1), i.e. a substrate of peroxidase (30,42). We applied the strategy in models of orthotopic human gliomas that either expressed the wild-type EGFR or both the wild type receptor and EGFRvIII (43). The anti-EGFR mAb (EMD72000) was covalently linked with HRP and GOX, i.e. to the enzymes that function as a self-complementing enzymatic signal amplification system (30). In cell culture experiments these conjugates showed a remarkable preference for truncated EGFRvIII mutant form, which may be explained by the sterical constraints in accessibility of mAb epitope (Ser460-Gly461) on EGFR domain III (44). We anticipated that our strategy allows reliable MR imaging of EGFRvIII, a marker of aggressive gliomas with high specificity due to the retention of CA at the sites of mAb conjugates binding to the tumor cells.

To test this assumption, we designed experiments that directly compared *in vivo* elimination kinetics of diTyr-GdDTPA in the same tumor-bearing animals.

These experiments were performed initially in the absence of mAb conjugates and then after the pre-injection of a mixture of conjugates at the optimized HRP:GOX ratio. As a result, we were able to compare kinetics of the measured MR signal decrease due to the washout of diTyr-GdDTPA and its reactive products from the total tumor volume, as well as from volumes corresponding to highly vascularized tumor “interface” (Figs. 6.6 and 6.3) and the remaining “core” volumes. From the quantitative kinetic analysis of the MR signal intensities, we concluded that the initial MR signal intensity enhancement for both interface and core regions was significantly higher for Gli36 $\Delta$ EGFR tumors that were pre-treated with EGFR-targeted mAb conjugates (Day 2) as compared to the same tumors before the injection of conjugates (Day 1), or Gli36wt tumors. When non-targeted mAb conjugates (control) were preinjected into Gli36 $\Delta$ EGFR tumors, no significant signal change was observed compared to Day 1. Binding of paramagnetic products of enzymatic reaction to the EGFRvIII-positive cells results in a long-term retention/enhancement (Fig. 6.5A), while oligomerization or binding to proteins in the extracellular compartment result in more short-term tumor enhancement. The effects caused by paramagnetic products binding was previously observed and characterized in several similar enzyme-mediated reactions (32,45).

The long-term enhancement was more pronounced since the products of enzymatic reaction are more efficient MR contrast agents. The increase of  $r_1$  that reflects the efficiency was sufficient to cause the initial transient MR signal

enhancement observed after anti-EGFR mAb conjugate pre-injection in the presence of the same concentration of CA – relative to that observed without conjugate injection.

The retention of  $T_1$ -weighted MR signal enhancement in tumors that were pre-treated with specific targeted conjugates relative to those that were not, resulted in an increase of DTC ( $\tau$ ) (i.e. in a slower CA elimination) consistent with the binding of the CA to the target cells in the presence of targeted enzyme amplification pair. The signal enhancement of the tumor interface was consistently higher than that of the rest of the tumor volume (“core”), independent of whether the animals were preinjected with conjugates or not. This was caused by high vascular density of the tumor interface (Fig. 6.5), which corresponds to an area of enhanced transvascular permeability. This higher local permeability translates into higher concentrations of targeted conjugates as well as the substrate compared to less vascularized core. The results of direct staining for HRP activity or detection of HRP in tumors by using immunofluorescence suggest this difference (Figs. 6.5 and 6.6). The early phase of strong enhancement in tumors that were pre-treated with EGFR-targeted conjugates (Day 2) can be explained by rapid binding of the activated substrate to macromolecules in tumor extravascular space and tumor cells since highly vascularized tumor-brain interface regions should display higher retention of contrast relative to poorly vascularized regions due to the higher functional blood

volume (46). This hypothesis is supported by the tumor interface showing a significantly higher MR signal DTC than that of the core (Table 6.2).

The inevitable variations in tumor size and tumor heterogeneity dictated the need in a parameter that would allow comparing MR imaging results obtained in different animals and tumors. We determined that kinetic analysis of temporal decay of the normalized MR signal intensities can be used for this purpose (Table 6.2). The calculated DTC values can be correlated to tumor perfusion, vascular permeability, and the volume of the extravascular extracellular space (EES).

The DTCs of diTyr-GdDTPA derived from the temporal decay of the normalized signal intensities were used as the basis for comparing the CA kinetics between individual animals. This approach is analogous to that employed in dynamic contrast-enhanced MRI (DCE-MRI) (47) except that only the washout portion of the kinetic curve was measured in our study. Although the kinetic parameters calculated in this study differ from those used in the model of Tofts and Kermode (47), the parameters still relate to tumor perfusion, vascular permeability, and the volume of the EES.

By performing signal intensity decay analysis we found that in the absence of conjugate preinjection, the washout of diTyr-GdDTPA was monoexponential throughout the tumor volume generating a single DTC ( $\tau_0$ ) in both tumor models (Fig. 6.7A; Table 6.2). In each case  $\tau_0$  was attributed to the washout of the free

CA since the substrate does not bind to plasma proteins. This assignment is justified because diTyr-GdDTPA is not expected to have any affinity for tumor cells in the absence of receptor-targeted conjugates. The control EpCAM-targeted conjugate in Gli36 $\Delta$ EGFR tumors (Day 2) as well as EGFR-targeted conjugate in Gli36wt cells (Day 2) similarly resulted in monoexponential decay (Table 6.2) since control anti-EpCAM conjugates did not bind to glioma cells of our study and Gli36wt cells were binding very low amounts of EMD72000 conjugates.

Following the pre-injection of Gli36 $\Delta$ EGFR -bearing animals with EGFR-targeted conjugates on Day 2, the diTyr-GdDTPA elimination changed from monoexponential to biexponential for both the tumor interface and core regions (Fig. 6.7; Table 6.2). The elimination of free (and/or oligomerized) substrate was responsible for short DTC ( $\tau_2$ ) while the long DTC ( $\tau_1$ ) component was attributed to paramagnetic reaction products retained by tumor cells. Importantly, the comparison of both  $\tau_1$  and  $\tau_2$  DTC values suggest that delayed MR imaging in addition to dynamic imaging can also be potentially useful in imaging receptors: the retention of tumor bound paramagnetic product of specific enzymatic reaction can be detectable at in the tumor interface for several hours post administration of the substrate while the free substrate is eliminated within an hour.

### 6.6.1. Derivation of Relationship Between Decay Time Constant and EES Volume Using the Tofts and Kermode Model

The short DTCs ( $\tau_2$ ) for free diTyr-GdDTPA following conjugate pre-treatment (Day 2) was significantly shorter than the corresponding diTyr-GdDTPA DTCs ( $\tau_0$ ) without conjugate pre-treatment (Day 1). The reduced DTCs for free diTyr-GdDTPA following conjugate pre-treatment may arise from a decrease in vascular permeability which could occur due to a reduction in the volume of the EES (derivation shown below). This reduction in volume might arise due to a “binding site barrier” effect (48), which would imply that successful binding of the anti-EGFR conjugates impedes the penetration of unbound conjugates, thus leaving less EES volume available for the CA to permeate into from the blood plasma (48,49). Using the Tofts and Kermode model, we established that a reduction in the DTC is proportional to a reduction in the EES volume fraction.

The Tofts and Kermode model derives the lesion curve  $C_1(t)$  by solving a first-order linear differential equation (Eq. A9 in (47)), which has the following solution (Eq. A10 in (47)):

$$C_1(t) = D \left( \frac{m_3 a_1}{m_3 - m_1} e^{-m_1 t} + \frac{m_3 a_2}{m_3 - m_2} e^{-m_2 t} + c e^{-m_3 t} \right) \quad [6.6]$$

where  $a_1$ ,  $a_2$ ,  $m_1$ , and  $m_2$  are parameters that are calculated from the plasma curve  $C_p(t)$  (Eq. 1 in (47)),  $D$  is the contrast dose administered,  $c$  is a constant that is calculated from the initial condition  $C_1(0_+) = 0$ , and  $m_3$  is the variable that is calculated from applying this model to a lesion curve data set with wash-in and wash-out phases. The parameter  $m_3$  is defined as the exchange rate constant between EES and blood plasma ( $k_{ep}$ ) as defined by Tofts *et. al.* (50):

$$k_{ep} = K^{trans} / v_e = 1 / \tau_c \quad [6.7]$$

where  $K^{trans}$  is the volume transfer constant between blood plasma and the EES,  $v_e$  is the volume fraction of the EES, and  $\tau_c$  is the DTC. In our study we calculated the DTC, which is inversely proportional to  $k_{ep}$ . We can establish from this relationship that  $\tau_c$  is directly proportional to  $v_e$ . Thus, a decrease of the DTC would suggest that there is a decrease of EES volume fraction.  $K^{trans}$  can also be reduced (due to a decrease in transendothelial permeability in the presence of conjugates) since it is equal to the permeability surface area product between blood plasma and the EES per unit volume of tissue (50). However, the decrease in  $v_e$  is greater than the decrease of  $K^{trans}$ , which is supported by the fact that we observed a decrease of diTyr-GdDTPA DTCs on Day 2, i.e. after the pre-injection of conjugates.



## 6.7. Conclusion

We performed quantitative analysis of MR dynamic signal enhancement in human glioma xenografted animals that were: 1) imaged first by using “non-specific” paramagnetic CA; 2) imaged with the same CA after preinjecting of anti-EGFR antibody conjugates. The enzyme linked to EGFR-targeted antibodies converted the CA into reactive products thereby profoundly changing the tissue elimination kinetics. Therefore, in addition to imaging of the MR signal enhancement associated with tumor tissues *in vivo* the amplification strategy results in a kinetic signature. The analysis of images acquired dynamically or by using end point imaging can establish the presence of cell surface marker and quickly delineate the areas where this marker molecule can be targeted for therapeutic purposes.

## 6.8. Acknowledgements

This work was supported by 5R01EB000858 grant to AB. We are grateful to Dr. Suresh Gupta, Jamie O’Callaghan and Dr. Hye-Won Kang for assistance with several aspects of this work, including cell culture experiments and animal surgery. We acknowledge Merck KGaA (Darmstadt, Germany) for providing EMD72000 antibody.

## References

1. Bigner SH, Humphrey PA, Wong AJ, Vogelstein B, Mark J, Friedman HS, et al. Characterization of the epidermal growth factor receptor in human glioma cell lines and xenografts. *Cancer Res.* 1990;50:8017-22.
2. Sauter G, Maeda T, Waldman FM, Davis RL, Feuerstein BG. Patterns of epidermal growth factor receptor amplification in malignant gliomas. *Am J Pathol.* 1996;148:1047-53.
3. Schwegheimer K, Huang S, Cavenee WK. EGFR gene amplification--rearrangement in human glioblastomas. *Int J Cancer.* 1995;62:145-8.
4. Schlessinger J. Ligand-induced, receptor-mediated dimerization and activation of EGF receptor. *Cell.* 2002;110:669-72.
5. Shinojima N, Tada K, Shiraishi S, Kamiryo T, Kochi M, Nakamura H, et al. Prognostic value of epidermal growth factor receptor in patients with glioblastoma multiforme. *Cancer Res.* 2003;63:6962-70.
6. Ekstrand AJ, Longo N, Hamid ML, Olson JJ, Liu L, Collins VP, et al. Functional characterization of an EGF receptor with a truncated extracellular domain expressed in glioblastomas with EGFR gene amplification. *Oncogene.* 1994;9:2313-20.
7. Nishikawa R, Ji XD, Harmon RC, Lazar CS, Gill GN, Cavenee WK, et al. A mutant epidermal growth factor receptor common in human glioma confers enhanced tumorigenicity. *Proceedings of the National Academy of Sciences of the United States of America.* 1994;91:7727-31.
8. Ciardiello F. Epidermal growth factor receptor inhibitors in cancer treatment. *Future Oncol.* 2005;1:221-34.
9. Wagner TD, Yang GY. Cetuximab: its use in combination with radiation therapy and chemo-therapy in the multimodality treatment of head and neck cancer. *Recent Pat Anticancer Drug Discov.* 2008;3:76-83.

10. Weber J, McCormack PL. Panitumumab: in metastatic colorectal cancer with wild-type KRAS. *BioDrugs*. 2008;22:403-11.
11. Gleysteen JP, Newman JR, Chhieng D, Frost A, Zinn KR, Rosenthal EL. Fluorescent labeled anti-EGFR antibody for identification of regional and distant metastasis in a preclinical xenograft model. *Head Neck*. 2008;30:782-9.
12. Koyama Y, Barrett T, Hama Y, Ravizzini G, Choyke PL, Kobayashi H. In vivo molecular imaging to diagnose and subtype tumors through receptor-targeted optically labeled monoclonal antibodies. *Neoplasia*. 2007;9:1021-9.
13. Adams KE, Ke S, Kwon S, Liang F, Fan Z, Lu Y, et al. Comparison of visible and near-infrared wavelength-excitable fluorescent dyes for molecular imaging of cancer. *J Biomed Opt*. 2007;12:024017.
14. Diagaradjane P, Orenstein-Cardona JM, Colon-Casasnovas NE, Deorukhkar A, Shentu S, Kuno N, et al. Imaging epidermal growth factor receptor expression in vivo: pharmacokinetic and biodistribution characterization of a bioconjugated quantum dot nanoprobe. *Clin Cancer Res*. 2008;14:731-41.
15. Nunn AD, Linder KE, Tweedle MF. Can receptors be imaged with MRI agents? *Q J Nucl Med*. 1997;41:155-62.
16. Rudin M, Weissleder R. Molecular imaging in drug discovery and development. *Nat Rev Drug Discov*. 2003;2:123-31.
17. De Leon-Rodriguez LM, Lubag AJ, Malloy CR, Martinez GV, Gillies RJ, Sherry AD. Responsive MRI agents for sensing metabolism in vivo. *Acc Chem Res*. 2009;42:948-57.
18. Cerdan S, Lotscher HR, Kunnecke B, Seelig J. Monoclonal antibody-coated magnetite particles as contrast agents in magnetic resonance imaging of tumors. *Magn Reson Med*. 1989;12:151-63.

19. To SY, Castro DJ, Lufkin RB, Soudant J, Saxton RE. Monoclonal antibody-coated magnetite particles as contrast agents for MR imaging and laser therapy of human tumors. *J Clin Laser Med Surg.* 1992;10:159-69.
20. Remsen LG, McCormick CI, Roman-Goldstein S, Nilaver G, Weissleder R, Bogdanov A, et al. MR of carcinoma-specific monoclonal antibody conjugated to monocrystalline iron oxide nanoparticles: the potential for noninvasive diagnosis. *AJNR Am J Neuroradiol.* 1996;17:411-8.
21. Suwa T, Ozawa S, Ueda M, Ando N, Kitajima M. Magnetic resonance imaging of esophageal squamous cell carcinoma using magnetite particles coated with anti-epidermal growth factor receptor antibody. *Int J Cancer.* 1998;75:626-34.
22. Yang L, Mao H, Wang YA, Cao Z, Peng X, Wang X, et al. Single chain epidermal growth factor receptor antibody conjugated nanoparticles for in vivo tumor targeting and imaging. *Small.* 2009;5:235-43.
23. Nasongkla N, Bey E, Ren J, Ai H, Khemtong C, Guthi JS, et al. Multifunctional polymeric micelles as cancer-targeted, MRI-ultrasensitive drug delivery systems. *Nano Lett.* 2006;6:2427-30.
24. Kobayashi H, Brechbiel MW. Nano-sized MRI contrast agents with dendrimer cores. *Adv Drug Deliv Rev.* 2005;57:2271-86.
25. Netti PA, Hamberg LM, Babich JW, Kierstead D, Graham W, Hunter GJ, et al. Enhancement of fluid filtration across tumor vessels: implication for delivery of macromolecules. *Proceedings of the National Academy of Sciences of the United States of America.* 1999;96:3137-42.
26. Neuwelt EA, Specht HD, Hill SA. Permeability of human brain tumor to <sup>99m</sup>Tc-gluco-heptonate and <sup>99m</sup>Tc-albumin. Implications for monoclonal antibody therapy. *J Neurosurg.* 1986;65:194-8.

27. Artemov D, Mori N, Okollie B, Bhujwala ZM. MR molecular imaging of the Her-2/neu receptor in breast cancer cells using targeted iron oxide nanoparticles. *Magn Reson Med*. 2003;49:403-8.
28. Artemov D, Mori N, Ravi R, Bhujwala ZM. Magnetic resonance molecular imaging of the HER-2/neu receptor. *Cancer Res*. 2003;63:2723-7.
29. Zhu W, Okollie B, Bhujwala ZM, Artemov D. PAMAM dendrimer-based contrast agents for MR imaging of Her-2/neu receptors by a three-step pretargeting approach. *Magn Reson Med*. 2008;59:679-85.
30. Bogdanov A, Jr., Kang HW, Querol M, Pretorius PH, Yudina A. Synthesis and testing of a binary catalytic system for imaging of signal amplification in vivo. *Bioconjug Chem*. 2007;18:1123-30.
31. Bogdanov A, Jr., Matuszewski L, Bremer C, Petrovsky A, Weissleder R. Oligomerization of paramagnetic substrates result in signal amplification and can be used for MR imaging of molecular targets. *Mol Imaging*. 2002;1:16-23.
32. Querol M, Bennett DG, Sotak C, Kang HW, Bogdanov A, Jr. A paramagnetic contrast agent for detecting tyrosinase activity. *Chembiochem*. 2007;8:1637-41.
33. Rodeck U, Herlyn M, Menssen HD, Furlanetto RW, Koprowsk H. Metastatic but not primary melanoma cell lines grow in vitro independently of exogenous growth factors. *Int J Cancer*. 1987;40:687-90.
34. Ichikawa T, Hogemann D, Saeki Y, Tyminski E, Terada K, Weissleder R, et al. MRI of transgene expression: correlation to therapeutic gene expression. *Neoplasia*. 2002;4:523-30.
35. Sena-Esteves M, Saeki Y, Camp SM, Chiocca EA, Breakefield XO. Single-step conversion of cells to retrovirus vector producers with herpes simplex virus-Epstein-Barr virus hybrid amplicons. *J Virol*. 1999;73:10426-39.

36. Masui H, Kawamoto T, Sato JD, Wolf B, Sato G, Mendelsohn J. Growth inhibition of human tumor cells in athymic mice by anti-epidermal growth factor receptor monoclonal antibodies. *Cancer Res.* 1984;44:1002-7.
37. Rasband W. ImageJ. In: Health USNIo, editor. Bethesda, Maryland, USA: <http://rsb.info.nih.gov/ij/>; 1997.
38. Clark PR, Chua-anusorn W, St Pierre TG. Bi-exponential proton transverse relaxation rate (R2) image analysis using RF field intensity-weighted spin density projection: potential for R2 measurement of iron-loaded liver. *Magn Reson Imaging.* 2003;21:519-30.
39. Bevington P, Robinson K. *Data Reduction and Error Analysis for the Physical Sciences.* 3rd ed. New York: McGraw-Hill; 2003.
40. Reimer P, Weissleder R, Lee AS, Wittenberg J, Brady TJ. Receptor imaging: application to MR imaging of liver cancer. *Radiology.* 1990;177:729-34.
41. Weissleder R, Moore A, Mahmood U, Bhorade R, Benveniste H, Chiocca EA, et al. In vivo magnetic resonance imaging of transgene expression. *Nat Med.* 2000;6:351-5.
42. Querol M, Bogdanov A, Jr. Amplification strategies in MR imaging: activation and accumulation of sensing contrast agents (SCAs). *J Magn Reson Imaging.* 2006;24:971-82.
43. Ichikawa T, Hogemann D, Saeki Y, Tyminski E, Terada K, Weissleder R, et al. MRI of transgene expression: correlation to therapeutic gene expression. *Neoplasia (New York).* 2002;4:523-30.
44. Kamat V, Donaldson JM, Kari C, Quadros MR, Lelkes PI, Chaiken I, et al. Enhanced EGFR inhibition and distinct epitope recognition by EGFR antagonistic mAbs C225 and 425. *Cancer Biol Ther.* 2008;7:726-33.
45. Rodriguez E, Nilges M, Weissleder R, Chen JW. Activatable magnetic resonance imaging agents for myeloperoxidase sensing: mechanism of activation, stability, and toxicity. *J Am Chem Soc.* 2009;132:168-77.

46. JuanYin J, Tracy K, Zhang L, Munasinghe J, Shapiro E, Koretsky A, et al. Noninvasive imaging of the functional effects of anti-VEGF therapy on tumor cell extravasation and regional blood volume in an experimental brain metastasis model. *Clin Exp Metastasis*. 2009;26:403-14.
47. Tofts PS, Kermode AG. Measurement of the blood-brain barrier permeability and leakage space using dynamic MR imaging. 1. Fundamental concepts. *Magn Reson Med*. 1991;17:357-67.
48. Fujimori K, Covell DG, Fletcher JE, Weinstein JN. Modeling analysis of the global and microscopic distribution of immunoglobulin G, F(ab')<sub>2</sub>, and Fab in tumors. *Cancer Res*. 1989;49:5656-63.
49. Thurber GM, Schmidt MM, Wittrup KD. Antibody tumor penetration: transport opposed by systemic and antigen-mediated clearance. *Adv Drug Deliv Rev*. 2008;60:1421-34.
50. Tofts PS, Brix G, Buckley DL, Evelhoch JL, Henderson E, Knopp MV, et al. Estimating kinetic parameters from dynamic contrast-enhanced T(1)-weighted MRI of a diffusable tracer: standardized quantities and symbols. *J Magn Reson Imaging*. 1999;10:223-32.

# **CHAPTER VII**

# **CONCLUSION**



## 7.1. Concluding Remarks

In this dissertation use of contrast agents (CAs) was explored in MRI studies to differentiate between compartments, to study dose dependence of relaxation times, and to characterize tumors using signal amplifying enzymes in the brain.

### 7.1.1 Compartmental Differentiation

In the compartment differentiation study, the goal was to differentiate between the water signal emanating from the intracellular (IC) and extracellular (EC) space. This information would be useful in measuring the compartmental apparent diffusion coefficient (ADC) values during diffusion-weighted NMR experiments. Such measurements could eventually lead to an early diagnosis of stroke since abnormalities in ADC measurements indicate the early onset of stroke. This is an important goal because proper therapeutic intervention during the early stage of stroke can prevent the progression of ischemic injury.

Past studies have measured compartment-specific diffusion coefficients using gadolinium (Gd-DTPA) as the MR contrast agent in yeast cells to distinguish between the IC and EC water proton signals based on differences in their respective longitudinal ( $T_1$ ) relaxation times (1). Gd-DTPA was employed as an EC contrast agent, thereby reducing the  $T_1$  value of the EC space. In our study we applied an alternate approach by using manganese ( $Mn^{2+}$ ) as an IC contrast agent. It was hypothesized that  $Mn^{2+}$  uptake by cells would cause

shortening of the  $T_1$  relaxation time of the IC water. The relative difference in  $T_1$  relaxation times between the IC and EC compartments could then be used to discriminate between the MR signals arising from water in the respective compartments.

From our experiments we were unable to conclude with certainty whether  $Mn^{2+}$  can differentiate between the IC and EC compartments. When  $Mn^{2+}$  is administered in the animals,  $Mn^{2+}$  resides first in the EC compartment and then in the IC compartment. At some point in time,  $Mn^{2+}$  occupies both compartments as  $Mn^{2+}$  is taken up by the cells. Also, once in the IC compartment,  $Mn^{2+}$  can be sequestered within organelles. Thus, it is unclear which water population the  $Mn^{2+}$  affects.

To test the hypothesis of using  $Mn^{2+}$  to differentiate between the IC and EC compartments, perhaps a simpler biological model than the brain should be investigated. For example, some sort of cell suspension studies could be done where  $Mn^{2+}$  is isolated to the IC compartment (with a larger water volume fraction) and any  $Mn^{2+}$  in the EC compartment (lower volume fraction) is excluded from the system. That way an accurate assessment can be made whether  $Mn^{2+}$  can differentiate between the IC and EC compartments.

### **7.1.2 Dose Response**

In the dose response study, the goal was to investigate the MRI dose response of  $Mn^{2+}$  in rat brain following SC administration of  $Mn^{2+}$ . From our

experiments, we showed a dose-dependent response of  $Mn^{2+}$  on  $T_1$  relaxation times in different regions of the rat brain following SC injection of  $Mn^{2+}$  which was comparable to a previous dose response study using IV injection of  $Mn^{2+}$  (2). This study also suggests that SC administration of  $Mn^{2+}$  at a high dose (near  $LD_{50}$  value) can deliver a greater amount of  $Mn^{2+}$  than the highest non-toxic dose possible with intrathecal injection in the rodent brain.

SC administration of  $Mn^{2+}$  also led to prolonged enhancement in the brain than IV administration since SC route avoids the immediate elimination of  $Mn^{2+}$  from plasma via bile (3) upon injection which occurs during IV injection. A high dose SC  $Mn^{2+}$  injection releases  $Mn^{2+}$  in the plasma at a slow rate, thus avoiding systemic toxic effects; the same high dose  $Mn^{2+}$  injection via IV route releases the entire dose directly into the plasma which can lead to cardiac dysfunction.

The dose dependence and temporal dynamics of  $Mn^{2+}$  after SC injection can prove useful for longitudinal *in vivo* studies that require brain enhancement to persist for a long period of time to visualize neuroarchitecture like in Alzheimer's disease, Parkinson's disease, amyotrophic lateral sclerosis, and other neurodegenerative diseases.

### **7.1.3 Tumor Characterization**

The imaging of EGF receptors in brain tumors is essential for visualizing overexpression of EGFR as a signature of highly aggressive gliomas and for identifying patients that would benefit from anti-EGFR therapy.

Several methods have been utilized in the last three decades to visualize gliomas in the brain using MRI. The simplest of all is a straightforward administration of paramagnetic CAs such as Gd-DTPA in the vasculature (4-8). This method makes the glioma readily detectable due to the leakiness of the blood vessels in the glioma. The small molecular weight of Gd-DTPA (<1kD) causes rapid extravasation from the vascular space into the interstitial space. Sometimes, the CAs are bound to macromolecular proteins to keep the CAs circulating within the vascular space (9, 10). This is desirable since an intravascular CA can detect alterations in tumor vasculature that cannot be revealed by extravascular CA which leak out of the vascular space (11, 12). In either case, the CA only provides non-specific enhancement. Since gliomas tend to have a heterogeneous morphology, regions of the glioma that are poorly vascularized will show inadequate enhancement.

Utilizing monoclonal antibodies is an approach that specifically targets the extracellular domain of EGFR. Several investigators have used CAs conjugated with monoclonal antibodies to detect different types of tumors (13-15). Anti-EGFR monoclonal antibodies have a high affinity for binding to the receptor. Once the antibody is bound to other molecules, its binding affinity gets compromised. The CA concentration achieved by directly labeling monoclonal antibodies while maintaining appropriate binding affinity of mAb is not sufficient to generate adequate MR contrast. Other studies attempted to go around this problem by coating magnetic particles with mAb not having to chemically alter

the mAb (16-18). However, the resolution obtained using this method is not suitable to properly characterize tumors. A few studies have looked into alternate use of mAb in enhancing tumors (19, 20). Artemov *et al.* developed an indirect way of enhancing breast carcinomas by injecting CAs that bind to receptor bound mAbs (19). They pre-labeled the extracellular domain of HER-2/*neu* receptor with biotinylated mAb and injected Gd-labeled avidin after clearance of unbound mAb. The Gd-labeled avidin bound to the biotinylated mAb with high affinity and produced high  $T_1$  contrast. They were able to target and image the receptors specifically.

In the tumor characterization study, we investigated a novel pretargeting imaging approach using humanized monoclonal antibody (anti-EGFR mAb, EMD72000) linked to enzymes with complementing activities that use a low-molecular weight paramagnetic molecule (diTyr-GdDTPA) as a reducing substrate administered following the mAb conjugates. We performed quantitative analysis of MR dynamic signal enhancement in human glioma xenografted animals that were: 1) imaged first by using “non-specific” paramagnetic CA; 2) imaged with the same CA after preinjecting of anti-EGFR antibody conjugates.

The enzyme linked to EGFR-targeted antibodies converted the CA into reactive products thereby profoundly changing the tissue elimination kinetics. Therefore, in addition to imaging of the MR signal enhancement associated with tumor tissues *in vivo* the amplification strategy results in a kinetic signature

(biexponential contrast decay). The analysis of images acquired dynamically or by using end point imaging can establish the presence of cell surface marker and quickly delineate the areas where this marker molecule can be targeted for therapeutic purposes. For future studies, it will be interesting to see if other types of tumors display the same type of contrast washout kinetics with our novel pretargeting imaging approach.

## References

1. Silva MD, Helmer KG, Lee JH, Han SS, Springer CS, Jr., Sotak CH. Deconvolution of compartmental water diffusion coefficients in yeast-cell suspensions using combined T(1) and diffusion measurements. *J Magn Reson.* 2002;156:52-63.
2. Lee JH, Silva AC, Merkle H, Koretsky AP. Manganese-enhanced magnetic resonance imaging of mouse brain after systemic administration of MnCl<sub>2</sub>: dose-dependent and temporal evolution of T1 contrast. *Magn Reson Med.* 2005;53:640-8.
3. Bertinchamps AJ, Miller ST, Cotzias GC. Interdependence of routes excreting manganese. *Am J Physiol.* 1966;211:217-24.
4. Runge VM, Jacobson S, Wood ML, Kaufman D, Adelman LS. MR imaging of rat brain glioma: Gd-DTPA versus Gd-DOTA. *Radiology.* 1988;166:835-8.
5. Norman AB, Thomas SR, Pratt RG, Samaratinga RC, Sanberg PR. A magnetic resonance imaging contrast agent differentiates between the vascular properties of fetal striatal tissue transplants and gliomas in rat brain in vivo. *Brain Res.* 1989;503:156-9.
6. Norman AB, Bertram KJ, Thomas SR, Pratt RG, Samaratinga RC, Sanberg PR. Magnetic resonance imaging of rat brain following in vivo disruption of the cerebral vasculature. *Brain Res Bull.* 1991;26:593-7.
7. Leenders W, Kusters B, Pikkemaat J, Wesseling P, Ruiter D, Heerschap A, et al. Vascular endothelial growth factor-A determines detectability of experimental melanoma brain metastasis in GD-DTPA-enhanced MRI. *Int J Cancer.* 2003;105:437-43.
8. Gibbs-Strauss SL, Samkoe KS, O'Hara JA, Davis SC, Hoopes PJ, Hasan T, et al. Detecting epidermal growth factor receptor tumor activity in vivo during cetuximab therapy of murine gliomas. *Acad Radiol.* 2010;17:7-17.

9. Boschi F, Marzola P, Sandri M, Nicolato E, Galie M, Fiorini S, et al. Tumor microvasculature observed using different contrast agents: a comparison between Gd-DTPA-Albumin and B-22956/1 in an experimental model of mammary carcinoma. *MAGMA*. 2008;21:169-76.
10. Marzola P, Degrassi A, Calderan L, Farace P, Crescimanno C, Nicolato E, et al. In vivo assessment of antiangiogenic activity of SU6668 in an experimental colon carcinoma model. *Clin Cancer Res*. 2004;10:739-50.
11. Turetschek K, Preda A, Floyd E, Shames DM, Novikov V, Roberts TP, et al. MRI monitoring of tumor response following angiogenesis inhibition in an experimental human breast cancer model. *Eur J Nucl Med Mol Imaging*. 2003;30:448-55.
12. Turetschek K, Preda A, Novikov V, Brasch RC, Weinmann HJ, Wunderbaldinger P, et al. Tumor microvascular changes in antiangiogenic treatment: assessment by magnetic resonance contrast media of different molecular weights. *J Magn Reson Imaging*. 2004;20:138-44.
13. Matsumura A, Shibata Y, Nakagawa K, Nose T. MRI contrast enhancement by Gd-DTPA-monoclonal antibody in 9L glioma rats. *Acta Neurochir Suppl (Wien)*. 1994;60:356-8.
14. Gohr-Rosenthal S, Schmitt-Willich H, Ebert W, Conrad J. The demonstration of human tumors on nude mice using gadolinium-labelled monoclonal antibodies for magnetic resonance imaging. *Invest Radiol*. 1993;28:789-95.
15. Go KG, Bulte JW, de Ley L, The TH, Kamman RL, Hulstaert CE, et al. Our approach towards developing a specific tumour-targeted MRI contrast agent for the brain. *Eur J Radiol*. 1993;16:171-5.
16. Suwa T, Ozawa S, Ueda M, Ando N, Kitajima M. Magnetic resonance imaging of esophageal squamous cell carcinoma using magnetite particles coated with anti-epidermal growth factor receptor antibody. *Int J Cancer*. 1998;75:626-34.



17. Cerdan S, Lotscher HR, Kunnecke B, Seelig J. Monoclonal antibody-coated magnetite particles as contrast agents in magnetic resonance imaging of tumors. *Magn Reson Med*. 1989;12:151-63.
18. To SY, Castro DJ, Lufkin RB, Soudant J, Saxton RE. Monoclonal antibody-coated magnetite particles as contrast agents for MR imaging and laser therapy of human tumors. *J Clin Laser Med Surg*. 1992;10:159-69.
19. Artemov D, Mori N, Ravi R, Bhujwala ZM. Magnetic resonance molecular imaging of the HER-2/neu receptor. *Cancer Res*. 2003;63:2723-7.
20. Artemov D, Mori N, Okollie B, Bhujwala ZM. MR molecular imaging of the Her-2/neu receptor in breast cancer cells using targeted iron oxide nanoparticles. *Magn Reson Med*. 2003;49:403-8.

# APPENDIX

**MOHAMMED SALMAN SHAZEEB**

200 East Mountain Street #250, Worcester, MA 01606 • (617) 823-8034 • shazeeb@alum.bu.edu

---

**EDUCATION:**

Worcester Polytechnic Institute and University of Massachusetts Medical School, Worcester, MA

**Ph.D., Biomedical Engineering & Medical Physics (Joint Program)**, November 2010, GPA: 3.82/4.0  
Dissertation title: MRI contrast agent studies of compartmental differentiation, dose-dependence, and tumor characterization in the Brain

Worcester Polytechnic Institute, Worcester, MA

**M.E., Biomedical Engineering**, December 2007, GPA: 4.0/4.0

Boston University, College of Engineering, Boston, MA

**B. S., *Summa Cum Laude*, Biomedical Engineering**, May 2004, GPA: 3.73/4.0

Senior project: Quantitative study of 2,3-butanedione 2-monoxime on the electrophysiological properties of isolated rat hearts.

**MRI RESEARCH EXPERIENCE:****Nuclear Magnetic Resonance Lab Research Assistant, Department of Biomedical Engineering**

WPI, Worcester, MA (October 2006 – Present)

- Designed and executed experiments in deconvolving the intra- and extracellular water components in the rat brain using Manganese Enhanced Magnetic Resonance Imaging (MEMRI).
- Prepared contrast solutions and performed intravenous, subcutaneous, and intrathecal injections on the rat.
- Executed experiments in studying the kinetics of contrast agent washout from implanted tumors in the rat brain.
- Conducted MR imaging and spectroscopy – data acquisition and pulse sequence optimization using BRUKER Biospin 2T imaging scanner (ParaVision 2.1 Software) and PHILIPS 3T clinical scanner.
- Designed and made radio frequency (RF) coils for MRI experiments.
- Wrote custom MATLAB software for MR image processing, data analysis, and statistical evaluation of mathematical models.
- Performed maintenance and upkeep of 2T BRUKER system including cryogen fills.

**Lab Rotation, Department of Biomedical Engineering**

WPI, Worcester, MA (February 2005 – August 2005)

- Conducted experiments investigating the relative contributions of intra- and extracellular water apparent diffusion coefficient changes during ischemia using manganese as an intracellular MRI contrast agent.
- Prepared contrast solutions and performed intracerebroventricular injection on rat using stereotactic frame.
- Performed MR imaging – data acquisition and pulse sequence optimization using BRUKER Biospin 2T imaging scanner (ParaVision 2.1 Software).
- Designed and made radio frequency (RF) coils for MRI experiments.
- Wrote custom MATLAB and IDL software for MR image processing and analysis.

**RELATED COURSES:**

- Principles of In Vivo Nuclear Magnetic Resonance Imaging
- Principles of Nuclear Magnetic Resonance Spectroscopy
- Medical Imaging Systems
- Digital Image Processing
- Digital Signal Processing
- Applied Statistics for Scientists & Engineers
- Biomedical Instrumentation
- Biochemistry
- Cell Biology
- Human Physiology
- Laboratory Animal Surgery
- Quantum Mechanics
- Engineering Mathematics
- Signals and Systems

**TEACHING EXPERIENCE:****Graduate Teaching Assistant, Department of Biomedical Engineering, WPI, Worcester, MA**

Principles of *In Vivo* Nuclear Magnetic Resonance Imaging (September 2007 – December 2007)

- Taught two lectures about NMR principles explaining the difference between  $T_1$ ,  $T_2$ , and proton-density weighted images using notes on the blackboard as the mode of teaching.
- Assisted students in performing laboratories using Bruker Avance Spectrometer.

**Graduate Teaching Assistant, Department of Biomedical Engineering, WPI, Worcester, MA**

Biomedical Imaging (February 2009)

- Taught two lectures about image processing techniques and image filtering using PowerPoint slides and transparencies as the mode of teaching.
- Assisted students in MATLAB programming in a lab session.

**Teaching Lab Assistant, Biomedical Engineering Department**

Boston University, Boston, MA (February 2004 – May 2004)

- Worked in the biomedical engineering teaching lab assisting in the lab preparation of biomedical engineering courses and acting as a teaching aid to the students.

**OTHER EXPERIENCE:****Lab Rotation, Department of Radiology, Division of Nuclear Medicine**

University of Massachusetts Medical School, Worcester, MA (September 2005 – January 2006)

- Programmed a UNIX system using IDL/C++ to further the motion correction studies during cardiac SPECT imaging.
- Assisted in the data collection process through patient contact.

**Lab Coordinator, Center for BioDynamics, Department of Biomedical Engineering**

Boston University, Boston, MA (May 2004 – August 2004)

- Assistant to Director of Center for BioDynamics, Dr. James J. Collins.
- Responsible for petty cash disbursement/reimbursement to staff and students.
- Manage grant charges for lab group and maintain grant charges record using Microsoft Excel Spreadsheet

**ResNet Consultant, ResNet**

Boston University, Boston, MA (September 2003 – May 2004)

- Worked as a Computer Lab Consultant assisting users with technical help in using network lab computers.

**Senior Project Research, Electrophysiology Lab**

Beth Israel Deaconess Medical Center, Brookline, MA (January 2003 – December 2003)

- Analyzed the effects of different concentrations of an uncoupler on the electrophysiological properties of isolated rat hearts in furtherance of an independent study dealing with the effects of implanted stem cells on cardiac arrhythmias of rat hearts.

**Undergraduate Research Assistant, Neurodynamics Lab**

Boston University, Boston, MA (May 2002 – August 2002)

- Programmed a LINUX-based dynamic clamp system using C/C++ to simplify the model of the structure into small modules for better organization and faster processing speed.

**COURSE PROJECT EXPERIENCE:****Digital Image Processing, Department of Computer Science**

WPI, Worcester, MA (September 2005 – December 2005)

- Implemented a generic MATLAB algorithm to read incomplete image data and restore the information in the missing sections with only the available data.

**In vivo Magnetic Resonance Imaging, Department of Biomedical Engineering**

WPI, Worcester, MA (September 2004 – December 2004)

- Designed MATLAB program for the analysis of raw MRI data to generate  $T_1$  and  $T_2$  maps.

**Digital Signal Processing, Department of Electrical and Computer Engineering**

WPI, Worcester, MA (September 2004 – December 2004)

- Investigated the performance of different algorithms in detecting and classifying the QRS complex of ECG recordings using MATLAB as the software platform.

**Biomedical Imaging, Department of Biomedical Engineering**

Boston University, Boston, MA (September 2003 – December 2003)

- Designed a MATHCAD program to reconstruct the image of an object using Radon transforms, rotations, and filter-back projections.

**Mechanics, Engineering Core Curriculum**

Boston University, Boston, MA (September 2001 – December 2001)

- Designed and built a truss model and wrote a program in MATLAB to accomplish theoretical analysis of different dimensions of the truss.

**SKILLS:**

**Operating Systems:** UNIX, LINUX, DOS, Windows (All versions)

**Programming Languages:** C/C++, PASCAL, MATLAB, IDL, MATHCAD, LABVIEW

**Statistical Software:** SAS, SPSS, MS EXCEL

**Lab Equipment:** Capable of fully operating BRUKER and PHILIPS MRI scanners

**Foreign Languages:** Arabic, Bengali, Hindi, English, French, Urdu.

**FELLOWSHIPS/GRANTS:**

Research Assistantship, WPI, Worcester, MA (May 2007 – present)

WPI Fellowship, WPI, Worcester, MA (August 2006 – May 2007)

Stedman Smith Fellowship, WPI, Worcester, MA (August 2005 – August 2006)

Robert H. Goddard Fellowship, WPI, Worcester, MA (August 2004 – August 2005)

**HONORS/AWARDS:**

Educational Stipend Award, Joint Annual Meeting ISMRM-ESMRMB, Stockholm, Sweden (May 2010)  
 Graduate Student Government Award for Conference Travel (May 2010)  
 Student Travel Stipend Award, Gordon Research Conference, Andover, NH, USA (July 2008)  
 Summa Cum Laude (2004)  
 Dean's List (2000 – 2004)  
 Boston University Academic Scholarship (2000 – 2004)  
 Recipient of Research for Engineering Undergraduates Award (2002)

**ACTIVITIES:**

**President** of Muslim Students Association at WPI (September 2007 – May 2008)  
**Vice President** of Muslim Student Association at WPI (September 2005 – May 2007)  
**President** of Islamic Society of Boston University (September 2002 – May 2004)  
 Volunteer work for Muslim American Society Boston Chapter (May 2002 – 2005)  
 Intramural soccer (Fall 2000, Fall 2001, Spring 2010)

**PUBLICATIONS/ CONFERENCE PROCEEDINGS:**

**Shazeeb MS**, Sotak CH, Bogdanov A. Targeted Imaging of EGF Receptor Expression in Gli36 Tumor Xenografts Using Monoclonal Antibody Conjugates. *Submitted to Cancer Research (2010)*.

**Shazeeb MS**, Sotak CH. Dose-dependent effect of Manganese Chloride on Relaxation Times in the Rat Brain. *Manuscript in Preparation*.

**Shazeeb MS**, Sotak CH. Deconvolving the Intra- and Extracellular Water Components in the Rat Brain Using Manganese Enhanced MRI (MEMRI). *Manuscript in Preparation*.

Beach Richard D., Feng Bing, **Shazeeb Mohammed S.**, King Michael A., Determining Patient 6-Degrees-of-Freedom Motion from Stereo Infrared Cameras During Supine Medical Imaging, *Progress in Biomedical Optics and Imaging* 7(2) 2006: n°29, [Note(s): 614337.1-614337.9].

**Shazeeb MS**, Sotak CH. Dose Dependence of  $T_1$  Relaxation Time in the Rat Brain after Subcutaneous Injection of  $MnCl_2$ . **Submitted** to International Society for Magnetic Resonance in Medicine (ISMRM) Conference, May 7-13 2011, Montréal, Québec, Canada.

**Shazeeb MS**, Sotak CH, Bogdanov AA. Specific Targeting of EGF Receptor Expression with Monoclonal Antibody Conjugates in Human Gliomas Using MRI. **Submitted** to International Society for Magnetic Resonance in Medicine (ISMRM) Conference, May 7-13 2011, Montréal, Québec, Canada.

Bogdanov AA, Xie Y, **Shazeeb MS**. Novel hydroxytryptophan-based Gd chelating substrate for imaging myeloperoxidase activity. **Submitted** to International Society for Magnetic Resonance in Medicine (ISMRM) Conference, May 7-13 2011, Montréal, Québec, Canada.

Bogdanov AA, **Shazeeb MS**, Sotak CH. Imaging EGF Receptor Expression in Gli36 Tumor Xenografts Using Targeted MR Signal-Amplifying Enzymes. **Oral Presentation**. Proceedings for World Molecular Imaging Congress (WMIC), September 8-11, 2010, Kyoto, Japan.

**Shazeeb MS**, Sotak CH, Bogdanov A. Targeted Imaging of EGF Receptor Expression in Gli36 Tumor Xenografts Using Monoclonal Antibody Conjugates. *Oral Presentation*. Proceedings for Joint Annual Meeting ISMRM-ESMRMB (International Society for Magnetic Resonance in Medicine and European Society for Magnetic Resonance in Medicine and Biology), May 1-7, 2010, Stockholm, Sweden.

**Shazeeb MS**, Sotak CH. Dose Dependence and Temporal Evolution of the  $T_1$  Relaxation Time and MRI Contrast in Rat Brain after Subcutaneous Injection of  $MnCl_2$ . *Poster Presentation*. Proceedings for Contrast-Enhanced Biomedical Imaging, 12<sup>th</sup> Bi-Annual Conference on Contrast Agents and Multimodal Molecular Imaging, May 19-21, 2010, Mons, Belgium.

**Shazeeb MS**, Sotak CH, Bogdanov A. Targeted Imaging of EGF Receptor Expression in Gli36 Tumor Xenografts Using MR Signal-Amplifying Enzymes. *Oral Presentation*. Proceedings for Contrast-Enhanced Biomedical Imaging, 12<sup>th</sup> Bi-Annual Conference on Contrast Agents and Multimodal Molecular Imaging, May 19-21, 2010, Mons, Belgium.

Bogdanov A, DeLeo M, **Shazeeb MS**, Kang HW, Sotak CH. Anti-EGF receptor antibody conjugates in MR imaging of human glioma xenografts using enzyme-mediated signal amplification. *Poster Presentation*. Proceedings for American Association for Cancer Research (AACR) Conference, April 18-22, 2009, Denver, CO, United States.

Wang YY, **Shazeeb MS**, Sotak CH, Fischer GS. Optimization of Piezoelectric Motors to Enhance MR Compatibility for Interventional Devices. *Poster Presentation*. Proceedings for International Society for Magnetic Resonance in Medicine (ISMRM) Conference, April 18-24, 2009, Honolulu, HI, United States.

Bogdanov A, DeLeo M, **Shazeeb MS**, Kang HW, Sotak CH. Paramagnetic Substrate for Molecular MR Imaging of EGF Receptor in Human Glioma Model Using Targeted Antibody-Conjugated Enzymatic System. *Poster Presentation*. Proceedings for World Molecular Imaging Congress (WMIC), September 10-13, 2008, Nice, France.

Nair G, **Shazeeb MS**, Bouley J, Helmer KG, Fisher M, Sotak CH. Deconvolution of compartmental water diffusion coefficients in stroke using DW-IR MEMRI. *Poster Presentation*. Proceedings for International Society for Magnetic Resonance in Medicine (ISMRM) Conference, May 6-12, 2006, Seattle, WA, United States.

Beach, Richard D., Feng, Bing, **Shazeeb, Mohammed S.**, King, Michael A., Determining Patient 6-Degrees-of-Freedom Motion from Stereo Infrared Cameras During Supine Medical Imaging, (Submitted 8/1/2005, Accepted 10/1/2005) – SPIE Medical Imaging Conference, February 11-16, 2006, Town and Country Hotel, San Diego, CA, United States.

Beach, Richard D., Gifford, Howard C., **Shazeeb, Salman**, Bruyant, Philippe P., Feng, Bing, Gennert, Michael A., Nadella, Suman, King, Michael A., Stereo-Infrared Tracking to Monitor and Characterize Rigid-Body Motion and Respiration During Cardiac SPECT Imaging: Progress Towards Robust Clinical Utilization, In: Conference Record (May 11, 2005) - IEEE Nuclear Science Symposium, Medical Imaging Conference (NSS/MIC) October 23-29, 2005, Wyndham El Conquistador Hotel, Puerto Rico.

# Determining patient 6-degrees-of-freedom motion from stereo infrared cameras during supine medical imaging

Richard D. Beach, Bing Feng, Mohammed S. Shazeeb, and Michael A. King  
Department of Radiology, University of Massachusetts Medical School  
55 Lake Avenue North, Worcester, MA 01655

## ABSTRACT

Patient motion during SPECT acquisition causes inconsistent projection data and reconstruction artifacts which can significantly affect the diagnostic accuracy of SPECT. The tracking of motion by infrared monitoring spherical reflectors (markers) on the patient's surface can provide 6-Degrees-of-Freedom (6-DOF) motion information capable of providing clinically robust correction. Object rigid-body motion can be described by 3 translational DOF and 3 rotational DOF. Polaris marker position information obtained by stereo infrared cameras requires algorithmic processing to correctly record the tracked markers, and to calibrate and map Polaris co-ordinate data into the SPECT co-ordinate system. Marker data then requires processing to determine the rotational and translational 6-DOF motion to ultimately be used for SPECT image corrections. This processing utilizes an algorithm involving least-squares fitting, to each other, of two 3-D point sets using singular value decomposition (SVD) resulting in the rotation matrix and translation of the rigid body centroid. We have demonstrated the ability to monitor 12 clinical patients as well as 7 markers on 2 elastic belts worn by a volunteer while intentionally moving, and determined the 3 axis Euclidian rotation angles and centroid translations. An anthropomorphic phantom with Tc-99m added to the heart, liver, and body was simultaneously SPECT imaged and motion tracked using 4 rigidly mounted markers. The determined rotation matrix and translation information was used to correct the image resulting in virtually identical "no motion" and "corrected" images. We plan to initiate routine 6-DOF tracking of patient motion during SPECT imaging in the future.

**Keywords:** Motion, monitoring, correction, infrared, cameras

## 1. INTRODUCTION

Patient motion during SPECT acquisition causes inconsistent projection data and reconstruction artifacts which can significantly affect the diagnostic accuracy of SPECT if not corrected [1-4]. There has been a significant amount of research on motion detection and correction in recent years. Optical and infrared cameras have been utilized to track patient motion [5-8]. Our current hypothesis is that the detection of patient motion by optical or infrared monitoring of the motion of spherical reflectors on the patient's surface can provide 6-Degree-of-Freedom (6-DOF) motion information which can be used for clinically robust correction of patient motion [9, 10].

## 2. METHODS

Rigid-body motion of an object can be described by 3 translational degrees-of-freedom and 3 rotational degrees-of-freedom (i.e., 6-DOF). We have previously demonstrated the feasibility of monitoring reflective spheres on elastic belts placed on the upper chest and lower abdomen of supine patients [8].

### 2.1 Setup for patient motion tracking

Fig.1 shows the setup used for tracking patient motion. A volunteer is shown on the imaging table of the SPECT system employed positioned similar to that employed with patients. The upper and lower belts containing 4 retro-reflective markers each, are both in the imaging volume. The Polaris system can be seen mounted on the wall to the right.

### 2.2 Analysis methods

Marker position information obtained by Polaris stereo-infrared cameras requires algorithmic processing to remove false marker indications, and then to calibrate and map the Polaris data into the SPECT co-ordinate system [8, 11]. A



Neural Network algorithm [11] then decomposes marker data into periodic respiratory and non-periodic (assumed rigid-body) motion.

This assumed rigid-body motion marker data is then processed to determine patient 6-DOF motion. The x, y, and z motion data from the markers on the two belts is then input into an algorithm which involves the least-squares fitting of two 3-D point sets. One set is the initial marker positions and the second set the positions after a time period. The algorithm uses singular value decomposition (SVD) and results in the rotation matrix and translation of the rigid body centroid [12] from the initial to the time period position. Simulations of known rotations and translations have been successfully used to verify algorithm operation.

Ultimately the 6-DOF data will be used for SPECT image corrections as previously demonstrated [10]. The image correction method works as the interpolation step during projection and backprojection. It moves the current emission voxel estimates and attenuation maps to the new location when calculating the projection, and moves back the contribution to the voxel estimates to the original location after performing backprojection.

### **2.3 Volunteer feasibility study**

A total of 14 volunteers were monitored by Polaris while positioned for SPECT imaging, but without SPECT image acquisition. The 5 males and 9 females were successfully tracked by the Polaris system. This served as an initial test as to the feasibility of monitoring to acquire the necessary marker position data to compute the 6-DOF motion information necessary for image motion correction.

One male volunteer was asked to move during this testing phase in order to validate the 6-DOF rotation and translation computation based on the rigid-body motion component obtained by our Neural Network algorithm decomposition [11].

The remaining 4 males and 9 females were asked to remain motionless, thus the respiratory motion was the primary component. Detailed results of the respiratory amplitudes observed for a medially located sphere on the upper and lower belts for the lateral X axis, vertical Y axis and axial Z axis have been reported previously for these volunteers [13].

### **2.4 Clinical patient acquisitions**

A total of 12 clinical patients (4 females, 8 males) were monitored by Polaris while wearing the upper chest and lower abdomen 4 marker belts and undergoing clinical SPECT imaging. A total of at least 3 markers from the two belts, with at least 2 from either belt, are necessary to compute 6-DOF information when the body is assumed to be moving as a rigid-body. It should be noted that one large girth male tested only showed 1 lower belt marker, one female showed only the lower belt 4 markers due to a garment fold obscuring the upper belt markers, and another female showed 1 marker each on the upper and lower belts (reason unknown). As we improved our technique for belt placement and became aware of garment folds that could obscure marker viewing, we were successfully monitoring all 8 markers more consistently.

### **2.5 Anthropomorphic phantom acquisition**

An anthropomorphic phantom experiment was conducted to determine if the 6-DOF motion obtained from SVD of the Polaris data could be used to correct for motion. The relative concentrations of Tc-99m in the heart, liver, and background were 1.0, 1.0, 0.1, respectively. The phantom was simultaneously SPECT imaged and motion tracked using 4 rigidly mounted markers for 3 simulated motion steps. The SVD processing produced 6-DOF motion data which was used in image reconstruction.

## **3. RESULTS AND DISCUSSION**

### **3.1 General**

For reference, Fig. 2 shows the SPECT image coordinate system to which the Polaris marker positions were mapped.

### **3.2 Volunteer feasibility study**

An example of the variation in location of the markers for the volunteer who was requested to move slightly during motion tracking is shown in Fig. 3. This figure shows the initial and 5 other positional states observed during motion tracking displayed in a 3D plot. Note only 7 of the 8 markers were successfully observed in this volunteer. The marker positions from this volunteer were used to estimate the 6-DOF rotational and translational motion of this volunteer. Fig. 4 shows the resulting calculated variation in the 6-DOF position of the volunteer relative to their initial location for the

selected 5 time points illustrated in Fig. 3. As expected from viewing the 3D plot of the positions in Fig 3. the greatest variation was in a y-axis (vertical) translation with the rest of the 6-DOF motion being smaller in magnitude.

### 3.3 Clinical patient acquisitions

Fig. 5 shows a single clinical patient's non-periodic motion after removal of the respiratory (periodic) component by the use of our Neural Network algorithm [11]. The motion plotted is the change from the baseline position. The left side 3 graphs, from the top down, are for the Upper Chest lateral X axis, vertical Y axis, and axial Z axis showing motion for markers 1 through 4 during the approximately 16 minute period of SPECT acquisition. The right side graphs, from the top down, are for the Lower Abdomen lateral X axis, vertical Y axis, and axial Z axis motion for markers 5 through 8. At a Polaris sample rate of 20 samples per second for the approximately 16 minute (1000 sec) duration of SPECT acquisition resulted in about 20,000 recordings of the X, Y, and Z location for each marker. For display purposes in this manuscript we have plotted the results at 500 sample (25 second) intervals.

What can be seen is that the lateral X axis motion is between 0 to -2 mm for both the upper and lower belts, with all the markers on each behaving similarly. The vertical Y axis upper chest shows all 4 markers tending to go downwards, between -3 to -7 mm during the course of SPECT acquisition. The vertical Y axis lower abdomen shows more downward motion, with all 4 markers drifting downwards between -10 to -11 mm. Thus the abdomen shows a settling indicative of what may be a decrease in the magnitude of respiration during SPECT acquisition. This might be an indication of what causes "cardiac creep" which is a gradual upward movement of the heart in the chest during acquisition and is noted clinically in some patient studies. The axial Z axis shows a general upward change for both the upper and lower belt markers of about +2 to + 4 mm and this would be indicative of the patient shifting in a direction away from the SPECT gantry towards his own head. The only other interesting observation is the upper chest marker 1 Z axis motion downwards then back upwards between 175 and 375 seconds, and this could be indicative of the patient taking his arm from behind his head and lowering it towards his side and then putting it back behind his head.

Fig. 6 shows the 6-DOF calculated motion relative to the initial location of the patient for the clinical patient whose marker information was shown in Fig. 5. The data for the remaining 11 patients is not displayed herein due to space limitations. The translations shown in Fig. 6a are in millimeters (mm) showing the change from the baseline position, and of most interest is the translation in the Y axis of about -8 mm. The rotation matrix information, Fig. 6b, has been converted to Euclidian angles showing rotation of the assumed rigid-body about each of the respective X, Y, and Z axes. What is of the most interest is the rotation about the X axis, which can be visualized as the patient's abdomen lowering, and this can be seen to be about -2 degrees.

The behavior in Fig. 6a and 6b showing downward Y axis abdomen marker movement is consistent with the actual marker data shown in Fig. 5c and 5d showing similar downward Y axis motion. This shows the consistency of the computed 6-DOF motion information and the actual individual marker motions.

### 3.4 Anthropomorphic phantom acquisition

The anthropomorphic phantom experiment tracked the 4 rigidly mounted markers for the 3 motion steps. The determined 6-DOF information for each of the steps was used during reconstruction to correct for the observed motion. This resulted in virtually identical "no motion" and "corrected" images as shown in Fig. 7.

## 4.0 CONCLUSIONS

We have successfully monitored 12 clinical patients while undergoing actual SPECT acquisitions as demonstrated herein, and have computed 6-DOF rigid-body motion rotation matrices and centroid translations providing the basis for image motion correction. The 6-DOF motion, determined during the anthropomorphic phantom experiment, was successfully used to correct the SPECT image for motion artifacts demonstrating the promise of our methodology. A comparison of actual marker motion changes from baseline position compared to the calculated rigid-body 6-DOF motion shows evidence of residual non rigid-body motion and will be evaluated in further future studies.

## ACKNOWLEDGEMENTS

This work was supported by the National Institute for Biomedical Imaging and Bioengineering (NIBIB), grant R01 EB001457. The contents are solely the responsibility of the authors and do not necessarily represent the official views of the National Institutes of Health.

## REFERENCES

- [1] E. H. Botvinick, Y. Y. Zhu, W. J. O'Connell, and M. W. Dae, "A quantitative assessment of patient motion and its effect on myocardial perfusion SPECT images," *J.Nucl.Med*, vol. 34, no. 2, pp. 303-310, Feb.1993.
- [2] F. M. Prigent, M. Hyun, D. S. Berman, and A. Rozanski, "Effect of motion on thallium-201 SPECT studies: a simulation and clinical study," *J.Nucl.Med*, vol. 34, no. 11, pp. 1845-1850, Nov.1993.
- [3] J. A. Cooper, P. H. Neumann, and B. K. McCandless, "Effect of patient motion on tomographic myocardial perfusion imaging," *J.Nucl.Med*, vol. 33, no. 8, pp. 1566-1571, Aug.1992.
- [4] C. Bai, and R. Conwell, "A Systematic Simulation Study of the Effects of Patient Motion on Cardiac Perfusion Imaging Using Single Photon Emission Computed Tomography," [abstract], Society of Nuclear Medicine 52<sup>nd</sup> Annual Meeting, June 18-22, 2005, Toronto, Canada.
- [5] R. R. Fulton, S. Eberl, S. R. Meikle, B. F. Hutton, and M. Braun, "A practical 3D tomographic method for correcting patient head motion in clinical SPECT," *IEEE Trans Nucl Sci*, vol. 46, no. 3, pp. 667-672, 1999.
- [6] B. J. Lopresti, A. Russo, W. F. Jones, T. Fisher, D. G. Crouch, D. E. Altenburger et al., "Implementation and performance of an optical motion tracking system for high resolution brain PET imaging," *IEEE Trans Nucl Sci*, vol. 46, no. 6, pp. 2059-2067, 1999.
- [7] R. R. Fulton, S. R. Meikle, S. Eberl, J. Pfeiffer, R. T. Constable, and M. J. Fulham, "Correction for head movements in positron emission tomography using an optical motion-tracking system.," *IEEE Trans Nucl Sci*, vol. 49, no. 1, pp. 116-123, 2002.
- [8] R. D. Beach, P. H. Pretorius, G. Boening, P. P. Bruyant, B. Feng, R. R. Fulton, M. A. Gennert, S. Nadella, M. A. King, "Feasibility of stereo-infrared tracking to monitor patient motion during cardiac SPECT imaging," *IEEE Trans Nucl Sci*, vol. 51, pp. 2693-2698, 2004.
- [9] Boening G, Bruyant PP, Beach RD, Byrne CL, King MA. Motion correction for cardiac SPECT using a RBI-ML partial-reconstruction approach. Proceedings of 2004 IEEE Medical Imaging Conference, M4-6, in press.
- [10] Bing Feng<sup>1</sup>, Howard C. Gifford<sup>1</sup>, Richard D. Beach<sup>1</sup>, Guido Boening<sup>1</sup>, Michael A. Gennert<sup>2</sup>, Michael A. King<sup>1</sup>,<sup>1</sup>Radiology, University of Massachusetts Medical School, Worcester, MA, USA, <sup>2</sup>Computer Science, Worcester Polytechnic Institute, Worcester, MA, United States, Use of Three-Dimensional Gaussian Interpolation in the Projector/Backprojector Pair for Compensation of the Known Rigid-Body Motion in SPECT, IEEE Transactions on Medical Imaging, (February 2006, in press)
- [11] R. D. Beach, H. Depold, G. Boening, P. P. Bruyant, B. Feng, H. C. Gifford, M. A. Gennert, S. Nadella, M. A. King, "An Adaptive Neural-Network Approach to Decomposing Patient-Motion Tracking Data Acquired During Cardiac SPECT Imaging", In: Conference Record 2004, IEEE Nuclear Science Symposium, Medical Imaging Conference (NSS/MIC) October 2004, IEEE, Rome, Italy.
- [12] K. S. Arun, T. S. Huang, S. D. Blostein, Least-Squares Fitting of Two 3-D Point Sets, IEEE Transactions on Pattern Analysis and Machine Intelligence, Vol. PAMI-9, No. 5, September 1987.
- [13] Beach, Richard D., Gifford, Howard C., Shazeeb, Salman, Bruyant, Philippe P., Feng, Bing, Gennert, Michael A., "Stereo-Infrared Tracking to Monitor and Characterize Rigid-Body Motion and Respiration During Cardiac SPECT Imaging: Progress Towards Robust Clinical Utilization", In: Conference Record (May 11, 2005) – IEEE Nuclear Science Symposium, Medical Imaging Conference (NSS/MIC) October 23-29, 2005, Wyndham El Conquistador Hotel, Puerto Rico.



**Fig. 1.** The Polaris system is seen on the far right mounted on the wall. It views the Infrared (IR) reflecting spheres (white spots) on the anterior surface of patients on two elastic belts. The upper chest belt, by our chosen convention, contains markers 1 through 4, starting with 1 on the patient's right. Similarly, the lower abdomen belt has markers 5 through 8, starting with 5 on the patient's right.

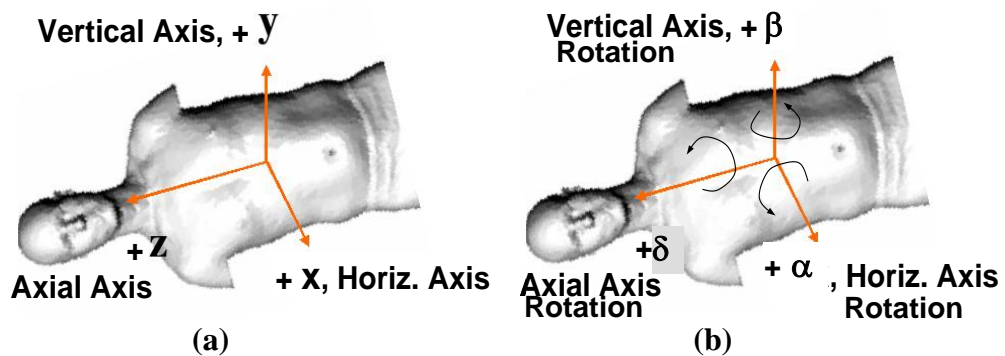


**Fig. 2.** (a) SPECT imaging axis convention utilized for mapping of Polaris position data – Right Handed System, (b) 6 Degree of Freedom (6-DOF) convention for + angular rotations about the 3 Axes (i.e. Counter clockwise (CCW) looking inwards towards the origin will be the + angular rotation)

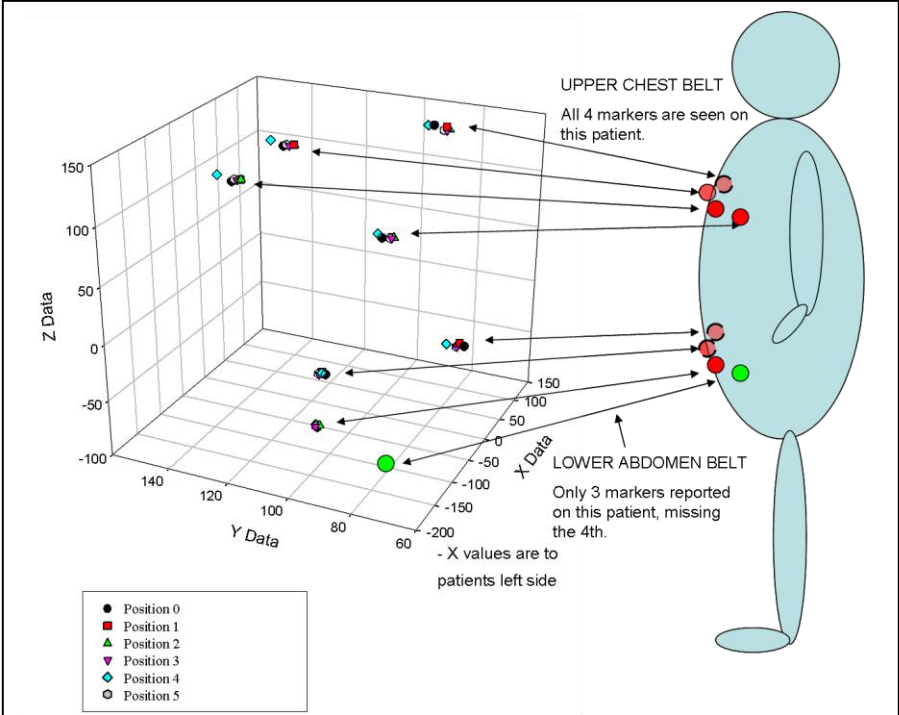


**Fig. 3.** Marker positions shown in 3D axis of SPECT mapped co-ordinate system showing original and 5 later positions.

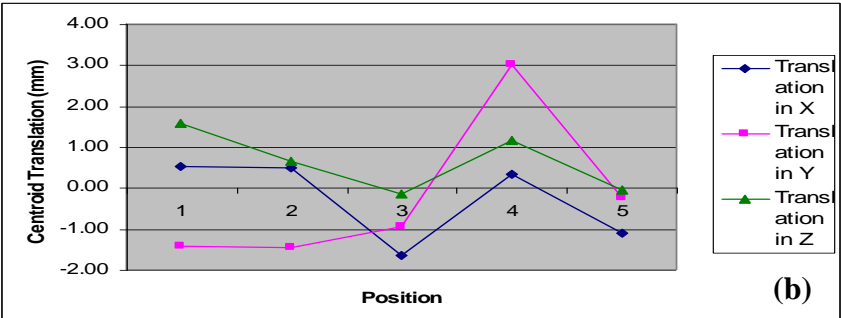
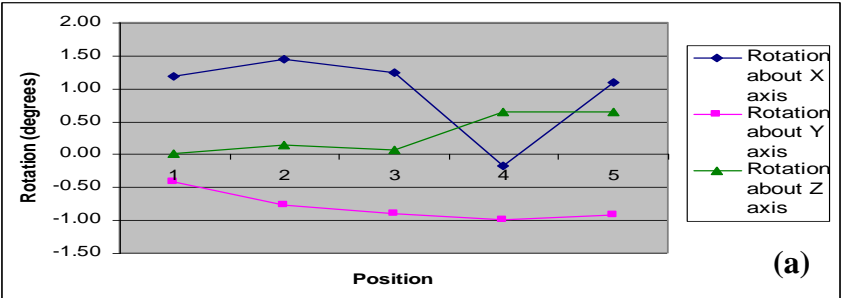


**Fig. 4.** (a) Euclidian Rotation Degrees (derived from rotation matrix) and (b) centroid translation of the 7 marker assumed rigid-body motion at the 5 volunteer positions of Fig. 3 relative to the starting position.

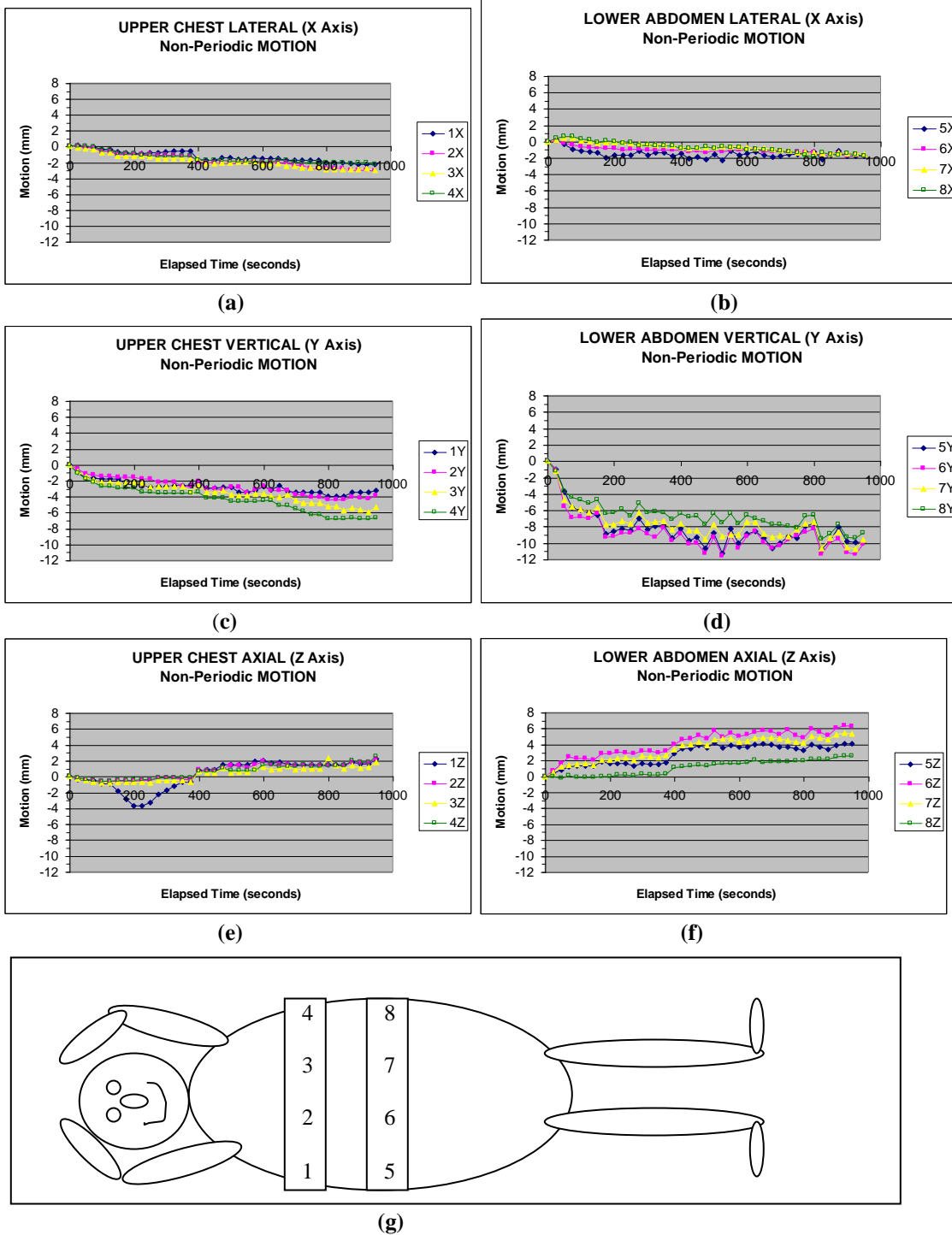


**Fig. 5.** Clinical patient Non-Periodic or assumed to be rigid-body motion, relative to the baseline position of the 8 individual markers. The displayed data for this assumed rigid-body motion were obtained using our Neural Network algorithm processing to decompose the combined motion data into respiration (periodic) and remaining patient motion (non-periodic) components. Motion data was obtained over an approximately 16 minute SPECT acquisition with Polaris motion data gathered at 20 samples per second. Shown is a sample at 500 sample intervals from the approximately 20,000 samples recorded showing : (a) Upper Chest Horizontal Lateral (X axis) markers 1 thru 4, (b) Lower Abdomen Horizontal Lateral (X axis) markers 5 thru 8, and similarly (c) Upper Chest Vertical (Y axis), (d) Lower Abdomen Vertical (Y Axis), (e) Upper Chest Axial (Z Axis), (e) Lower Abdomen Axial (Z Axis), (g) Numbering convention for the Upper Chest and Lower Abdomen 4 marker belts.

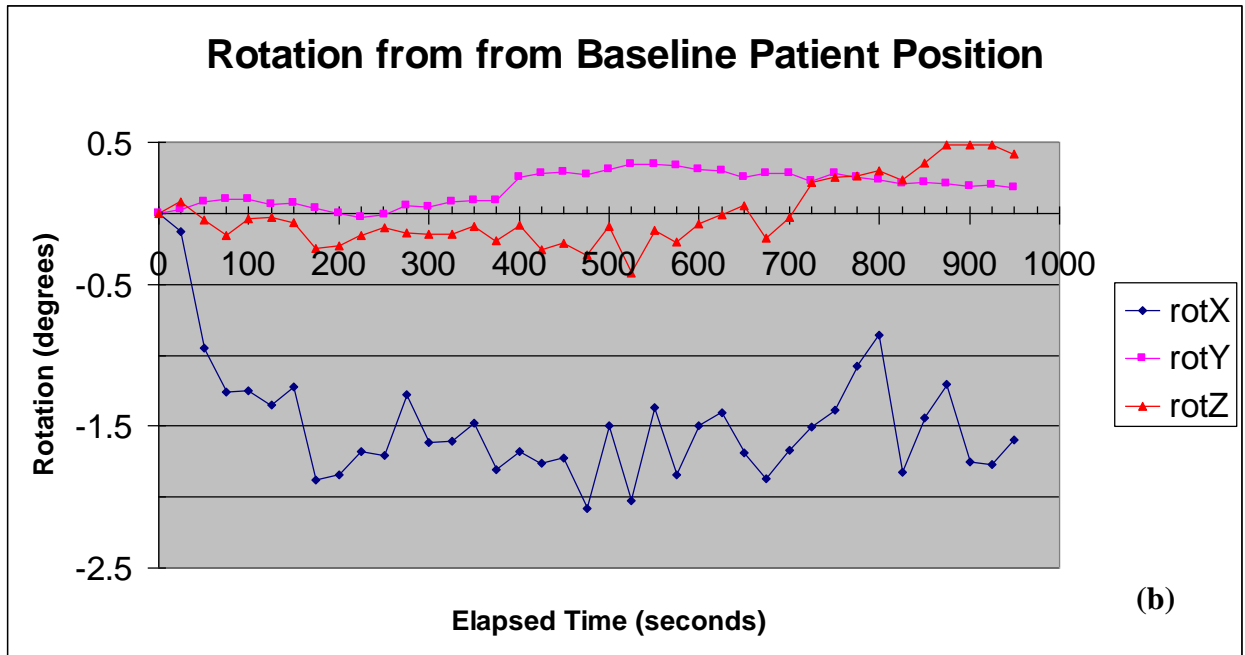
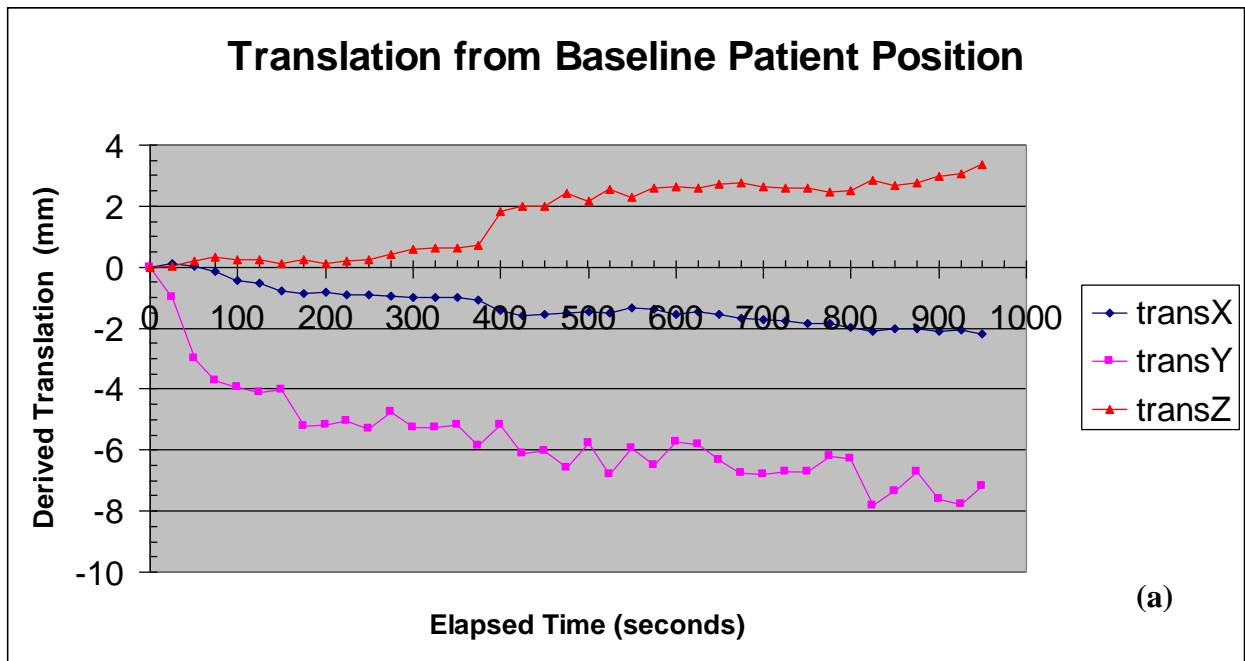


**Fig. 6.** Clinical patient 6-DOF motion during an actual 16 minute SPECT acquisition with Polaris motion data gathered at 20 samples per second. Shown at 500 sample intervals over the approximately 20,000 samples recorded showing: (a) translation of the 8 marker assumed rigid-body centroid from the baseline position, (b) Rotation of the 8 marker assumed rigid-body about its centroid around the horizontal X axis (rotX, denoted by angle  $\alpha$  in Fig. 2), around the vertical Y axis (rotY, denoted by angle  $\beta$  in Fig. 2), and around the axial Z axis (rotZ, denoted by angle  $\delta$  in Fig. 2) from the baseline orientation position.

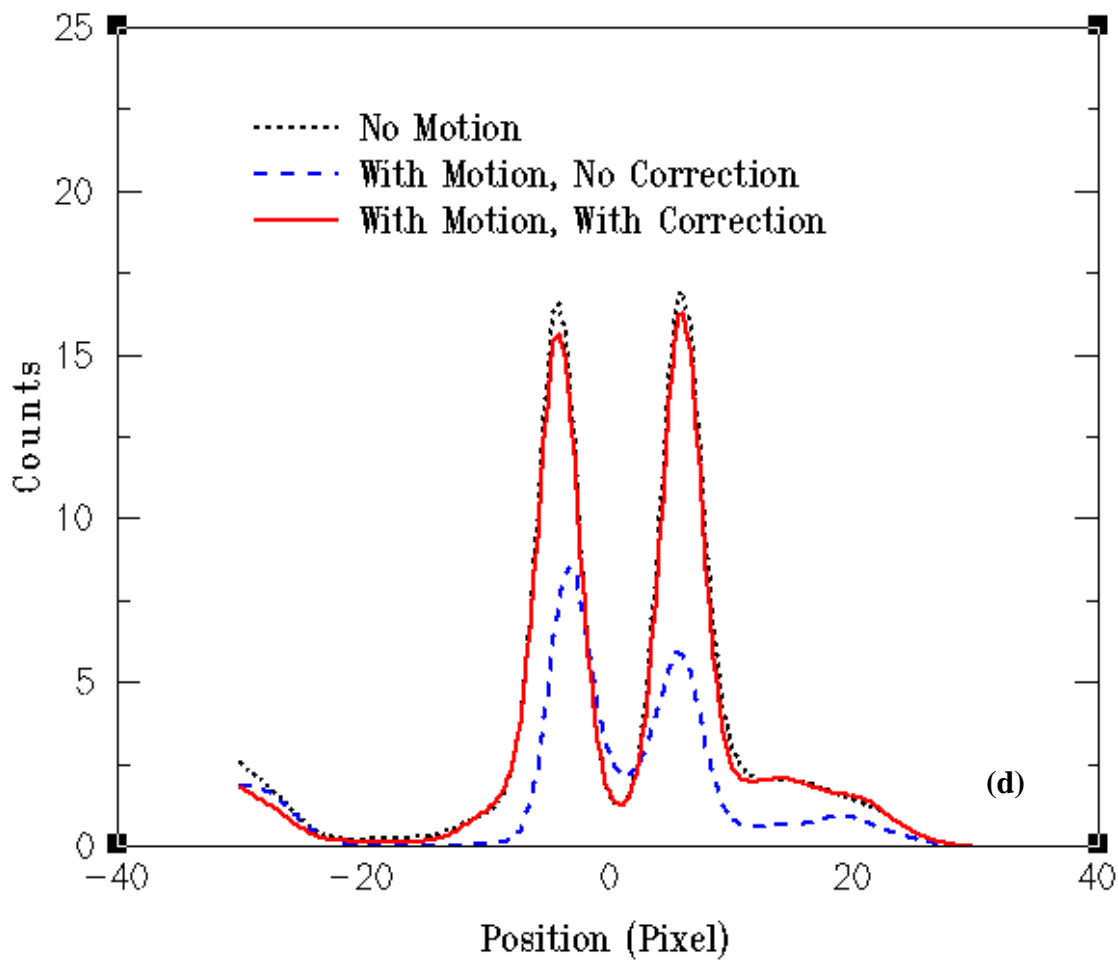
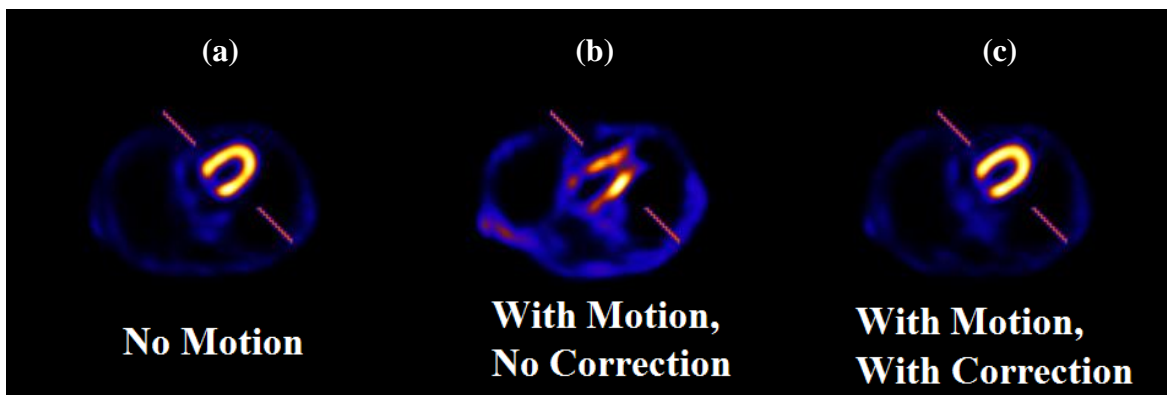


Fig. 7. Anthropomorphic Phantom: reconstructed slice through heart: (a) no motion, (b) motion no correction, (c) after motion correction, (d) count profile from locations indicated by bars in a, b, and c.



# Stereo-Infrared Tracking to Monitor and Characterize Rigid-Body Motion and Respiration During Cardiac SPECT Imaging: Progress Towards Robust Clinical Utilization

Richard D. Beach, *Senior Member IEEE*, Howard C. Gifford, *Member*, Salman Shazeeb, Philippe P. Bruyant, *Member IEEE*, Bing Feng, Michael A. Gennert, Suman Nadella, and Michael A. King, *Senior Member IEEE*.

**Abstract**— Patient motion during cardiac SPECT imaging can cause diagnostic imaging artifacts. Our approach is to monitor patient motion during cardiac SPECT imaging using the Polaris stereo-IR real-time motion-tracking system. In our earlier work [1] we obtained excellent correlation of axial and vertical motion as measured by our SPECT system with the Polaris. We also showed a good correlation for Polaris tracking of respiration for volunteers with data from a pneumatic bellows. Herein, we show the successful monitoring of patients during cardiac SPECT perfusion imaging. We wrapped elastic belts with four IR reflecting spheres on each about the chest and abdomen of the patients. The Polaris system reported the 3D location of these spheres in a random order intermixed with the location of “phantom” spheres. We developed routines to automatically recognize and discard the Phantom spheres, consistently order the true spheres, and covert Polaris coordinates to SPECT coordinates given a calibration. For our 12 analyzed clinical patients the data shows that both males and females at rest were primarily abdomen breathers with the male peak to peak average vertical respiration amplitude larger at 9.2 mm than that for the females at 5.6 mm. The male chest average vertical amplitude was also a bit larger at 1.6 mm vs. 1.4 mm for females. During the 16 minute SPECT acquisition the average vertical axis difference between end-expiration levels for the abdomen for combined males and females was -4.2 mm, with males slightly larger at -4.72 mm vs. females at -3.81 mm. The largest vertical end expiration change was -9.0 mm, and was observed in the male with the highest Body Mass Index (BMI) of 44.2.

**Index Terms**— motion, position, SPECT, clinical

## I. INTRODUCTION

Patient motion can be a major cause of diagnostic imaging artifacts, especially in SPECT and PET imaging. Motion

---

Manuscript received November 11, 2005. This work was supported by the National Institute for Biomedical Imaging and Bioengineering (NIBIB), grant R01 EB001457. The contents are solely the responsibility of the authors and do not necessarily represent the official views of the National Institutes of Health.

R.D. Beach, H.C. Gifford, S. Shazeeb, P.P. Bruyant, B. Feng, and, M.A. King are from the University of Massachusetts Medical School, Division of Nuclear Medicine, Worcester, MA 01655 USA (telephone: 508-856-6735, e-mail: Richard.Beach@umassmed.edu).

M.A. Gennert and S. Nadella are from the Department of Computer Science, Worcester Polytechnic Institute, Worcester, MA, USA.

information obtained from a six-degree-of-freedom (6-DOF) stereo-infrared system can provide input for compensation of patient motion as part of iterative reconstruction [1, 2], and has also been demonstrated during PET brain imaging [3]. We are utilizing the passive version of the Polaris Tracking System from Northern Digital Inc., which uses infrared (IR) reflection from small spherical targets to provide real-time tracking of position and orientation with manufacturer stated 0.35 mm accuracy and 0.2 mm repeatability. The spheres may be grouped into “tools” with fixed geometry that may be tracked as one; or the spheres may be individually tracked. We have selected the latter mode as being more flexible, and better suited to our imaging geometry. As illustrated in Fig. 1, Polaris is oriented such that it views the elastic-belt-mounted spheres, positioned on the anterior surface of patients, through the tunnel of the SPECT gantry. Polaris reports the locations of the spheres at approximately 20 samples/second enabling the tracking of both respiratory and body motion. The choice of tracking individual spheres presented us with a number of design issues to be overcome to permit robust tracking of patient motion in the clinic. Our goal herein is to present our solution to these issues and the results of our first clinical usage of the system..



Fig. 1. The Polaris system is seen on the far right mounted on the wall. The white spots on the 2 belts are the attached IR reflecting spheres. Volunteer and SPECT camera setup was performed by a technologist matching what would be employed clinically.

## II. METHODS

### A. Equipment used

We utilized the passive version of the Polaris Tracking System from Northern Digital Inc. as shown in Fig. 1. As employed herein it uses infrared (IR) reflection from small 11 mm diameter spherical targets to provide real-time tracking of the position and orientation in 3 dimensions (3D) of individual spheres. The sphere locations as reported in the Polaris coordinate system are transformed to that of the SPECT system by use of a matrix transformation based on calibration studies [1] so that the axes are X (lateral), Y (vertical), and Z (axial). Calibration is performed by acquiring the location of 4 spheres by both Polaris and SPECT. Thus for calibration mapping purposes, a small amount of Tc-99m is deposited in wells at the top of the bases to which the spheres are attached. Fig. 2(a) shows a tool with 3 spheres rigidly attached to the back side of the tunnel of the SPECT gantry in a location where it is unlikely to be disturbed during patient imaging. We use imaging of this to assure the Polaris has not moved thus invalidating a previous calibration necessitating a new one. Fig. 2(b) shows chest and abdomen belts worn by a volunteer, which were typical of those used on the clinical patient. The belts were made of a disposable sticky elastic bandage material (cost about \$1 each) and the plastic bases on which the spheres were mounted were attached to the belts by eight ½ inch sticky back Velcro dots (cost about \$0.05 each) for a total cost per patient of \$2.40. The low cost was important as it allows the belts to be disposed of after each use for infection control. The spherical markers and mounting bases were reusable since they are considerably more expensive. Plastic risers of about ½ inch maximum height were used on the upper (chest) belt of males if required to facilitate viewing but were not needed on females.

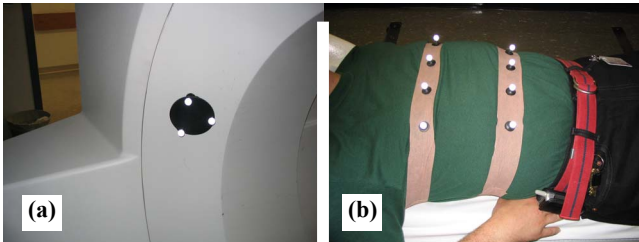


Fig. 2. Showing: (a) The gantry mounted 3 sphere tool used for calibration stability monitoring; (b) volunteer with two 4-sphere elastic belts placed about the upper (chest) and lower (abdomen) torso.

### B. Can Polaris Reliably View Patients undergoing SPECT

The first major issue was determining if the system could reliably view the chest and upper abdomen of patients being imaged by our Philips Medical Systems Irix SPECT system. The need to monitor the motion of both the chest and abdomen stems from patients generally falling into the categories of abdomen breathers (primarily breathe with diaphragm) and chest breathers (primarily breathe by rocking ribs hinged at back-bone). We therefore place a stretchable belt with spheres about both the chest and abdomen. The dual belts shown in Fig. 1 and Fig. 2 (b) were successfully tracked by Polaris for 11 clinical patients undergoing actual SPECT acquisitions, as well as for 9 female and 5 male volunteers of

different body shapes and sizes. In one additional male patient solely a sphere on the abdomen belt was visible. Fig. 3 is an example of the type of body habitus which presented this problem for Polaris in viewing the spheres on the chest belt. We recently incorporated a small variable height elevation of the spheres on the belts when necessary, to overcome viewing limitations due to physique variations. Similar issues can arise due to garment cloth folds between the upper and lower belts which would have the same effect.

Fig. 4 shows an example of typical volunteer Polaris recorded data after conversion to IRIX coordinates. A medially located marker on both the abdomen and chest are shown. This volunteer data was gathered over a 2 minute time period at about 20 samples per second, thus about 2500 samples are shown.

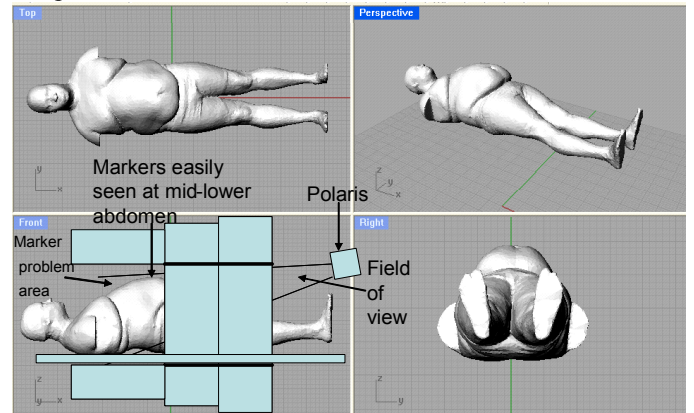


Fig. 3. Body habitus potential belt viewing limitations such that upper (chest) belt mounted 4 markers may not be seen by Polaris, while lower (abdomen) belt mounted 4 markers will be easily seen.

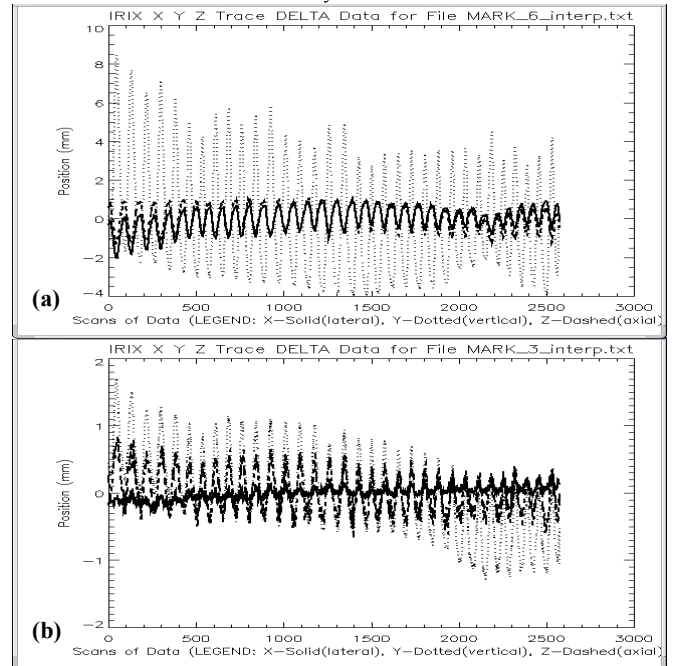


Fig. 4. Plots of recorded Polaris position data (Actual-Average) for a typical volunteer taken during a 2 minute duration showing the motion in 3 axes by solid line X (lateral), dotted line Y (vertical), and dashed line Z (axial) for: (a) an abdomen and; (b) chest spheres. Note the use of finer scale for the chest locations plotted in (b).

### C. How Many Markers are Required to Determine Motion

A second major issue was to determine the optimal number and arrangement of spheres based on our desire to track respiration, 6-DOF rigid-body motion, and in the future, non-rigid-body motion. Tradeoff considerations are the minimum number of spheres to obtain the required information while minimizing the potential number of Polaris “phantom” spheres, which potentially number  $(N)*(N-1)$  where  $N$  is the true number of markers. Phantom spheres are false spheres which appear to be present when Polaris decodes its stereo-IR images, but do not correspond to actual physical spheres. Typically, the number of phantoms does not reach its maximum, but does vary during data acquisition. Fig. 5 shows sphere positional data and the typical appearance of phantoms reported in the vicinity of the two 4-sphere elastic belts. The more varied the geometry of sphere placement, the more complex the phantom detection handling algorithm becomes. We thus settled on utilizing 2 belts, each with a linear arrangement of 4 markers laterally. Fig. 6 is a diagram showing how Polaris creates the untrue phantom locations which our processing algorithm must deal with.

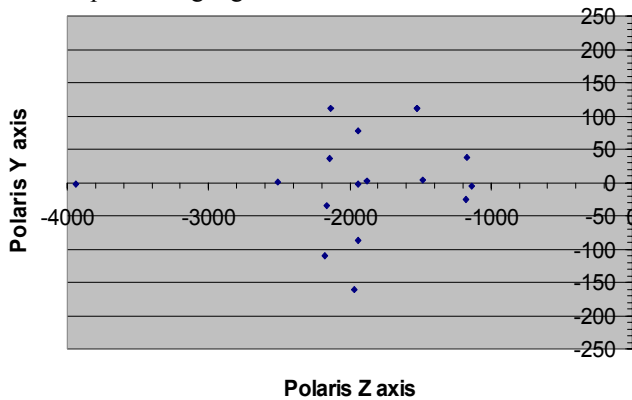


Fig. 5. An overhead plot of sphere locations for two volunteer worn 4-sphere belts with 9 phantom locations also shown. The true 4 sphere vertical alignments of the belts can be seen at about -2000 and -2200 on the Polaris Z axis (axial) axis.

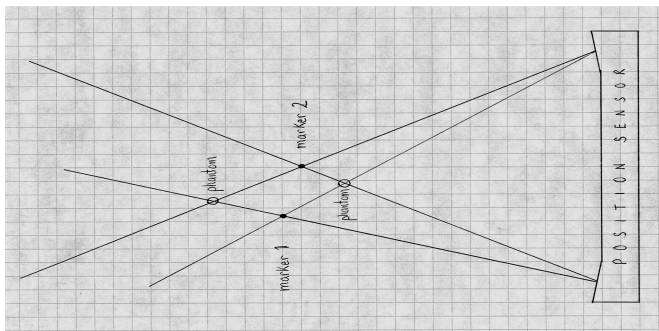


Fig. 6. Phantom sphere location creation. If Polaris detects 2 true spheres in the same plane extending from Polaris, it creates 2 untrue phantoms at the intersection of the rays.

#### D. Algorithm to Process Raw Polaris Coordinate Data into SPECT Image Coordinates

The third major issue was how Polaris randomly switches the reported order of spheres and intermixes the locations of phantom spheres. We have successfully implemented a processing algorithm which uses gamma-camera geometrical

constraints, belt-geometry characteristics, and patient physical motion rate limitations to remove phantoms and reflections and order the valid spheres so motion can be tracked. Details of this processing will be given in our manuscript to be submitted for peer-review.

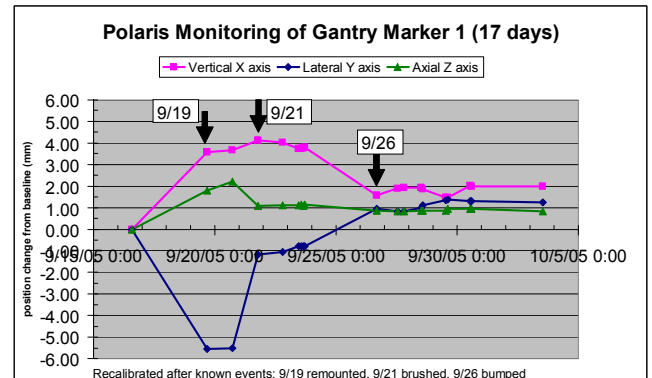


Fig. 7. Plot of Polaris vertical, lateral, and axial position data for a gantry a mounted sphere (marker) shown in Fig 2 (a) used for monitoring calibration stability..

### III. RESULTS AND DISCUSSION

Fig. 7 shows Polaris sphere positional information in IRIX co-ordinates for one of the three spheres used to monitor the stability of the Polaris to SPECT calibration during the time clinical patients studies were acquired. Known remounting of Polaris on 9/19, brushing into Polaris on 9/21, and bumping into Polaris on 9/26 necessitated re-calibrations which can clearly be seen. However, from 9/26 through 10/3 nine patients were processed with the same calibration since Polaris was not disturbed. Closer observation of all 3 sphere values showed similar stability justifying the decision.

#### A. Can Polaris Reliably View Patients undergoing SPECT

As mentioned earlier, in one male case only 1 abdomen marker was visible. Also, in one female case a garment cloth fold resulted in only the 4 abdomen markers being visible. In all other cases at least some markers on both belts were seen. In the cases where spheres on both belts were not seen, spheres on the abdomen belt were seen. The 45 mm unstretched spacing between belt spheres stretches to about a 70 mm spacing when placed on the patients or volunteers. The distance from the leftmost sphere to the rightmost marker is then about 210 mm on the four marker belts which cover the regions of interest on the upper chest and lower abdomen. These marker spacings were determined to be optimal providing sufficient lateral chest and abdomen coverage for useful torso motion information and still be viewable by Polaris.

Fig. 8 shows average peak-to-peak “Vertical” axis amplitude of respiratory motion on medially located spheres on the chest and abdomen belts. In Fig. 8 (a), 14 volunteers were asked to remain motionless and breathe normally. Vertical amplitude of respiratory movement of spheres on the abdomens was larger than the vertical movement of spheres on the chests for all 9 females (avg. 5.8 mm vs 1.8 mm) and 5

males (avg. 10.4 mm vs 1.7 mm). In Fig. 8 (b), 12 clinical patients were monitored during rest perfusion SPECT imaging with IRB approval, with similar results to the volunteers. For the 4 females the abdomen versus chest average vertical amplitude was 5.6 mm vs. 1.4 mm, and for 8 males it was 9.2 mm vs. 1.6 mm. The chest belt was not visible for one female and male thus those averages were based on 3 and 7 respectively. On average the abdomen sphere vertical motion was larger for males than for females. In both studies, the abdomen-sphere axial amplitude generally remains below 3 mm, with chest-sphere below 2 mm. Lateral amplitudes are generally the smallest due to the medial location of the spheres chosen for reporting. There does not appear to be any noticeable correlation between Body Mass Index (BMI) and respiration amplitude for males or females.

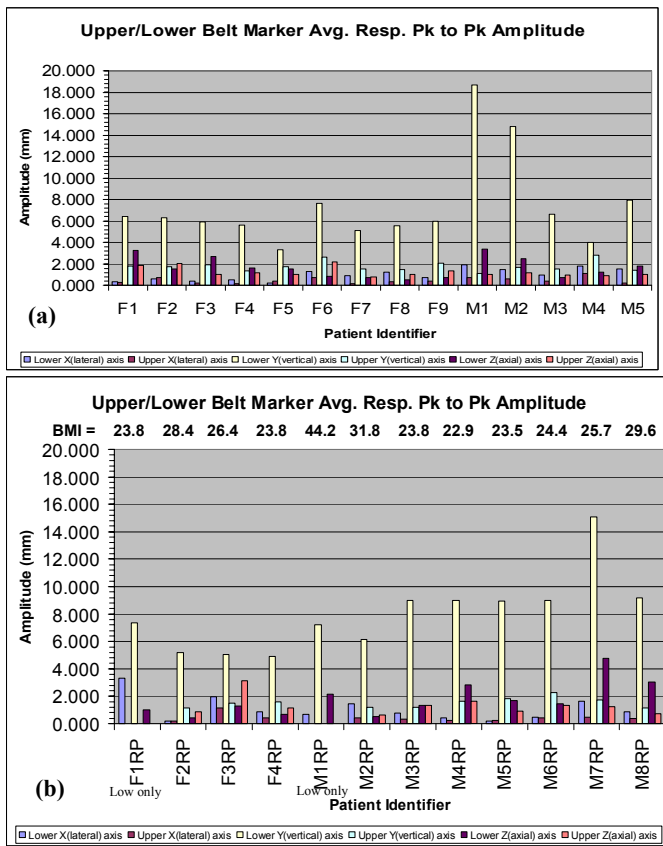


Fig. 8. Average respiratory peak-to-peak amplitude in mm for motion of abdomen and chest spheres located medially on the belts for: (a) 9 female (F1-F9), and 5 male (M1-M5) volunteers; (b) 12 clinical patients, 4 females (F1RP-F4RP), and 8 males (M1RP-M8RP).

### B. How Many Markers are Required to Determine Motion

The upper and lower belts have 4 markers on each belt which span the torso (about 210 mm), Fig. 2 (b), and are still normally viewable by Polaris for most patients. The belts were typically centered on the patients or volunteers, and the most lateral markers are at 105 mm, with the most medial at 35 mm considering a 70 mm marker stretched belt spacing.

Anatomical patient variations sometimes prevent markers from being seen, Fig. 3, (e.g. upper belt markers on an obese

patient), and during respiration and other patient motion markers are sometimes not visible by Polaris. Folds of hospital garments or other clothing sometimes block a marker.

For these reasons the 4 marker belt was utilized in lieu of a 3 marker version which was considered. The reasoning being, that if some markers were not visible on either the upper or lower belt a sufficient number of markers would still be visible to allow 6-DOF motion computations. This requires a minimum of 3 visible markers, with 1 or more from each belt. This would allow rigid-body motion determination for the full patient torso. However, if 3 or 4 markers are visible on a single belt such as the upper one, 6-DOF motion determination for the anatomy in the vicinity of the heart could still be very useful as well..

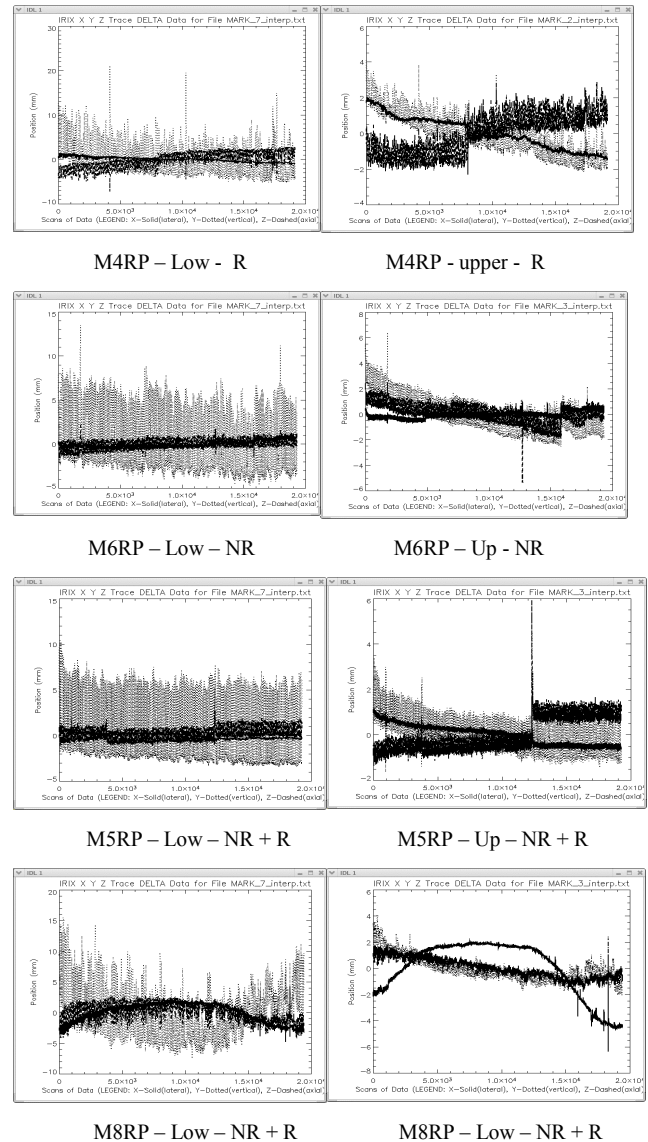


Fig. 9. Typical patient plots of abdomen and chest sphere position data (shown as “actual value”-“average value” for plotting purposes) during the full 16 minute clinical SPECT acquisitions. IRIX SPECT image coordinate axes are: X (lateral), Y (vertical), Z (axial). “R” indicates potential Rigid-Body Motion, and “NR” potential Non-Rigid motion.

### C. Algorithm to Process Raw Polaris Coordinate Data into SPECT Image Coordinates

Fig. 9 shows examples of typical clinical patient data recorded for a single medially located sphere on each of the belts during the approximately 16 minute SPECT acquisitions. The plots shown are the Polaris data after processing to remove phantoms, sort the valid belt markers, and map Polaris coordinate system values to IRIX SPECT image coordinates. Each of the patient plots are paired left and right, showing identifying number first, then Low (abdomen) belt or Up (chest belt), followed by either an R, NR, or NR + R. The R indicates cases of suspect rigid-body motion since motion in both belts can be seen. NR are cases of suspect non-rigid body motion since motion is seen in one belt but not the other. NR + R cases are suspect of both motion types. Fig. 10 plots the change (delta) in end expiration levels for X (lateral), Y (vertical), and Z (axial) axis motions between the beginning and end of the SPECT acquisition. This delta data was derived from the plotted Polaris data for all 12 clinical patients, examples of which are shown in Fig. 9. See Fig. 11 for a detail of how the delta values were derived from the plots for each axis. The largest Y (vertical) end expiration delta seen was -9.00 mm, and was observed in the male with the highest BMI of 44.2.

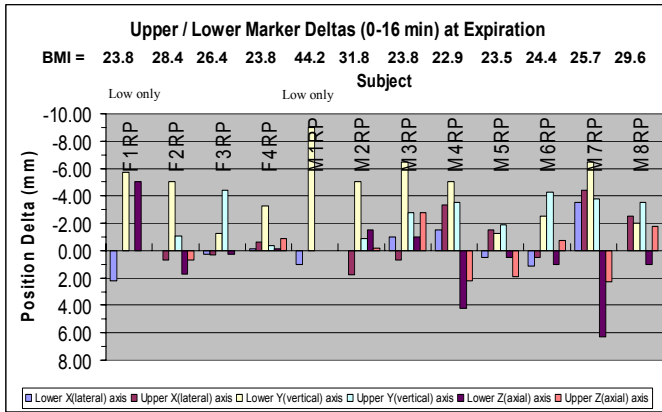


Fig. 10. Plot of X (lateral), Y (vertical), and Z (axial) axis deltas, where (delta=end - beginning) position change for abdomen (lower) and chest (upper) markers for 12 clinical patients.

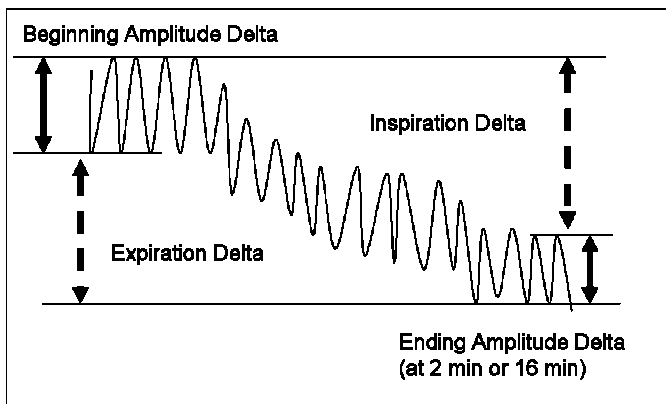


Fig. 11. Detail of how expiration delta values were derived for each axis from the 12 clinical patient plots, examples of which are shown in Fig. 9.

Table 1 shows that the average deltas for All (males and females) of lower belt Y (vertical) axis are largest at an average of -4.42 mm. The Z (axial) axis shows the next largest deltas, and X (lateral) axis the smallest changes from start to end of the clinical SPECT acquisition. The average Male delta of the lower belt Y (vertical) is larger than for Females (-4.72 mm vs. -3.81 mm). The average Male delta of the upper belt Y (vertical) is also larger than for the Females (-2.93 mm vs. -1.93 mm).

TABLE I  
UPPER (CHEST) AND LOWER (ABDOMEN) MEDIAL MARKER DELTAS FOR 12 CLINICAL PATIENTS IN THE X (LATERAL), Y (VERTICAL) AND Z (AXIAL) AXES

	X avg. (mm)	X SD (mm)	Y avg. (mm)	Y SD (mm)	Z avg. (mm)	Z SD (mm)
Lower Female	0.59	1.09	-3.81	2.00	-0.79	2.91
Male	-0.42	1.54	-4.72	2.65	1.31	2.65
Upper Female	0.12	0.65	-1.93	2.16	-0.08	0.79
Male	-1.24	2.31	-2.93	1.18	0.14	2.03
Lower All	-0.08	1.44	-4.42	2.40	0.61	2.80
Upper All	-0.83	2.02	-2.63	1.48	0.07	1.71

### IV. CONCLUSIONS

We have successfully demonstrated the ability of Polaris to monitor 12 clinical patients during actual SPECT acquisitions. We have also quantified the X, Y and Z axis motion observed using end expiration deltas between the start and end of the 16 minute SPECT acquisition, as well as determined the average peak to peak respiration amplitudes over the same time period.

### V. REFERENCES

- [1] Beach, Richard.D., Pretorius, P. Hendrik, Boening, Guido, Bruyant, Philippe P., Feng, Bing, Fulton, Roger R., Gennert, Michael A., Nadella, Suman, King, Michael A., Feasibility of Stereo-Infrared Tracking to Monitor Patient Motion During Cardiac SPECT Imaging, IEEE Transactions on Nuclear Science, Vol. 51, No. 5, 2693-2698, Oct. 2004.
- [2] Beach, Richard.D., Depold, Hans, Boening, Guido, Bruyant, Philippe P., Feng, Bing, Gifford, Howard C., Gennert, Michael A., Nadella, Suman, King, Michael A., An Adaptive Neural Network Approach to Decomposition of Patient Stereo-Infrared Tracking Motion Data During Cardiac SPECT Imaging Using Asymmetric Median Filters, In: Conference Record 2004 - IEEE Nuclear Science Symposium, Medical Imaging Conference (NSS/MIC) October 2004, IEEE, Rome, Italy
- [3] R. R. Fulton, S. R. Meikle, S. Eberl, J. Pfeiffer, R. T. Constable, and M. J. Fulham, "Correction for head movements in positron emission tomography using an optical motion-tracking system", IEEE Transactions on Nuclear Sciences, vol. 49, no. 1, pp. 116-123, 2002.

# Deconvolution of Compartmental Water Diffusion Coefficients in Stroke Using DW-IR MEMRI

G. Nair<sup>1,2</sup>, M. Shazeeb<sup>1,2</sup>, J. Bouley<sup>3</sup>, K. G. Helmer<sup>1</sup>, M. Fisher<sup>3,4</sup>, C. H. Sotak<sup>1,4</sup>

<sup>1</sup>Biomedical Engineering, Worcester Polytechnic Institute, Worcester, MA, United States, <sup>2</sup>GSBS, University of Massachusetts Medical School, Worcester, MA, United States, <sup>3</sup>Neurology, UMassMemorial Health Care, Worcester, MA, United States, <sup>4</sup>Radiology, UMassMemorial Health Care, Worcester, MA, United States

**Introduction:** The apparent diffusion coefficient (ADC) of brain water is known to decrease in ischemia.<sup>1</sup> Although the mechanism of the decrease is not well understood, it is thought to be related to relative changes in the intra- and extra-cellular volume fractions during ischemia.<sup>2,3</sup> We sought to identify the relative contributions of intra- and extracellular water ADC changes during ischemia using Mn<sup>2+</sup> as an intracellular MRI contrast agent. Intracerebroventricular (ICV) infusion of Mn<sup>2+</sup> results in neuronal uptake, selectively shortening the T<sub>1</sub> and T<sub>2</sub> relaxation times of intracellular water. The relative differences in T<sub>1</sub> or T<sub>2</sub> relaxation times between the two compartments can be used to selectively null the signal from one of the compartments.<sup>4</sup> In the first set of experiments, the average T<sub>1</sub> and T<sub>2</sub> relaxation times of water were measured in the intra- and extracellular compartments post-Mn<sup>2+</sup> infusion. Secondly, diffusion-weighted inversion-recovery (DW-IR) images were acquired from each compartment by choosing an inversion time (TI) to selectively null the MRI signal from the other compartment.

**Methods:** All MR imaging was performed on a Bruker Biospin 2T/45 cm horizontal bore system equipped with 200mT/m gradients and a surface coil for RF transmit and receive. Two groups of rats (SD, 275-300g) were used in this study. The first group (n=5) was anesthetized with intraperitoneal injection of chloral hydrate (400 mg/kg) and immobilized on a stereotactic frame. Manganese, 50 µl of 25 mM MnCl<sub>2</sub> in saline, was infused ICV over 2 mins through a burr hole the skull (0.8 mm posterior, 1.2 mm lateral to the bregma, and 4mm below the skull). T<sub>1</sub> was measured using an IR sequence acquired at 2, 12, 24, 48, 72 and 96 hrs time-points post-ICV infusion of Mn<sup>2+</sup>. A sech pulse was used for adiabatic spin-inversion and TI values (21) were spaced logarithmically from 14.88-5000 ms. Other imaging parameters were TR = 7.5 s, TE = 7 ms, FOV = 31 mm, 64 × 64 data matrix with an in-plane resolution of 484 microns and 5 slices of 1mm thickness. T<sub>2</sub> was measured using a CPMG sequence with identical resolution (TR = 5 s, TE varied in 24 steps between 4.5 ms and 108 ms). Bi-exponential T<sub>1</sub> and T<sub>2</sub> maps were calculated using Matlab.

In a second group (n=4), Mn<sup>2+</sup> was infused (ICV) 72 hrs prior to middle cerebral artery occlusion (MCAO). MRI was performed 2 hrs post-MCAO. Eleven DW-IR MRIs were acquired with b-values from 5-1080 s/mm<sup>2</sup> and TR = 5 s, TE = 27 ms, FOV = 31 mm, 64 × 64 matrix acquisition (in-plane resolution of 484 microns), 5 1-mm-thick slices, δ = 8 ms, Δ = 13 ms and diffusion gradients applied in three directions simultaneously. TI values of 100 ms and 450 ms were used to null the intra- and extracellular water signals, respectively. Average ADC was calculated from each brain hemisphere and compared across all 5 slices. A single-tailed, paired-t-test analysis was used; p<0.05 was considered statistically significant.

**Results and Discussion:** T<sub>1</sub>-weighted images acquired at various time points showed uniform enhancement in the brain at 72 hours post-ICV Mn<sup>2+</sup> infusion (the time point used for all experiments). The average bi-exponential T<sub>1</sub> values were T<sub>1a</sub> ~ 150 ms; M<sub>0a</sub> = 64%; T<sub>1b</sub> ~ 700 ms; M<sub>0b</sub> = 34% (**Fig 1**); the bi-exponential T<sub>2</sub> values were T<sub>2a</sub> ~ 9 ms; M<sub>0a</sub> = 66%; T<sub>2b</sub> ~ 51 ms; M<sub>0b</sub> = 34%. Extracellular ADC values calculated from DWIs with TI = 100 ms (intracellular water signal nulled) decreased significantly from 1.3 × 10<sup>-3</sup> mm<sup>2</sup>/s to 1.1 × 10<sup>-3</sup> mm<sup>2</sup>/s during ischemia (**Fig 2**). Similarly, intracellular ADC values calculated from DWIs with TI = 450 ms (extracellular water signal nulled) showed a significant reduction from 0.88 × 10<sup>-3</sup> mm<sup>2</sup>/s to 0.72 × 10<sup>-3</sup> mm<sup>2</sup>/s in the ischemic hemisphere (**Fig 3**). Since Mn<sup>2+</sup> distribution was not uniform in all brain regions, there may be some signal cross-contamination between compartments if each component is not completely nulled at their respective TI values.

**Conclusion:** ICV infusion of Mn<sup>2+</sup> appears to achieve sufficient intracellular concentrations of Mn<sup>2+</sup> to move the inter-compartmental equilibrium water exchange into the slow-exchange regime<sup>5</sup>. When this is the case, it is in principle possible to separate the intra- and extracellular water signals on the basis of differences in their respective T<sub>1</sub> and T<sub>2</sub> relaxation times. The ADCs measured separately from intra- and extracellular water in ischemic rat brain showed a significant reduction during cerebral ischemia. However, the absolute values of both the intra- and extracellular ADCs are somewhat higher than the combined rat-brain ADCs measured from both compartments (~0.8 × 10<sup>-3</sup> mm<sup>2</sup>/s). Furthermore, the percent-ADC reduction following ischemia is not as large in these studies (~15-18%) as that observed from the combined compartments (~30-35%) under similar ischemic conditions. However, the effect of inter-compartmental equilibrium water exchange is not accounted for in either of these cases and this issue may be responsible for some of these differences.

**Reference:** 1) Moseley et al MRM 1990;14:330 2) Neil JJ et al MRM 1996;35:329 3) Duong TQ et al MRM 1998;40:1 4) Silva et al MRM 2002;48:826 5) Labadie et al JMR Ser B 1994;105:99

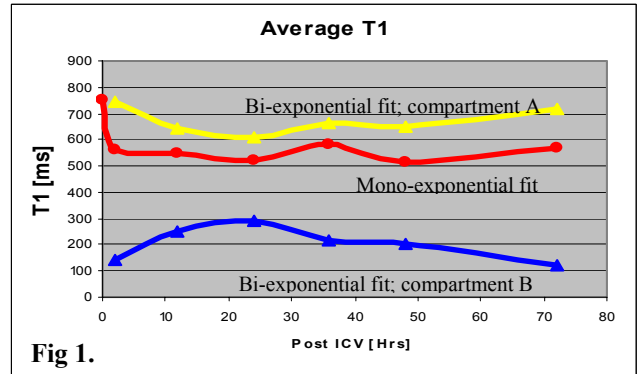


Fig 1.

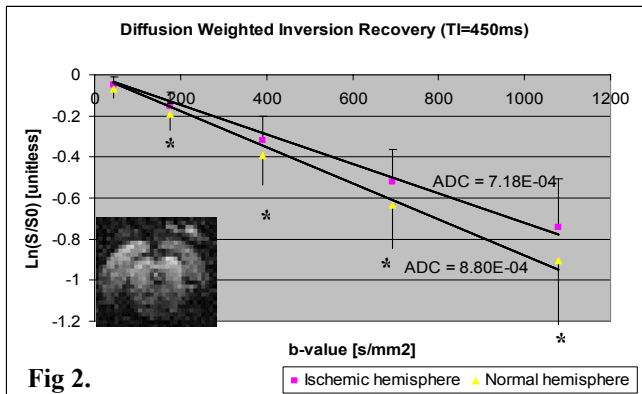


Fig 2.

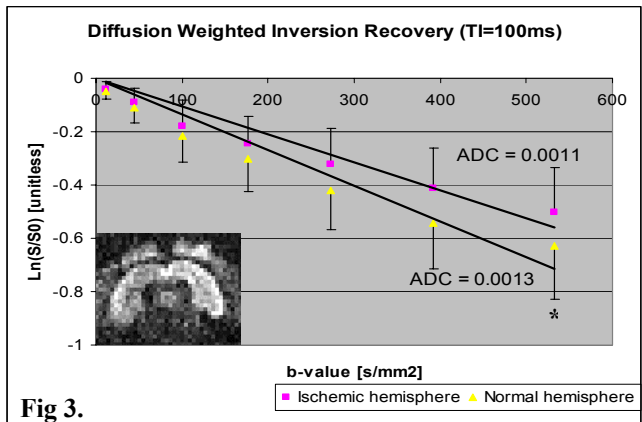


Fig 3.

## Optimization of Piezoelectric Motors to Enhance MR Compatibility for Interventional Devices

Y. Y. Wang<sup>1</sup>, M. S. Shazeeb<sup>2,3</sup>, and G. S. Fischer<sup>1</sup>

<sup>1</sup>Mechanical Engineering, Worcester Polytechnic Institute, Worcester, MA, United States, <sup>2</sup>Biomedical Engineering, Worcester Polytechnic Institute, Worcester, MA, United States, <sup>3</sup>Medical Physics, University of Massachusetts Medical School, Worcester, MA, United States

**Introduction:** MR provides the ability to perform closed loop image-guided surgery. However, the inability to use conventional sensors and actuators in high-field MR limits the availability of assistive technologies for interventional procedures. MR-compatible robotic systems have been investigated by several groups and a review can be found in [1]. The field of MR-compatible robots has yet to come to maturity, with many groups reinventing the wheel when it comes to actuator selection and evaluation. A side by side comparison of actuation techniques with the intent of a fair comparison between technologies is presented in [2]. Inherently MR-compatible actuation techniques include those that require no electrical connection to their controller; thus pneumatic and hydraulic actuation schemes, as well as remote actuation through mechanical means are suitable. Although pneumatics have been successfully used for control of robots in MRI, they either require a complex control scheme to generate the required accuracy for servo control [3] or a complex mechanism and controller design with an inherently limited accuracy for open loop stepping control [4]. A technology that shows significant promise as an actuator for MR-compatible interventional devices is the piezoelectric motor. In their “out of the box” configuration, the Nanomotion piezoelectric linear motor has shown to be adequate for many applications, but far from ideal with SNR losses reported at 20% when running in the scanner [2]. A closed-loop controller based on the PiezoMotor piezoelectric linear motor is independently evaluated in [5] with SNR loss reported at 14%. We present our development of a technique to optimize the PiezoMotor actuator and controller such that the effects on image quality are negligible.

**Materials/Methods:** The motor used in this study is the nonmagnetic version of the Piezo LEGS (PiezoMotor, Uppsala, Sweden). These motors are available in both linear and rotary versions. The motor is powered through a 5m shielded, 24G 6-conductor cable. To ensure adequate shielding, the ground strap on the cable shield is physically attached to the motor housing and the exposed shield and leads extending to the motor are wrapped in aluminum tape with conductive adhesive. The cable runs to a controller (PiezoMotor driver) situated in an RF shielded aluminum enclosure with the cable shield fully grounded to the enclosure at the entrance point with aluminum tape. Inside of the enclosure, a filter bank is placed between the motor leads on the amplifier outputs. The filter is an L-C filter in a Pi configuration with a cutoff frequency of 65 kHz ( $L = 12\mu\text{H}$ ,  $C/2 = 1\mu\text{F}$ ). This cutoff frequency allows the drive signal that reaches a maximum of 3KHz to pass through unaffected while filtering out any residual noise in frequencies near the Larmor frequency (63.9MHz for 1.5T to 127.8MHz for 3T) that would affect image quality. A clean power supply was provided to the amplifier board using 12VDC power from two 6V lantern-type batteries placed inside of the enclosure. The enclosure is fully sealed with conductive aluminum tape and connected to the scanner room ground. The experiments were performed in a Bruker Biospin 2T/45 cm horizontal bore system equipped with 200mT/m gradients. The phantom used in the imaging study was a 25mm ID tube filled with 0.25mM  $\text{MnCl}_2$ . The motor and phantom were placed inside of a custom-made 50mm diameter birdcage coil for RF transmit and receive. The configuration used provides for a very sensitive instrument for measuring degradation of image quality. In the experiments, the controller was placed approximately 3m from the scanner bore.

**Experiments and Results:** The configurations evaluated include: baseline of phantom only, motor with no shielding or filtering (powered and unpowered), motor with exposed inline filters (powered and unpowered), and fully shielded, grounded and filtered motor (powered and unpowered). Ten images were acquired for each configuration under each of two imaging protocols. The two image protocols used in this study were: 1) T1-weighted images, 256X256, TR=400ms, TE=15ms, SW=45.4kHz,  $st/is=2/2.2\text{mm}$ , FOV=8cm, 10slices, Gain = 1200, NEX=2 and 2) T2-weighted images, 256X256, TR=2252ms, TE=150ms, SW=20kHz,  $st/is=2/2.2\text{mm}$ , FOV=8cm, 10slices, Gain = 7000, NEX=1. The SNR of the acquired images was used as the metric of image quality. SNR was calculated as the mean signal in a 25pixel (~8mm) square ROI inside of the phantom divided by the standard deviation of the noise in a 25pixel (~8mm) square ROI in the periphery of the image outside of the phantom and nearby ringing artifacts. The SNR for each configuration was normalized by the average SNR of the 10 baseline images for each imaging protocol. The results are shown in Fig. 1, where the large symbol represents the mean normalized SNR for each configuration and imaging protocol and the smaller points represent the normalized SNR for each of the individual images in the set. The SNR degradation of the final configuration proved to be visually unidentifiable and resulted in a mean SNR loss of 3% in the worst case.

**Discussion:** We have optimized the usage of the PiezoMotor PiezoLEG actuator such that the effect on image quality is negligible. As such, it now appears that if appropriate shielding and filtering is utilized, these motors may serve as viable candidates for high accuracy MRI-compatible manipulators. We are currently developing a custom multi-axis driver and power distribution boards for these motors with incorporated filtering and shielding. The initial application for these motors will be a robotic device for neurosurgery where high precision without loss of image quality is essential.

### References:

- [1] Tsekos, N.V., Khanicheh, A., Christoforou, E., Mavroidis, C. Magnetic resonance-compatible robotic and mechatronics systems for image-guided interventions and rehabilitation. *An Rev BME*. Aug 2007; 9:351-387
- [2] Fischer G.S., Krieger A., Iordachita I., Csoma C., Whitcomb L., Fichtinger G., Mri compatibility of robot actuation techniques – a comparative study. *MICCAI*. Sep 2008; 5242: 509-517.
- [3] Fischer G.S., Iordachita I., Csoma C., Tokuda J., DiMaio S.P., Tempany C.M., Hata N., Fichtinger G., Mri-compatible pneumatic robot for transperineal prostate needle placement. *Trans Mech*. Jun 2008; 13(3):295-305.
- [4] Stoianovici, D., Patriciu, A., Petrisor, D., Mazilu, D., Kavoussi, L. A new type of motor: pneumatic step motor. *Trans Mech*. Feb 2007; 12(1): 98-106.
- [5] Elhawary, H., Zivanovic, A., Rea, M., Davies, B., Besant, C., McRobbie, D., de Souza, N., Young, I., Lamprth, M.: The feasibility of mr-image guided prostate biopsy using piezoceramic motors. *MICCAI*. Nov 2006; 4190:519-526.

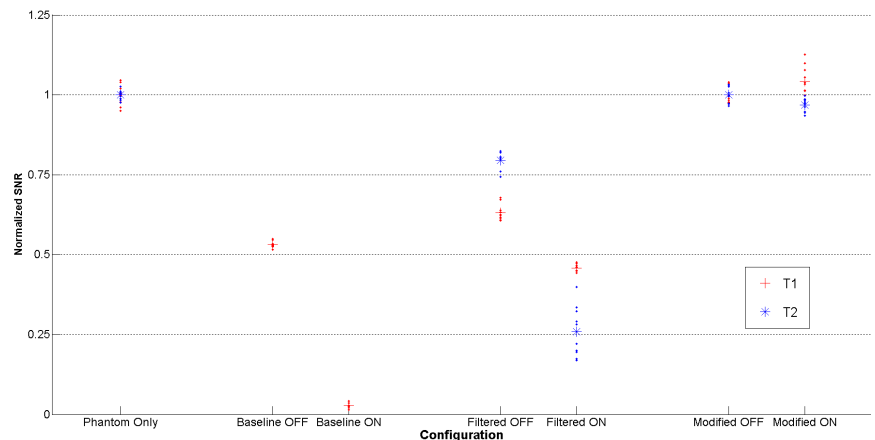


**Figure 1:** Evaluation of MR-compatibility in varying configurations under two imaging protocols. Large markers represent mean normalized SNR and smaller points represent individual SNR values for each of the ten images in the set. In the final filtered and shielded configuration, mean SNR loss was limited to only 3% at the worst case under the more sensitive T2 imaging.

# Targeted Imaging of EGF Receptor Expression in Gli36 Tumor Xenografts Using Monoclonal Antibody Conjugates

M. S. Shazeeb<sup>1,2</sup>, C. H. Sotak<sup>1,3</sup>, and A. Bogdanov<sup>3</sup>

<sup>1</sup>Department of Biomedical Engineering, Worcester Polytechnic Institute, Worcester, MA, United States, <sup>2</sup>Graduate School of Biomedical Sciences, University of Massachusetts Medical School, Worcester, MA, United States, <sup>3</sup>Department of Radiology, University of Massachusetts Medical School, Worcester, MA, United States

**Introduction:** Overexpression of wtEGFR (170kD epidermal growth factor receptor) due to gene amplification is implicated in the development of aggressive gliomas. Receptor imaging *in vivo* could potentially provide more accurate tumor detection, typing, and staging. The goal of this study was to image EGFR-overexpressing orthotopic human glioma tumors using local retention of a paramagnetic molecular substrate di(tyramido)-DTPA(Gd) (diTyr-DTPA(Gd), Fig. 1A) as a strategy of targeted MR signal enhancement. EGF receptor was targeted by using monoclonal antibody (humanized mAb EMD72000, Merck KGaA) conjugates with peroxidase (HRP) and glucose oxidase (GO) as a self-complementing enzymatic signal amplification system (Bogdanov et al. 2007). The substrate (hydrogen peroxide) for the key enzymatic reaction, catalyzed by a HRP conjugate was generated by a conjugate of mAb with glucose oxidase (GO) as depicted in Fig. 1B. MR signal was generated at the EGFR expression sites due to a binding of reactive intermediate products of diTyr-DTPA(Gd) oxidation by HRP.

**Methods:** Paramagnetic substrate diTyr-DTPA(Gd) was synthesized as shown in Fig. 1A (Querol et al. 2007). mAb conjugates were synthesized by linking HRP or GO to mAb via bisaromatic hydrazone bonds. Size-exclusion HPLC purified conjugates were characterized in human glioma Gli36 cell culture and the ratios of HRP and GO conjugates were selected to provide the maximum signal at the lowest toxicity. Gli36ΔEGFR tumor xenografts were stereotactically implanted in the brains of athymic rats. MR images were acquired in a Philips Achieva 3.0T/60 cm equipped with 80mT/m actively shielded gradients. T1-weighted (T1wt) spin-echo (SE) MRI was performed with the following parameters: TR/TE = 700ms/8.2ms, FOV = 2.56 cm X 2.56 cm, matrix = 256x128, NEX = 4. Two weeks after tumor implantation, each animal was anesthetized with isoflurane and imaged on two occasions. 1) Day 1 – a pre-contrast image was acquired followed by IV injection of 0.1 mmol/kg diTyr-DTPA(Gd). Twenty T1wt images were then acquired over a 2-h period. 2) Day 2 – targeted mAb conjugates (100 μg mAb/animal) were injected IV. Three hours later, a pre-contrast image was acquired followed by IV injection of 0.1 mmol/kg diTyr-DTPA(Gd). Thirty T1wt images were then acquired over a 3-h period. Pre-contrast T2wt SE images were acquired on both days to corroborate the presence of tumor observed in the T1wt slices. Animals were sacrificed and the frozen brain sections were stained for peroxidase activity and EGFR expression.

**Results and Discussion:** T1wt images showed strong initial enhancement of the tumor within minutes after IV contrast injection – either with (Day 2) or without (Day 1) the preinjection of mAb conjugates (Fig. 2). However, the initial enhancement of the tumor following IV injection of diTyr-DTPA(Gd) with the conjugates (Fig 2B – 8 min) was significantly higher than that on Day 1 in the same animal (Fig. 2A – 9 min). Furthermore, contrast agent retention was higher on Day 2 (Fig. 2B) – as compared to Day 1 (Fig. 2A) – particularly in the tumor rim region over the same time period. Spatial deconvolution of the tumor signal showed different rates of contrast agent washout for the rim and the core regions. Bioelimination of diTyr-DTPA(Gd) was quantified by fitting the temporal signal-intensity decay for each tumor region. For Day 1, a monoexponential [Eq. 1] best modeled the data. For Day 2, a biexponential [Eq. 2] was a more appropriate model.

$$y_{mono} = A_0 \cdot e^{-t/\tau_0} + offset \quad [Eq. 1]$$

$$y_{bi} = A_1 \cdot e^{-t/\tau_1} + A_2 \cdot e^{-t/\tau_2} \quad [Eq. 2]$$

For the contrast agent without conjugates (Day 1), the washout time constant ( $\tau_0$ ) for the rim (54±20 ms) was significantly higher ( $P < 0.02$ ) than that of the core region (35±9 ms) (Fig. 3A). This difference was attributed to the higher vascular density in the periphery of the tumor. For the Day 1 data, the single component – with time constant  $\tau_0$  – was attributed to unbound contrast agent. For the contrast agent with conjugates (Day 2), the biexponential model yielded a long and a short signal-decay time constant ( $\tau_1$  and  $\tau_2$ , respectively) for both the tumor rim and core regions (Fig. 3B). The component with the short time constant ( $\tau_2$ ) was attributed to unbound contrast agent while the component with the long time constant ( $\tau_1$ ) was attributed to contrast agent bound to the conjugate. The time constant associated with the bound contrast agent ( $\tau_1$ ) was not significantly different between the rim and the core regions. However, for the component associated with the unbound contrast agent, the time constant ( $\tau_2$ ) for the rim (22±9 ms) was significantly higher ( $P < 0.03$ ) than that of the core region (9±4 ms) (Fig. 3B). Furthermore, for the Day 2 data, the time constants associated with the unbound contrast agent ( $\tau_2$ ) in the tumor rim and core regions were significantly less than the corresponding washout time constants ( $\tau_0$ ) in the same regions on Day 1 (22±9 ms vs. 54±20 ms in the rim ( $P < 0.002$ ); 9±4 ms vs. 35±9 ms in the core ( $P < 0.00003$ ), respectively). Although the contrast agent is considered to be unbound in each case, the reduced washout times on Day 2 may arise from a decrease in vascular permeability due to the perivascular accumulation of high-affinity antibody-conjugates (Thurber et al. 2008) and associated cytotoxicity. The presence of extravasated and bound conjugates in tumor tissue was proven by using anti-HRP and anti-GO histochemical staining of the frozen brain sections.

**Conclusions:** Following conjugate administration (Day 2), the increase in contrast agent retention was attributed to a second contrast-agent component (with the long time constant,  $\tau_1$ ) that was not present when diTyr-DTPA(Gd) alone was administered (Day 1). This long-retained component is consistent with enzyme-mediated coupling of the paramagnetic agent to EGFR-overexpressing cells in the tumor; allowing effective MRI visualization of conjugate co-localization at the targeted site.

**References:** Bogdanov, A., et al. (2007). *Bioconjug Chem* 18: 1123-30. Querol, M., et al. (2007). *ChemBiochem* 8: 1637-41. Thurber, GM, et al. (2008). *Adv Drug Del Revs* 60: 1421-1434.

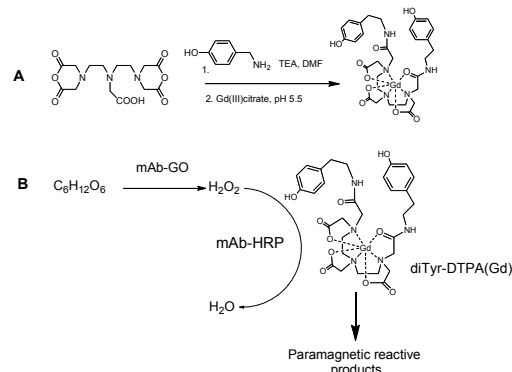


**Fig. 1 A** – Chemical synthesis diTyr-DTPA(Gd); **B** – Reaction of peroxidase substrate diTyr-DTPA(Gd) with the enzyme pair (glucose oxidase/peroxidase) conjugated to anti-EGFR mAb.

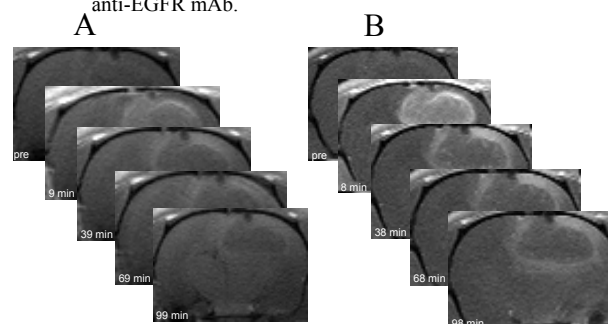


**Fig. 2** – Sequential T1wt rat brain images showing Gli36 tumor xenografts. **A**) Day 1 – after IV injection of diTyr-DTPA(Gd) with no conjugates. **B**) Day 2 – after IV injection of di-(tyramido)-DTPA (Gd) with conjugates in the same animal.

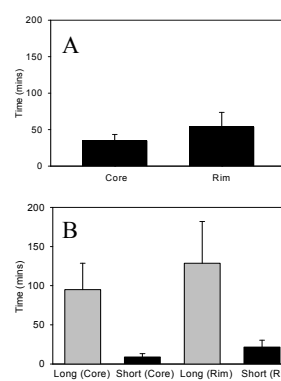


**Fig. 3 – A**) Day 1 – washout time constants  $\tau_0$  for diTyr-DTPA(Gd) in the absence of conjugates in tumor rim and core regions (n=8).

**B**) Day 2 – long  $\tau_1$  and short  $\tau_2$  washout time constants for diTyr-DTPA(Gd) in the presence of conjugates in tumor rim and core regions (n=4).



## Novel hydroxytryptophan-based Gd chelating substrate for imaging myeloperoxidase activity.

A. A. Bogdanov<sup>1</sup>, Y. Xie<sup>2</sup>, and M. S. Shazeeb<sup>2</sup>

<sup>1</sup>Radiology, UMASS Medical School, Worcester, MA, United States, <sup>2</sup>UMASS Medical School

**Introduction:** Myeloperoxidase (MPO) is one of the crucial imaging targets that has clear outcome- predictive value in several diseases, including myocardial infarction and stroke [1]. MPO has also been implicated in the progression of cancer, several CNS pathologies, and in the development of unstable atheroma. Because the catalytic activity of MPO is preserved in live tissue, the enzymatic activity of MPO can be used as a marker of inflammation sites *in vivo*. We previously synthesized and tested several paramagnetic complexes of mono- and bis- amides of macrocyclic and linear chelates that “sense” MPO activity [2-4]. As a result of MPO-mediated catalysis, the above sensors oligomerize and/or form covalent bonds with proteins resulting in increased molar relaxivity ( $r_1$  and  $r_2$ ). This enables MR imaging of MPO activity *in vivo*. Although the existing paramagnetic MPO sensors have very high kinetic stability [5], the thermodynamic stability of bisamides is usually compromised and the solubility of substituted tryptamides in water is limited. The goal of the current study was to synthesize and characterize a novel bifunctional MPO sensor with the same number of donor atoms as in DTPA (i.e. N3O5) in anticipation of improved thermodynamic stability and better solubility.

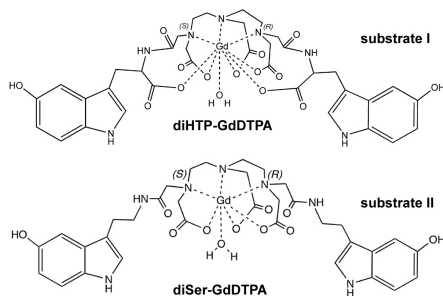


Fig. 1. Structures of MPO substrates I and II

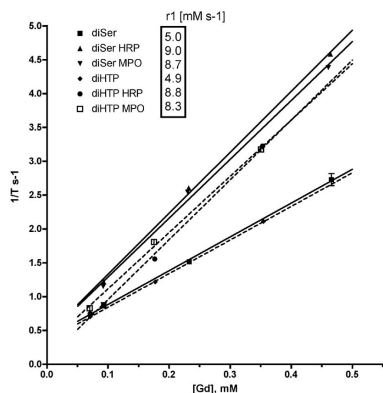


Fig. 2. Relaxivities of chelated Gd in substrate I and substrate II and relaxivities of reaction mixtures containing MPO/GOX or HRP/GOX enzyme pairs.

a potential mechanism of relaxivity increase as a consequence of an MPO-catalyzed reaction. No apparent cross-linking of proteins was observed in the case of substrate II. Imaging of phantoms at 3T (Fig. 3, spin-echo sequence, TR/TE=200/30ms, NEX=1), as expected, showed smaller increase of  $r_1$  (20%) at this field strength than at 0.47T. HRP resulted in a strong 1.9-fold increase of  $r_2$  in the case of substrate II but no such changes were observed with substrate I proving a lack of product aggregation.

**Conclusions:** Bis-HTrp-DTPA(Gd) is a novel paramagnetic reducing substrate of MPO. It results in MPO-mediated increase of Gd relaxivity similar to that of bis-5HT-DTPA(Gd). However, Bis-HTrp-DTPA(Gd) has high water solubility and undergoes MPO-specific conversion into protein cross-linking reactive intermediates. We anticipate it to be an efficient sensor for *in vivo* imaging of MPO activity due to potential binding to tissue proteins in inflammatory lesions.

**References:** 1. Brennan ML *et al.* NE J Med 349: 1595, 2003; 2. Ronald JA *et al.* Circulation 120:592, 2009; 3. Chen JW *et al.* MRM 52:1021, 2004; 4. Querol M *et al.*, Org Lett. 17, 1719, 2005; 5. Rodriguez E *et al.* JACS 132:168, 2009,

**Methods:** An octadentate ligand (bis-amide of DTPA) was synthesized by reacting hydroxytryptophan, a naturally occurring amino acid, with DTPA dianhydride in the presence of pyridine. Gadolinium was trans-chelated from Gd citrate. The resultant chelate was purified by acetone precipitation and purified by C18-HPLC using a gradient of acetonitrile. The obtained product (bis-HTrp-DTPA(Gd), substrate I) was characterized by using <sup>1</sup>H, <sup>13</sup>C NMR and TI-MS. The control substrate (bis-5-hydroxytryptamide) of Gd DTPA (substrate II) was synthesized as described in [4]. The comparative substrate activation studies were performed using glucose oxidase GOX/MPO or GOX/horseradish peroxidase (HRP, positive control) as complementing activity-coupled enzymatic pairs (3 iU GOX : 1.5 iU MPO or HRP) in the presence of 0.1-5 mM of paramagnetic MPO substrate and 5 mM glucose. The reaction was terminated by sodium azide (5 mg/ml) after 0.5 h (HRP) or 2 h (MPO). Gradient SDS-PAGE (5-15%) was performed using samples incubated in the presence or the absence of the substrates to account for potential protein cross-linking using silver staining.

**Results and Discussion:** The structure of the purified chelate was proven by 1H NMR spectrometry and MALDI-ITMS ( $m/z$  796.4 ( $C_{36}H_{43}N_7O_{14} - H^+$ )). The gadolinium complex of the above chelate ( $m/z$  951.3, Fig. 1), i.e. substrate I, was further tested in the presence of peroxide-generating GOX and either MPO, or HRP. The additional substrate *in vitro* efficacy testing involved comparing the MPO and HRP-mediated relaxivity increase in the presence of a hydrogen peroxide source (glucose/glucose oxidase) to that of a previously described and *in vivo* tested substrate II [2,5].

We observed an MPO-dependent increase of molar relaxivity of Gd in the reaction mixture from 4.9 to 8.3 [ $mM \cdot s$ ]<sup>-1</sup> (1.7 fold at 0.47T) at 2 h (Fig. 2). HRP, which has a higher effective kinetic constant, showed a similar 1.8-fold increase of relaxivity under identical conditions. In the case of bis-5HT-DTPA(Gd), we observed very similar changes of relaxivity (1.7 vs. 1.8 times, respectively), suggesting that both Gd chelates I and II were used by peroxidases as reducing substrates. However, there were notable differences in terms of the type of reaction products: substrate II and HRP gave insoluble cross-linked final products if the reaction proceeded for several hours while the products of substrate I were soluble. Gradient SDS-PAGE analysis of enzymatic activation of substrate I showed the formation of 10-20 kDa oligomerized products (Fig. 3, arrow) in the case of HRP, while in the reaction mixture containing MPO we observed the formation of a new band of cross-linked proteins. This result suggested covalent binding to proteins as

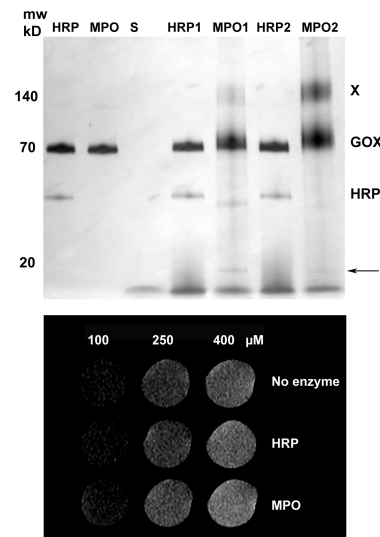


Fig. 3. Top: Gel electrophoresis of MPO and HRP-containing reaction mixtures. Cross-linked product is marked with X. Bottom: T1W SE images of reaction mixtures containing MPO/GOX or HRP/GOX enzyme pairs at 3T.

## Dose Dependence of $T_1$ Relaxation Time in the Rat Brain after Subcutaneous Injection of $MnCl_2$

M. S. Shazeeb<sup>1,2</sup>, and C. H. Sotak<sup>1,3</sup>

<sup>1</sup>Biomedical Engineering, Worcester Polytechnic Institute, Worcester, MA, United States, <sup>2</sup>Graduate School of Biomedical Sciences, University of Massachusetts Medical School, Worcester, MA, United States, <sup>3</sup>Radiology, University of Massachusetts Medical School, Worcester, MA, United States

**Introduction:** Divalent manganese ion ( $Mn^{2+}$ ) is a widely used  $T_1$  contrast agent in manganese-enhanced MRI (MEMRI) studies to visualize functional neural tracts and anatomy in the brain *in vivo*. In animal studies, the goal is to use a dose of  $Mn^{2+}$  that will maximize the contrast while minimizing its toxic effects. In rodents, systemic administration of  $Mn^{2+}$  via intravenous (IV) injection has been shown to create unique MRI contrast in the brain at a maximum dose of 175 mg/kg [1, 2]. The subcutaneous (SC) route can deliver  $Mn^{2+}$  at a maximum dose of 320 mg/kg (LD<sub>50</sub> value). However, IV administration of  $Mn^{2+}$  results in faster bioelimination of excess  $Mn^{2+}$  from the plasma due to a steep concentration gradient between plasma and bile. By contrast, following SC injection,  $Mn^{2+}$  is released more slowly into the bloodstream, thus avoiding immediate hepatic elimination [3]. Therefore, SC administration of  $Mn^{2+}$  will result in prolonged accumulation of  $Mn^{2+}$  in the brain via the choroid plexus than that obtained via IV administration of  $Mn^{2+}$ . The goal of this study was to investigate the MRI dose response of  $Mn^{2+}$  in rat brain following SC administration of  $Mn^{2+}$ .

**Methods:** Experiments were carried out using 12 male Sprague Dawley rats weighing 200-450 g.  $MnCl_2$  was administered using SC injection at three different doses: 75 (n=3), 150 (n=3), and 300 (n=6) mg/kg. All MR imaging was performed at 2.0T. Multi-slice  $T_1$ -weighted ( $T_1$ -WT) MR images (TR/TE = 700/15 ms) were acquired pre-injection and 6, 24, 72, and 168 h following the SC injection of  $Mn^{2+}$ .  $T_1$  relaxation times were measured using an inversion recovery sequence (TR/TE = 10,000/4.8 ms, 16 inversion time (TI) points ranging from 15 ms to 3300 ms) acquired at the same time points as the  $T_1$ -WT images. Three different brain regions of interests (ROIs) were selected (cortex, sub-cortical region, and caudate nucleus) from three acquired slices. A mean ROI value from each TI point was used to calculate the respective tissue  $T_1$  values.

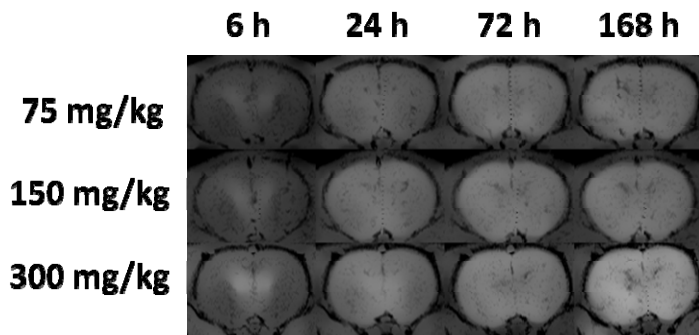


**Fig. 1** – Dose dependence and time course of MEMRI contrast.  $T_1$ -weighted axial MR image sets are shown as a function of varying doses of  $MnCl_2$  and as a function of time after subcutaneous injection of  $MnCl_2$ .

**Results and Discussion:**  $T_1$ -WT signal enhancement (SE) was apparent in the rat brain at 6 h which expanded from the ventricles to the sub-cortical and cortex regions. Uniform enhancement was achieved throughout the brain by the 72 h time-point at all administered  $Mn^{2+}$  doses which persisted up to 168 h. The  $T_1$ -WT SE was proportional to the dose of  $Mn^{2+}$  administered. Greater  $Mn^{2+}$  uptake occurred in the sub-cortical region than the cortex for all the SC  $Mn^{2+}$  doses administered causing greater shortening of the  $T_1$  relaxation time in the sub-cortical region ROI than the cortex ROI (Fig. 2). ANOVA test for mixed models showed a significant effect of  $Mn^{2+}$  dose ( $P < 0.01$ ) and time point after  $Mn^{2+}$  injection ( $P < 0.0001$ ) on the reduction of  $T_1$  relaxation times in the cortex (Fig. 2A) and sub-cortical (Fig. 2B) regions. Similar dose-dependent behavior of  $T_1$  relaxation times has been observed in different regions of the mouse brain following IV injection of  $Mn^{2+}$  [2]; however, the prolonged enhancement obtained with SC  $Mn^{2+}$  injection (up to at least 168 h) is contrary to the short-term enhancement observed when  $Mn^{2+}$  was administered via IV [1] or even intrathecal injection [4].

**Conclusion:** This study is the first to demonstrate a dose-dependent response of  $Mn^{2+}$  on  $T_1$  relaxation times in the rat brain following SC injection of  $Mn^{2+}$ . SC administration of  $Mn^{2+}$  leads to a more prolonged enhancement in the brain than IV  $Mn^{2+}$  administration which can be useful for longitudinal *in vivo* studies that require brain enhancement to persist for a long period of time to visualize neuroarchitecture like in Alzheimer's disease, Parkinson's disease, amyotrophic lateral sclerosis, and other neurodegenerative diseases.

**References:** [1] Aoki *et al.* (2004). *NeuroImage* **22**: 1046-59; [2] Lee *et al.* (2005). *Magn Reson Med* **53**(3): 640-648; [3] Bertinchamps *et al.* (1966). *Am J Physiol* **211**(1): 217-224; [4] Liu *et al.* (2004). *Magn Reson Med* **51**(5): 978-987.

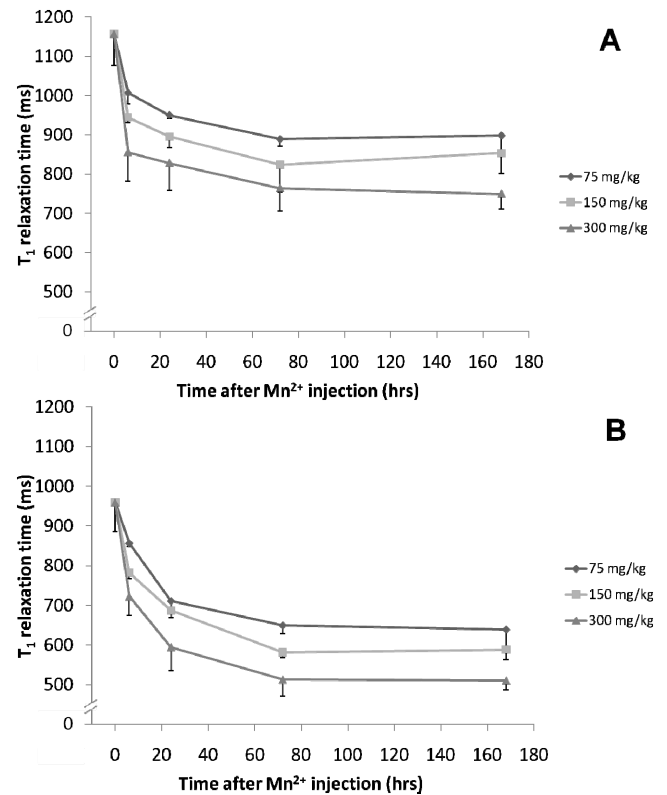


**Fig. 2** – Plots of *in vivo* mean  $T_1$  relaxation times ( $-1$  SD) as a function of time after subcutaneous injection of  $MnCl_2$  at three different doses in the A) cortex ROI, and B) sub-cortical region

M. S. Shazeeb<sup>1,2</sup>, C. H. Sotak<sup>1,3</sup>, and A. Bogdanov, Jr.<sup>3,4</sup>

<sup>1</sup>Biomedical Engineering, Worcester Polytechnic Institute, Worcester, MA, United States, <sup>2</sup>Graduate School of Biomedical Sciences, University of Massachusetts Medical School, Worcester, MA, United States, <sup>3</sup>Radiology, University of Massachusetts Medical School, Worcester, MA, United States, <sup>4</sup>Cell biology, University of Massachusetts Medical School, Worcester, MA, United States

**Introduction:** The goal of this study was to image EGFR- and EGFRvIII-overexpressing aggressive orthotopic human glioma tumors using local retention of peroxidase-generated products of a paramagnetic molecular substrate di(tyramido)-DTPA(Gd) (diTyr-DTPA(Gd), Fig. 1). EGFR receptor variants were targeted by using specific humanized anti-EGFR EMD72000 and non-specific anti-EpCAM mAb monoclonal antibody (mAb) conjugates. The conjugates were synthesized using peroxidase (HRP) and glucose oxidase (GO) as a self-complementing enzymatic signal amplification system [1] as depicted in Fig. 1. MR signal was generated at the EGFR expression sites due to co-localization of targeted conjugates which resulted in specific binding of reactive intermediate products of diTyr-DTPA(Gd) oxidation by HRP-mAb conjugate.

**Methods:** The paramagnetic substrate diTyr-DTPA(Gd) was synthesized as described in [2]; mAb conjugates were synthesized by linking HRP or GO to mAb via bisaromatic hydrazone bonds. Size-exclusion HPLC purified conjugates were characterized in human glioma Gli36ΔEGFR cell culture and the ratios of HRP and GO conjugates were selected to provide the maximum signal with low cytotoxicity. Gli36ΔEGFR tumor xenografts were stereotactically implanted in the brains of athymic rats. MR images were acquired at 3T. T1-weighted (T1-WT) spin-echo MRI was performed with the following parameters: TR/TE = 700ms/8.2ms, FOV = 2.56 cm X 2.56 cm, matrix = 256x256, NEX = 4. Two weeks after tumor implantation, each animal was anesthetized with isoflurane and imaged on two occasions. 1) Day 1 – a pre-contrast image was acquired followed by IV injection of 0.1 mmol/kg diTyr-DTPA(Gd). Twenty T1-WT images were then acquired over a 2-h period. 2) Day 2 – either specific anti-EGFR or non-specific EpCAM conjugates (100 μg mAb/animal) were injected IV. Four hours later, a pre-contrast image was acquired followed by IV injection of 0.1 mmol/kg diTyr-DTPA(Gd). Thirty T1-WT images were then acquired over a 3-h period. Animals were sacrificed and frozen brain sections were stained for peroxidase activity and EGFR expression.

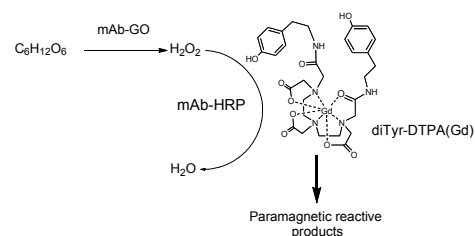


**Fig. 1** – Reaction of peroxidase substrate diTyr-DTPA(Gd) with the enzyme pair (glucose oxidase/peroxidase) conjugated to either anti-EGFR or anti-EpCAM mAb.

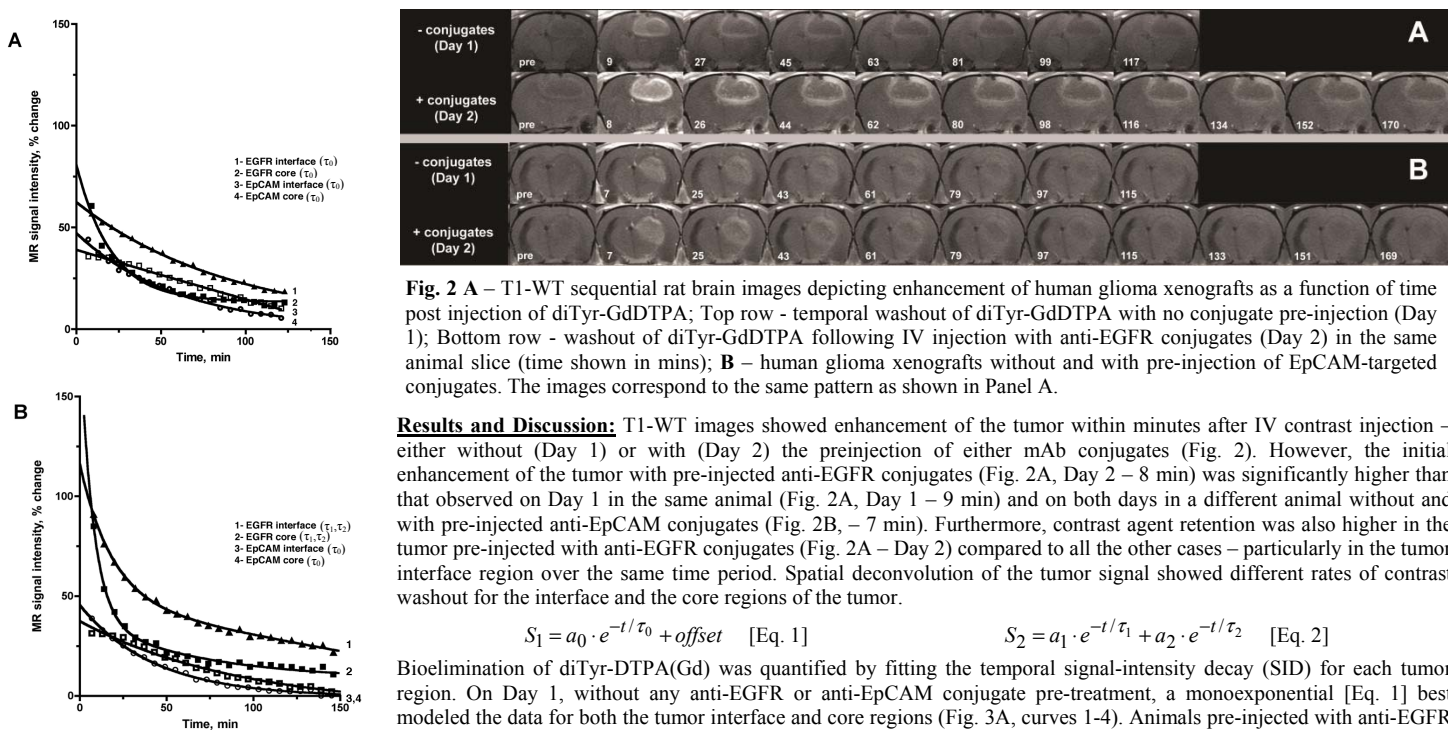


**Fig. 2 A** – T1-WT sequential rat brain images depicting enhancement of human glioma xenografts as a function of time post injection of diTyr-GdDTPA; Top row - temporal washout of diTyr-GdDTPA with no conjugate pre-injection (Day 1); Bottom row - washout of diTyr-GdDTPA following IV injection with anti-EGFR conjugates (Day 2) in the same animal slice (time shown in mins); **B** – human glioma xenografts without and with pre-injection of EpCAM-targeted conjugates. The images correspond to the same pattern as shown in Panel A.

**Results and Discussion:** T1-WT images showed enhancement of the tumor within minutes after IV contrast injection – either without (Day 1) or with (Day 2) the preinjection of either mAb conjugates (Fig. 2). However, the initial enhancement of the tumor with pre-injected anti-EGFR conjugates (Fig. 2A, Day 2 – 8 min) was significantly higher than that observed on Day 1 in the same animal (Fig. 2A, Day 1 – 9 min) and on both days in a different animal without and with pre-injected anti-EpCAM conjugates (Fig. 2B, – 7 min). Furthermore, contrast agent retention was also higher in the tumor pre-injected with anti-EGFR conjugates (Fig. 2A – Day 2) compared to all the other cases – particularly in the tumor interface region over the same time period. Spatial deconvolution of the tumor signal showed different rates of contrast washout for the interface and the core regions of the tumor.

$$S_1 = a_0 \cdot e^{-t/\tau_0} + offset \quad [\text{Eq. 1}]$$

$$S_2 = a_1 \cdot e^{-t/\tau_1} + a_2 \cdot e^{-t/\tau_2} \quad [\text{Eq. 2}]$$

Bioelimination of diTyr-DTPA(Gd) was quantified by fitting the temporal signal-intensity decay (SID) for each tumor region. On Day 1, without any anti-EGFR or anti-EpCAM conjugate pre-treatment, a monoexponential [Eq. 1] best modeled the data for both the tumor interface and core regions (Fig. 3A, curves 1-4). Animals pre-injected with anti-EGFR conjugates (Fig. 3B, curves 1,2) exhibited biexponential signal decay both in the tumor interface and core regions; however, after the pre-injection of non-specific anti-EpCAM conjugates (Fig. 3B, curves 3,4), the SID showed only a single decay component. The single component of monoexponential decay – decay time constant (DTC)  $\tau_0$  – was attributed to unbound contrast agent. The two components of the biexponential model yielded a long and a short DTC ( $\tau_1$  and  $\tau_2$ , respectively). The component with the short DTC ( $\tau_2$ ) was attributed to unbound contrast agent while the component with the long DTC ( $\tau_1$ ) was attributed to contrast agent bound to the cells.

**Conclusions:** Following anti-EpCAM conjugate pre-treatment or no conjugate administration, a monoexponential SID of the contrast agent indicates the absence of specific mAb conjugates binding to the tumor. This is expected since anti-EpCAM conjugates do not bind to glioma cells and diTyr-DTPA(Gd) does not bind to tumor cells in the absence of conjugates. With anti-EGFR conjugate administration, a biexponential mode of contrast SID indicates specific binding of paramagnetic products to cells, which led to long-term enhancement of MR signal (Fig. 2A – Day 2). This long-lasting MR signal component is consistent with enzyme-mediated coupling of the paramagnetic agent to EGFR-overexpressing cells in the tumor allowing effective MRI visualization of conjugate co-localization at the specific targeted site.

**Fig. 3** – Normalized T1-WT signal intensities (derived from the same tumors shown in Fig. 2) measured in the interface or core regions of Gli36ΔEGFR tumors prior to injection of conjugates (A), and after the pre-injection of either specific anti-EGFR (“EGFR”) or non-specific EpCAM (“EpCAM”) conjugates (B) as a function of time post-diTyr-DTPA(Gd) injection.